

HIGH-PERFORMANCE PERIODIC ANTENNAS  
WITH HIGH ASPECT RATIO VERTICAL FEATURES AND  
LARGE INTERCELL CAPACITANCES  
FOR MICROWAVE APPLICATIONS

A Thesis Submitted to the College of  
Graduate Studies and Research  
In Partial Fulfillment of the Requirements  
for the Degree of Doctor of Philosophy  
In the Department of Electrical and Computer Engineering  
University of Saskatchewan  
Saskatoon

by  
Mehdi Hosseini

## **Permission to Use**

In presenting this thesis in partial fulfillment of the requirements for a Postgraduate degree from the University of Saskatchewan, I agree that the Libraries of this University may make it freely available for inspection. I further agree that permission for copying of this thesis in any manner, in whole or in part, for scholarly purposes may be granted by the professor or professors who supervised my thesis work or, in their absence, by the Head of the Department or the Dean of the College in which my thesis work was done. It is understood that any copying, publication, or use of this thesis or parts thereof for financial gain shall not be allowed without my written permission. It is also understood that due recognition shall be given to me and to the University of Saskatchewan in any scholarly use which may be made of any material in my thesis.

Requests for permission to copy or to make other use of material in this thesis in whole or part should be addressed to:

Head of the Department of Electrical and Computer Engineering

University of Saskatchewan

Saskatoon, Saskatchewan, Canada

S7N 5A9

## Abstract

Modern communications systems are evolving rapidly to address the demand for data exchange, a fact which imposes stringent requirements on the design process of their RF and antenna front-ends. The most crucial pressure on the antenna front-end is the need for miniaturized design solutions while maintaining the desired radiation performance. To satisfy this need, this thesis presents innovative types of periodic antennas, including electromagnetic bandgap (EBG) antennas, which are distinguished in two respects. First, the periodic cells contain thick metal traces, contrary to the conventional thin-trace cells. Second, such thick traces contain very narrow gaps with very tall sidewalls, referred to as high aspect ratio (HAR) gaps.

When such cells are used in the structure of the proposed periodic antennas, the high capacitance of HAR gaps decreases the resonance frequency, mitigates conduction loss, and thus, yields considerably small high efficiency antennas. For instance, one of the sample antenna designs with only two EBG cells offers a very small XYZ volume of  $0.25\lambda \times 0.28\lambda \times 0.037\lambda$  with efficiency of 83%. Also, a circularly polarized HAR EBG antenna is presented which has a footprint as small as  $0.26\lambda \times 0.29\lambda$  and efficiency as high as 94%.

The main analysis method developed in this thesis is a combination of numerical and mathematical analyses and is referred to as HFSS/Bloch method. The numerical part of this method is conducted using a High Frequency Structure Simulator (HFSS), and the mathematical part is based on the classic Bloch theory. The HFSS/Bloch method acts as the mainstay of the thesis and all designs are built upon the insight provided by this method. A circuit model using transmission line (TL) theory is also developed for some of the unit cells and antennas.

The HFSS/Bloch perspective results in a HAR EBG TL with radiation properties, a fragment of which (2 to 6 cells) is introduced as a novel antenna, the self-excited EBG resonator antenna (SE-EBG-RA). Open (OC) and short circuited (SC) versions of this antenna are studied and the inherently smaller size of the SC version is demonstrated.

Moreover, the possibility of employing the SE-EBG-RA as the element of a series-fed array structure is investigated and some sample high-efficiency, flat array antennas are rendered. A microstrip antenna is also developed, the structure of which is composed of  $3 \times 3$  unit cells and shows fast-wave behaviors. Most antenna designs are *resonant* in nature; however, in one case, a low-profile efficient *leaky-wave* antenna with scanning radiation pattern is proposed.

Several antenna prototypes are fabricated and tested to validate the analyses and designs. As the structures are based on tall metal traces, two relevant fabrication methods are considered, including CNC machining and deep X-ray lithography (DXRL). Hands-on experiments provide an outlook of possible future DXRL fabricated SE-EBG-RAs.



## **Acknowledgement**

First, my appreciation goes to my wife who sincerely supported me to her best during this challenging endeavor.

I would also like to express my gratitude to my academic supervisor, Dr. David M. Klymyshyn, for his guidance, support, and encouragement throughout my research activities and the preparation of this thesis. Also, I would appreciate Mr. Garth Wells who is a science associate with the Canadian Light Source (CLS), for his technical recommendations, and sharing his hands-on experiences during the time the research was underway at CLS. I would also like to state that exposure to Dr. Sven Achenbach's knowledge of microfabrication techniques has paved the way towards the completion of the prototyping part of my research, something that is appreciated.

Aside from the faculty and staff, I would thank my colleague, Mr. Diamond Liu, for giving a friendly assistance with the process of radiation pattern measurement.

Last but not least, I would thank my friend and colleague Dr. Atabak Rashidian for welcoming us to Canada (Saskatoon), and thereby, helping me start my research relatively faster.

## Table of Content

Permission to Use .....	i
Abstract .....	ii
Acknowledgement .....	iv
Table of Content .....	v
List of Figures .....	vii
List of Tables .....	xvii
List of Abbreviations .....	xix
List of Symbols .....	xxi
1 Introduction and Thesis Organization.....	1
1.1 Introduction.....	1
1.2 Research Objectives.....	8
1.3 Thesis Organization .....	9
References.....	12
2 Motivation and State-of-the-Art .....	14
2.1 Motivation behind Utilizing EBG structures .....	15
2.2 Motivation behind Utilizing the Third Dimension .....	35
References.....	47
3 Analysis Methods and Verification .....	55
3.1 Comparing Alternative Methods .....	64
3.2 Fabrication and Experimental Verification.....	65
References.....	66
4 Analysis and Design of Self-Excited EBG Resonator Antennas.....	68
4.1 A Novel High-Performance Antenna: SE-EBG-RA .....	69
4.2 SC versus OC SE-EBG-RA: Miniaturization by a Shorting Plate .....	87
4.3 Aperture Efficiency Enhancement for Electrically Large SE-EBG-RAs .....	110
4.4 TL Circuit Model for HAR EBG Cells and SE-EBG-RAs .....	117
4.5 Unit Cell Miniaturization and Applications to SE-EBG-RAs Design.....	128
References.....	136
5 Extended Ideas and Designs .....	140

5.1 Low-Profile Efficient Leaky-Wave Antennas with Proposed EBG Cells .....	141
5.2 Series-Fed Array Antennas with Proposed EBG Cells.....	155
5.3 A Novel EBG Microstrip Antenna with Fast-Wave Behavior .....	163
5.4 Compact Circularly Polarized SE-EBG-RAs .....	168
References.....	174
6 Conclusions and Recommendations for Future Work .....	177
6.1 Research Summary .....	177
6.2 Conclusions and Contributions.....	178
6.3 Future Works .....	182
APPENDICES .....	183
Appendix A: Three-Antenna Measurement Method .....	184
Appendix B: Wheeler Cap Method .....	187
Appendix C: Antenna Prototyping Employing DXRL Process.....	189
Appendix D: The Electromagnetic Spectrum and Wireless Applications.....	206
Appendix E: The high data rate wireless landscape [1] © IEEE 2009.....	207

## List of Figures

Fig. 1.1	Dimensions and positions of the battery and multiple antennas on a Samsung Galaxy S Smartphone [14]; used with permission; some annotations are added. ....	3
Fig. 1.2	An overview of ideas and designs to be presented throughout the thesis. ....	11
Fig. 2.1	A corrugated metal slab with HI effects at its surface, if the corrugations are quarter-wavelength deep. This is a polarization dependent surface with E-fields in the Z-direction observing the HI effect [3] © 1999 IEEE. ....	16
Fig. 2.2	A conventional 2D planar EBG surface (a), comparison between the operation of a dipole antenna adjacent to an EBG ground plane (b), and a PEC metal ground plane (c); parts of the figure are from [3] © 1999 IEEE; some modifications and annotations are applied. ....	17
Fig. 2.3	The role of a PEC ground plane in support of surface waves (a), the role of an EBG ground plane in suppression of surface waves [3] © 1999 IEEE; some modifications are applied. ....	18
Fig. 2.4	A dipole antenna in close proximity of an EBG ground plane with very limited number of cells [118] © 2008 IEEE; some modifications are applied. ....	19
Fig. 2.5	The concept of a TEM UC-PBG waveguide; a rectangular waveguide using artificial magnetic boundaries on vertical walls, realized by PBG/EBG cells at around resonance [119] © 1999 IEEE. ....	19
Fig. 2.6	Top side of three EBG structures connected with microstrip lines and their measured S21 parameters [120] © 2008 IEEE; some modifications are applied. ....	20
Fig. 2.7	A full-space scanning 1D Fabry-Pérot LWA using EBG cells on the ground plane (called HIS, i.e. HI surface) © 2012 IEEE. ....	21
Fig. 2.8	Geometry of a grounded dielectric slab. ....	24
Fig. 2.9	A low impedance PEC ground plane (a) compared to uniform (b) and non-uniform (c) EBG high impedance surfaces. EBG surfaces are adjacent to a dipole antenna yielding BW enhancement [12], © 2006 IEEE; some details on original figures are removed, and some texts are manipulated for quality enhancement. ....	25
Fig. 2.10	A miniaturized patch antenna on an EBG high impedance surface with 95% efficiency [20], ©2004 IEEE. ....	26
Fig. 2.11	Demonstration of how EBG surfaces are typically used on the ground plane to isolate the antenna from the human head in personal mobile communications [30] © IEEE 2010. ....	27
Fig. 2.12	Different EBG unit cells designed to achieve different features such as angular stability [8], multiband functionality [38] © 2005 IEEE, compact size [8], ease of tunability [49] © 2005 IEEE, etc. ....	29

Fig. 2.13	Two different circuit model representations of EBG cells, a) the via-less version of mushroom-like structure [20] © 2004 IEEE, b) Jerusalem cross EBG [36] © 2008 IEEE; some of the information on original figures is removed and texts are manipulated for quality enhancement.....	29
Fig. 2.14	Suppression of surface waves and mutual coupling in array antennas, a) 2-element array of patch antenna isolated by fork-like EBG cells [49] © 2005 IEEE, b) 4-element array of patch isolated by mushroom-like EBG cells [60] © 2006 IEEE; some of the information on original figures is removed for simplicity. ....	31
Fig. 2.15	Realizing reflectarray concept using EBG unit cells with tunable reflection properties, left) a waveguide feed illuminating a flat rectangular EBG surface, right) a waveguide feed illuminating a circular EBG surface with 23dBi directivity [115] © 2007 IEEE. ....	34
Fig. 2.16	A DRA as an example of a non-planar (vertical) radiator on EBG ground planes, a) a circular DRA on UC-EBG unit cells [72] © 2011 IEEE, b) a circular DRA on a circular mushroom-like EBG surface [73] © 2009 IEEE; some parts of the original figure are removed or manipulated for printing better quality.....	34
Fig. 2.17	Antenna as a transition device, bridging the TL to the free-space, left) source-to-rectangular waveguid-to-horn antenna transition [102], right) current distribution on a lossless two-wire TL, flared TL, and a linear dipole antenna [102] Copyright © 2005 by John Wiley & Sons Inc; used with permission.....	37
Fig. 2.18	A Vivaldi antenna with thick top metal layer on GaAs substrate. The first part is a TL with bound fields and then due to being flared, fields start to radiate at the end [79] © 1998 IEEE; some annotations are added to the original figure.....	38
Fig. 2.19	Gradual transition from a MSL to a microstrip antenna through gradually increasing the strip width, a) $W=0.91\text{mm}$ , b) $W=5\text{mm}$ , c) $W=15\text{mm}$ , d) $W=18\text{mm}$ ; for all cases: $h=1\text{mm}$ , $\epsilon_r=9.9$ , $\tan\delta=0.003$ , $30\text{mm}\times 30\text{mm}$ , $L_s=7.28\text{mm}$ , $W_s=0.91\text{mm}$ (50 $\Omega$ line), $L=14.6\text{mm}$ . ....	39
Fig. 2.20	Description of radiating and non-radiating apertures of a typical microstrip antenna; the feed line is a narrow strip, and hence, does not radiate (TL) while the patch part is a very wide version of the same TL and performs well as an antenna.....	39
Fig. 2.21	3D and side view of a 50 $\Omega$ MSL on PEC a grounded dielectric slab, a) non-flared case with $\psi=0^\circ$ , b) flared case with $\psi\neq 0^\circ$ ; $L_s=7.28\text{mm}$ , $W_s=0.91\text{mm}$ (50 $\Omega$ line); $L=14.6\text{mm}$ . ....	40
Fig. 2.22	Radiation gain of the antennas in Fig. 2.21, a) Fig. 2.21 (a), b) Fig. 2.21 (b) with $\psi=5^\circ$ ; the gain includes directivity and $\eta$ , but not the input matching; the dashed line corresponds to $\phi=0^\circ$ and the solid line to $\phi=90^\circ$ (E-plane). ....	41
Fig. 2.23	a) A sample microstrip antenna on a microwave substrate with two different $\tan\delta$ , numerically simulated in HFSS, b) simulated gain of a compact slot antenna on an infinite substrate with $\epsilon_r=4.0$ ( $1-j\tan\delta$ ) [111] © IEEE 2003; the	

	slot is printed on the only copper side and is excited by a microstripline printed on the other side of the substrate. ....	44
Fig. 3.1	HFSS/Bloch method is applied to a sample periodic structure and <i>absolute</i> values of $\beta/k_0$ and $\alpha/k_0$ are plotted, a) MSL periodically loaded with open stubs, b) the related cascade network, c) the dispersion diagram for Fig. 3.1 (a). For comparison, $\beta/k_0$ of a normal MSL, with no stubs, is also included; traces are 0.91mm ( $Z_0 \sim 50\Omega$ ). ....	56
Fig. 3.2	General Bloch unit cell for a 1D periodically-loaded transmission-line made of an infinite number of such symmetrical cells [4]. © 2006 IEEE.....	57
Fig. 3.3	The proposed HFSS/Bloch analysis method: step-by-step progression to generate the Bloch dispersion diagram for a structure composed of EBG cells. ....	58
Fig. 3.4	Two fundamentally different antennas in this thesis developed using the HFSS/Bloch dispersion diagram. ....	60
Fig. 3.5	An example of using RPD to analyze EBG grounded antennas [8] © 2003 IEEE; where the phase is zero (at cell resonance), the surface is imitating a PMC boundary; notice the resonance drops when $W$ increases.....	61
Fig. 3.6	An example of using Brillouin's dispersion diagram to evaluate surface wave suppression properties and bandgaps of EBG surfaces [10] © 2006 IEEE.....	61
Fig. 3.7	An example of applying the insertion loss ( $\text{dB} S_{21} $ ) evaluation method [13] for deriving bandgaps of EBG surfaces. © 2006 IEEE.....	63
Fig. 3.8	a) Unit cell modeling in HFSS using waveport as proposed in [17] © 2009 IEEE, b) PEC symmetry planes, c) PMC symmetry planes.....	64
Fig. 3.9	a) The prototype to appear in Sec. 4.2, which undergoes a complete set of antenna measurements, as depicted. ....	65
Fig. 4.1.1	2-port analysis of the 5-cell EBG TL and its gap-less version [17] © 2012 IEEE, a) geometry and HFSS modeling, b) $S_{11}$ and $S_{21}$ , c) group delay and normalized loss in (4.1.2), d) realized gain, gain, directivity, and $\eta$ ; detailed dimensions of the EBG cell are as in Fig. 4.1.3.....	70
Fig. 4.1.2	Circuit model for the proposed EBG cells. The real power radiation is modeled as a conductance [17] © 2012 IEEE.....	73
Fig. 4.1.3	Unit cell and the 3D model details for, a) the tall MSL, b) the gap loaded (EBG) tall MSL, c) normalized $\gamma$ in (4.1.3); $w=9$ , $\epsilon_r=9.9$ , $\tan\delta=0.003$ , $\sigma=5.8\text{e}7\text{s/m}$ . ....	74
Fig. 4.1.4	Different views of the EBG unit cell of Fig. 4.1.3 (b) together with the distribution of real Poynting vectors adjacent to the cell aperture at 4.15GHz. ....	76
Fig. 4.1.5	General field distribution around the EBG cell gap: a) E-fields are parallel to the PEC ground, b) illustration of the equivalent magnetic current based on Huygens' principle, c) in phase image of $M_S$ above a PEC (no field cancellation). 76	

Fig. 4.1.6	3D geometry of two SE-EBG-RA versions which are identical with the exception of the trace height; right) 2mm tall (i.e. thick), left) 0.03mm tall (i.e. thin); $\lambda$ is wavelength at 4.15GHz; unit cell details are rendered in Fig. 4.1.3. ....	78
Fig. 4.1.7	a) radiation pattern of the tall SE-EBG-RA at 4.15GHz, b) antenna 3D view and the definition of major radiation planes, c) comparison of $\text{dB} S_{11} $ of the tall (-18.5dB) and thin (-2.8dB) SE-EBG-RAs of Fig. 4.1.6. ....	79
Fig. 4.1.8	Comparison between realized gain and $\eta$ of the tall and non-tall SE-EBG-RAs; the gain is for the ground plane size (XY size in Fig. 4.1.6) of $0.51\lambda \times 0.41\lambda$ . ....	80
Fig. 4.1.9	HFSS/Bloch unit cell model for one (a), two (b), and three (c) identical unit cells; HFSS/Bloch method is applied to all cases to verify how close the dispersion diagrams are. ....	81
Fig. 4.1.10	Dispersion diagram by the HFSS/Bloch method for the three cells in Fig. 4.1.9. The curves are corresponding so closely that the difference in estimating the cut-off frequency is less than 0.3%. ....	81
Fig. 4.1.11	HFSS model for a) the UC-EBG cell, b) the same cell with PEC on top layer, together with c) the geometry of the top metal layer and the definition of physical parameters for the cell; $D=0.9$ , $\delta=t=0.07$ , $d=0.4$ , $h=0.3$ (all in mm), and $\epsilon_r=5.99$ ; the geometry, waveport excitation, and PEC/PMC symmetry planes are highlighted. ....	82
Fig. 4.1.12	Reflection phase diagram for the cells shown in Fig. 4.1.11. ....	83
Fig. 4.1.13	The HFSS model for a the proposed EBG cell; the geometry and the wave-port excitation as well as the PEC and PMC symmetry planes are highlighted and are arranged the same as Fig. 4.1.11; the radiation box width is enlarged enough to make the images in Y direction far enough. ....	84
Fig. 4.1.14	Reflection phase diagram for the EBG cell shown in Fig. 4.1.13. The $\pm 90^\circ$ phase range area is highlighted by a color box. ....	85
Fig. 4.1.15	Dispersion diagram calculated by the HFSS/Bloch method. The curves show the real and imaginary part of the normalized propagation constant ( $\gamma/k_0 = \alpha/k_0 + j\beta/k_0$ ). AMC zone is highlighted and overlaps the leaky zone. ....	86
Fig. 4.2.1	3D view of the EBG TL together with its Bloch line impedance, $Z_B$ plotted versus frequency; for comparison, the line impedance of the same TL when gaps are removed is also included. ....	90
Fig. 4.2.2	The dispersion diagram by HFSS/Bloch method for the unit cell in Fig. 4.2.1, i.e. the normalized propagation constant ( $\alpha/k_0 + j\beta/k_0$ ) versus frequency ( $k_0$ is the free-space wavenumber); for comparison, $\beta/k_0$ of the same cell with no gap is also included. ....	91
Fig. 4.2.3	3D view of a 5-cell OC SE-EBG-RA and its radiation pattern; the input transformer is 3.3mm wide, 7.34mm long, and 30 $\mu$ m thick; cell dimensions are provided in Fig. 4.2.1; BW=2.6% and $G_r=3.12\text{dBi}$ . ....	94

Fig. 4.2.4	Magnitude of the current on the ground plane, demonstrating the actual electrical length of the antenna, a) 6-cell OC SE-EBG-RA, b) 2-cell OC-SE-EBG-RA, c) 3-cell SC SE-EBG-RA; antennas are as in Table 4.2.1.....	95
Fig. 4.2.5	A 2-cell SC SE-EBG-RA a) with a relatively large ground plane of $0.58\lambda \times 0.58\lambda$ , b) with highly truncated ground plane of $0.25\lambda \times 0.28\lambda$ , c) radiation pattern for Fig. 4.2.5 (a), d) radiation pattern for Fig. 4.2.5 (b); the transformer dimensions for both antennas are 0.35mm and 8mm; the $50\Omega$ feedline is 0.92mm wide and 8mm long; all thin traces are 30um thick MSL; cell dimensions are as in Fig. 4.2.1. ....	98
Fig. 4.2.6	Comparison between the performance of a microstrip patch antenna and an OC SE-EBG-RA with 5 cells, both matched at 3.73GHz; ground planes are both 50mm $\times$ 50mm; substrate material and thickness for both antennas and the unit cell of Fig. 4.2.6 (b) are given in Fig. 4.2.1; thin traces are 30 $\mu$ m thick MSL. ....	99
Fig. 4.2.7	Fabrication process of SC and OC SE-EBG-RAs serving as proof-of-principle prototypes; dimensions of $\lambda_g/4$ transformers are 6.68mm & 3.9mm for the OC antenna and 7.4mm & 3.7mm for the SC one. ....	101
Fig. 4.2.8	AUT (Fig. 4.2.7 (b)) and the two extra fabricated antennas, mounted on thin plywood sheets, and prepared for the radiation pattern and three-antenna measurement implementation. ....	102
Fig. 4.2.9	Absorbers and stands in use during the measurement.....	103
Fig. 4.2.10	ECCOSORB® HR should be bonded to a metal surface for optimal performance; aluminum foil is applied on the backside.....	103
Fig. 4.2.11	a) Typical reflectivity of ECCOSORB® HR-25 absorbers supplied by Emerson & Cuming Microwave Products Inc ( <a href="http://www.eccosorb.com">http://www.eccosorb.com</a> ); results may vary depending on application, b) absorbers mounted on custom made wooden stands with adjustable heights. ....	104
Fig. 4.2.12	Measured and simulated radiation patterns for the fabricated 3-cell OC SE-EBG-RA; a) E-plane, i.e. $\phi=0^\circ$ , b) H-plane, i.e. $\phi=90^\circ$ (XYZ axes are as in Fig. 4.2.7 (b)); $f_r=3.99$ GHz. ....	105
Fig. 4.2.13	Antenna efficiency measurement using Wheeler cap method, a) the parts cut out of a copper sheet, b) assembled cap and the SE-EBG-RA prototype, c) the cap mounted on the antenna and sealed using metal foil. ....	106
Fig. 4.2.14	Demonstration of dielectric slab loading of the SC SE-EBG-RA.....	107
Fig. 4.2.15	Comparison of $\text{dB} S_{11} $ for the fabricated 3-cell OC and 2-cell SC SE-EBG-RAs with and without RO3010 slabs ( $\epsilon_r=10.2$ ). ....	107
Fig. 4.2.16	Comparison between E-plane radiation patterns of the fabricated antennas in Fig. 4.2.7, with and without slabs in the gaps; H-plane radiation patterns are all symmetrical and similar to the HFSS result in Fig. 4.2.8 (b). ....	108
Fig. 4.3.1	A 2-cell SC EBGRA on a relatively large ground plane; $\eta=76\%$ , $D=6.3$ dBi, $f=3.75$ GHz; the XY size is 70.17mm $\times$ 70mm; this design has already presented	



	in Fig. 4.2.5, but with smaller ground plane; the thick HI elements are 12.5mm long and 3mm wide, and the first one has 9mm offset form the center. ....	112
Fig. 4.3.2	The antenna in Fig. 4.3.1 supported with 4 HI resonating elements around the main radiator; $\eta=82\%$ , $D=6.85\text{dBi}$ , $f=3.72\text{GHz}$ ; Ground plane size is the same as Fig. 4.3.1.....	113
Fig. 4.3.3	The antenna in Fig. 4.3.1 supported with 8 HI resonating elements around the main radiator; $\eta=84\%$ , $D=7.31\text{dBi}$ , $f=3.71\text{GHz}$ ; Ground plane size is the same as Fig. 4.3.1.....	114
Fig. 4.3.4	Comparison of the input matching quality if antennas in Fig. 4.3.1 to 4.3.3. ....	115
Fig. 4.3.5	3D plot of the directivity of the antenna in Fig. 4.3.3. ....	115
Fig. 4.4.1	a) Bloch unit cell and circuit model representation for a cascade of small thick metal patches on a PEC-backed substrate; b) circuit model for the SE-EBG-RA composed of three EBG cells. ....	118
Fig. 4.4.2	Side and top views of EBG unit cells with a thick metal layer and high gap capacitance; (a) cell with narrow HAR gap; (b) cell with interdigitated gap; c) detailed dimensions of the interdigits in Fig. 4.4.2 (b).....	121
Fig. 4.4.3	The fabricated thin 3-cell antenna with micron-scale gaps; metal traces are $4\mu\text{m}$ thick plated Ni; cells are as in Fig. 4.4.1 with $d=1.81\text{mm}$ ; $W=7.8\text{mm}$ , $h=1\text{mm}$ , $g=27\mu\text{m}$ ; $\epsilon_r=9.9$ , $\tan\delta=0.003$ .....	125
Fig. 4.4.4	Measured, HFSS-simulated, and modeled input reflections for a) the antenna in Fig. 4.4.3, b) the antenna in Fig. 4.4.5; both Y-axes show $\text{dB} S_{11} $ .....	125
Fig. 4.4.5	The fabricated 3-cell antenna; the metal traces are made of $30\mu\text{m}$ thick copper; the $\lambda/4$ transformer is $1.94\text{mm}$ wide and $6.96\text{mm}$ long.....	126
Fig. 4.4.6	HFSS-simulated radiation pattern of the 2nd prototype at $4.06\text{GHz}$ for $30\text{mm}\times 38\text{mm}$ ground plane size. ....	126
Fig. 4.5.1	Step-by-step development and miniaturization of the thick metal EBG unit cell (side/top views depicted); the substrate in this example is alumina with $\epsilon_r=9.9$ and $\tan\delta=0.003$ ; the aspect ratio, AR, is $t/g$ .....	128
Fig. 4.5.2	a) 1D array structure of the EBG cell in Fig. 4.5.1 (b), b) the complex propagation constant ( $\gamma=\alpha+j\beta$ ) along Y-axis normalized by free-space wavenumber ( $k_0$ ) for EBG cells described in Fig. 4.5.1/Table 4.5.1; the twin curves (a) to (e) are related to Fig. 4.5.1 (a) to (e) and Result 1 to 5 in Table 4.5.1. ....	130
Fig. 4.5.3	Visual comparison between size, thickness, and footprint of the EBG cells in Table 4.5.1. Dimensions of cells (b) and (e) in Fig. 4.5.1 are scaled to operate at the same resonance ( $f_c=4.83\text{GHz}$ ) of the basic thin EBG cell (a).....	131
Fig. 4.5.4	Comparison of the input matching of SE-EBG-RAs composed of different EBG cells in Fig. 4.5.1; results are based on HFSS/Bloch method.....	133

Fig. 4.5.5	3D view of SE-EBG-RAs composed of EBG cells in Fig. 4.5.1 (b) and (c); Radiation pattern (c)/(d) corresponds to the antennas in (a)/(b); Dashed/solid line is the E/H-plane pattern; ground plane size is 30×37mm; input 50Ω MSLs are 0.3mm wide, 5.25mm long, and 2mm tall (same as cells); the cell size is given in Fig. 4.5.1.....	134
Fig. 4.5.6	Comparison of the resonance frequency and efficiency for the SE-EBG-RAs in Fig. 4.5.5; based on full-wave analysis. ....	135
Fig. 5.1.1	General description of an automotive radar system with a frequency scanning LWA antenna on the car front. The transmit frequency is swept continuously over the leaky range, making the pattern scan. The receive signal is then inspected for possible frequency components returned from the object (every component represents a unique angle).....	142
Fig. 5.1.2	a) The unit cell and HFSS model for the HAR EBG cell (size $\sim \lambda/11 \times \lambda/11 \times \lambda/28$ ), b) dispersion behavior expressed by the normalized propagation constant versus frequency; the substrate is Alumina with $\epsilon_r=9.9$ , $\tan\delta=0.003$ , and metal is copper, $\sigma=5.8e7s/m$ . ....	143
Fig. 5.1.3	HFSS model of the proposed LWA with 12 EBG cells. A $\lambda/4$ transformer with the same thickness as the antenna matches the antenna to a 50Ω line; ground plane size is 30mm×103mm ( $1.24\lambda \times 0.36\lambda$ ); cell Size is $\sim \lambda/11 \times \lambda/11 \times \lambda/28$ ; $\lambda$ is the wavelength at matching frequency. ....	144
Fig. 5.1.4	The realized gain of the HAR EBG LWA at three different frequencies, showing the typical beam scanning of LWAs, a) rectangular radiation pattern ( $\phi=0$ ), b) polar radiation pattern at ZX plane ( $\phi=0$ ).....	145
Fig. 5.1.5	Radiation efficiency and return loss of the HAR EBG LWA around the LW zone in Fig. 5.1.2 (b). ....	146
Fig. 5.1.6	Top layer view of the periodic planar LWA presented in [6], which is designed employing coplanar waveguides; © IEEE 2002.....	146
Fig. 5.1.7	The top and bottom views of the periodic planar LWA presented in [3]; © IEEE 2010. ....	147
Fig. 5.1.8	3D view of a 2-element array of the HAR EBG LWA shown in Fig. 5.1.3; ground plane is 118mm×60mm ( $0.72\lambda \times 1.38\lambda$ ); $\lambda$ is the wavelength at matching frequency; the transformer provides 50Ω input impedance. ....	148
Fig. 5.1.9	Rectangular plot of the realized gain at scanning plane ( $\phi=0$ ) for the 2-element HAR LWA array. ....	148
Fig. 5.1.10	The scaled LWA, a) modeled by rectangular a waveport, as assumed for design #1 in Table 5.1.2, b) modeled when replacing the rectangular wavport with a 50Ω SMA connector excited by a circular waveport. ....	151
Fig. 5.1.11	Comparison between the simulated input matching of the design #2 in Table 5.1.2 with and without the SMA connector.....	151

Fig. 5.1.12	a) 3D view of the scaled LWA modeled when replacing the rectangular waveport with a 50 $\Omega$ SMA connector excited by a circular waveport (design #2 in Table 5.1.2); for clarification, two different enlarged views of the connector and feed point section are rendered as well. ....	152
Fig. 5.1.13	Bloch line impedance versus frequency generated by HFSS/Bloch method, associated with the dispersion diagram of Fig. 5.1.2, and the description of how the curve is used to design a matching network for the proposed LWA. ....	154
Fig. 5.2.1	Generalization of a $n$ -element series array of SE-EBG-RA antennas; the first element is OC-SE-EBG-RA and the rest are identical and classified as terminated SE-EBG-RA due to being loaded at the end. ....	157
Fig. 5.2.2	A 2-element series array of SE-EBG-RA; the substrate is alumina with $\epsilon_r=9.9$ and $\tan\delta=0.003$ ; the ground plane size is $72\times 30$ ; $W_1=1.1$ , $W_2\&W_4=0.912$ , $W_3=1.05$ (30 $\mu\text{m}$ thick), $g=0.1$ , $L_1=6.92$ , $L_2=7.04$ , $L_3=6.9$ , $L_4=1.86$ ; the array spacing is 35.56; all dimensions are in mm. ....	158
Fig. 5.2.3	Radiation pattern of the 2-element series array in Fig. 5.2.2. ....	159
Fig. 5.2.4	A 3-element series-fed array of SE-EBG-RA; the substrate material and dimensions are like Fig. 5.2.2; the ground plane size is 109mm $\times$ 30mm; elements #2 and #3 are the same as the second element in Fig. 5.2.2. ....	160
Fig. 5.2.5	Rectangular radiation pattern of the 3-element array of Fig. 5.2.4 (realized gain plotted). ....	160
Fig. 5.2.6	Two different views of the 3D radiation pattern of the 3-element array of Fig. 5.2.4 (realized gain plotted). ....	160
Fig. 5.2.7	Comparing the return loss of one-, two-, and three-element arrays shown in Fig. 5.2.1. ....	161
Fig. 5.3.1	Side (a) and top (b) views of the Bloch unit cell of the antenna in Fig. 5.3.2 (a); all gaps are 0.25mm; the Bloch cell size is $\lambda/7\times\lambda/12.3\times\lambda/59$ , and the cell is composed of two smaller identical portions (EBG cells) of size $\lambda/14\times\lambda/12.3\times\lambda/59$ ( $\lambda$ at 4GHz). ....	164
Fig. 5.3.2	Microstrip antenna versus its gap-loaded version both resonating at 4GHz; both ground planes are 16mm $\times$ 24.3mm; both substrates are 1.27mm thick RO3010 ( $\epsilon_r=10.2$ , $\tan\delta=0.0023$ ); the unit cell of Fig. 5.3.2 (a) is given in Fig. 5.3.1; metal traces are 30 $\mu\text{m}$ thick copper. ....	164
Fig. 5.3.3	Simulated realized gains of antennas in Fig 5.3.2 (a) and Fig. 5.3.2 (b); the dashed/solid line is related to E-/H-plane. ....	166
Fig. 5.3.4	Fabricated gap-loaded patch antenna of Fig. 5.3.2 (a) with a large ground plane. ....	167
Fig. 5.3.5	dB S <sub>11</sub>   of the antennas in Fig. 5.3.2 and Fig. 5.3.4. ....	167
Fig. 5.4.1	Top (a) and 3D (b) views of the CP HAR EBG antenna along with detailed dimensions of the feed section (c); the cell size is $\sim\lambda/16\times\lambda/16\times\lambda/23$ ; the substrate is alumina with $\epsilon_r=9.9$ and $\tan\delta=0.003$ ; the metal is copper with $\sigma=5.8\text{e}7\text{s/m}$ ; the	

	ground plane size is 33mm×30mm; the trace width for the 50Ω line is 1.2mm and for 80Ω line is 0.7mm. ....	170
Fig. 5.4.2	A regular square patch antenna, traditionally fed by two cross MSLs at the center of two adjacent sides; to provide the condition for CP radiation, feedlines must be in the right size, as described. ....	170
Fig. 5.4.3	dB S <sub>11</sub>   for the antenna in Fig. 5.4.1.....	171
Fig. 5.4.4	Realized gain of the CP EBG antenna; the dashed/solid line is for phi=90°/phi=0° plane.....	172
Fig. 5.4.5	3D plot of the realized gain for the CP antenna in Fig. 5.4.1, at the matching frequency of 2.62GHz. ....	172
Fig. 5.4.6	AR (a) together with the magnitude (b) and phase (c) of $E_\theta$ for the CP antenna in Fig. 5.4.1; curves are plotted at the matching frequency of 2.62GHz; the dashed/solid line is for phi=90°/phi=0° plane.....	173
Fig. A.1	A typical communications link and the Friis transmission equation [1] governing the system.....	185
Fig. B.1	Description of the Wheeler Cap method and the related equivalent circuit model [3].....	187
Fig. C.1	Illustration of DXRL fabrication process [11] © 1998 IEEE.....	192
Fig. C.2	The progression from antenna simulation and design to Cr mask. ....	193
Fig. C.3	Different steps of the UV lithography process using the Cr mask towards achieving an in-house X-ray mask. ....	195
Fig. C.4	Different steps of the UV lithography process using the Cr mask towards achieving an in-house graphite X-ray mask. ....	196
Fig. C.5	Unsuccessful attempts due to over plating (a), plating underneath the resist (b), and incorrect dose resulting in sloped sidewalls (b); the best wafer obtained with vertical sidewalls is also shown (c). ....	197
Fig. C.6	Attaching a support ring to the wafer to achieve the graphite X-ray mask processed at SyLMAND.....	198
Fig. C.7	Description of how the X-ray mask and the sample are mounted onto the scanner; photos are created by the author and show the fabricated X-ray mask and the sample. ....	198
Fig. C.8	The first sample wafer undergoing an X-ray lithography experiment. The same designs shown on the Cr mask (Fig. C.4), and then translated to the X-ray mask, are transferred into a 150μm thick PMMA resist on a Si substrate.....	199
Fig. C.9	3D view of how the antenna shown in Fig. C.8 should look after development (a); 3D view of the antenna when the voids in Fig. C.9 (a) are filled with electroplating. ....	200

Fig. C.10	SEM micrographs of the second antenna sample after the development step.....	201
Fig. C.11	An example of dicing and attaching the microwave connector to antennas; the prototype shown is made by UV lithography and Ni plating on Alumina, and is successfully used to verify the circuit model in Sec. 4.4.....	203

## List of Tables

Table 1.1	Total size of some Intel processors for different personal internet-based devices; the table is created based on the data on a figure in [24].....	5
Table 2.1	Comparison of the simulated gain and $\eta$ for the antennas in Fig. 2.12; the analysis frequency is 4GHz. ....	39
Table 2.2	Comparison of the simulated efficiency for the antenna in Fig. 2.14 (b) with different flaring angle. ....	40
Table 2.3	Comparison between the dielectric and conduction losses of two 50 $\Omega$ MSL with different substrate permittivities, at low and high frequencies; results assume remaining in TEM mode, otherwise some extra loss will also appear. ....	42
Table 4.1.1	Performance comparison of 2 unit cells: low loss MSL, and EBG ( $Z_{in}$ and RL are given for a 3-cell OC piece of each case) .....	74
Table 4.1.2	Comparison of radiation properties of a tall and a non-tall 50 $\Omega$ MSL; $Z_c$ is the characteristic impedance.....	77
Table 4.2.1	Parametric study on characteristics of OC and SC SE-EBG-RA versus the number of unit cells in their structure; $l=nd$ where $n$ is the number of cells and $d=7.2\text{mm}$ (cells size as in Fig. 4.2.1) ; antennas are first matched to a 50 $\Omega$ line by a $\lambda_g/4$ transformer as $R_{in}$ is not necessarily 50 $\Omega$ . ....	92
Table 4.2.2	Parametric study on properties of a 3-cell OC SE-EBG-RA versus the thickness of its top metal layer. Antennas are matched to a 50 $\Omega$ line by a proper $\lambda_g/4$ transformer. Parameters are found by HFSS; the ground plane size is 30mm $\times$ 40mm; $G_r$ stands for the realized gain; unit cell is as in Fig. 4.2.1. ....	96
Table 4.2.3	Parametric study on $G_r$ and $\eta$ of a 2-cell SC SE-EBG-RA versus its ground plane size in two different dimensions. Antennas are matched to a 50 $\Omega$ line by a proper $\lambda_g/4$ transformer; cell dimensions are as in Fig. 4.2.1. ....	97
Table 4.2.4	Comparison between the gain obtained by the Three-Antenna-Measurement method and HFSS at 3.99GHz for the AUT and the two other antennas fabricated as reference antennas. ....	105
Table 4.2.5	Properties of antenna prototypes in Fig. 4.2.7, with and without slabs in the gaps, as demonstrated in Fig. 4.2.14. Results are based on HFSS simulation. ....	108
Table 4.4.1	Dimensions and characteristics of the four SE-EBG-RA samples based on four different unit cells; $\lambda_r$ is wavelength at $f_r$ , and $\Delta$ is the difference between $f_r$ given by the model and HFSS, divided by the HFSS value; dimensions are in millimeters. ....	122
Table 4.4.2	$f_r$ of SE-EBG-RAs composed of cells in Fig. 4.4.2 (a) and (b), given by the model and HFSS. $C_{pp}$ and $C_{pp}$ are also calculated by the model; $\Delta$ is the difference between $f_r$ by the model and HFSS, divided by the HFSS value. ....	124

Table 4.4.3	Properties of the antenna in Fig. 4.4.5 calculated by the model; $\Delta$ is the difference between $f_r$ given by the model and experiment, divided by the experimental value.....	127
Table 4.5.1	Electrical and physical properties of the EBG cells in Fig. 4.5.1; $\lambda_c$ is the wavelength at $f_c$ .....	130
Table 5.1.1	Comparison between physical, electrical, and radiation properties of both 1- and 2-element LW antennas; $\lambda$ is the wavelength at matching frequency; $G_r$ is the realized gain.....	149
Table 5.1.2	Comparison between the physical, electrical, and radiation properties of the LWA in Fig. 5.1.3 and its scaled version; $\lambda$ is the wavelength at matching frequency; $G_r$ is the realized gain. ....	150
Table 5.3.1	HFSS/Bloch analysis of the unit cell in Fig. 5.3.1 with and without gaps and simulated parameters of patch antennas based on them in Fig. 5.3.2; $G_r$ is the realized gain including the dB S <sub>11</sub>   effect. ....	165
Table C.1	Comparison between properties of some microfabrication techniques, which are available for realization of HAR features [7].....	190

## List of Abbreviations

ADS	Advanced Design System
AMC	Artificial Magnetic Conductor
AR	Aspect Ratio
AR	Axial Ratio (Referring to Circular Polarization)
AUT	Antenna Under Test
BW	Bandwidth
CLS	Canadian Light Source
CP	Circular Polarization
CPW	Coplanar Waveguide
DRA	Dielectric Resonator Antenna
DXRL	Deep X-Ray Lithography
EBG	Electromagnetic Bandgap
F/B	Front-To-Back Radiation Ratio
FEM	Finite Element Method
HAR	High Aspect Ratio
HFSS	High Frequency Structure Simulator
HI	High Impedance
HIS	High Impedance Surface
LIGA	German Acronym for Lithographie, Galvanoformung, and Abformung (Lithography, Electroplating, and Molding)
LWA	Leaky-Wave Antenna
LW	Leaky-Wave
MEMS	Microelectromechanical Systems
MSL	Microstripline
OC	Open-Circuited
PBC	Periodic Boundary Condition
PCB	Printed Circuit Board
PEC	Perfect Electric Conductor
PMC	Perfect Magnetic Conductor
PMMA	Polymethylmethacrylate
Q	Quality Factor
RAM	Radar Absorbing Material
RF	Radio Frequency
RPD	Reflection Phase Diagram



SAR	Specific Absorption Rate
SC	Short-Circuited
SE-EBG-RA	Self-Excited EBG Resonator Antenna
SEM	Scanning Electron Microscope
SLL	Side Lobe Level
SNR	Signal-to-Noise Ratio
S-Parameters	Scattering Parameters
TAM	Three Antenna Measurement Method
TL	Transmission Line
1D	One Dimensional
UV	Ultra Violet

## List of Symbols

$\lambda$	Wavelength
$\Delta$	Difference
$\eta$	Antenna Efficiency
$\gamma$	Complex Propagation Constant
$\alpha$	Real Part of the Complex Propagation Constant
$\beta$	Imaginary Part the of Complex Propagation Constant
$\epsilon_r$	Dielectric Constant (Relative Permittivity)
$\delta_s$	Skin Depth
$c$	Speed of Light in Vacuum
$k$	Wave Number
$\mu$	Permeability
$\epsilon$	Permittivity
$\sigma$	Electrical Conductivity
$\omega$	Angular Frequency

# Chapter 1

## Introduction and Thesis Organization

### 1.1 Introduction

In every decade or so, wireless technology undergoes significant reviews and sometimes evolutionary changes. The main reason is the need to keep up with the ever-growing and insatiable demand in data communications. Another reason is to bring forth the opportunity to apply the most recent state-of-the-art generated by researchers. In order to be able to keep up with this trend, a wide variety of communications standards [1], [2], [3] are developed and released by the agencies like ITU<sup>1</sup>, IMT<sup>2</sup>, and 3GPP<sup>3</sup> to standardize the process of coordinating different wireless products designed and manufactured by different entities. For example, the well-known standard, IEEE 802.11, which includes a variety of versions and releases (most recently 802.11n, 802.11ac and 802.11ad [3]) is an example which is involving everyone's life when using internet over Wi-Fi (i.e. WLAN<sup>4</sup>) anywhere around the globe.

People are constantly moving towards ever-increasing dependency on wireless and mobile communication services for everyday activities. In the near future, all-IP networks implemented

---

<sup>1</sup> International Telecommunication Union

<sup>2</sup> International Mobile Telecommunications

<sup>3</sup> 3rd Generation Partnership Project

<sup>4</sup> Wireless Local Area Network

through ultra-high speed 4th generation (4G) mobile technology will provide IP telephony, interactive gaming services, HDTV<sup>5</sup>, and other multimedia streamings [4] to users who could be mobile or stationary. The concept of Internet-of-Things (IoT), as another emerging area [5-6], will also bring about interest in intelligent automation through an internet connection (provided by apps on a Smartphone) that will cause an avalanche of demand for data, and hence, demand for more efficient communications systems. The need to apply heavier online data encryptions for security and the emerging idea of cloud-computing, which requires users to have remote access to high capacity processors, also provides incentives to seek faster wireless connectivity. On the other hand, the current growth in battery capacity is far below the needs of today's mobile communications systems [7], and some of the solutions to this issue require using free off-device (nearby) computing resources (i.e. cyber foraging [8]) which again requires using more data. Statistics spanning from 1980 to 2013 show that the annual increase in the average speed of a high-end personal internet connection is more than 50% [9], a fact known as Nielson's law, similar to the well-established Moore's law in microelectronics. Speaking of the Smartphone as a symbol of data usage, in 2011 more Smartphones were sold than desktop PCs, notebooks, netbooks, and tablets together. The total worldwide Smartphone sales reached 472 million units in 2011 [10].

In an effort to satisfy this demand, new releases of WiFi standards, like IEEE 802.11ac (not yet in the market), target multi-station WLAN throughput of at least 1Gbit/s and a single link throughput of at least 500Mbit/s. Such advanced standards allow the use of wider RF bandwidths, more MIMO<sup>6</sup> spatial streaming (up to 8 streams), multi-user MIMO, and high-density modulation schemes (up to 256-QAM<sup>7</sup>) [11]. To obtain just a glimpse of the future bit rates, it is worth noting that in Jan 2014, IEEE 802.11ac was amended to allow up to 7Gbit/s at 5GHz WiFi band [12]<sup>8</sup>. Another similar standard, which will imminently affect mobile communications, is IEEE 802.16ac for Wimax<sup>9</sup>, which is incorporating new technological advances that could exceed the expectation of 4G systems. *Proliferation* of such *standards* and *frequency* bands has become an indispensable part of the rapidly growing technology.

---

<sup>5</sup> High Definition TV

<sup>6</sup> Multiple Input Multiple Output

<sup>7</sup> Quadrature Amplitude Modulation

<sup>8</sup> These standards obviously fit within the definition of 4G communication systems because IMT-advanced specifications released by ITU-R in March 2008 define a 4G system as a system with 100Mbit/s for high mobility communication and 1Gbit/s for low mobility or stationary cases [13].

<sup>9</sup> Worldwide Interoperability for Microwave Access

A question arising here is, "What would be the implications of such evolutions to the antenna technology?"; An answerer to this question is that upcoming portable communications systems like Smartphones and tablets are expected to be compatible with more of these standards, and therefore, accommodate *more antennas than before*. However, the main issue is that the natural expectation of end users is always multiple functionality and better data rates, but with the same size or even smaller devices, a fact which makes the design requirements of such systems increasingly more difficult. To provide a tangible example, Fig. 1.1 shows an interesting layout [14] describing the number of antennas and the dimensions and location of each in a Samsung Galaxy S Smartphone (phone released in June 2010).

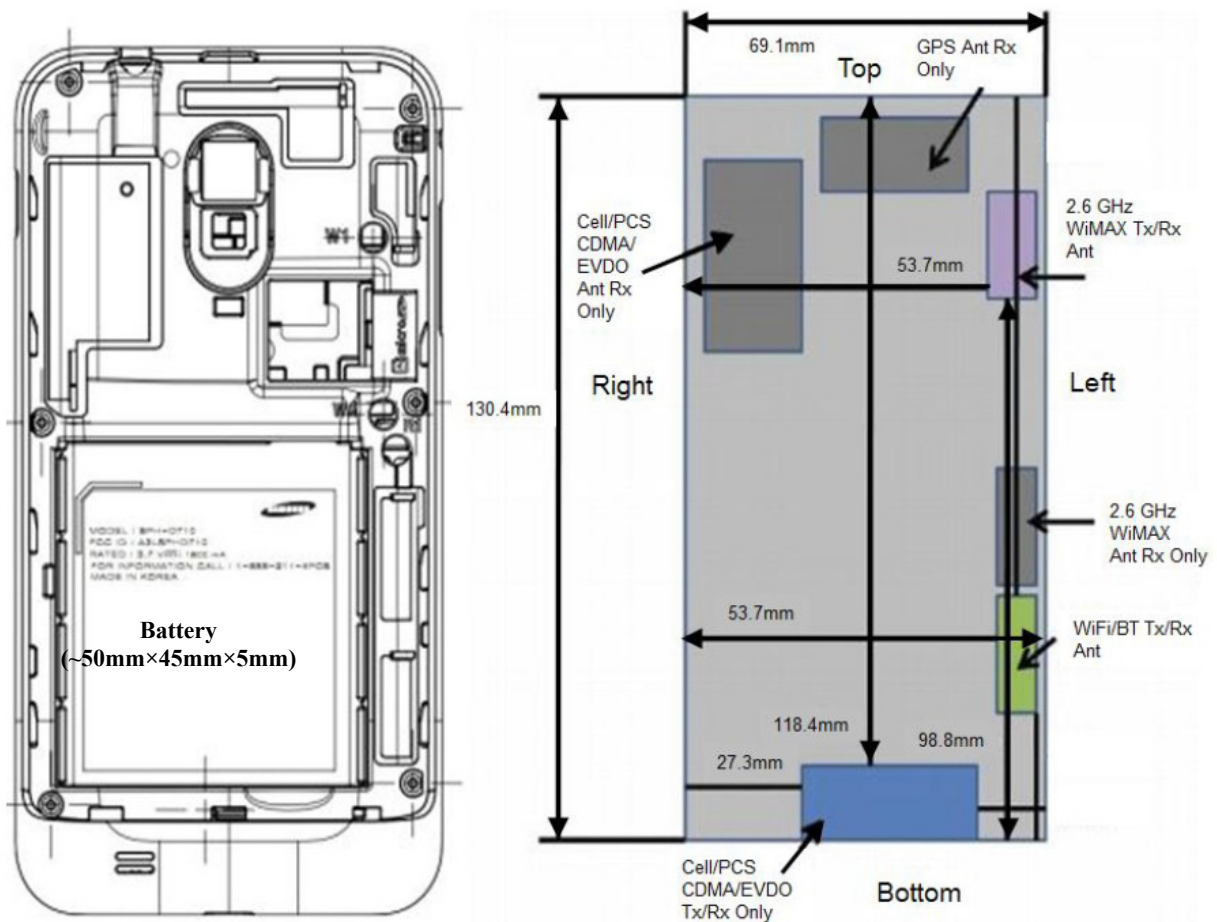


Fig. 1.1 Dimensions and positions of the battery and multiple antennas on a Samsung Galaxy S Smartphone [14]; used with permission; some annotations are added.

As seen, there are six different antennas fitting within the limited form factor of the smart phone, each of which structurally is very slim. Among the antennas are two Wimax antennas, which are well separated and are most probably part of the MIMO scenario and bring about signal diversity. A WiFi and a GPS<sup>10</sup> antenna are also embedded which are indispensable parts of any contemporary Smartphone in the market.

In a similar manner, future devices are expected to have co-existing front-ends for<sup>11</sup> Wimax (more than one to offer MIMO), WiFi (2.4/5GHz, multiple MIMO antennas might appear here as well), Bluetooth (2.4GHz), Digital TV, UWB [15] (3.1GHz to 10.6GHz [16]), GPS (mostly 1.57GHz), and a range of front-ends for WWAN<sup>12</sup> [17], including different types of GSM (850/900/1800/1900 MHz), or any similar legacy (1G, 2G, and 3G) or new wide area coverage (4G, 5G [18]) that will be offered by carriers in the future. In addition, according to projections to the future by standards like IEEE 802.11ad [3], the new generation of devices might have at least one antenna at 60GHz to provide higher data rate for short-range WLAN/WiFi communications which will supplement the current 2.4GHz/5GHz WiFi. Moreover, the 60GHz radio employed in a WPAN<sup>13</sup> scenario [19] will soon become an essential part of any personal digital system like cameras, laptops, tablets, wireless HDTV screens, game controllers, wireless security cameras, wireless home safety systems, etc. Not only could 60GHz radio make a local wireless network of such systems, but also, it could connect them to the internet through 60GHz access points (planned by IEEE 802.11ad).

Consequently, future laptop or even Smartphone manufacturers will have to deal with mmWave technology at the RF level and specifically at the most bulky and lossy section, the *antenna front-end*. Even more surprisingly, researchers at the Polytechnic Institute of New York University are currently working on 28GHz and 38GHz for future (micro) cellular mobile networks applicable to densely populated areas like New York city [18]. This technology is presented as a new attempt in moving beyond the borders of 4G communications, into the 5G realm.

On the processing and microelectronics side of this evolution, major companies specialized in engineering personal mobile communications products (e.g. Qualcomm [20]) are striving to

---

<sup>10</sup> Global Positioning System

<sup>11</sup> The wireless landscape, electromagnetic spectrum, and typical wireless applications in this spectrum are provided in Appendix D and Appendix E.

<sup>12</sup> Wireless Wide Area Network

<sup>13</sup> Wireless Personal Area Network

develop tiny low power high-capacity chipsets which are multi-standard, multi-mode, and universal. These companies have relatively few problems with processing, considering the tremendous rate of development in microelectronics and its anticipated future. The roadmap issued by ITRS<sup>14</sup> [21] describes the current and upcoming VLSI<sup>15</sup> technology nodes and envisages where the future of semiconductor industry would most probably move to. According to this roadmap, by the end of 2013, 32nm half-pitch nodes should be readily available to the industry (this expectation might not have been met yet), and then, by about 2016 and 2022, respectively, 22nm and 11nm nodes will also be introduced. The following two examples could help understand how realistic this envisaged map might be. In 2006, researchers presented a sub-5nm transistor in a VLSI conference [22], and later on in 2010, Australian researchers announced the smallest transistor built with only seven atoms [23]. In addition, Table 1.1 compares three Intel processors used in common mobile personal devices and provides a visual sense of the size occupied by the processing units incorporating such small transistors.

Table 1.1 Total size of some Intel processors for different personal internet-based devices; the table is created based on the data on a figure in [24].

<b>Processor</b>	Intel®Atom™ Z500-Z540	Intel®Atom™ N270	Intel®Celeron®
<b>Lateral Dimensions</b>	13mm×14mm	22mm×22mm	35mm×35mm
<b>Example of Devices Using the Processor</b>	MID <sup>16</sup> /UMPC <sup>17</sup>	Netbook	Traditional Notebook

The ITRS roadmap and examples like Fig. 1.1 and Table 1.1 imply that the development rate in the semiconductor sector outpaces the current advancements in efficient and low-profile RF front-ends of communications systems. This is not only because of fundamental electrical size limitation of RF components, but also because of the rise in the number of coexisting RF sections at different frequencies.

One significant side effect of enhanced processing power is that faster processors could justify the use of advanced technologies like MIMO [25]. MIMO systems rely on antenna diversity

<sup>14</sup> International Technology Roadmap for Semiconductors

<sup>15</sup> Very Large Scale Integration

<sup>16</sup> Mobile Internet Devices

<sup>17</sup> Ultra-Mobile Personal Computer

(multiple antennas) to enhance the performance of communication links through reducing the multipath fading and co-channel interference [26]. Realization of a MIMO system requires signal processing, which is now readily provided by semiconductors. This fact will increase the number of MIMO antennas in future mobile devices. However, in MIMO-based small wireless mobile terminals, high electromagnetic coupling between multiple antenna elements disturbs the radiation pattern and the input impedance of elements [27], increases the signal correlation and undermines the effectiveness of the MIMO scenario. Although in theory coupling could be minimized by placing elements more than a half-wavelength apart [27], this condition is difficult to meet for the space-limited form factors of future devices. Hence, the large size of the antennas section will be a critical issue to the future wireless technology.

To address aforementioned trends and requirements on the RF/antenna front-end, the present research is focused on the design of *high-performance slim antennas* with the potential to be easily integrated into future communications devices. It is demonstrated that the proposed antennas have the potential to be *miniaturized* and at the same time maintain or even slightly improve the *radiated power efficiency*. Two main schemes simultaneously help achieve these desired features. The first scheme is to employ periodic cells, and the second one is to thicken the top metal layer of these cells, and hence, the planar antenna composed of them. These periodic cell arrangements exhibit electromagnetic bandgap (EBG) behaviors, which enhances the performance of the antennas. The periodic nature of the cells and thickening causes the top layer to contain periodically applied narrow gaps with very tall sidewalls. Although the top traces of the antenna structures are thickened, this thickening *does not* significantly increase the *electrical thickness* of the whole antenna structure and it remains as thin as  $\lambda/25$  or potentially less. The research tries to show that the trace thickness reduces the ohmic loss (increased ohmic efficiency), and the thick metal traces incorporating narrow gaps provide enhanced capacitive coupling between adjacent cells, thus reducing the antenna resonance frequency. On the other hand, EBG cells per se act as artificial boundary conditions and contribute to the overall performance.

Such schemes could reduce the pressure enforced by the fundamental limitations of antennas. In fact, in terms of size, most conventional RF components such as filters, power dividers, impedance transformers, and especially antennas contain structures with feature dimensions of at least  $\lambda/4$ , or often several times  $\lambda/4$ . For instance, the well-known branch-line coupler has four



$\lambda/4$  sections [28-29]. The classic patch antenna is  $\lambda/2$  long, while its required ground size is typically at least  $1.2\lambda$  (free-space wavelength) for a satisfactory radiation [30]. This means that the antenna size for a given application does not depend much on the technology utilized, but is determined by physics laws [31], a fact which imposes fundamental limitations [32-33]. Such laws state that any attempt to reduce the antenna size yields the degradation of its bandwidth (BW), or gain, or efficiency.

To obtain a better view of sizing challenges, the size of the processor unit of a MID/UMPC device in Table 1.1 can be compared to the GPS antenna in Fig. 1.1. The former occupies  $13\text{mm}\times 14\text{mm}$ , as compared to the latter with  $\sim 20\text{mm}\times 40\text{mm}$ , and this space is only taken by one out of six antennas in Fig. 1.1. This relatively huge size is obviously a fraction of the whole size of the RF section, which not only comprises antennas but also filters, power splitters, phase shifters, diplexers/duplexers, up/down convertors, LNAs<sup>18</sup>, switches, multiplexers, SSPAs<sup>19</sup>, and the harness. In addition to space occupied, the RF module also consumes most of the stored energy, and generates most of interfering power as well. Considering that such components tackle the highest frequencies in the device and conduct the highest power levels as well, in case they are not miniaturized deliberately, they can show much reduced efficiencies and dissipate a large portion of the power. Biocompatibility, if in proximity to human tissue, is also another strict requirement on the antenna section of most devices, especially mobile phones. Although the SAR<sup>20</sup> [34] limit is  $1.6\text{W/kg}$ <sup>21</sup>, most devices have to stay well away from this limit to be able to compete with rivals.

It should be emphasized that potential applications of the proposed antennas are not limited to antenna miniaturization for mobile communications. Wireless capsule endoscopy is an example in biomedical engineering, which similarly requires small antennas in tight form factors. Besides miniature antennas, high-gain low-loss slim planar antennas are also in demand for radar systems, DSB<sup>22</sup> reception [35-36], earth-to-satellite links, fixed point-to-point microwave links (e.g. backhaul), etc. Hence, some of the thesis sections employ the single high-performance antenna element and show how it could be arrayed to achieve high-gain array antennas. There

---

<sup>18</sup> Low Noise Amplifier

<sup>19</sup> Solid State Power Amplifier

<sup>20</sup> Specific Absorption Rate

<sup>21</sup> The SAR limit set by Federal Communication Commission is  $1.6\text{W/kg}$  averaged over 1 gram of tissue, and the limit recommended by the Council of the European Union is  $2\text{W/kg}$  averaged over 10g (e.g. for Samsung Galaxy S, SAR reportedly is  $0.33\text{W/kg}$ )

<sup>22</sup> Direct Satellite Broadcasting

are also special applications requiring high-gain antennas (preferably planar) able to radiate circularly polarized (CP) waves. Reference [37] is an example of a radar system for concealed weapon detection demanding such waves. To address such applications, a very efficient CP antenna is proposed that could be used as a CP element in an array topology for the high gain demanded.

Automotive radar systems operating at 24GHz and 77GHz are also another attractive area that could benefit from the research. The RF front-ends of such radar systems require frequency scanning antennas. Hence, a novel leaky-wave antenna is presented which addresses such a requirement. It is demonstrated that this antenna fundamentally functions differently as the resonance frequency is within the leaky-wave region of the dispersion diagram of the antenna unit cells.

## **1.2 Research Objectives**

The specific research objectives are outlined as follows:

1. To achieve antennas with the potential to be electrically small while maintaining the desirable radiation properties. Antennas based on periodic unit cells are proposed. The unit cells are unconventionally thickened on the top layer (with thick metal traces) to provide high capacitive coupling between adjacent cells (reduced resonance and cell miniaturization), reduced conduction loss in the thick metal traces, and reduced interaction of the fields with high dielectric substrates (one source of loss in high frequencies). The research attempts to demonstrate that such features result in small antennas with relatively high radiation efficiencies.
2. To provide a fast and computationally efficient way of analysis and design for such structures. A new analysis approach is proposed, specific to unit cell based periodic structures. Closed-form equations are developed that could expedite the design process of such structures with reduced numerical computation loads.
3. To demonstrate the applicability of such high-performance miniaturized antennas to applications demanding larger high-efficiency apertures.
4. To demonstrate that the high-performance radiating elements have the potential to be employed in an array to yield very high gain flat antennas.

5. To demonstrate that the fundamental knowledge of unit cells helps develop antenna structures that could operate in different modes, resulting in both resonant and leaky-wave (with frequency-scanning radiation pattern) antennas.
6. To develop the designs so that they are compatible with microfabrication methods, for instance deep X-ray lithography (DXRL), for realizing fine high aspect ratio (HAR) features that could be applied to very high microwave frequencies.
7. To develop linearly and circularly polarized antennas based on HAR unit cells with high efficiencies and small volume.

### 1.3 Thesis Organization

After clarification of trends and the requirements of current and future antenna technology in this section, Chap. 2 describes the motivation behind the study and explains why the proposed structures are formed of periodic cells, contain HAR features, and can exhibit EBG behaviors which can enhance performance. The motivations are supported by dedicated analyses and comparisons, especially to justify the rewards of using thick metal traces. A comprehensive state-of-the-art review is also included in Chap. 2. Next, Chap. 3 reviews the analysis methods presented in literature for periodic structures, especially EBG structures. A new analysis approach called HFSS/Bloch is also presented which extends from the classic Bloch theory and is mainly used later in the thesis. Some other methods will accompany the HFSS/Bloch for verification.

As the main body of the thesis, Chaps. 4 and 5 expand on the nine sub-themes shown conceptually in Fig. 1.2. This figure introduces all ideas and the designs based on them, and shows how the HFSS/Bloch method contributes to the development of each design. Almost all ideas in Chaps. 4 and 5 are established upon a centerpiece which is a radiating periodic TL (Sec. 4.1). The HFSS/Bloch method is used to extract a dispersion diagram for understanding this structure. Next the idea of the open circuit SE-EBG-RA which is a fragment of this periodic TL is introduced (Sec. 4.1).

The next step is to introduce a short circuit version of SE-EBG-RA with a miniaturized nature (Sec. 4.2). Sec. 4.3 investigates the effect of enlarging the ground plane for this version and how to maintain the radiation by extra periodic parasitic elements. Then Sec. 4.4 presents a circuit model, entirely closed form, to describe the proposed HAR cells and the SE-EBG-RAs made of

those cells. Afterwards, Sec. 4.5 is dedicated to unit cell miniaturization and replaces the regular cells of the SE-EBG-RA with some miniaturized cells to reach smaller antennas. Chap. 5 presents some ideas related to Chap. 4, which are based on the same HAR cells and their dispersion diagram. As a naturally different class of antennas, Sec. 5.1 shows how cells could be used in leaky-wave mode to yield leaky-wave antennas with a scanning pattern. An innovative series-fed array of SE-EBG-RA is also presented in Sec 5.2. The next section, Sec. 5.3, presents a periodic patch antenna, with much improved performance due to EBG effects, the body of which is composed of six HAR cells. The final antenna in Chap. 5 is a CP version of the SE-EBG-EA with a very compact electrical footprint and high-efficiency (Sec. 5.4). Finally, Chap. 6 summarizes the study, concludes on the research outcomes, and discusses the contributions that the research has offered. It is noted that following the HAR antenna designs appearing throughout the thesis, Appendix C reviews a special microfabrication method called deep X-ray lithography (DXRL) with the potential to realize the proposed structures with small HAR gaps and high structure quality. Some of the relevant processing steps using this method together with some experimental demonstrations are discussed in this section.

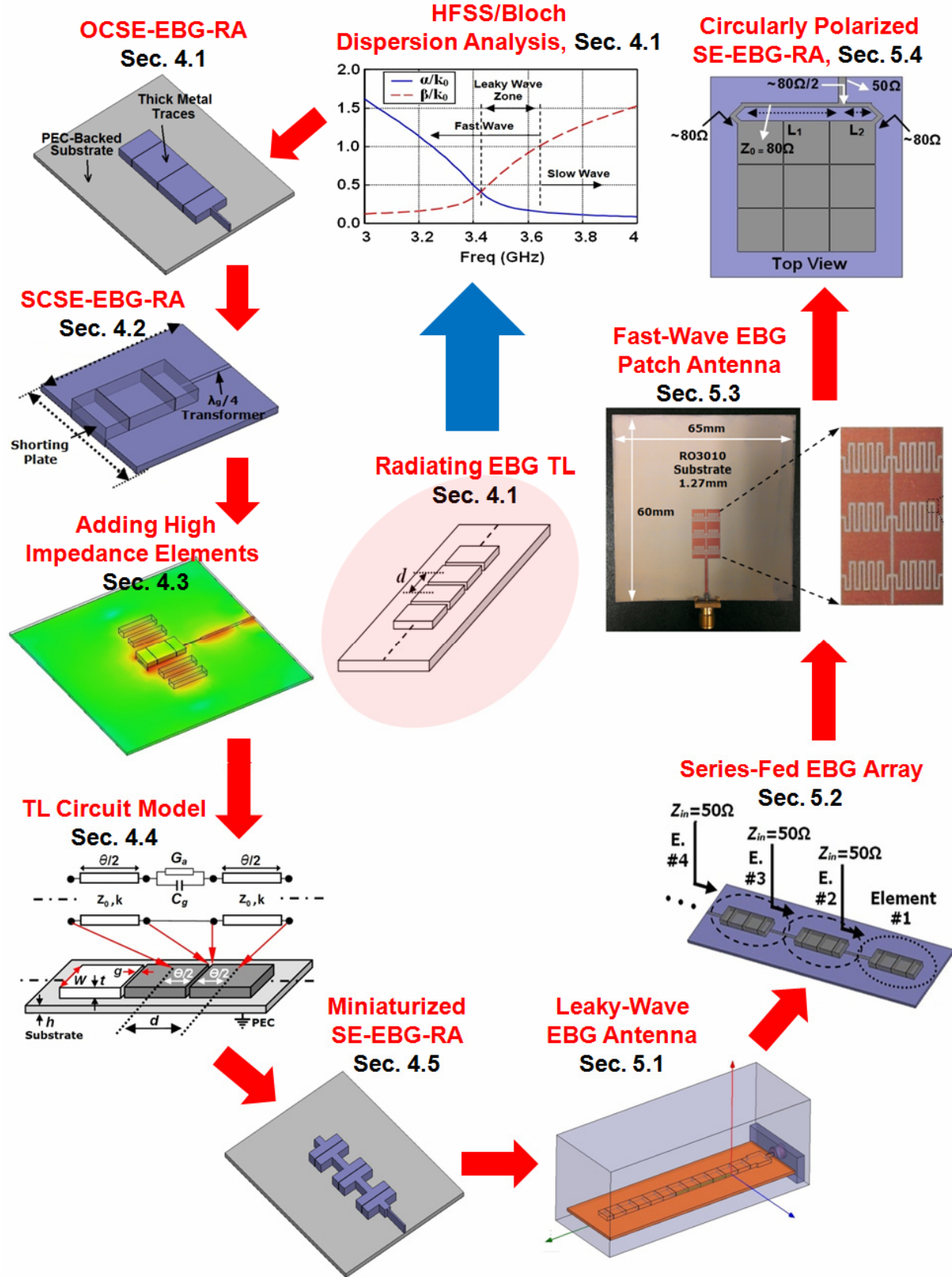


Fig. 1.2 An overview of ideas and designs to be presented throughout the thesis.

## References

- [1] G. Weinberger, "The new millennium: Wireless technologies for a truly mobile society," *Int. Solid-State Circuits Conf. Tech. Dig.*, pp. 20–24, Feb. 2000.
- [2] R. Harrison, "A Software-Defined Platform for Current and Future Communications Systems," *Instrumentation Newsletter*, Q1 2006.
- [3] Emna Charfi, Lamia Chaari, and Lotfi Kamoun, "Phy/Mac Enhancements And Qos Mechanisms For Very High Throughput Wlans: A Survey," *IEEE Commun. Surveys & Tutorials*, vol. 15, no. 4, 4th Quarter, 2013.
- [4] S. Parkvall, E. Dahlman, A. Furuskär, Y. Jading, M. Olsson, S. Wänstedt, and K. Zangi, "LTE Advanced – Evolving LTE towards IMT-Advanced," *Vehicular Technology Conference*, September 2008.
- [5] Khan, R. ; Khan, S.U. ; Zaheer, R. ; Khan, S., "Future Internet: The Internet of Things Architecture, Possible Applications and Key Challenges," *10th Intern. Conf. on Frontiers of Information Tech. (FIT)*, Islamabad, Pakistan, Dec. 2012.
- [6] Feki, M.A.; Kawsar, F.; Boussard, M.; Trappeniers, L., "The Internet of Things: The Next Technological Revolution," *Computer*, vol. 46, no. 2, Feb. 2013.
- [7] K. Wei; W. Zhang; Y. Yang, "Prolonging battery usage time in smart phones," *IEEE International Conference on Communications (ICC)*, Budapest, June 2013
- [8] Parkkila, J.; Porras, J., "Improving battery life and performance of mobile devices with cyber foraging," *IEEE 22nd International Symposium on Personal Indoor and Mobile Radio Communications (PIMRC)*, Toronto, Canada, Sept. 2011.
- [9] Jakob Nielsen, "Nielsen's law of internet bandwidth," <http://www.nngroup.com/articles/nielsens-law-of-internet-bandwidth/>
- [10] Flipsen, B.; Geraedts, J. ; Reinders, A. ; Bakker, C. ; Dafnomilis, I. ; Gudadhe, A., "Environmental sizing of smartphone batteries," *Electronics Goes Green 2012+ (EGG)*, Berlin, Germany, Sept. 2012.
- [11] Michael Kassner, "Cheat sheet: What you need to know about 802.11ac," *TechRepublic*, 2013-06-26.
- [12] Vivian Kelly (2014-01-07). "New IEEE 802.11ac™ Specification Driven by Evolving Market Need for Higher, Multi-User Throughput in Wireless LANs," *IEEE*. Retrieved 2014-01-11.
- [13] D. Rouffet, S. Kerboeuf, L. Cai, V. Capdevielle, "4G Mobile Technical Paper," *Alcatel Telecommunications Review*, 2nd Quarter 2005, [www.alcatel.com/atr](http://www.alcatel.com/atr)
- [14] Retrieved April 20 2014, from <http://www.antenna-theory.com/antennas/patches/pifa.php>
- [15] F. Koshiji, Y. Akiyama, K. Koshiji, "UWB antenna built into 3G smartphones," *IEEE Intern. Conf. on Ultra-Wideband*, Sydney, Australia, Sept. 2013.
- [16] Duixian Liu, Brian Gaucher, Ulrich Pfeiffer, Janusz Grzyb, *Advanced Millimeter-wave Technologies: Antennas, Packaging and Circuits*, Wiley, 2009.
- [17] Seong-Youp Suh ; Intel Corp., Santa Clara ; Sooliam Ooi, "Challenges on multi-radio antenna system for mobile devices," *IEEE Inter. Symp. on Antennas and Propagation*, Honolulu, HI, USA, June 2007.

- [18] Rappaport, T.S.; Shu Sun; Mayzus, R.; Hang Zhao; Azar, Y.; Wang, K.; Wong, G.N.; Schulz, J.K.; Samimi, M.; Gutierrez, F., "Millimeter Wave Mobile Communications for 5G Cellular: It Will Work!" *IEEE Access*, vol.1, pp. 335-349, May 2013.
- [19] R. Fisher, "60GHz WPAN standardization within IEEE 802.15.3c," *International Symposium on Signals, Systems, and Electronics*, Montreal, Canada, 2007.
- [20] Retrieved April 20 2014, from <http://www.qualcomm.com/chipsets/gobi/rf-solutions/qualcomm-rf360-front-end>.
- [21] Banqiu Wu, Ajay Kumar, "Extreme Ultraviolet Lithography: Towards the Next Generation of Integrated Circuits," *Optics and Photonics Focus*, vol. 7, Nov. 2009
- [22] Lee Hyunjin, et al., "Sub-5nm all-around Gate FinFET for Ultimate Scaling," *Symposium on VLSI Technology*, Honolulu, HI, USA, 2006.
- [23] Bob Beale, "Quantum leap: World's smallest transistor built with just 7 atoms," *Phys. Org.*, May 24, 2010.
- [24] Brooke Crothers, *Intel Atom N270 processor set for Netbooks*, April 7, 2008, Retrieved April 20 2014, from <http://www.cnet.com/news/intel-atom-n270-processor-set-for-netbooks/>
- [25] G. J. Foschini and M. J. Gans, "On limits of wireless communications in a fading environment when using multiple antennas," *Wireless Pers. Commun.*, vol. 6, pp.311-33S, 1998.
- [26] P. Mattheijssen, M. Herben, G. Dolmans, and L. Leyten, "Antenna pattern diversity versus space diversity for use at handhelds," *IEEE Trans. Veh. Technol.*, vol. 53, no. 4, pp. 1035–1042, Jul. 2004.
- [27] W. L. Stutzman, and G. A. Thiele, *Antenna Theory and Design*, New York Wiley, 2nd Edition, 1998.
- [28] D.M. Pozar, *Microwave Engineering*, 2nd ed., John Wiley & Sons, 1998.
- [29] C.A. Balanis, *Antenna Theory: Analysis and Design*, 3rd Ed., NJ: Wiley, 2005.
- [30] S. Collins and Y.M.M. Antar, "Antenna size reduction using Yagi-Uda loops and shorted circular patches," *IEEE Trans. Antennas Propag.*, vol. 52, no. 3, pp. 855-864, Mar. 2004.
- [31] A. K. Skrivervik, J. F. Zurcher, O. Staub, and J. R. Mosig, "PCS antenna design: The challenge of miniaturization," *IEEE Antennas and Propag. Mag.*, vol. 43, no. 4, pp. 12-27, Aug. 2001.
- [32] H. A. Wheeler, "Fundamental Limitations of Small Antennas," *Proc. of the IRE*, vol. 35, no. 12, pp. 1479-1484, Dec. 1947.
- [33] W. Geyi, "Physical Limitations of Antenna," *IEEE Trans. Antennas Propag.*, vol. 51, no. 8, Aug. 2003.
- [34] R. Ikeuchi and A. Hirata, "Dipole Antenna above EBG Substrate for Local SAR Reduction," *IEEE Antenn. Wireless Propag. Lett.*, vol. 10, pp. 904-906, 2011.
- [35] Ghiyasvand, M.; Dalili Oskouei, H.R.; Forooraghi, K., "Broadband proximity coupled microstrip antenna for direct broadcast satellite reception using PBG structures," *Asia-Pacific Conference Microwave Conference (APMC)*, Suzhou, China, Dec. 2005
- [36] R. Azadegan, "A Ku-Band Planar Antenna Array for Mobile Satellite TV Reception with Linear Polarization," *IEEE Trans. Antennas Propag.*, vol. 58, no. 6, pp. 2097-2101, June 2010.
- [37] D. J. Kozakoff and V. Tripp, "Antennas for Concealed Weapon Detection," *5th International Conference on Antenna Theory and Techniques*, Kyiv, Ukraine, May 2005.

# Chapter 2

## Motivation and State-of-the-Art

### 2 Motivation and State-of-the-Art

The terms "HAR<sup>23</sup> Vertical Features" and "EBG<sup>24</sup> Antennas" frequently used in this thesis convey the simultaneous application of HAR structures with periodic structures, and specifically EBG structures. Popular usage of the term "EBG" is to apply this term quite generally to a wide range of periodic structures, and that is also the approach taken in this thesis, even though these might not be "true" EBG structures by the strictest definitions. There also appears to be some differences in the literature over what constitutes an EBG structure. Consequently, this section clarifies the motivations behind the study in two distinct parts. The first part points out the motivation for employing the EBG concept, and qualifies how the proposed structures might exhibit EBG and/or "EBG-like" behaviors, and the second part indicates the motivation behind using HAR structures.

---

<sup>23</sup> High Aspect Ratio

<sup>24</sup> Electromagnetic Bandgap



## **2.1 Motivation behind Utilizing EBG structures**

In order to understand the importance of EBG structures, a literature review is conducted to provide a background on the terms like, “EBG concept”, “EBG structures”, and “EBG unit cells”. Although the EBG concept has made a widespread contribution to many areas of Electromagnetics, in the following, the literature review is mostly oriented towards “Antenna Theory & Design”.

### **2.1.1 Background and Literature Review**

EBG structures have been found to be one of the most attractive concepts introduced in Electromagnetics. Such structures have drawn so much attention and have been so promising that some outstanding researchers have found enough reasons for speaking about “Marvels of EBG Structures” [1]. EBG structures, which are composed of electrically small EBG unit cells, have involved and influenced electromagnetic (EM) problems as a new boundary condition that could be conceived theoretically, but was not available in nature (as opposed to regular boundaries which are readily realized, e.g. by metal surfaces). This boundary is generally a high impedance (HI) boundary, or more specifically, an artificial magnetic conductor (AMC) (artificial version of the hypothetical Perfect Magnetic Conductor, PMC). Such surfaces have the ability to block the propagation of surface waves/currents, and consequently, they can show very deep and close-to-ideal stopbands in some frequency ranges (i.e. bandgaps) while being almost transparent to signals in other frequencies. With the introduction of the EBG concept, these artificial boundary conditions (most of them possessing a planar surface) started being studied more seriously. Although previously introduced in Photonics and Physics (referred to as Photonic Bandgap, PBG [2]), as of 1999 in which EBG surfaces were formally brought into Electromagnetics by Sievenpiper [3], many researchers have showed interest in applying them to EM-related applications and theories. Afterwards, most conventional and canonical EM problems started being reviewed, now noting the possibility of realizing a PMC in practice. In general, such efforts can be categorized into two main streams:

- EBG concept and “Antenna Theory and Design”
- EBG concept and “Microwave Theory and Techniques”

Reviewing the literature reveals that considerable research has been separately focused on each stream, and many outcomes are now available after a decade or so. As for the first stream, some successful researchers in the field have collected the published articles in the form of a book [4]. In the following, first the origin and the definition of such periodic structures are clarified. Then, the recent contributions to the *antenna stream* are reviewed and the most relevant technical areas are categorized.

#### 2.1.1.1 The Origin of Bandgap Structures

The idea of periodic EBG surfaces originates from the early efforts to realize a practical high impedance (HI) surface to be used as PMC (boundary condition) for electromagnetic problems. Fig. 2.1 shows a corrugated metal slab with corrugations of quarter-wavelength depth. Each groove can be considered a  $\lambda/4$  parallel plate TL which is shorted at the end (bottom), and hence, has an ideally infinite input impedance at the top surface over a narrow frequency band. This surface is considered a 1D high impedance surface, as it provides HI effects only to E-fields in the Z-direction. This surface is both physically and electrically thick due to the  $\lambda/4$  structure.

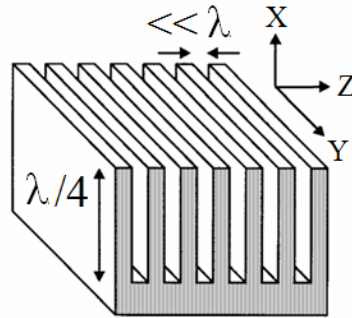


Fig. 2.1 A corrugated metal slab with HI effects at its surface, if the corrugations are quarter-wavelength deep. This is a polarization dependent surface. Only E-fields in the Z-direction observe the HI effect [3] © 1999 IEEE.

In time, 2D versions of this surface were introduced as shown in Fig. 2.2 (a). These surfaces are formed by arrays of electrically small square (or other shaped) patches on a narrow dielectric slab, connected to the ground by vias. It can be shown [3] that each cell forms a parallel *LC* tank circuit and can result in the desired resonance behavior, however with an electrical thickness much smaller than shown in Fig. 2.1. The tank circuit is later illustrated further.

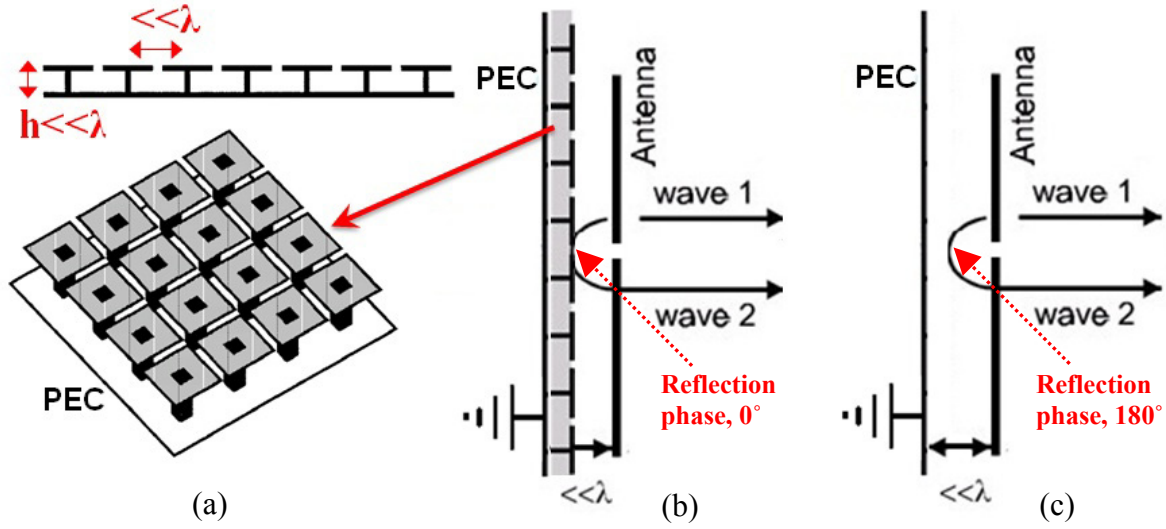


Fig. 2.2 A conventional 2D planar EBG surface (a), comparison between the radiation of a dipole antenna adjacent to an EBG ground plane (b), and a PEC metal ground plane (c); parts of the figure are from [3] © 1999 IEEE; some modifications and annotations are applied.

Fig. 2.2 demonstrates the difference in the reflection phase operation of a dipole antenna on PEC versus EBG ground planes. As seen in Fig. 2.2 (b) and (c), the waves reflected from the PEC are out of phase while those reflected from the EBG are in phase. Therefore, in Fig. 2.2 (c), the dipole image in the PEC cancels its current and opposes constructive radiation while in case of Fig. 2.2 (b), radiation is constructive. This advantage is obtained for the EBG dipole while the overall substrate thickness is very small. If the dipole operating frequency is exactly at the cells resonance, the cells ideally behave like a PMC. However, if the dipole resonance has a frequency offset from the resonance of individual cells, this condition is provided partially, yet results in a similar behavior (as demonstrated [e.g. 20-21]). In this case, the term HI surface is a general name that can describe the HI nature of the surface over a narrow band close to the PMC resonance frequency. Some thorough studies [e.g. 20-21] on dipole and patch antennas show that after the antenna is fined-tuned on the EBG surface and well matched, the final resonance frequency of the entire structure is *slightly below* the resonance of individual cells. Accepting a frequency offset from resonance supports the notion of cell truncation in EBG antennas while still benefitting from HI behavior. In fact, right at resonance, the cells are typically highly coupled with their neighbor cells and are electromagnetically sensitive to truncation. In Sec. 4.1, efforts are made (through reflection phase analysis) to show that for the proposed EBG antennas, this resonance unconventionally happens *slightly above* the cell resonance (Fig. 4.1.15), yet close

enough to benefit from the HI nature of the cells. Similarly, it will be shown that mutual coupling between cells is negligible (Fig. 4.1.10), most probably due to this upward frequency offset.

A key advantage of EBG structures is that the surface waves interact with an artificial HI surface that suppresses their tendency to travel as guided waves, as they might on typical ground planes. As shown in Fig. 2.3 (a), if there are no EBG cells, the PEC supports such waves and they reach the ground plane edges (in practice, the plane is usually finite and small) and diffract, resulting in backward radiation and disturbed forward radiation. As in Fig. 2.3 (b), this effect is controlled, even on a truncated ground plane with a finite number of cells.

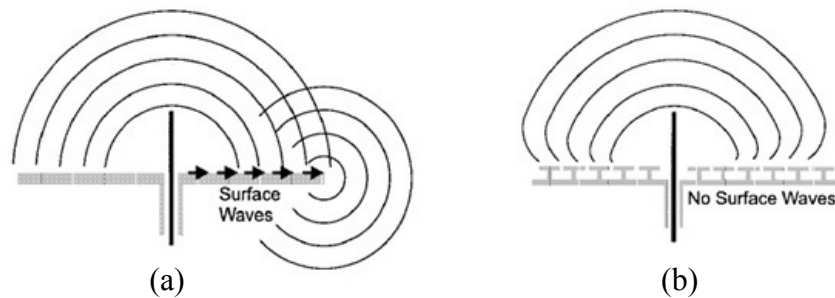


Fig. 2.3 The role of a PEC ground plane in support of surface waves (a), the role of an EBG ground plane in suppression of surface waves [3] © 1999 IEEE; some modifications are applied.

### 2.1.1.2 The Definition of EBG Structures

There are differing opinions on what constitutes EBG structures, surfaces, and cells, which should be clarified here. Early reported surfaces and much research since has been based on 2D surfaces, although this is not a fundamental requirement, because 1D and 3D versions can also show similar results (for instance the 1D structure of Fig. 2.1, only supports one polarization). When it comes to 3D EBG structures, it is not difficult to conceive them as a simple multilayer EBG surface (stacked), as indicated by Sievenpiper [3]. However, for 1D cells, the case remains somewhat controversial because the cells are typically not symmetrically periodic, as with the conventional 2D EBG HI surfaces. Nonetheless, there have been a number of such structures presented and adopted in both microwave and antenna engineering, which exhibit similar behaviors to the 2D counterparts, and support the notion that 1D EBG structures under certain conditions can belong to the larger family of EBG structures.

For instance, in [116] a band-notched ultra wideband monopole antenna is proposed that uses small EBG cells. The whole EBG structure operates as a bandstop filter. Only *one* EBG cell is

enough to obtain a notch-band, while only two EBG cells in one direction (with different size) can generate dual notch-bands. In [117], a novel planar power divider is proposed for which some of the sections are composed of only a few EBG cells deployed in one dimension. In addition, the authors use dispersion diagrams very similar to the Bloch/HFSS diagram used in this work. Reference [118] is another example in the antenna realm that, as seen in Fig. 2.4, uses a limited number of cells around the dipole to improve its performance. The truncation of the cells (3 cells across) and their 1D nature at various positions is apparent. The performance of this truncated structure is similar to other works, which use larger EBG grounds covered by a larger number of cells [e.g. 21].

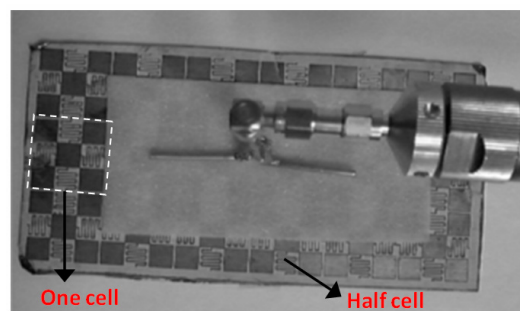


Fig. 2.4 A dipole antenna in close proximity to an EBG ground plane with very limited number of cells [118] © 2008 IEEE; some modifications are applied.

In [119], the EBG cells are utilized on the vertical walls of a rectangular waveguide, as in Fig. 2.5, providing a PMC boundary condition that supports TEM propagation in the waveguide near the EBG resonance frequency. As seen, *only two* cells in the Y-direction are sufficient to provide this condition.

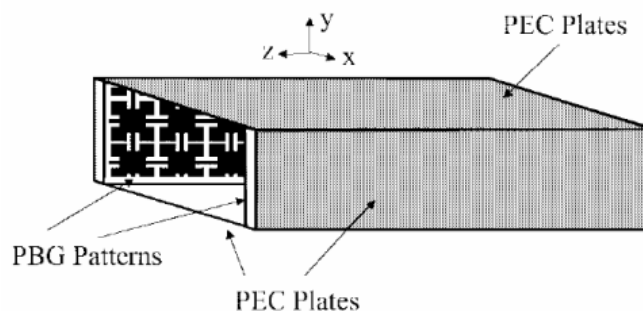


Fig. 2.5 The concept of a TEM UC-PBG waveguide; a rectangular waveguide using artificial magnetic boundaries on vertical walls, realized by PBG/EBG cells at around resonance [119] © 1999 IEEE.

Another example is in filter design, where 2-port EBG surfaces provide very deep bandgaps (see Fig. 2.6) where the propagating waves are severely suppressed, in this case with -40dB insertion loss. Again, all three filters are using only 2 cells in widths and 5 cells in length and successfully perform as a HI EBG surface. These designs further support the notion that similar surfaces, like the 1D EBG structure in Fig. 4.1.1, with only one cell in width could also have the potential to display EBG behaviors.

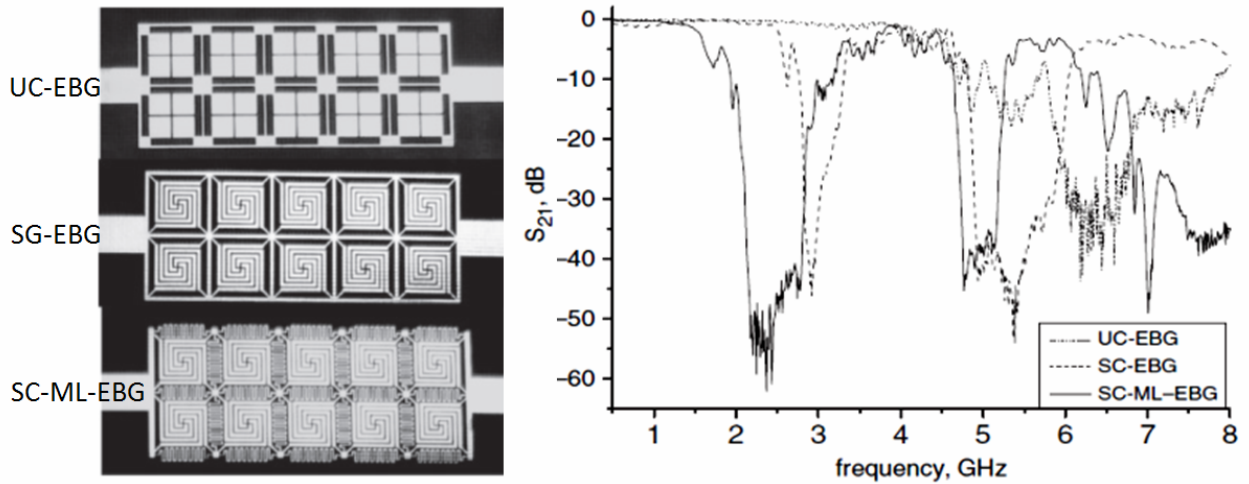


Fig. 2.6 Top side of three EBG structures connected with microstrip lines and their measured  $S_{21}$  parameters [120]  
© 2008 IEEE; some modifications are applied.

As in Fig. 2.7, in the leaky-wave antenna (LWA) domain, the authors of [121] render novel 1D LWA using tiny EBG cells, which are acting as high impedance surfaces. Reference [122], also renders another example of such 1D EBG LWAs.

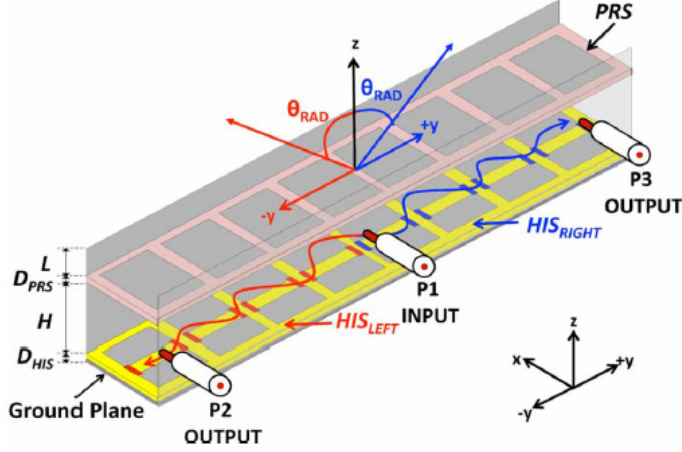


Fig. 2.7 A full-space scanning 1D Fabry-Pérot LWA using EBG cells on the ground plane (called HIS, i.e. HI surface) © 2012 IEEE.

Finally, the authors of [123] particularly focus on 1D EBG structures and, using the Floquet-Bloch theory, discuss bandgap behaviors and the effect of truncation of cells on bandgaps. From the material presented there, it is deduced that if truncation happens, the behavior of a 1D EBG structure could be slightly disturbed; however, bandgaps are still available and could be utilized.

Such publications along with many more demonstrate that the microwave and antenna communities tend to adopt the term EBG for a wide range of periodic cells demonstrating EBG-like behaviors, regardless of being 1D, 2D, or 3D. In addition, it is useful to apply periodic theories and cell modeling methods to gain a practical understanding of the behavior of *truncated* periodic structures.

According to such publications, as long as a structure is composed of electrically small unit cells (small lateral size), and is based on grounded dielectric slabs, which are also electrically very small ( $\lambda/15$  or less), the structure could be considered an EBG structure. It is noted that many of the 1D structures exhibit behaviors very similar to 2D structures, if the polarization of the fields excited by the adjacent radiator are oriented with their one-dimensional structure.

The proposed EBG antennas of this thesis are mainly 1D EBG structures (except for Sec. 5.3 and Sec. 5.5) that exhibit similar behaviors to more conventional 2D EBG surfaces, and are, therefore, generally considered to be of the same family. As opposed to the conventional EBG structures of Fig. 2.2 (b), the *Self-Excited EBG Resonator Antenna*, presented in this work does not have any separate radiator like the dipole in Fig. 2.2 (b); instead the EBG surface and the radiator are the same (integrated). Two to six EBG cells (as presented in Chap. 4) are cascaded in

one direction on the ground plane to form the body of the radiating structures and are directly fed by a microstripline from one side. The term EBG is adopted in this thesis and specifically used to describe such antennas, as they exhibit a range of properties and behaviors that are consistent with most conventional EBG antennas.

Some of the most important of these traits are briefly listed here and will be systematically demonstrated throughout the thesis:

- Employing unit cells with typically small electrical footprint of  $\sim \lambda/12 \times \lambda/12$  and potentially smaller
- Having small overall thicknesses of  $\lambda/25$  and potentially thinner
- Showing very high radiation effects
- Having reduced conduction and dielectric losses (hence, high efficiencies)
- Typically using highly truncated ground planes of e.g.  $0.25\lambda \times 0.25\lambda$
- Maintaining a high front-to-back radiation ratio and broadside radiation pattern on such truncated planes
- Showing enhanced group delays and radiation losses at some narrow bands (Fig. 4.1.1)
- Exhibiting similar unconventional effects on two alternative dispersion diagrams (Fig. 4.1.14)

The clarification rendered here is supplemented by the review on the analysis methods for EBG and periodic structures, which will appear in Chap. 3.



### 2.1.1.3 Surface Wave Suppression

One of the most beneficial features of EBG cells is the ability to suppress surface waves [3, 5]. It has been this feature that allows EBG cells to be a substitute for PEC ground planes traditionally used for antennas [5]. Due to the high impedance behavior, EBG cells can act as an Artificial Magnetic Conductor (AMC) [6-8], imitating the role of a Perfect Magnetic Conductor (PMC) at some frequency bands. As defined theoretically, a PMC has a high impedance nature, suppressing surface waves and surface currents. Such waves can be induced by tangential magnetic fields [3] on sheets of metal (PEC). In practice, such sheets are the ground planes of planar antennas covered on top by a thin dielectric slab. Surface waves can travel inside or even above the substrate, or also, in the form of induced current on the ground surface, reach the edges of the plane, and diffract unfavorably. While being impinged by plane waves, the AMC condition of an EBG surface occurs at frequencies where the magnitude/phase of the reflection coefficient is  $1/0^\circ$  [7-8]. It has been repeatedly shown that such structures can considerably improve antenna performance. Also, as demonstrated in [9-10], reducing surface waves enhances the antenna radiation pattern and causes less coupling between elements of an array [11].

However, what really are the surface waves and how are they excited?

Such waves could travel along the dielectric interfaces in canonical (with classical boundary) and practical (with complicated boundary conditions) electromagnetic problems with various geometries. When the problem specifically involves a thin grounded dielectric slab, the magnitude of such waves is stronger at the interface and exponentially decays as the distance increases from the interface (towards the outside of the dielectric). Even though no real power is theoretically allowed to propagate in the direction, which is perpendicular to the dielectric surface, the power can still be guided along the surface, and therefore, the fields are confined but traveling inside the system. For most practical planar antennas, such as patch antennas, inverted-L antenna, etc. the geometry is similar to the grounded dielectric slab, and hence, the structure can accommodate a considerable amount of surface waves traveling to the edge of the size-limited ground plane. These waves then diffract from the edges, most of the time uncontrollably and destructively, depending on the exact geometry. For example, as for the patch antenna, when truncating the ground plane, the effect of such waves is to distort the broadside radiation pattern, cause a slight backward radiation, and introduce surface wave loss which drops the antenna efficiency.

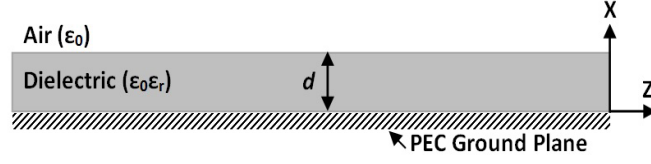


Fig. 2.8 Geometry of a grounded dielectric slab.

For the grounded slab in Fig. 2.8, the cut-off frequencies ( $f_c$ ) for TM and TE modes are as given by the following equations, respectively, where the first and second dominant modes are  $TM_0$  and  $TE_1$  [13]:

$$f_c = \frac{nc}{2d\sqrt{\epsilon_r - 1}}, \quad n = 0, 1, 2, \dots \quad (2.1)$$

$$f_c = \frac{(2n-1)c}{4d\sqrt{\epsilon_r - 1}}, \quad n = 1, 2, 3, \dots \quad (2.2)$$

As seen, if  $d$  and/or  $\epsilon_r$  increase,  $f_c$  will drop, and the possibility of accommodating more of such modes at the operating frequency increases. For example, for a 1mm alumina slab ( $\epsilon_r=9.9$ ), the first two dominant modes start to be excited at 0 GHz and 25.14GHz. Thus, in case working below 25.14GHz, the only unwanted surface mode that could be possibly excited is  $TM_0$ . This mode has two E-field components ( $E_z$  and  $E_x$ ) and one H-field component ( $H_y$ ) and travels along the Z axis (Fig. 2.8). As many of the proposed designs are using high-dielectric alumina substrates in this work, it is important to apply new boundaries in form of discontinuities or parasitic or resonating elements to suppress the  $TM_0$  and possible higher order modes, and this is the role that the proposed EBG cells will play. It is worth noting that for patch antennas, it is well-known that increasing the dielectric thickness and/or relative permittivity can considerably decrease the efficiency [14], a behavior which, as explained above, is partly related to the surface wave excitation.

#### 2.1.1.4 BW Enhancement

There are a number of studies specifically focused on the antenna BW enhancement, and how the special abilities of EBG cells can help achieve such an objective. For example, [15] proposes a wideband dipole on an EBG ground. Also, [12] demonstrates how applying non-uniformity to the EBG structures can roughly double the BW. As shown in Fig. 2.9, this work compares the

performance of a dipole antenna on a PEC and two different EBG high impedance ground planes. Ultra-wideband characteristics are also demonstrated [16], offering the BW of 70% covering 9-19GHz. Such examples clearly prove that EBG cells are very helpful in developing a new generation of wideband antennas.

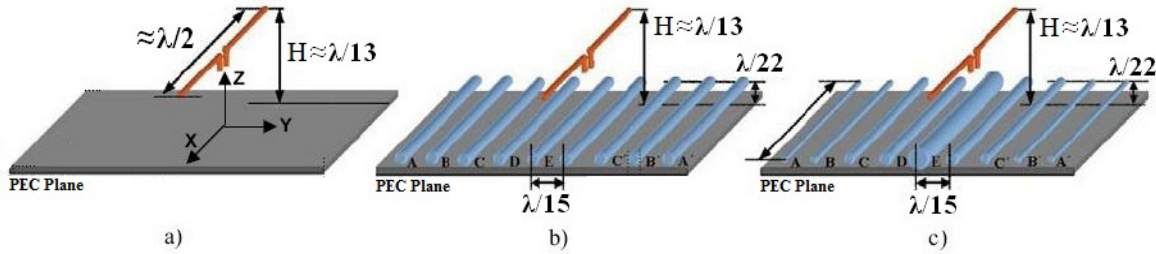


Fig. 2.9 A low impedance PEC ground plane (a) compared to uniform (b) and non-uniform (c) EBG high impedance surfaces. EBG surfaces are adjacent to a dipole antenna yielding BW enhancement [12], © 2006 IEEE; some details on original figures are removed, and some texts are manipulated for quality enhancement.

### 2.1.1.5 Gain Enhancement

Gain as another very important antenna parameter has also benefited from EBG structures. Similar to BW enhancement, there are many studies specifically focusing on gain enhancement. To exemplify, [17] has achieved a new design for planar patch antenna on an EBG substrate having  $\sim 3\text{dB}$  more gain than the conventional patch-on-PEC antenna. Noting such an effect, the same author has studied another type of antenna (a DRA<sup>25</sup>) with the same EBG cells [18], and the same  $\sim 3\text{dB}$  improvement is observed again. Moreover, in [19], it is shown how a previously proposed EBG ground can be used with DRA at around 60GHz. The work demonstrates 15dB enhancement in F/B together with a better gain. Such efforts confirm that regardless of the type of the main radiator, replacing a PEC with an EBG ground will improve performance.

### 2.1.1.6 Miniaturization

There are a number of studies, which have used EBG structures to reduce the antenna physical size while maintaining the electrical size. In fact, such a feature can provide a longer electrical length with the same physical length (footprint) or equivalently, the same electrical length with a smaller footprint. It has been repeatedly demonstrated [e.g. 3, 20-24] that as opposed to traditional antennas, when using a truncated (less cell numbers than usual) EBG ground plane for

<sup>25</sup> Dielectric Resonator Antenna

an EBG antenna, input matching quality remains robust or at least remains probable to maintain (slight frequency shift). At the same time with a good matching, high efficiency and radiation are also possible to obtain. Efficiencies close to ideal [20] have been observed for patch antennas supported by EBG planes, while it is well-known that it is impossible for a patch to render such a high efficiency simultaneous with matching and reasonable directivity.

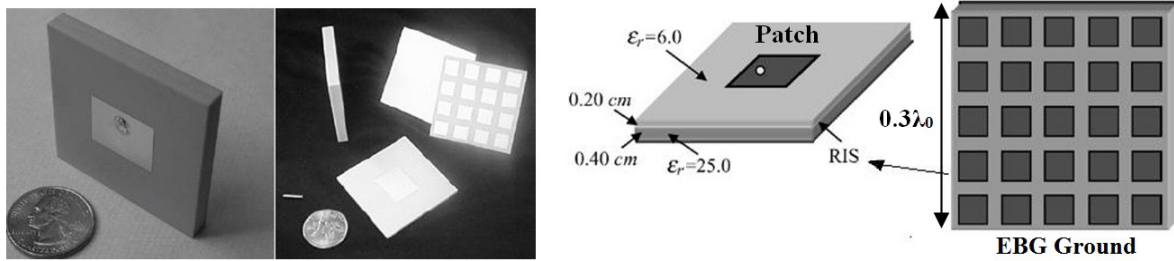


Fig. 2.10 A miniaturized patch antenna on an EBG high impedance surface with 95% efficiency [20], ©2004 IEEE.

The works presented in [3, 20-24] provide some examples of antenna miniaturization based on the EBG concept. For instance, Fig. 2.10 shows a miniature patch antenna on an EBG high impedance surface with 95% efficiency [20]. In the following chapters, some designs will be presented which feature a smaller electrical footprint and a comparable efficiency thanks to the properties of the proposed HAR EBG cells.

#### 2.1.1.7 Combination of Gain, Efficiency, and BW Improvement

There are also efforts [25-26] demonstrating that not only the improvement is separately achievable on gain, size, or BW, but also a combination of all these factors is attainable. In [25], it is clearly demonstrated that using an EBG substrate (ground plane) rather than a PEC one for a patch antenna can provide ~3dB gain enhancement and at the same time increase the BW from 5% to 25%. Also, in [26] the same ~3dB gain improvement is observed with a significant improved ohmic efficiency, again for EBG microstrip patch antenna.

#### 2.1.1.8 Reduction of Biological Harms

Reviewing literature shows a growing interest in wearable, body-worn, or close-to-body communication systems. The most important issue with such systems is the intrusion of lossy human tissue (body) to the performance of devices and vice versa. Because most of these systems operate from ~1 to 5GHz, the wavelength is large relative to the typical sizes of these

systems (e.g. compare  $\lambda=12.5\text{cm}$  at 2.4GHz used for Bluetooth to the size of a mobile phone). Because traditional antennas need at least  $1.2\lambda$  ground plane size to work properly, a large wavelength results in a large footprint. Usually in practice, the size available is even much less than  $1.2\lambda$  [27], and hence, the ground plane has to be truncated. However, this can cause mutual interaction between the body and antenna near fields and yield degradation. The frequency shift or totally losing input matching, drop in efficiency, deformation of radiation pattern, shorter battery lifetime, and most importantly the biological harm to the body are possible aftermaths. Again, thanks to EBG cells ability to combat surface waves, EBG grounded antennas can be matched and work efficiently with  $\sim 0.5\lambda$  [20, 29]. Noting this fact, some researchers interested in wearable mobile antenna technologies have utilized EBG structures [29-35].

In fact, EBG antennas are small while still presenting a relatively high F/B [29] ratio, and hence, the fields infiltrating the body located at the antenna backside could be negligible. This feature causes the parameter called Specific Absorption Rate (SAR) to be less than standard limits and allows these antennas to be compatible with the body [29-33]. In such investigations, it is clearly shown that parameters like efficiency and gain are still stable and well maintained. Fig. 2.11 describes an example of how EBG structures could be applied to develop low SAR body-compatible antennas.

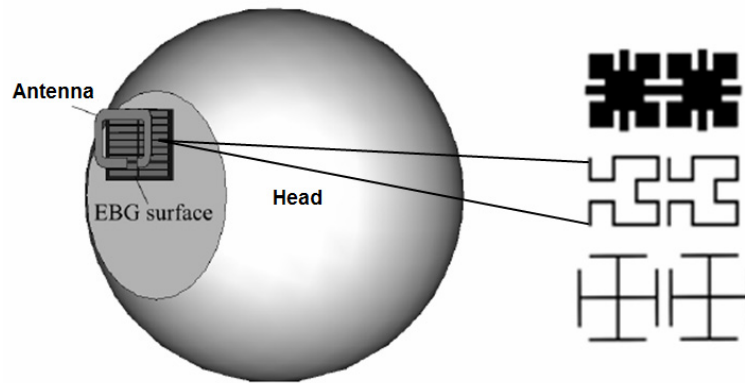


Fig. 2.11 Demonstration of how EBG surfaces are typically used on the ground plane to isolate the antenna from the human head in personal mobile communications [30] © IEEE 2010.

### 2.1.1.9 Unit Cell Design

Reviewing the literature shows that some research activities focus on the design of improved EBG unit cells per se without indicating a direct application [8, 36-48]. Typically, the desirable properties are enhanced BW [23, 43-44], smaller size [8, 44], and stability of the resonance frequency against the angle of incident plane wave [8, 38, 42], the properties that can be potentially applied to a myriad of applications. The philosophy behind this approach is that in case these improved unit cells are employed in the structure of traditional antennas, similar improvements could be observed for the new EBG antenna. Some of the presented unit cells possess dual or even multi-band [38, 46] bandgap characteristics making them suitable for satisfying the multi-band requirement of many commercial communications systems [38]. Interestingly, some efforts are dedicated to the design of angularly stable AMC/EBG cells [8, 42]. In fact, authors argue that the smaller the size is and the more improved angular stability is achieved, the more ideally the cells imitate a hypothetical Perfect Magnetic Conductor. Finally, some researchers show interest in the derivation of closed form formula and circuit models for prediction of EBG cells characteristics [36, 45]. The motivation behind such efforts is that even a roughly accurate prediction of the cell resonance can help designers swiftly choose the unit cell geometry with properties as close as possible to the desired ones. Fig. 2.12 shows different EBG unit cell designs tailored to achieve different properties. The cells are mostly composed of a metallic Frequency Selective Surface (FSS) of various shapes placed on a thin PEC-backed dielectric slab [8, 36-39, 42-43, 47]. Fig. 2.13 also shows prevalent  $LC$  circuit model representations.

One of the rewards of using tall/HAR EBG cells instead of the common thin-trace cells is to enhance the side coupling capacitance,  $C$ , of such models. The tiny HAR gaps with vertical side walls behave as enhanced parallel plate capacitors. Because the cell resonance is inversely proportional to  $\sqrt{LC}$ , such an increase in  $C$  results in unit cell miniaturization.

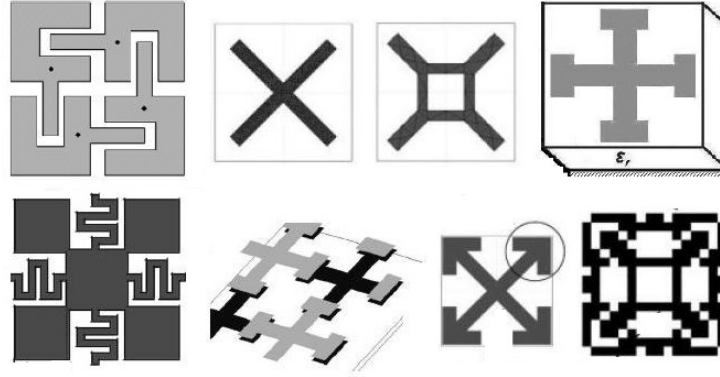


Fig. 2.12 Different EBG unit cells designed to achieve different features such as angular stability [8], multiband functionality [38] © 2005 IEEE, compact size [8], ease of tunability [49] © 2005 IEEE, etc.

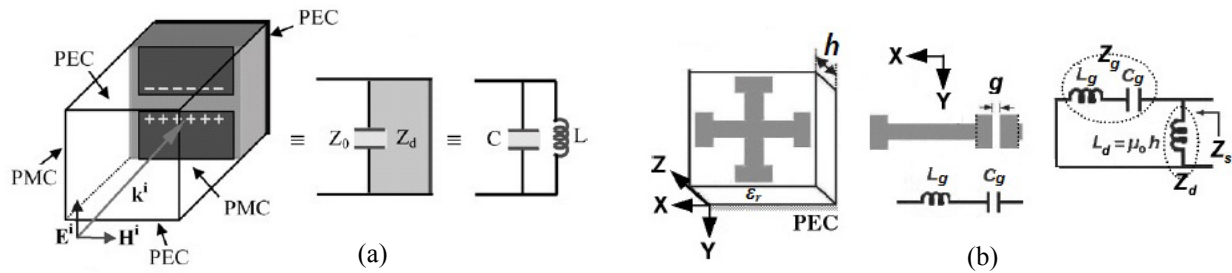


Fig. 2.13 Two different circuit model representations of EBG cells, a) the via-less version of mushroom-like structure [20] © 2004 IEEE, b) Jerusalem cross EBG [36] © 2008 IEEE; some of the information on original figures is removed and texts are manipulated for quality enhancement.

#### 2.1.1.10 Circularly Polarized EBG Antennas

Circularly Polarized (CP) radiation can be desirable to circumvent many problems caused by poor wave propagation in communications channels. Although CP antennas are usually easier to make with traditional methods, some EBG based radiators are also able to generate this type of polarization [23, 37, 50-54], while incorporating the aforementioned benefits of EBG structures, including reduced size and design flexibility. Some previous works have first presented polarization dependent EBG surfaces [37], and have developed new CP EBG antennas [53-54]. Others have even applied the EBG concept to the very low frequencies and developed easy to fabricate CP wire antennas [52] based on non-uniform EBG surfaces [23]. Such a design renders a noticeable gain, relatively small size, with a pure CP waves while the structure is only fed from one single feed point.

#### **2.1.1.11 Planar EBG Structures**

A planar structure could be defined as a flat unified set of different thin substrates stacked together with patterned metallic layers in between and/or on each side. Literature review shows that most EBG structures presented possess a planar configuration [11, 20-21, etc.]. Noting the potential advantages, some researchers do not bound themselves to simple cases and turn to structures, which are planar but composed of more layers, sometimes with more complexities [20]. However, cases with only one substrate with metal traces on one side and PEC ground on the other side [38] are the most demanded due to the simplicity of design, fabrication, and integration. Accordingly, in this study, the designs are based on single layer configurations. Fig. 2.10 and Fig. 2.12 showed a few examples of different EBG unit cells.

#### **2.1.1.12 Tall/Thick EBG Cells**

To the best of our knowledge and investigation, there is no publication, which seriously pays attention to tall/HAR EBG structures. In one case [55], authors have tried to utilize a somewhat projected (called elongated) metallic parts in design of EBG unit cells. The lack of published work in the area is an opportunity for further research, and it is one of the motivations for following the proposed research track. In Sec. 2.2, and later on when the proposed structures are rendered, it will be shown how thickening the cells on the top layer reduces the loss in the antenna structure made of the cells and brings about some tangible justification to adopt the proposed EBG structures in practice.

#### **2.1.1.13 EBG Concept in Array Antenna Design**

One of the most successful contributions of the EBG concept is applied to array antennas design. As mentioned earlier, one of the rewards of EBG high impedance surface (HIS) is surface waves suppression. Simply speaking, having a HIS provides an open circuit to block the current which may be excited (by tangential fields) on the surface. As a result, such currents will either not be excited, or even though excited, will be damped quickly. This is in contrast to the case where the ground is a low impedance PEC surface (short circuit). In fact, this damping is a particularly desirable effect in array antenna design. A major issue when deploying antenna elements to form an array with a wider aperture and more radiation is mutual coupling [56,114]. The issue stems from the fact that in practice the behavior of an array element placed adjacent to other elements is not exactly the same as what is experienced when the element is alone. Hence, input matching,



radiation efficiency, and even sometimes radiation pattern of the elements are deviated in the array, making it difficult to implement the pure array theory in practice. Inspecting the reason for such a deviation reveals that the uncontrolled surface waves excited by one element can travel and interact with those of the next elements. These interactions can change the fields around the source and is observed as some kinds of far/near-field disturbance. The traditional remedy is to increase the element spacing to more than at least  $\lambda/2$  [56]. However, on the one hand, based on array theory, spacing more than  $\lambda$  causes undesirable grating lobes in the radiation pattern. On the other hand, according to the super-directive array theory, the closer the elements are, the more the overall directivity can be [56, 114], and hence, increasing the element spacing is not an optimum use of the available surface area. This fact opens up an opportunity to apply EBG surfaces. It has been shown [56-60] that proper placement of rows of EBG cells between adjacent elements can dampen the surface waves, reduce mutual interaction, and increase the array performance. For example, [59] shows an obvious enhancement in side lobe level (SLL) and gain as a result of surface wave suppression. Fig. 2.14 shows two different EBG cells applied to two array antennas to reduce the adverse effects of mutual coupling.

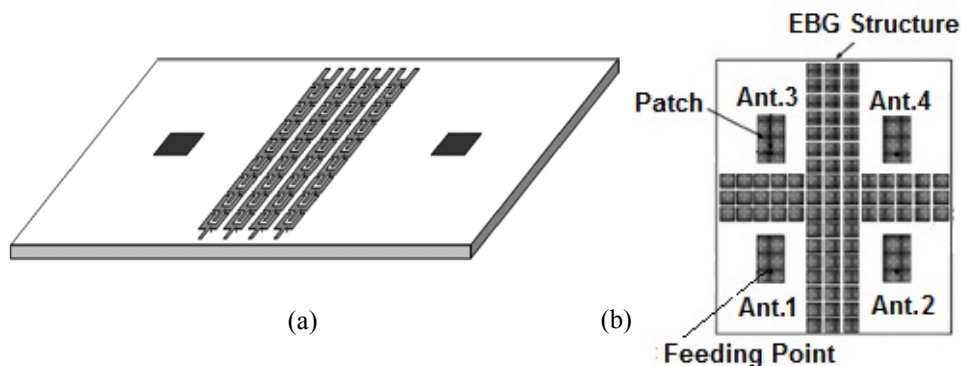


Fig. 2.14 Suppression of surface waves and mutual coupling in array antennas, a) 2-element array of patch antenna isolated by fork-like EBG cells [49] © 2005 IEEE, b) 4-element array of patch isolated by mushroom-like EBG cells [60] © 2006 IEEE; some of the information on original figures is removed for simplicity.

Some researchers have demonstrated how using EBG based elements can yield a combination of size, BW, and gain improvement [56] in arrays. Although, one reason can still be the same surface wave and coupling reduction, EBG-based elements are improved elements in terms of performance and obviously when they act in a system such as an array configuration, they can improve the whole system performance. Another challenge in array antennas is how to design

optimum phase shifters. Phase shifters are an integral part of phase array antennas and any improvement in their performance directly ameliorates the whole array system. For example, compact phase shifters can help make better use of the physical space available, have better phase and magnitude distribution all over the aperture, and reduce the intrusion with the radiation of the whole array system. Miniaturization, BW enhancement, and flexibility in design are advantages that EBG structures add to conventional phase shifters to help them more efficiently realize complicated phase array antennas, as shown in [62-63]. These works present tunable phase shifters for beam-scanning array antennas, taking the advantage of the tunability of the circuit model of each EBG cell.

#### **2.1.1.14 EBG Cells for Very High and Very Low Frequencies**

This part reviews the role of EBG cells in very high and very low frequency. The interest in applying EBG cells (as tiny resonators) in severely high frequencies is growing. Although most researchers first started using the concept for relatively low frequency applications [39], after enough progress and success, they have recently turned to the cells even at much higher frequencies. In [21] for example (published in 2003), the mushroom-like EBG unit cell is investigated and analyzed numerically over the wide range of 5-30GHz for the possibility of being an efficient high impedance ground plane for dipole antennas. Following this, the use of EBG structures in very high frequency applications has grown, ranging from around 15GHz to the upper limit of the usual microwave/mmWave regime of about 100GHz, or even higher (up to 300GHz). The drive for such a changeover is the rapid progress in the micro- and even nano-fabrication techniques and the availability of theoretical and practical knowledge in realizing micro scale feature sizes. As the frequency increases, the realization of feature sizes, which are now somewhere from a few 100nm to a few 100 $\mu$ m, is a real challenge but still feasible with some fine technologies. To exemplify, in [64] an EBG cell on LTCC substrates is proposed to be used at V-band ranging from 50GHz to 75GHz. It is noted that in the United States, the FCC<sup>26</sup> has allocated a part of the V-band from 57 to 64 GHz to unlicensed wireless systems. These systems are primarily used for high capacity, short distance communications at Gbit/second rates [65].

---

<sup>26</sup> Federal Communications Commission

As a matter of interest, EBG cells in [66] utilize MEMS technology at 30GHz and the work is presented in a conference on nano/micro engineered and molecular systems. Such works are evidences for potentials of nano/micro fabrication in increasing the operational frequency of EBG cells. Also, [67] is an example of efforts on EBG antennas in passive silicon (on-chip antenna). Not settling for such high frequencies, the authors of [68] step further even beyond the mmWave regime and investigate a 500GHz EBG TL and power divider again using MEMS and micromachining technologies, although technically the study fits under the general umbrella of Photonics.

Due to the fundamental contribution of the EBG concept which stems from being a versatile boundary condition, they have also infiltrated very low frequency applications [12, 23, 69-70] in which antennas are mostly wire-made [12, 23]. The results published prove that in low frequencies [12, 23], the EBG concept yields the same advantages as it does in other frequencies.

#### **2.1.1.15 Some Other Applications**

There are many more interesting applications for the EBG concept. For example, [71] demonstrates how EBG structures can improve high-gain array antennas to be used in radar systems. EBG cells potentials have also infiltrated the domain of reflect-array antennas. The reflector part of these antennas is composed of the EBG unit cells rendering a flat reflector behaving like the legacy parabolic reflectors. The reflection characteristics of the cells are deliberately tapered all over the reflector. The engineered reflector is able to provide the same reflection phase that the parabolic geometry of a reflector can cause. Applying a similar scheme, [115] integrates a number of controllable varactor capacitors into the EBG surface to actively control the resonance of each individual unit cell. This way any reflection phase distribution is achievable thanks to a central processing unit controlling the capacitors. This method makes it possible to achieve shaped or deflected radiation patterns demanded in satellite communications and by many radar systems. Fig. 2.15 shows the two examples of the reconfigurable reflect-array antennas described above.

Although EBG cells have been mostly applied to conventional antennas like dipole, patch, and inverted-L antennas, in some cases, researchers have shown the possibility of using them along with rather non-planar antennas like dielectric resonator antenna (DRA) [18-19].

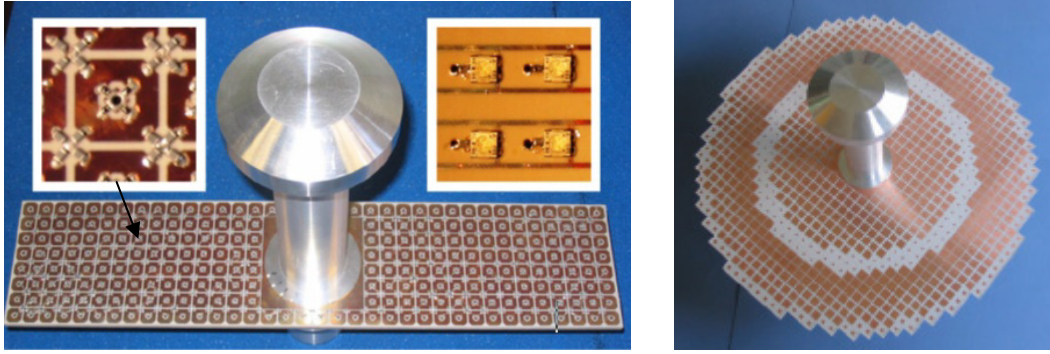


Fig. 2.15 Realizing reflectarray concept using EBG unit cells with tunable reflection properties, left) a waveguide feed illuminating a flat rectangular EBG surface, right) a waveguide feed illuminating a circular EBG surface with 23dBi directivity [115] © 2007 IEEE.

In [72], it has explained how a previously proposed EBG ground plane can be used along with DRA at around 60GHz. The work demonstrates 15dB improved F/B together with a slightly improved gain. In addition, [73] demonstrates that the well-known mushroom-like EBG ground plane can provide ~3dB gain improvement as compared to a PEC ground plane. Fig. 2.16 depicts the two EBG DRA designs indicated above.

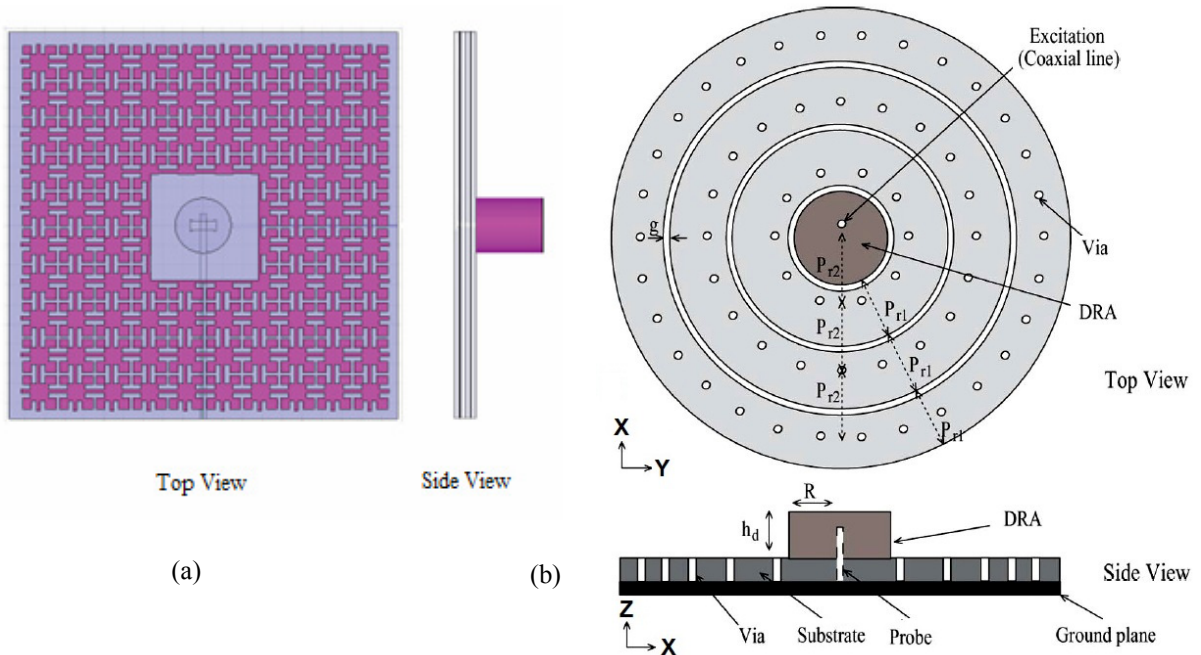


Fig. 2.16 A DRA as an example of a non-planar (vertical) radiator on EBG ground planes, a) a circular DRA on UC-EBG unit cells [72] © 2011 IEEE, b) a circular DRA on a circular mushroom-like EBG surface [73] © 2009 IEEE; some parts of the original figure are removed or manipulated for printing better quality.

In another work [74], absorbing EBG surfaces have been exploited to realize radar absorbing materials (RAM) for antenna systems. These materials are aimed to mostly absorb signals impinging the antenna body and therefore reduce the radar cross section of the system using the antenna. The last case to indicate is a broadband proximity coupled EBG microstrip antenna designed for direct broadcast satellite reception [75].

## **2.2 Motivation behind Utilizing the Third Dimension**

This part clarifies how the increased thickness of metal traces of the antennas proposed can serve as a rewarding parameter. A literature review is also carried out to provide a background on the terms like, “high aspect ratio structure (especially antennas)”, “tall/vertical structures”, and “thick metal structures”. Dedicated analyses are also rendered to highlight the fundamental connection between antennas and TLs<sup>27</sup>. Then according to such analyses, the capability of thickness especially in overcoming dielectric and conduction loss in the antenna structures is demonstrated. This demonstration will be confirmed throughout the thesis, where the high-performance nature of each proposed antenna is specifically demonstrated.

### **2.2.1 Background and Literature Review**

A rapid interest in communication systems at microwave and millimeter-wave frequency bands has been observed in recent years [76-101]. This is mainly because much larger percentage of BW is available at such high frequencies compared to the conventional spectrums. The other advantage is the shorter wavelength, which results in smaller RF devices and complies with the desire to achieve more integrated and compact design solutions.

Reviewing literature and many commercial products shows that researchers usually tend to base their structures on the well-established approach of using thin metal layers. This is a trend mainly formed based on the assumption of using low or medium frequency bands in which the tolerances in fabrication and also the surface roughness are not a significant issue. As mentioned, this trend is destined to change soon, and hence, this study will be aimed at investigating antenna structures with relatively thick metal films positioned on a thin grounded dielectric slab as the substrate. Apart from future trends, there are some profound reasons for turning to such

---

<sup>27</sup> Transmission Line

structures with thick metal traces. To clarify this, it is first essential to look back at the basics of antenna and TL theories.

As described in [102], in order to represent radiation and losses in a relatively small wire antenna (for instance, the dipole), the radiated and lost power can be represented by two real resistances,  $R_r$  and  $R_L$  respectively. The ratio of the radiated power to the total power entering the antenna (radiated plus lost) can be defined as antenna ohmic efficiency. This term can be described in terms of  $R_r$  and  $R_L$  [102]:

$$\eta = R_r / (R_L + R_r) \quad (2.3)$$

For a wire with length  $l$  and radius  $b$ , if the skin depth (see (2.9)) is much smaller than  $b$ , the current mainly travels on the surface, and hence, a high frequency ohmic surface resistance can be defined [102]:

$$R_L = \frac{l}{2\pi b} R_s \quad \text{where} \quad R_s = \sqrt{\frac{\omega\mu}{2\sigma}} \quad (2.4)$$

where  $\sigma$  is metal conductivity,  $\mu$  is metal permeability, and  $\omega$  is the angular frequency. As stated by (2.4),  $R_L$  is inversely proportional to  $b$ . This implies that thickening the wire reduces its loss, and therefore, as deduced from (2.3), increases  $\eta$ . A similar dependency on the thickness also holds for a circular wire (loop) [103]. Accordingly, in case the cross section of wire elements of an antenna (either straight or bent) increases, the loss drops and  $\eta$  of the antenna is enhanced. This behavior generally holds for various 3D metal shapes. Although some antennas are made of 2D thin strips rather than wires, it is demonstrated by many analyses and experiments that wires in an EM structure can generally be replaced by their equivalent thin-film strips [23, 42], while the EM behavior will remain roughly identical. This simple reasoning indicates the effect of thickening, based on antenna theory.

Taking a different viewpoint from microwave theory, it can be stated that any antenna is in fact a piece of transmission line (TL) for which the boundary conditions are intentionally changed so that the TL starts radiating/leaking EM power (switch from entirely bound to partially bound or unbound conditions). In [102], Balanis considers a segment of two-line TL and then illustrates how gradually increasing the spacing between lines (a “flared TL”) near the open end can cause transition from a non-radiating TL to a radiating TL, i.e. create an antenna. This idea is described in Fig. 2.17 (right). It is also shown that when the two parallel lines are

highly flared and spaced from each other and make a right angle with respect to the feedline, the open end is no longer a TL, but is the well-known dipole antenna. The same transition is also conceivable for a rectangular waveguide gradually being widened and turning into to a horn antenna which can ultimately radiate very well from its large open aperture, as in Fig. 2.17 (left).

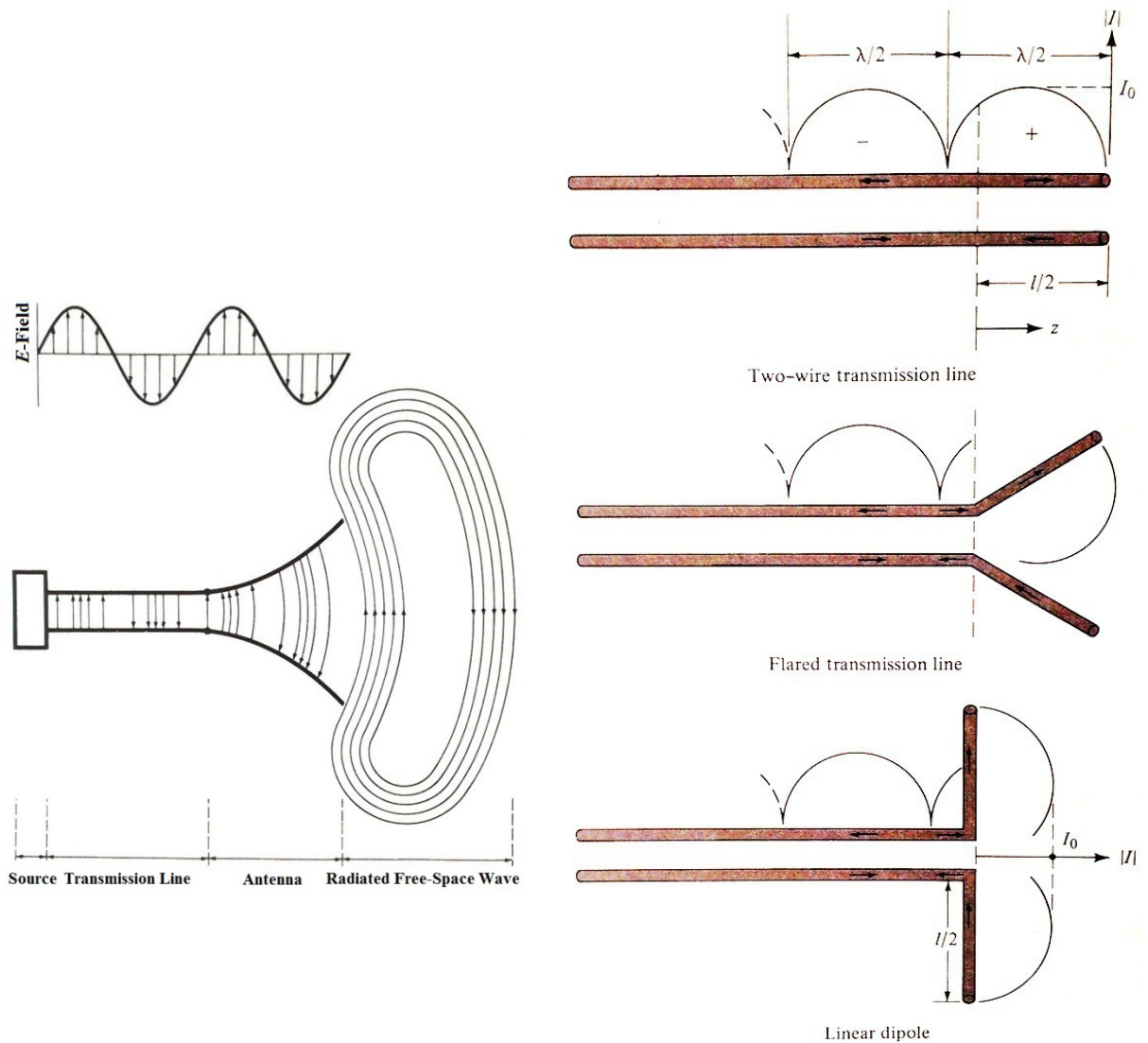


Fig. 2.17 Antenna as a transition device, bridging the TL to the free-space, left) source-to-rectangular waveguid-to-horn antenna transition [102], right) current distribution on a lossless two-wire TL, flared TL, and a linear dipole antenna [102] Copyright © 2005 by John Wiley & Sons Inc; used with permission.



The third case which could also demonstrate TL-to-antenna transition is illustrated in Fig. 2.18. As shown, two thick parallel coupled strips can first act as a TL, and when being flared (the spacing, being tapered), turn into a Vivaldi antenna which radiates from its open aperture.

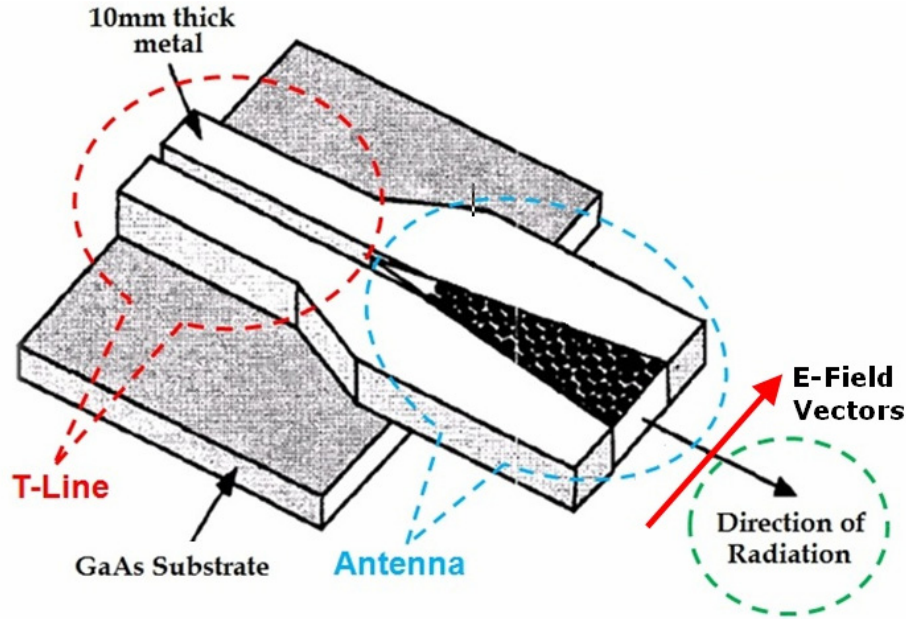


Fig. 2.18 A Vivaldi antenna with thick top metal layer on GaAs substrate. The first part is a TL with bound fields and then due to being flared, fields start to radiate at the end [79] © 1998 IEEE; some annotations are added to the original figure.

Another vivid example is the patch antenna, which in its dominant mode is in fact a  $\lambda/2$  piece of microstripline (MSL) with a very wide trace [104] to make it more radiating. Fig. 2.19 shows how a MSL can be transformed into a microstrip antenna. As in Fig. 2.19, a  $50\Omega$  MSL is widened gradually ( $W \uparrow$ ) at around its open end to approach the characteristics of a typical patch antenna.  $L$  in Fig. 2.19 is set so that the piece of MSL is  $\sim \lambda_g/2$  ( $L$  is kept fixed physically). As depicted in Fig. 2.20, by increasing  $W$ , the two radiating apertures of the patch antenna are increased gradually which allow the structure to leak real power, depending on the size of the aperture (size:  $W \times h$ ).



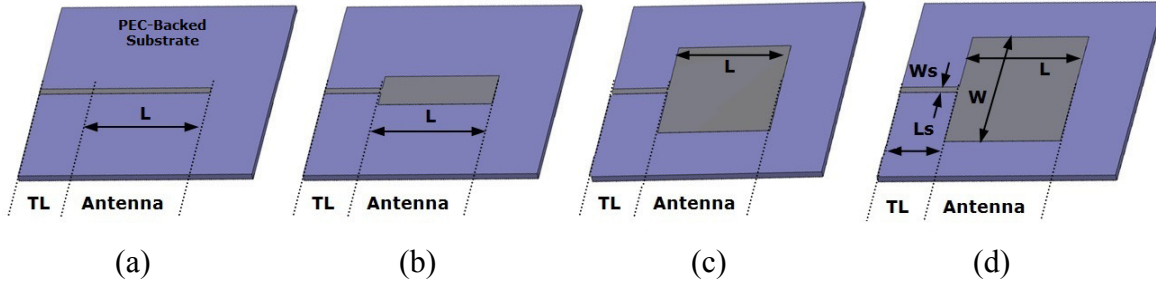


Fig. 2.19 Gradual transition from a MSL to a microstrip antenna through gradually increasing the strip width, a)  $W=0.91\text{mm}$ , b)  $W=5\text{mm}$ , c)  $W=15\text{mm}$ , d)  $W=18\text{mm}$ ; for all cases:  $h=1\text{mm}$ ,  $\epsilon_r=9.9$ ,  $\tan\delta=0.003$ ,  $30\text{mm}\times 30\text{mm}$ ,  $L_s=7.28\text{mm}$ ,  $W_s=0.91\text{mm}$  ( $50\Omega$  line),  $L=14.6\text{mm}$ .

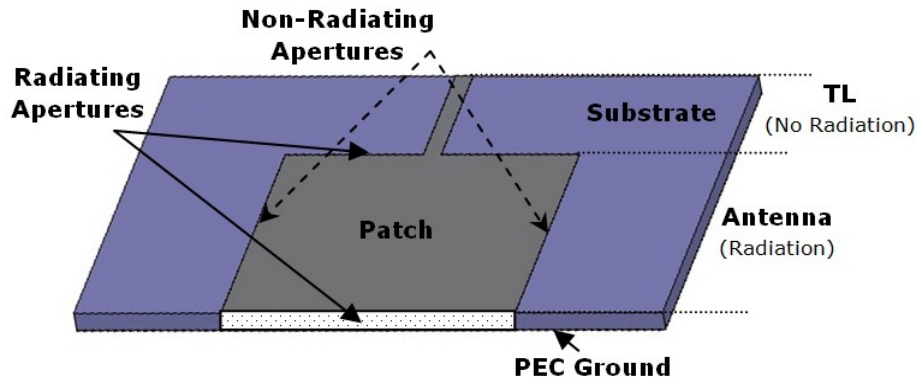


Fig. 2.20 Description of radiating and non-radiating apertures of a typical microstrip antenna; the feed line is a narrow strip, and hence, does not radiate (TL) while the patch part is a very wide version of the same TL and performs well as an antenna.

Table 2.1 Comparison of the simulated gain and  $\eta$  for the antennas in Fig. 2.19; the analysis frequency is 4GHz.

	Gain (dBi)	$\eta$ (%)	$W$ (mm)	$L$ (mm)
Fig. 2.19 (a)	-9.0	23	0.91	14.6mm
Fig. 2.19 (b)	-2.5	32	5	
Fig. 2.19 (c)	-1.36	39	15	
Fig. 2.19 (d)	-1.48	45	18	

Table 2.1 renders the simulated gain and  $\eta$  of the antennas in Fig. 2.19 and shows that both  $\eta$  and gain increase as  $W$  grows. Another way to have the fields radiate more is to gradually flare the spacing between the strip of Fig. 2.19 (a) and the ground plane. This is equivalent to gradually increasing the distance between the strip and its image in the ground which is similar to the flaring described in Fig. 2.17. Fig. 2.21 compares the non-flared strip and the version flared by the angle  $\psi$ .

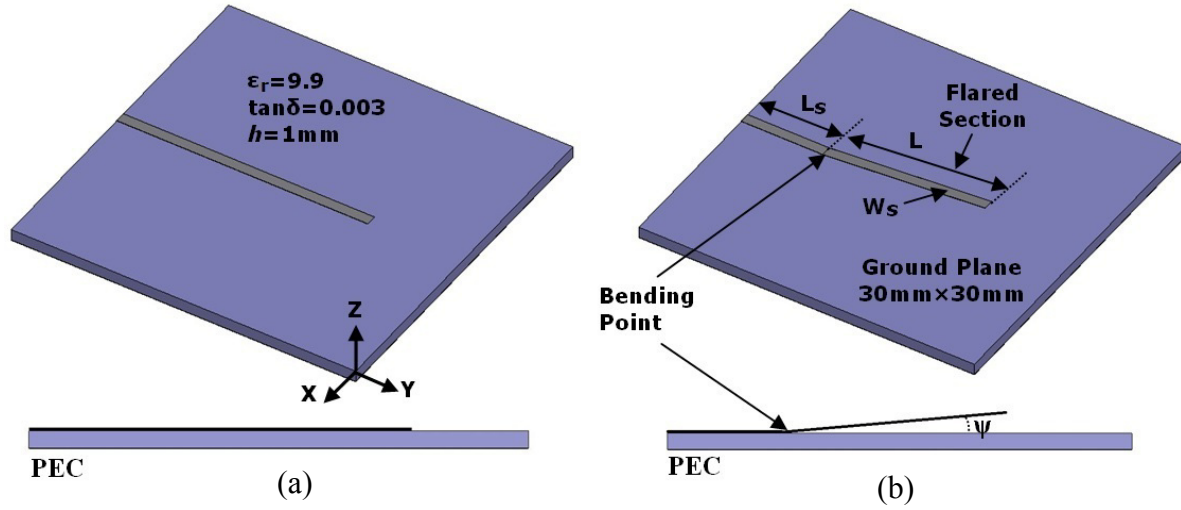


Fig. 2.21 3D and side view of a 50Ω MSL on PEC a grounded dielectric slab, a) non-flared case with  $\psi = 0^\circ$ , b) flared case with  $\psi \neq 0^\circ$ ;  $L_s = 7.28\text{mm}$ ,  $W_s = 0.91\text{mm}$  (50Ω line);  $L = 14.6\text{mm}$ .

For this case, Table 2.2 shows  $\eta$  versus  $\psi$  and demonstrates the radiation enhancement introduced by flaring. Furthermore, Fig. 2.22 compares the radiation pattern of Fig. 2.21 (b) for  $\psi = 0^\circ$  and  $\psi = 5^\circ$ . In fact, in case the strip is not flared, its image in the PEC ground plane underneath the substrate will be out of phase, and considering that  $h \ll \lambda$ , the current is cancelled out by its image, thus the system is non-radiating. As soon as flaring occurs, there will be non-zero field components perpendicular to the substrate that their image will be in phase, and hence, the structure can radiate. The larger  $\psi$  is, the larger such components will be, and higher  $\eta$  will be observed.

Table 2.2 Comparison of the simulated efficiency for the antenna in Fig. 2.21 (b) with different flaring angle.

Dimensions are as in Fig. 2.21 (b); the frequency is 4GHz	
$\eta$ (%)	$\psi$ (deg)
23	0
68	5
86	15
94	45

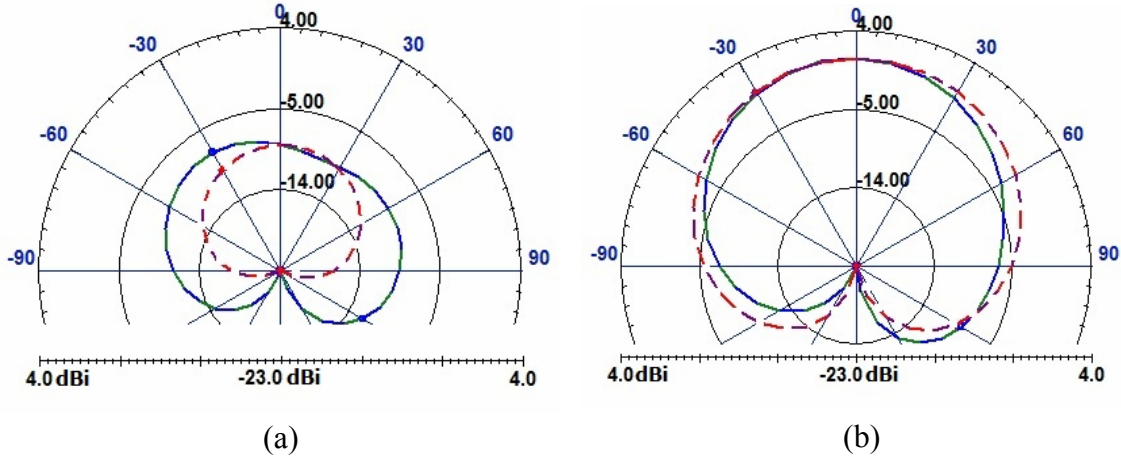


Fig. 2.22 Radiation gain of the antennas in Fig. 2.21, a) Fig. 2.21 (a), b) Fig. 2.21 (b) with  $\psi=5^\circ$ ; the gain includes directivity and  $\eta$ , but not the input matching; the dashed line corresponds to  $\phi=0^\circ$  and the solid line to  $\phi=90^\circ$  (E-plane).

According to the analyses and discussions presented above, any antenna is in fact a radiating TL. Therefore, any method capable to reduce the loss in TLs can cause the same effect to antennas and improve their efficiency, especially in case of planar antennas. The next step after clarifying the relation between antennas and TLs is to identify the relation between loss and trace thickness using TL theory. The objective is to show that thickness can alleviate loss in TLs, and therefore, in antennas, which are essentially a type of TL.

It is well-known [105-106] that increasing the trace thickness of planar TLs, such as coplanar waveguide (CPW) and MSL, results in decreasing the conductor loss. A thick MSL trace with width  $W$  and finite thickness  $t$  can be regarded as an effectively wider thin trace with width  $W+\Delta W$  [107] where

$$\Delta W = \frac{1}{2} \left( 1 + \frac{1}{\epsilon_r} \right) \frac{t}{\pi} \ln \left( 4e / \sqrt{\left( \frac{t}{h} \right)^2 + \left( \frac{1/\pi}{W/t+1.1} \right)} \right) \quad (2.5)$$

For a low loss MSL in the TEM mode, the attenuation constant is [13]:

$$\alpha_c + \alpha_d = \frac{R_s}{Z_0 W} + \frac{k_0 \epsilon_r (\epsilon_{\text{reff}} - 1)}{2(\epsilon_r - 1) \sqrt{\epsilon_{\text{reff}}}} \tan \delta \quad (2.6)$$

where  $k_0$  is free space wavenumber ( $\omega \sqrt{\mu_0 \epsilon_0}$ ),  $Z_0$  is the line impedance,  $W$  is trace width,  $\epsilon_{\text{reff}}$  is effective relative permittivity<sup>28</sup>,  $\epsilon_r$  is substrate relative permittivity, and  $\tan \delta$  is the loss tangent

<sup>28</sup>  $\epsilon_{\text{reff}}$  can be found using [13]:  $\epsilon_{\text{reff}} = 0.5(\epsilon_r + 1) + 0.5(\epsilon_r - 1) / \sqrt{1 + 12h/W}$

( $\tan \delta = \epsilon''/\epsilon'$ , where  $\epsilon = \epsilon' + j\epsilon''$  is the permittivity). The first term of (2.6) is related to the conduction loss in the metal and the second one is related to the dielectric loss. As seen, increasing  $W$  ( $W \rightarrow W + \Delta W$ ) reduces the first term. On the other hand, this increase can also decrease  $Z_0$  in the denominator, but because of thickening the trace, the ensuing  $\epsilon_{\text{reff}}$  will also be slightly less as a larger portion of fields infiltrates the air making  $Z_0$  relatively larger. Inspecting  $\alpha_c$  in (2.6) for finding the overall effect of  $W$  shows that increasing  $W$  introduces a *decrease* in  $\alpha_c$ , where the amount of this decrease depends on  $\epsilon_r$ ,  $W$ , and  $h$ . As stated by (2.6),  $W$  has no direct/apparent effect on the second term. However, the second term is proportional to frequency,  $f$ , (through  $k_0$ ) while the first term is proportional to  $f^{1/2}$  (through  $R_s$ ). Consequently, in very high frequency applications, the second term tends to dominate. This fact indicates the importance of predicting such effects and investigating the contribution of HAR traces to controlling this dielectric loss. On the bright side, as the trace thickness increases, the fields start infiltrating the air and the interaction with the substrate reduces [e.g. 108], which in turn can be experienced as a reduction in  $\epsilon_{\text{reff}}$ . Because (2.6) shows that for high dielectric materials (like alumina mainly used in this thesis),  $\alpha_d$  is *roughly* proportional to  $\epsilon_{\text{reff}}^{1/2}$  (i.e.  $\epsilon_r \uparrow \rightarrow \alpha_d \uparrow$ ), in very high frequencies, the application of HAR traces can compensate for the dielectric loss enhancement by reducing  $\epsilon_{\text{reff}}$ . It should be emphasized that although the discussion above was focused on MSL, similar arguments can be made for other TLs such as CPW.

Table 2.3 Comparison between the dielectric and conduction losses of two 50Ω MSL with different substrate permittivities, at low and high frequencies; results assume remaining in TEM mode, otherwise some extra loss will also appear.

Low dielectric loss: $\epsilon_r=9.9$ , $\tan\delta=0.003$ (alumina), $h=1\text{mm}$ , $t=30\mu\text{m}$ , $Z_0=50\Omega$ ( $W=0.915\text{mm}$ )				
		$\alpha_d$ (np/m)	$\alpha_c$ (np/m)	$\alpha_d/\alpha_c$
Frequency	4GHz	0.321	0.36	0.89
	40GHz	3.765	1.71	2.2
High dielectric loss: $\epsilon_r=2.85$ , $\tan\delta=0.04$ (SU8 resist [109]), $h=1\text{mm}$ , $t=30\mu\text{m}$ , $Z_0=50\Omega$ ( $W=2.32\text{mm}$ )				
Frequency	4GHz	2.55	0.13	19.6
	40GHz	27.62	0.43	64.23

Table 2.3 provides two quantitative examples to demonstrate the fact that frequency plays an integral role in changing the loss mechanism, especially for dielectric substrates with medium to high losses. The table compares the dielectric and conduction losses of two 50Ω MSL with different substrate permittivities, at low and high frequencies.

As seen, particularly for the lossy substrate,  $\alpha_d$  is significantly higher than  $\alpha_c$ . It is also shown that as the frequency increases,  $\alpha_d$  dominance becomes more obvious, and at 40GHz,  $\alpha_d$  is  $\sim 64$  times  $\alpha_c$ . It is important to note that Table 2.3 does not include the effect of roughness, which could increase  $\alpha_c$  slightly more. In practice, the roughness contributes extra losses at higher frequencies, which are observed as increased  $\alpha_c$ . To estimate how much roughness could contribute, (2.10) suggests that  $R_s$  could be at most doubled. As seen, this situation occurs if the roughness is much larger than  $\delta_s$ . In practice, the roughness of copper traces is less than 10μm, typically somewhere from 0.3μm to 5μm [110]. For example, based on (2.9), at 4GHz,  $\delta_s=1.05\mu\text{m}$ , and at 40GHz,  $\delta_s=0.33\mu\text{m}$ . Assuming 10μm roughness,  $10\mu\text{m} \gg \delta_s$ , and hence,  $R_s$  grows to the maximum  $\sim 2R_s$ . Under this condition,  $\alpha_c$  is doubled, but this increase can *hardly follow* the rapid increase rate of  $\alpha_d$  versus frequency, as explained before. This yields the conclusion that *when dealing with the typical conductor roughness of  $<10\mu\text{m}$  in high frequencies, the conductor loss is not the number one issue and can be easily dominated by the dielectric loss.*

It is very important to know that roughness could set a kind of limit on the maximum frequency of RF components, while also noting that this limit is still high enough for many of the RF applications. When it comes to high efficiency antennas of the present work, roughness is somewhat less problematic as the  $\eta$  is not directly affected by loss, but indirectly through the equation,  $\eta=R_r/(R_r+R_L)$ . For the proposed high-performance HAR antennas, even under the effect of a typical roughness,  $R_r \gg R_L$ , even up to very high frequencies. To quantify this, it is noted that a typical small matched SE-EBG-RA (see Sec. 4.2) has  $R_r \sim 50\Omega$ , and  $R_L \sim 4\Omega$ , which gives  $\eta=92\%$ . According to (2.10), roughness could adversely increase  $R_s$  by a factor on the order of 2, which means loss and the  $R_L$  will double. In that case,  $R_L \sim 8\Omega$ , and the  $\eta$  is 87%, which is still very high.

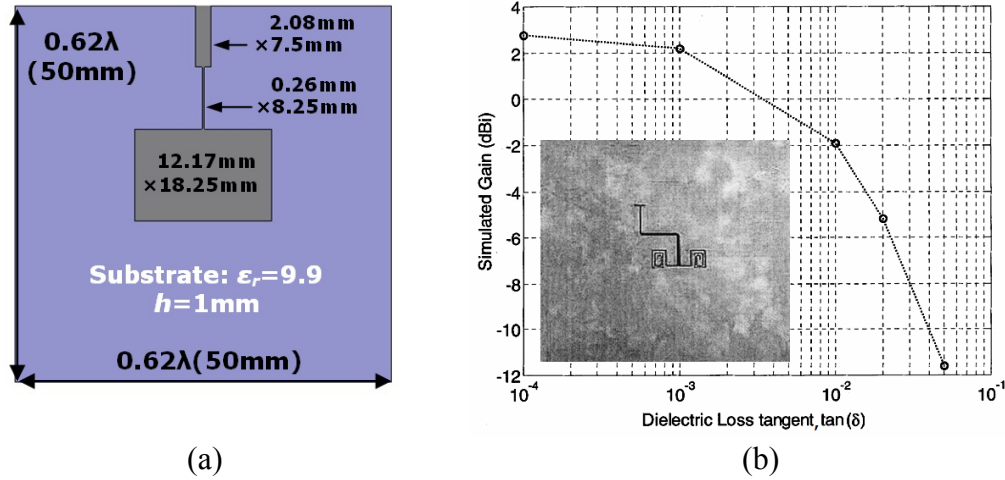


Fig. 2.23 a) A sample microstrip antenna on a microwave substrate with two different  $\tan\delta$ , numerically simulated in HFSS, b) simulated gain of a compact slot antenna on an infinite substrate with  $\epsilon_r=4.0 (1-j\tan\delta)$  [111] © IEEE 2003; the slot is printed on the only copper side and is excited by a microstripline printed on the other side of the substrate.

To highlight the importance of dielectric loss specifically in antenna applications, as in Fig. 2.23 (a), a microstrip antenna is designed on a substrate with  $\epsilon_r=9.9$  and with two different loss tangents ( $\tan\delta$ ) of 0.003 and 0.03 (10 times increased). At the matching (resonance) frequency of 3.73GHz, the ground plane is  $0.62\lambda \times 0.62\lambda$  and the thickness is  $\lambda/80$ . The antenna is matched to a  $50\Omega$  port using two quarter-wave transformers. The corresponding simulated efficiencies are 66% (gain=4.58dBi) and 0.19% (gain=-0.82dBi) respectively, which imply that the antenna gain drops by 5.4dB due to the increased dielectric loss. As shown in Fig. 2.23 (b), [112] also presents similar results by simulating the gain of a compact slot antenna on substrates with different  $\tan\delta$  and shows that increasing the loss from 0.001 to 0.01 decreases the gain by about 5dB. In fact, observing the same behavior for two planar antennas like patch and slot antennas, which are dual of each other in terms of operation, clearly demonstrates the importance of the dielectric loss in antenna design, especially at very high frequencies.

With recent advances in modern packaging and MMIC<sup>29</sup> technologies, the notion of integration of the whole system on a single chip, or at least, on a few separate chips but offering them in a single package, has drawn a lot of attention. However, the conventional Si wafers are inherently low resistivity ( $\rho$ ) and can dissipate much of the EM power inside. Under this condition, the loss tangent has to be modified as [113]

<sup>29</sup> Monolithic Microwave Integrated Circuits

$$\tan\delta = \frac{\varepsilon''}{\varepsilon'} + \frac{l}{\omega\varepsilon'\rho} \quad (2.7)$$

where  $\rho$  is the resistivity of the substrate,  $\varepsilon = \varepsilon' - j\varepsilon''$  is the complex permittivity of the substrate ( $\varepsilon_r = 11.68$  and  $\varepsilon''/\varepsilon' = 0.0018$  for Si [113]). Inserting these values into (2.7) yields

$$\alpha_d = \frac{\varepsilon_{eff} - 1}{\sqrt{\varepsilon_{eff}}} \left( 1.7905 \times 10^{-3} f + \frac{153.09}{\rho} \right) \text{ dB/cm} \quad (2.8)$$

where  $\rho$  is in  $\Omega\text{-cm}$  and  $f$  is in GHz. For low resistivity Si (LRS), with  $\rho = 1\text{-}10 \Omega\text{-cm}$ , the second term dominates and huge losses will appear. For high resistivity Si (HRS), with  $\rho = 2.4\text{-}10\text{k}\Omega\text{-cm}$ , the second term is small enough so that the design of microwave antennas on the Si with moderate efficiencies becomes possible at moderately high frequencies. One *advantage of thickening* the conductor line on top of such substrates is the reduction of the effective interaction of the fields with the substrate. This is because by thickening, a larger portion of the fields are trapped in the HAR air-filled gaps and this will reduce the loss in Si. This means that the HAR EBG antennas proposed are competent candidates for antenna-on-Si type technologies. Besides the relation to the dielectric and conduction losses, thickness can also have an important role in circumventing the roughness issue. When the frequency increases, the impacts of surface roughness increase. As stated by (2.6), the attenuation constant is proportional to  $R_s$ , and based on the following relation, it is also inversely proportional to the skin depth [13]:

$$\delta_s = \frac{l}{\sigma R_s} = \sqrt{\frac{2}{\sigma\omega\mu}} \quad (2.9)$$

The equation (2.6) is valid for an ideally smooth surface and the associated  $R_s$  is the minimum theoretical value. However, as the frequency increases, the wavelength ( $\lambda$ ) becomes comparable to  $\delta_s$  and the surface current experiences a longer path (in terms of  $\lambda$ ) due to the deformation of the surface. To include this effect, [106] and [13] show that instead of the usual  $R_s$  in (2.6), the following equation can be used:

$$R'_s = R_s \left[ 1 + \frac{2}{\pi} \tan^{-1} 1.4 \left( \frac{a}{\delta_s} \right) \right] \quad (2.10)$$

where  $a$  is the RMS<sup>30</sup> surface roughness.

---

<sup>30</sup> Root Mean Square

It is noted that according to (2.4),  $R_L$  is proportional to  $R_s$ , and this means, increased roughness will result in increased  $R_L$  and reduced radiation efficiency. Thus, a HAR EBG antenna with high efficiency (Sec. 4.1 and Sec. 4.2) is intended to dominate the total loss introduced by roughness and dielectric material. The improvement in  $R_r$  that the proposed antenna provides could dominate  $R_L$  and increase  $\eta$  in (2.3). The accuracy of (2.10) has been verified through experimentation in works like [110], and it is reportedly acceptable up to 10 GHz for practical microwave substrates with typical thicknesses.

The last step is to review the literature to answer the following question: *Has any similar antenna with thick metal HAR feature sizes been introduced before?*

Searching the literature for antennas with such characteristics reveals the lack of previous efforts. Willke proposed thick metal micromachined antennas in 1998 [79-80], but comparatively little has been published since then, while there have been several thin metal surface micromachined approaches [81-82]. Similarly, [83] published in 2009, presents a very HAR monopole antenna based on a new fabrication approach. Reference [84] is also one of the few works bringing EBG antennas into HAR realm by thickening the metal traces of the EBG surface embedded into the body of a patch antenna. Very recently, in the ECE department of the University of Saskatchewan, a series of investigations have been performed on HAR polymer-based DRAs<sup>31</sup> fabricated with the DXRL<sup>32</sup> process [85-86]. In such works, the antenna is made of HAR polymers structures, but the metal feed lines are out of thin films. The same research group has then proposed a new class of HAR antennas based on tall metal strips on a substrate [87]. Such strips are introduced as a TL and are manipulated to be integrated along with a dipole antenna made of the same HAR TL. This way the feedline and antenna are both HAR. Tall metal EBG cells have also been realized using DXRL [108], but applied to filters not to antennas.

Following such efforts, this work presents some novel HAR antennas which are new from two distinct aspects. Firstly, it is the first time that such HAR EBG cells (Chap. 4) and whole radiating structures based on them (Chap. 4 to Chap. 5) are proposed. Secondly, for the first time such HAR EBG antennas are investigated for the possibility of realization by a DXRL process (Appendix C).

---

<sup>31</sup> Dielectric Resonator Antenna

<sup>32</sup> Deep X-Ray Lithography



## References

- [1] Y. Rahmat-Samii, "The Marvels of Electromagnetic Band-gap (EBG) Structures," *ACES Journal*, vol. 18, no. 4, Nov. 2003.
- [2] J. Joannopoulos, R. Meade, and J. Winn, *Photonic Crystals: Molding the Flow of Light*. NJ: Princeton Univ. Press, 1995.
- [3] D. Sievenpiper, L. Zhang, R.F. Jimenez Broas, N.G. Alexopolous, and E. Yablonovitch, "High-impedance electromagnetic surfaces with a forbidden frequency band," *IEEE Trans. Microwave Theory Tech.*, vol. 47, no. 11, pp. 2059–2074, Nov. 1999.
- [4] F. Yang. and Y. Rahmat-Samii, *Electromagnetic Band Gap Structures in Antenna Engineering*, Cambridge Univ. Press, 2009.
- [5] Nuria Llombart, Andrea Neto, Giampiero Gerini, and Peter de Maagt, "Planar Circularly Symmetric EBG Structures for Reducing Surface Waves in Printed Antennas," *IEEE Trans. Antennas Propag.*, vol. 53, no. 10, 2005.
- [6] Feresidis, A. P., S. Wang, and J. C. Vardaxoglou, "Artificial magnetic conductor surfaces and their application to low-profile high-gain planar antennas," *IEEE Trans. Antennas Propag.*, vol. 53, no. 1, pp. 209-215, 2005.
- [7] Y. Zhang, J. V. Hagen, M. Younis, C. Fischer, and W. Weisbeck, "Planar artificial magnetic conductors and patch antennas," *IEEE Trans. Antennas Propagat.*, vol. 51, no. 10, pp. 2704-2712, Oct. 2003.
- [8] M. Hosseini, A. Pirhadi, and M. Hakkak, "Compact Angularly Stable AMCs Utilizing Skewed Cross-Shaped FSSs," *Microwave and Optical Technology Letters*, vol.49, no.4, April 2007.
- [9] Z. Li and Y. Rahmat-Samii, "PBG, PMC, and PEC ground planes: A case study of dipole antennas," *IEEE AP-S Symp*, 2000.
- [10] G. Poislane, "Antennas on high impedance ground planes: on the importance of the antenna isolation," *Progress in Electromagnetics Research*, vol. 41, pp. 237–255, 2003.
- [11] Fan Yang; Rahmat-Samii, Y. "Microstrip antennas integrated with electromagnetic band-gap (EBG) structures: a low mutual coupling design for array applications," *IEEE Trans. Antennas Propagat.* vol. 51, no. 10, pp. 2936-2946, 2003.
- [12] M. Hosseini, A. Pirhadi, R. Fallahi, "Bandwidth Enhancement of a Low Profile Antenna by Applying Non-Uniformity to Its High Impedance Ground Plane," *IEEE Mathematical Methods in Electromagnetic Theory*, Kharkiv, Ukraine, June 2006.
- [13] D.M. Pozar, *Microwave Engineering*, 2nd ed., John Wiley & Sons, 1998.
- [14] J. L. Volakis, *Antenna Engineering Handbook*, 4th ed., McGraw Hill Professional, 2007.
- [15] Lida Akhoondzadeh-Asl, Douglas J. Kern, Peter S. Hall, and Douglas H. Werner, "Wideband Dipoles on Electromagnetic Bandgap Ground Planes," *IEEE Trans. Antennas Propagat.*, vol. 55, no. 9, Sep. 2007.
- [16] Leila Yousefi, Baharak Mohajer-Iravani, and Omar M. Ramahi, "Enhanced Bandwidth Artificial Magnetic Ground Plane for Low-Profile Antennas," *IEEE Antennas and Wireless Propagation letters*, vol. 6, pp. 289-292, July 2007.

- [17] Halim Boutayeb, and Tayeb A. Denidni, "Gain Enhancement of a Microstrip Patch Antenna Using a Cylindrical Electromagnetic Crystal Substrate," *IEEE Trans. Antennas Propag.*, vol. 55, no. 11, Nov. 2007.
- [18] Tayeb A. Denidni, Yacouba Coulibaly, and Halim Boutayeb, "Hybrid Dielectric Resonator Antenna With Circular Mushroom-Like Structure for Gain Improvement," *IEEE Trans Antennas Propag.*, vol.57, no.4, April 2009.
- [19] Mu'ath J. Al-Hasan and Tayeb A. Denidni, Abdel-Razik Sebak, "A New UC-EBG Based-Dielectric Resonator Antenna for Millimeter-Wave Applications," *IEEE Int. Symp. on Antennas and Propaga.* (APS/URSI), Spokane, WA, July 2011.
- [20] Mosallaei, H. and K. Sarabandi, "Antenna miniaturization and bandwidth enhancement using a reactive impedance substrate," *IEEE Trans. Antennas Propag.*, vol. 52, no. 9, pp. 2403–2414, Sep. 2004.
- [21] Yang, F. and Y. Rahmat-Samii, "Reflection phase characterizations of the EBG ground plane for low profile wire antenna applications," *IEEE Trans. Antennas Propag.*, vol. 51, no. 10, pp. 2691-2703, 2003.
- [22] J.W. Wu, C.F. Jou, and C.J. Wang, "A compact wideband leaky-wave antenna with etched slot elements and tapered structure", *IEEE Trans. Antennas and Propag.*, vol. 58, no. 7, pp. 2176-2183, July 2010.
- [23] M. Hosseini, A. Pirhadi, and M. Hakkak, "Design of a Non-uniform High- Impedance Surface for a Low Profile Antenna," *J. of Electromagnetic Waves and Applications*, vol. 20, no. 11, pp. 1454-1464, 2006.
- [24] X. Mu, W. Jiang, S.-X. Gong, and F.-W. Wang, "Dual-band low profile directional antenna with high impedance surface reflector," *Progress In Electromagnetics Research Letters*, vol. 25, pp. 67-75, 2011.
- [25] D. Qu, L. Shafai and A. Foroozesh, "Improving microstrip patch antenna performance using EBG substrates," *IEE Proc.-Microw. Antennas Propag.*, vol. 153, no. 6, Dec. 2006.
- [26] Jing Liang and Hung-Yu David Yang, "Radiation Characteristics of a Microstrip Patch Over an Electromagnetic Bandgap Surface," *IEEE Trans. Antennas Propag.*, vol. 55, no. 6, pp. 169 -1697, June 2007.
- [27] M.C. Huynhand, and W. Stutzman, "Ground plane effects on planar inverted-F antenna (PIFA) performance," *IEE Proc. Microw. Antennas Propag.*, vol. 150, no. 4, August 2003.
- [28] Awadalla, K.H., and Maclean, T.S.M., "Input impedance of a monopole antenna at the center of a finite ground plane," *IEEE Trans. Antennas Propag.*, vol. 26, no. 2, pp. 244–248, 1978.
- [29] S. Bashir, M. Hosseini, R. M. Edwards, M. I. Khatkhat, and L. Ma "Bicep Mounted Low Profile Wearable Antenna Based on A Non-Uniform EBG Ground Plane – Flexible EBG Inverted-L (FEBGIL) Antenna," *Loughborough Antennas and Propagation Conference*, Loughborough, UK, March 2008.
- [30] Gomez-Villanueva, Ricardo; Jardon-Aguilar, Hildeberto; y Miranda, Roberto Linares, "State of the art methods for low SAR antenna implementation," *Proceedings of the Fourth European Conference on Antennas and Propagation (EuCAP)*, Barcelona, Spain, April 2010.
- [31] Sang il Kwak; Dong-Uk Sim; Jong Hwa Kwon; Je Hoon Yun, "Design of multilayer PIFA based on an EBG structure for SAR reduction in mobile applications," *Asia Pacific Microwave Conference (APMC)*, 2009.
- [32] S. Zhu and R. Langley, "Dual-band wearable antennas over EBG substrate," *Electronics Letters*, vol. 43 no. 3, Feb. 2007.

- [33] Ryo Ikeuchi and Akimasa Hirata, "Dipole Antenna Above EBG Substrate for Local SAR Reduction," *IEEE Antennas and Wireless Propagation letters*, vol. 10, pp. 904-906, 2011.
- [34] S. Kwak, D. Sim, J. Kwon and H. Choi, "Experimental tests of SAR reduction on mobile phone using EBG structures", *Electronics Letters*, vol. 44, no. 9, pp. 568-569, April 2008.
- [35] S. Kwak, D. Sim, J. Kwon, and H. Choi, "Comparison of the SAR in the Humand Head using EBG structures applied to a Mobile Handset", *Proc. 37th European Microwave Conference*, pp. 937-940, Munich, Germany, Oct. 2007.
- [36] M. Hosseini, M. Hakkak, "Characteristics Estimation for Jerusalem Cross Based Artificial Magnetic Conductors," *IEEE Antenn. Wireless Propag. Lett.*, vol.7, pp. 58-61, 2008.
- [37] F. Yang and Y. Rahmat-Samii, "Polarization dependent electromagnetic band gap (PDEBG) structures: designs and applications," *Microwave Optical Tech. Lett.*, vol. 41, no. 6, pp. 439-444, 2004.
- [38] G. Goussetis, Y. Guo, A. P. Feresidis, and J. C. Vardaxoglou, "Miniaturized and multiband artificial magnetic conductors and electromagnetic band gap surfaces," *IEEE Antennas Propagat. Society Int. Symp.*, June 2004.
- [39] D. J. Kern, D. H. Werner, A. Monorchio, L. Lanuzza, and M. J. Wilhelm, "The design synthesis of multiband artificial magnetic conductors using high impedance frequency selective surfaces," *IEEE Trans. Antennas Propagat.*, vol. 53, no. 1, pp. 8-17, Jan 2005.
- [40] Yang, F.R., K.P. Ma, Y. Qian, and T. Itoh, "A novel TEM waveguide using uniplanar photonic-bandgap (UCPGB) structure," *IEEE Trans. Microwave Theory Tech.*, vol. 47, no. 11, 2092-2098, Nov. 1999.
- [41] Y. Lee, X. Lu, Y. Hao, S. Yang, C.G. Parini and J.R.G. Evans, "Cylindrical EBG antenna for short range gigabit wireless communications at millimetre-wave bands," *Electronics Letters*, vol. 45, no. 3, Jan 2009.
- [42] C.R. Simovski, P. de Maagt, and I.V. Melchakova, "High-impedance surfaces having stable resonance with respect to polarization and incidence angle," *IEEE Trans Antennas Propag* vol. 53, no. 3, pp. 908-914, 2005.
- [43] L. Deias 1, G. Mazzarella 2, N. Sirena, "Bandwidth Optimization of EBG Surfaces Using Genetic Programming," *Loughborough Antennas & Propagation Conference*, Loughborough, UK, Nov. 2009.
- [44] Stark, A.; Prorok, S.; Jacob, A.F.; "Broadband EBG Structures with Compact Unit Cell," 38<sup>th</sup> *European Microwave Conference* (EuMC), 2008.
- [45] M. Rahman and M. A. Stuchly, "Transmission line-periodic circuit representation of planar microwave photonic bandgap structures," *Microwave and Optical Tech. Lett.*, vol. 30, no. 1, pp. 15-19, 2001.
- [46] G. Goussetis, Y. Guo, A. P. Feresidis, and J. C. Vardaxoglou, "Miniaturized and multiband artificial magnetic conductors and electromagnetic band gap surfaces," *IEEE Antennas Propagat. Society Int. Symp.*, June 2004.
- [47] M. Hiranandani, A. B. Yakovlev, and A. A. Kishk, "Artificial magnetic conductors realized by frequency selective surfaces on a grounded dielectric slab for antenna applications," *IEE Proc.-Microwave Antennas Propagat. (Part H)*, vol. 153, no. 5, pp. 487-493, Oct. 2006.
- [48] G. Gampala, Analysis and design of artificial magnetic conductors for X-band antenna applications, *Master's thesis*, University of Mississippi, 2007.

- [49] Li Yang, Mingyan Fan, Fanglu Chen, Jingzhao She, and Zhenghe Feng, "A Novel Compact Electromagnetic-Bandgap (EBG) Structure and Its Applications for Microwave Circuits," *IEEE Trans. Microwave Theory Tech.*, vol. 53, no. 1, Jan. 2005.
- [50] Michael Diblanc, Emmanuel Rodes, Eric Arnaud, Marc Thevenot, Thierry Monediere, and Bernard Jecko, "Circularly Polarized Metallic EBG Antenna," *IEEE Microwave Wireless Compon. Lett.*, vol.15, no.10, 2005.
- [51] A.R. Eskandari, M. N. Moghaddasi, and M.A. Honarvar, "Design of A Novel Circularly Polarized Microstrip Patch Antenna Using EBG Structure," *Mediterranean Microwave Symp. (MMS)*, Tangiers, Morocco, Nov. 2009
- [52] M. Hosseioni and S. Bashir, "A Novel Circularly Polarized Antenna Based On An Artificial Ground Plane," *Progress In Electromagnetics Research Letters*, vol. 5, pp. 13-22, 2008.
- [53] Fan Yang and Yahya Rahmat-Samii, "A Low Profile Circularly Polarized Curl Antenna over Electromagnetic Band-Gap (EBG) Surface", *Microwave Optical and Technology Letters*, vol. 31, no. 4, pp. 264-267, Nov. 2001.
- [54] Yang, F. and Y. Rahmat-Samii, "A low profile single dipole antenna radiating circularly polarized waves," *IEEE Trans. Antennas Propagat.*, vol. 53, no. 9, pp. 3083–3086, 2005.
- [55] Martin Coulombe, Sadegh Farzaneh Koodiani, and Christophe Caloz, "Compact Elongated Mushroom (EM)-EBG Structure for Enhancement of Patch Antenna Array Performances," *IEEE Trans. Antennas and Propaga.*, vol. 58, no. 4, April 2010.
- [56] Hansen, R.C., *Electrically Small Superdirective and Superconducting Antennas*, Wiley-Interscience, Hoboken, NJ, 2006.
- [57] Qiu-Rong Zheng, Yun-Qi Fu, and Nai-Chang Yuan, "A Novel Compact Spiral Electromagnetic Band-Gap (EBG) Structure," *IEEE Trans. Antennas Propagat.*, vol. 56, no. 6, June 2008.
- [58] Soham Ghosh, Thanh-Ngon Tran, and Tho Le-Ngo, "A Dual-layer EBG-based Miniaturized Patch Multi-antenna Structure," *IEEE Int. Symp. Antennas and Propaga. (APS/URSI)*, 2011.
- [59] Nanbo Jin, Ang Yu, Xuexia Zhang, "An enhanced  $2 \times 2$  antenna array based on a dumbbell EBG structure," *Microwave Optical Tech. Lett.*, vol. 39, Oct. 2003.
- [60] Akimasa Hirata, "Accuracy Compensation in Direction Finding Using Patch Antenna Array With EBG Structure," *IEEE Antennas and Wireless Propagation letters*, vol. 5, 2006.
- [61] Effect of mutual coupling on the performance of adaptive arrays," *IEEE Trans. Antennas Propagat.*, vol. 31, no. 5, pp. 785-791, Sep 1983.
- [62] Kazemi, H.; Higgins, J.A.; Herting, B.; Hao Xin; West, J.; Hacker, J., "Electromagnetic bandgap waveguide (EBG) phase shifters for low cost electronically scanned antennas (ESA)," *IEEE Antennas and Propaga. Society Int. Symp.*, Honolulu, HI, June 2007.
- [63] Chauraya, A.; Panagamuwa, C.; Vardaxoglou, J., "Beam scanning antenna with photonicly tuned EBG phase shifters," *IEEE Antennas and Propaga. Society Inter. Symp.*, Albuquerque, NM, July 2006.
- [64] Antti E. I. Lamminen, Antti R. Vimpari, and Jussi Säily, "UC-EBG on LTCC for 60-GHz Frequency Band Antenna Applications," *IEEE Trans. Antennas Propagat.*, vol. 57, no. 10, Oct. 2009

- [65] Y. Lee, X. Lu, Y. Hao, S. Yang, C.G. Parini and J.R.G. Evans, "Cylindrical EBG antenna for short range gigabit wireless communications at millimetre-wave bands," *Electronics Letters*, vol. 45, no. 3, Jan 2009.
- [66] Li Zhang, Jun Yao, Dajia Wang, Hongsheng Zhong, "Distributed MEMS transmission line-based uniplanar compact electromagnetic bandgap (UC-EBG) tunable filters," *IEEE Int. Conf. on Nano/Micro Engineered and Molecular Systems*, Shenzhen, China, Jan 2009.
- [67] R. Van Dijk, A. Neto, J.A.G. Akkermans, J. Mills, "EBG-Based 60 GHz On-Chip Antenna in Passive Silicon," *Proceedings of the 38th European Microwave Conference*, Amsterdam Oct. 2008.
- [68] Yong Liu; Shiyong Li; Siheng Zhu; Xin Lv, "New two-dimensional PBG structures for THz transmission line and antenna integrated design based on MEMS technology," *Int. Conf. on Microwave and Millimeter Wave Tech.*, China, 2010.
- [69] Best, S.; Hanna, D., "Design of a broadband dipole in close proximity to an EBG ground plane," *IEEE Antennas and Propagation Magazine*, vol. 50, no. 6, pp. 52-64, 2008.
- [70] M. Sanad and N. Hassan, "An Internal EBG Antenna for Indoor Reception of UHF Terrestrial Digital TV Broadcasting," 10th *Mediterranean Microwave Symposium (MMS)*, Northern Cyprus, August 2010.
- [71] Chreim, H.; Hajj, M.; Monediere, T.; Jecko, B., "Cylindrical array of EBG sectoral antennas for Radar applications," *IEEE International Workshop on Antenna Technology (iWAT)*, Lisbon, March 2010.
- [72] Ming-Hung Hsu, Tzu-Chun Tang, Ken-Huang Lin, "EBG reflector-backed MIMO antenna with wideband isolation and uni-directional radiation pattern MIMO antenna for MIMO radar," *IEEE Antennas and Propagation Society International Symposium (APS/URSI)*, Orlando, FL, July 2013
- [73] Iskander, M.F.; Kim, W.; Bell, J.; Celik, N.; Zhengqing Yun; Hyounghsun Youn, "Antenna arrays technologies for advanced wireless systems," *IEEE Intern. Conf. on Microwaves, Commun., Antennas, and Electronics Systems*, Tel Aviv, Nov. 2009.
- [74] You-Quan Li; Hui Zhang; Yun-Qi Fu; Nai-Chang Yuan, "RCS Reduction of Ridged Waveguide Slot Antenna Array Using EBG Radar Absorbing Material," *IEEE Antennas and Wireless Propagation Letters*, Vol. 7, pp. 473-476, 2008.
- [75] Ghiyasvand, M.; Dalili Oskouei, H.R.; Forooraghi, K., "Broadband proximity coupled microstrip antenna for direct broadcast satellite reception using PBG structures," *Asia-Pacific Conference Microwave Conference (APMC)*, Suzhou, China, Dec. 2005
- [76] Klymyshyn, D. M., Haluzan, D. T., Börner, M., Achenbach, S., Mohr, J., Mappes, T., "High Aspect Ratio Vertical Cantilever RF-MEMS Variable Capacitor," *IEEE Microwave Wireless Compo Lett*, no.17, pp.127-129, 2007.
- [77] D.M. Klymyshyn, M. Boerner, D. Haluzan, E. Gono Santosa, M. Schaffer, S. Achenbach, J. Mohr, "Vertical High-Q RF-MEMS Devices for Reactive Lumped Element Circuits," *IEEE Trans. Microwave Theory Tech.*, vol. 58, no.11, pp. 2976-2986, Nov. 2010.
- [78] Willke, T.L.; Gearhart, S.S., "LIGA micromachined planar transmission lines and filters," *IEEE Trans. Microwave Theory Tech.*, vol. 45, no. 10, pp. 1681-1688, 1997.

- [79] Steven S. Gearhart and Theodore Willke, "Integrated Antennas and Filters Fabricated Using Micromachining Techniques," *IEEE Aerospace Conference*, CO, USA, March 1998.
- [80] Willke, T.L.; Gearhart, S.S., "Micromachined thick-metal TSAs for high-permittivity substrates," *IEEE Antennas and Propagation Society International Symposium*, Atlanta, GA, USA, June 1998.
- [81] Bo Pan, Yong-Kyu Yoon, Pete Kirby, John Papapolymerou, Manos Tentzeris, and Mark G. Allen, "A W-band Surface Micromachined Monopole for Low-cost Wireless Communication Systems," *Proc. IEEE Int. Microwave Symp.*, pp.1934-1938, June, 2004, Fort Worth, TX.
- [82] Y. Yoon, Bo Pan, J. Papapolymerou, M. M. Tentzeris, and M. G. Allen, "A vertical W-band surface-micromachined Yagi-Uda antenna," *Proc. IEEE Antennas and Propaga. Society Int. Sym.*, July 2005.
- [83] Zhao, Yanzhu; Yoon, Yong-Kyu; Choi, Seong-O; Wu, Xiaosong; Liu, Zhan; Allen, Mark G., "Three dimensional metal pattern transfer for replica molded microstructures," *Applied Physics Lett.*, vol.94, no.2, 2009.
- [84] Martin Coulombe, Sadegh Farzaneh Koodiani, and Christophe Caloz, "Compact Elongated Mushroom (EM)-EBG Structure for Enhancement of Patch Antenna Array Performances," *IEEE Trans. on Antennas and Propaga.*, vol. 58, no. 4, April 2010.
- [85] A. Rashidian, D. M. Klymyshyn, M. Tayfeh Aligodarz, M. Boerner, and J. Mohr, "Photoresist-based polymer resonator antennas: lithography fabrication, strip-fed excitation, and multimode operation," *IEEE Antennas and Propagation Magazine*, vol. 53, no. 4, pp. 16-27, Aug. 2011.
- [86] A. Rashidian, D. M. Klymyshyn, M. Boerner, J. Mohr, "Deep X-ray Lithography Processing for Batch Fabrication of Thick Polymer-based Antenna Structures," *Journal of Micromechanics and Microengineering*, vol. 20, pp. 025-026, 2010.
- [87] Aligodarz, M.T., Klymyshyn, D.M. and Rashidian, "Air-Gap Standing Parallel Strips Waveguide for X-ray Lithography Fabrication: Characteristics and Antenna Application," *Proc. 5th European Conference on Antennas and Propagation* (Eucap 2011), Rome, Italy, April, 1526-1529.
- [88] Ma, Z., Klymyshyn, D. M., Achenbach, S., Börner, M., Dambrowsky, N., Mohr, J., , "An Ultra-Deep High-Q Microwave Cavity Resonator Fabricated using Deep X-Ray Lithography," *IEICE Transactions on Electronics*, E90-C, pp. 2192-2197, 2007.
- [89] H. C. Jayatilaka, D. M. Klymyshyn, M. Börner, and J. Mohr, "Compact thick metal diplexer with multi-coupled folded half wavelength resonators," *Progress In Electromagnetics Research C*, vol. 18, pp. 1-8, 2011.
- [90] Reid, J. R., D. Hanna, and R. T. Webster, "A 40/50GHZ diplexer realized with three dimensional copper micromachining," *IEEE MTT-S Digest*, pp. 1271-1274, June 2008.
- [91] Todd, S.T.; Bowers, J.E.; MacDonald, N.C., "Micromachined high aspect ratio coplanar waveguide with high impedance and low loss on low resistivity silicon," *IEEE Inter. Microwave Symp. (MTT)*, 2010.
- [92] M. J. Madou, *Fundamentals of Microfabrication: The Science of Miniaturization*, CRC Press, 2002.
- [93] Z. Ma, D. Klymyshyn, S. Achenbach and J. Mohr, "Microwave Cavity Resonators Using Hard X-Ray Lithography," *Microwave and Optical Tech. Letters*, vol. 47, no. 4, pp. 353-357, 2005.

- [94] Bley, P., J. Gottert, M. Harmening, and W. Menz, "The LIGA Process for the Fabrication of Micromechanical and Microoptical Components," *Micro System Technologies*, Berlin, May 1991.
- [95] Steven S. Gearhart and Theodore Willke, "Integrated Antennas and Filters Fabricated Using Micromachining Techniques," *IEEE Aerospace Conference*, CO, USA, March 1998.
- [96] Y.M. Shin, J. K. So, K. H. Jang, J. H. Won, A. Srivastava, S.T. Han, J. H. Kim, S. S. Chang, R. K. Sharma and S. N. Joshi, G. S. Park, "Experimental Investigation of 95GHz Folded Waveguide Backward Wave Oscillator Fabricated by Two-Step LIGA", *7<sup>th</sup> IEEE Inter. Conf. Vacuum Electronics*, USA, April 2006.
- [97] J. C. Tucek, D. R. Whaley, D. A. Gallagher, V. O. Heinen, K. E. Kreischer, D. C. Mancini, R. Divan, J. Yaeger, D. Ryding, "LIGA Fabrication of Folded Waveguide Circuits," *4th IEEE Inter. Conf. Vacuum Electronics*, May 2003.
- [98] Park, K.Y.; Park, J.Y.; Choi, H.K.; Lee, J.C.; Lee, B.; Kim, J.H.; Kim, N.Y.; Kim, G.H.; Kim, D.W.; Bu, J.U.; Chung, K.W., "A novel Ka-band bandpass filter using LIGA micromachined process," *Asia Pacific Microwave Conference*, Sydney, NSW, 2000.
- [99] Y. M. Shin, G.S. Park, S.T. Han, J.I. Kim, "Design of W-band coupled-cavity TWT by LIGA fabrication," *3rd IEEE International Vacuum Electronics Conf. (IVEC)*, 2002.
- [100] Jill Hruby, "Overview of LIGA Microfabrication," *Proc. of American Institute of physics conf.*, 2002.
- [101] Holger F Hofmann, Terukazu Kosako, Yutaka Kadoya, "Design parameters for a nano-optical Yagi-Uda antenna," *New Journal of Physics*, vol. 9, pp.217-217, 2007.
- [102] C.A. Balanis, *Antenna Theory: Analysis and Design*, 3rd Ed., NJ: Wiley, 2005.
- [103] Warren L. Stutzman, "Antenna theory and design", John Wiley & son, 1981.
- [104] R. Garg , Prakash Bhartia , Inder Bahl, *Microstrip Antenna Design Handbook*, Artech House, 2001.
- [105] R.E. Collin, *Foundations for Microwave Engineering*, 2nd ed., McGraw Hill: New York, 1992.
- [106] E. Hammerstad and Ø. Jensen, "Accurate Models for Microstrip Computer-Aided Design," *IEEE MTT-S International Microwave Symposium Digest*, pp. 407-409, June 1980.
- [107] H. A. Wheeler, "Transmission-Line Properties of a Strip on a Dielectric Sheet on a Plane," *IEEE Trans. Microwave Theory Tech.*, vol. 25, no. 8, pp. 631-647, Aug. 1977.
- [108] Klymyshyn, D.M., Jayatilaka, H.C., Boerner, M. and Mohr, J., "High-Aspect-Ratio Coplanar Waveguide Wideband Bandpass Filter With Compact Unit Cells," *IEEE Trans. Microwave Theory Tech.*, vol. 57, No. 11, pp. 2753-2760, Nov 2009.
- [109] Ghannam, A. Viallon, C. ; Bourrier, D. ; Parra, T., "Dielectric microwave characterization of the SU-8 thick resin used in an above IC process," *European Microwave Conference*, Rome, Italy, Sep 2009.
- [110] G. Brist and S. Hall, S. Clouser, and T. Liang, "Non-Classical Conductor Losses due to Copper Foil Roughness and Treatment," *10th electronic circuits world convention*, Anaheim, California, USA, 2005
- [111] K. Sarabandi and R. Azadegan, "Design of an Efficient Miniaturized UHF Planar Antenna," *IEEE Trans. Antennas Propag.*, vol. 51, no. 6, June 2003.
- [112] R. Azadegan, "Highly Miniaturized Antennas and Filters for Wireless Applications," *Ph.D. Dissertation*, University of Michigan 2004.

- [113] Ponchak, G.E., "RF Transmission Lines on Silicon Substrates," *29th European Microwave Conference*, Munich, Germany, Oct. 1999.
- [114] Best, S.R. Altshuler, E.E. Yaghjian, A.D. McGinthy, J.M. O'Donnell, T.H., "An Impedance-Matched 2-Element Superdirective Array," *IEEE Antenn. Wireless Propag. Lett.*, vol. 7, pp. 302-305, 2008.
- [115] P. Ratajczak, J. -M. Baracco, and P. Brachat, "Adjustable high impedance surface for active reflectarray applications," *Proc. EUCAP*, pp. 1-6, 11-16 Nov. 2007.
- [116] Lin Peng and Cheng-Li Ruan, "UWB Band-Notched Monopole Antenna Design Using Electromagnetic-Bandgap Structures," *IEEE Trans. Microwave Theory Tech*, vol. 59, no. 4, April 2011.
- [117] Ban-Leong Ooi, Compact EBG In-Phase Hybrid-Ring Equal Power Divider, *IEEE Trans. Microwave Theory Tech*, vol. 53, no. 7, July 2005.
- [118] M. F. Abedin, M. Z. Azad, and M. Ali, "Wideband Smaller Unit-Cell Planar EBG Structures and Their Application," *IEEE Trans. Antennas Propagat.*, vol. 56, no. 3, March 2008.
- [119] Yang, F.R., K.P. Ma, Y. Qian, and T. Itoh, "A novel TEM waveguide using uniplanar photonic-bandgap (UCPGB) structure," *IEEE Trans. Microwave Theory Tech.*, vol. 47, no. 11, 2092–2098, Nov. 1999.
- [120] B.-Q. Lin, X.-Y. Ye, X.-Y. Cao, and F. Li, "Uniplanar EBG structure with improved compact and wideband characteristics," *Electronics Letters*, vol. 44, no. 23, pp. 1362 - 1363, Nov. 2008.
- [121] Raúl Guzmán-Quirós, José Luis Gómez-Tornero, Andrew R. Weily, and Y. Jay Guo, "Electronic Full-Space Scanning With 1-D Fabry–Pérot LWA Using Electromagnetic Band-Gap," *IEEE Antennas and Wireless propagation letters*, vol. 11, 2012.
- [122] Garcia-Vigueras, M., Gomez-Tornero, J.L. ; Goussetis, G. ; Weily, A.R. ; Guo, Y.J., "1D-Leaky Wave Antenna Employing Parallel-Plate Waveguide Loaded With PRS and HIS," *IEEE Trans. Antennas Propagat.*, vol. 59, no. 10, pp. 3687-3694, Oct. 2011
- [123] Foroozesh, A., Shafai, L., "Wave Propagation in 1D EBGs: Periodic Multilayer Films Consisting of Two Different Materials," *IEEE Antennas and Propagation Magazine*, vol. 50, no. 2, pp. 175-182, April 2008.



# Chapter 3

## Analysis and Verification Methods

### 3 Analysis Methods and Verification

The method mainly employed in this work to analyze the structures is a combination of numerical and mathematical analyses (referred to as HFSS/Bloch). The numerical analyses are conducted using Ansoft's HFSS, which offers a standard full-wave analysis based on finite element method. On the other hand, the theoretical analyses are based on the Bloch theory, which is proposed for periodic structures [1-2]. Fig. 3.1 shows the Bloch unit cell of a periodically loaded microstripline (MSL) and the related dispersion diagram.

In chapter 8 of [1], Pozar presents an example of such slow-wave TL for which the Bloch dispersion curve is provided. In that specific case, equations are simplified and interpreted so that the related curve mathematically indicates a zero value for  $\beta$  ( $\gamma=\alpha+j\beta$ ) in the *gray area* shown in Fig. 3.1 (c) which is named (in [1]) as the stopband. In comparison, the curve in Fig. 3.1 (c) is found here by the HFSS/Bloch method when both the real and imaginary parts of the complex propagation constant are accurately plotted ( $\alpha$  is not plotted in [1]). In areas other than the stopband, the behavior shown in [1] is very similar to Fig. 3.1 (c). A close look shows that  $\beta/k_0$  curve has two maxima on both side of the gray zone. As seen, inside the stopband,  $\beta/k_0$  is reduced severely and reaches a minimum in the middle. For comparison,  $\beta/k_0$  (the propagation

constant normalized by the free space wavenumber) of a normal MSL, with no stubs, is also included in Fig. 3.1 (c). This second curve demonstrates that the open stubs (over the frequency range where stubs are capacitive:  $jb>0$ ) cause the loaded TL to have a considerably higher  $\beta/k_0$  and behave like a new TL with slow-wave characteristics. It is noted that according to the theory behind HFSS/Bloch method,  $\beta/k_0$  equals the square root of the effective relative permittivity ( $\epsilon_{\text{reff}}^{1/2}$ ) that waves experience along the structure.

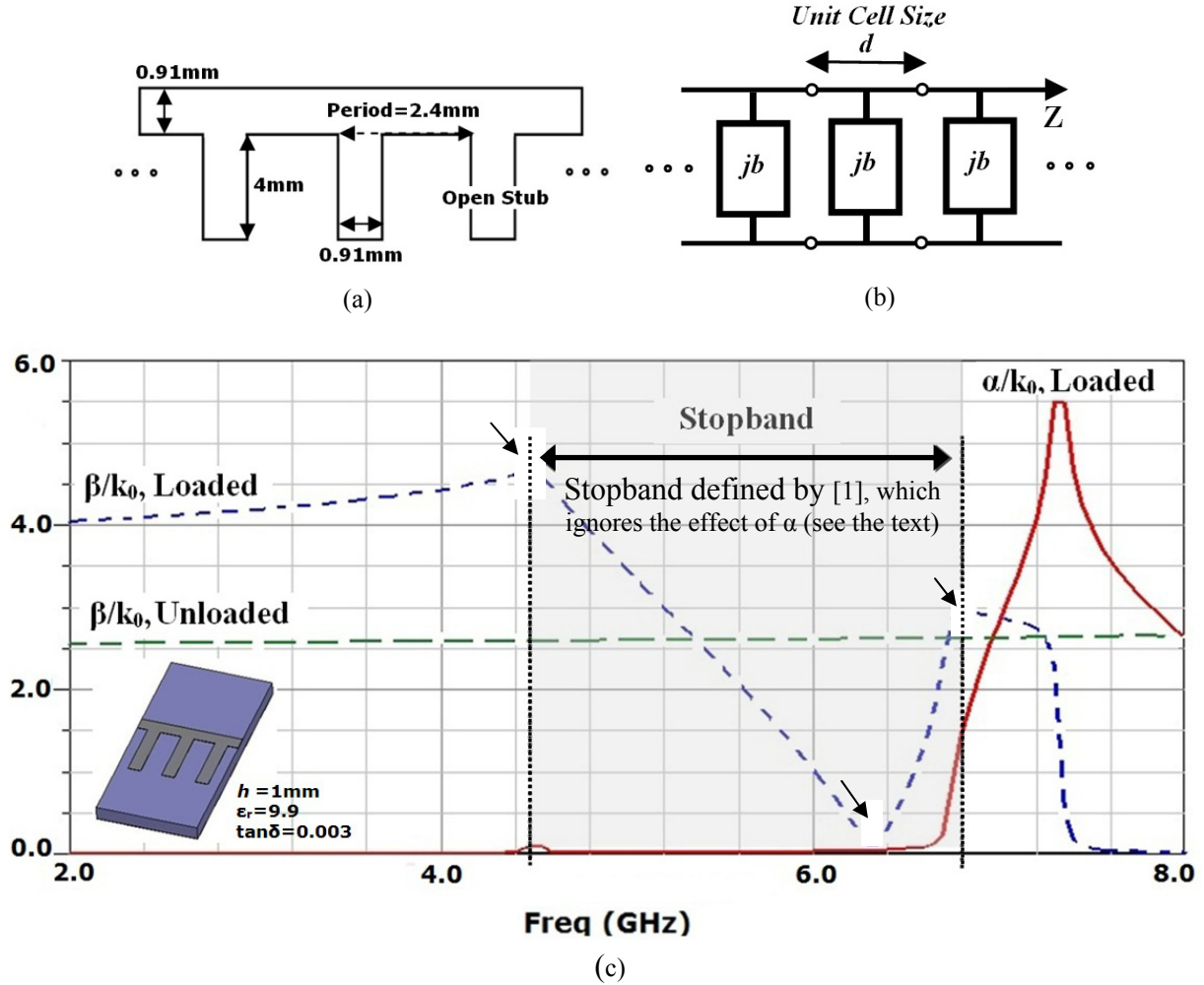


Fig. 3.1 HFSS/Bloch method is applied to a sample periodic structure and absolute values of  $\beta/k_0$  and  $\alpha/k_0$  are plotted, a) MSL periodically loaded with open stubs, b) the related cascade network, c) the dispersion diagram for Fig. 3.1 (a). For comparison,  $\beta/k_0$  of a normal MSL, with no stubs, is also included; traces are 0.91mm ( $Z_0 \sim 50\Omega$ ).

For the unloaded case in Fig. 3.1,  $\beta/k_0 \sim 2.6$  (a normal MSL with  $50\Omega$ ). Applying the classic closed-form equations [1] of a MSL to the given dimensions results in  $\epsilon_{\text{reff}}^{1/2} = \beta/k_0 \sim 2.56$ . This value is in a very good agreement with  $\sim 2.6$  from Fig. 3.1. The  $\epsilon_{\text{reff}}^{1/2}$  for the loaded case is severely frequency dependent as shown in Fig. 3.1. It is important to note that the plotted  $\beta/k_0$

curve is not accurate very close to the transitions (see the arrows in Fig. 3.1). Around those frequencies, the slopes sharply change, and at one specific point, the sign of slopes changes as well. In fact, one reason that the stopband zone is so called is that  $v_g$  is very low in this frequency zone. It is important to emphasize that the curves are normalized by  $k_0$  (free space wavenumber), which is a frequency dependent factor. Increasing the frequency resolution of analysis at and around the transitions could improve the curve. However, the current curve is plotted with lower resolution over a large frequency range to only show the general dispersive behavior of a MSL loaded with open stubs and demonstrate the ability of HFSS/Bloch method to calculate these curves. The open-stub loading case of Fig. 3.1 is a simple case and generalized cases are also considered in literature, for which the loading is more complicated [3-4]. For example, [4] presents equations for the general loading shown in Fig. 3.2 in which  $Z$  and  $Y$  could be any type of load.

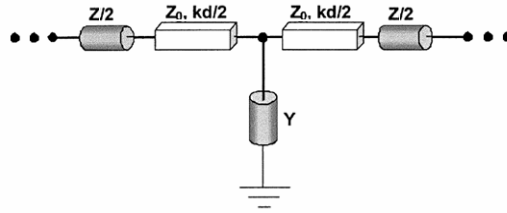


Fig. 3.2 General Bloch unit cell for a 1D periodically-loaded transmission-line made of an infinite number of such symmetrical cells [4]. © 2006 IEEE.

The dispersion relation for the cell in Fig. 3.2 is [4] (since  $AD-BC = 1$  and  $A=D$  due to symmetry)

$$\cosh \gamma d = \frac{A+D}{2} = A = \cos \theta + \frac{YZ}{2} \cos^2 \frac{\theta}{2} + \frac{j}{2} \left( \frac{Z}{Z_0} + \frac{Y}{Y_0} \right) \sin \theta \quad (3.1)$$

where  $A$ ,  $B$ ,  $C$ , and  $D$  are the cascade parameters of the unit cell. For example, if applying the particular case of Fig. 3.1 to (3.1),  $Z=0$  and  $Y=jb$  which simplifies (3.1) to [1]:

$$\cosh \gamma d = A = \cos \theta - \frac{bZ_0}{2} \sin \theta \quad (3.2)$$

As shown later *in this work*, instead of a shunt admittance like in (3.2), the unit cells proposed have a series impedance in the middle. Therefore, in (3.1),  $Y=0$ , which results in

$$\cosh \gamma d = A = \cos \theta + j \frac{Z}{2Z_0} \sin \theta \quad (3.3)$$

Later on in Sec. 4.4, (3.3) will be used to develop a circuit model for the proposed cells. In a similar manner,  $B$  as the second cascade parameters can also be expressed analytically as presented later. It is noted that most unit cells considered in literature, and also in this thesis, are symmetrical, and hence, only  $A$  and  $B$  are sufficient to provide a full description of the dispersive behavior. The other cascade parameter  $C$  is not necessary for Bloch analysis of symmetrical cells (also,  $D=A$  for a symmetrical unit cell).

Fig. 3.3 describes the different steps of the HFSS/Bloch analysis method. As seen, the process starts with modeling the cell in HFSS (Sec. 4.1). Then the scattering parameters, and from them, the cascade parameters of the cell are extracted. Because Bloch equations are based on cascade parameters (Fig. 3.3), using them, a dispersion diagram ( $\gamma$  versus frequency) can be generated which is able to exhibit how the whole periodic structure functions. The method also provides the equivalent Bloch line impedance ( $Z_B$ ) of the periodic TL, which along with the dispersion diagram allows to treat the structure as a periodically loaded TL with known impedance and propagation constant. This TL can be used to create microwave components like antennas.

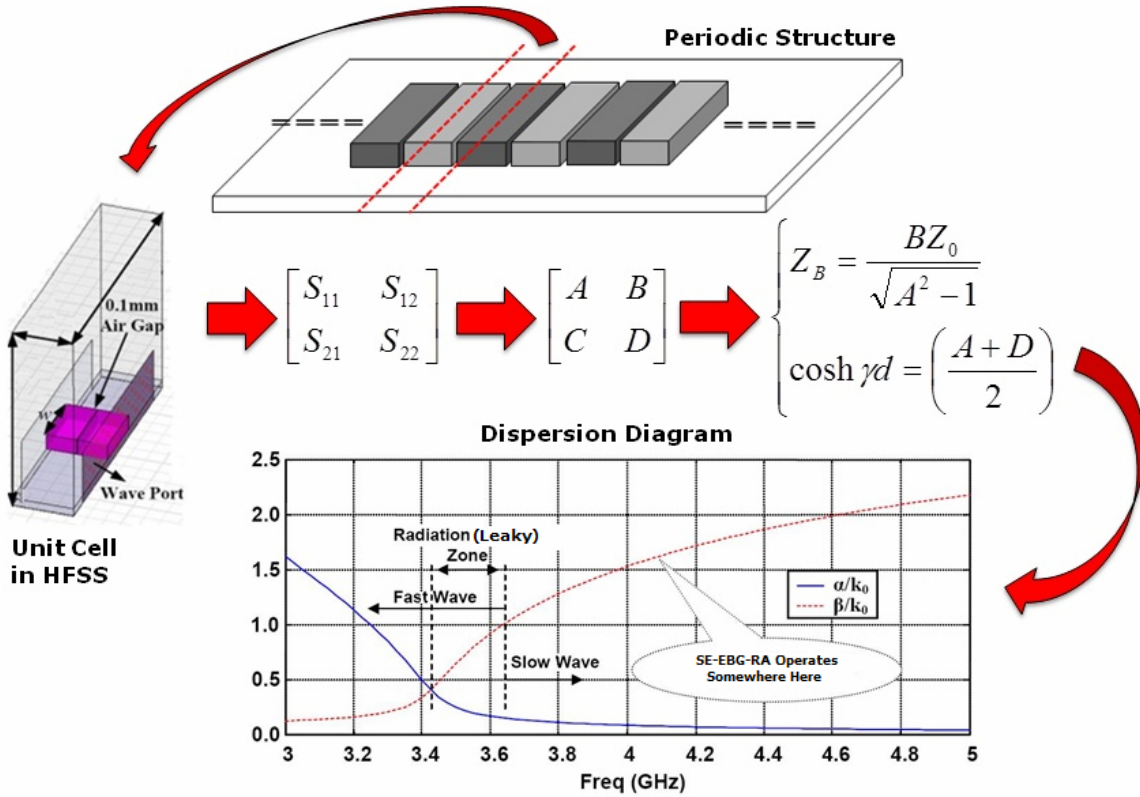


Fig. 3.3 The proposed HFSS/Bloch analysis method: step-by-step progression to generate the Bloch dispersion diagram for a structure composed of EBG cells.

It should be emphasized that in the antenna realm, curves such as Fig. 3.3 are conventionally used to understand leaky-wave (LW) antennas (see Sec. 5.1), in terms of their dispersive behavior and navigating the design process. However, it is observed in related works that little attention is usually paid to the capabilities that  $Z_B$  could also add to the design process and to the depth of the knowledge gained on the operation of such structures. One point of strength and novelty in this work is in the way the cells are modeled (using two waveports<sup>33</sup> rather than periodic boundary conditions (PBC), as described in Sec. 4.1). This provides the opportunity to extract  $Z_B$  along with  $\gamma$  and gain a more profound insight of the antenna structures as a lossy TL. The body of all proposed antennas is in fact a fragment of the cell-texture TL in Fig. 3.3, which could be described and controlled when having the associated  $Z_B$  and  $\gamma$ . This opportunity has resulted in the circuit model of Sec. 4.4 in which the antenna input impedance is derived relatively accurately (up to 4% difference for a range of different cells). In addition to this method, in Sec. 4.1.7, the unit cells are modeled using PBC, very similar to the way conventional EBG cells are analyzed, and the related reflection phase diagram is compared with the HFSS/Bloch diagram in Fig. 3.3.

Fig. 3.4 shows the two main classes of antennas that will be proposed in this work based on the HFSS/Bloch dispersion diagram. These antennas are classified according to the principle of their operation. Antennas, which are being matched and operating in the leaky zone (i.e. radiation zone in Fig. 3.3), are classified as leaky-wave antennas with frequency-scanning patterns (Sec. 5.1). On the other hand, antennas matched above the leaky zone (in slow-wave zone) are classified as resonant antennas with fixed broadside patterns mostly radiating like regular patch antennas (e.g. Sec. 4.1). More details will be presented in the related sections.

---

<sup>33</sup> It will be demonstrated that (see Fig. 4.1.10) for the proposed unit cells, mutual coupling is not an issue and the use of waveports rather than periodic boundary conditions is justified, and results in accurate estimations.

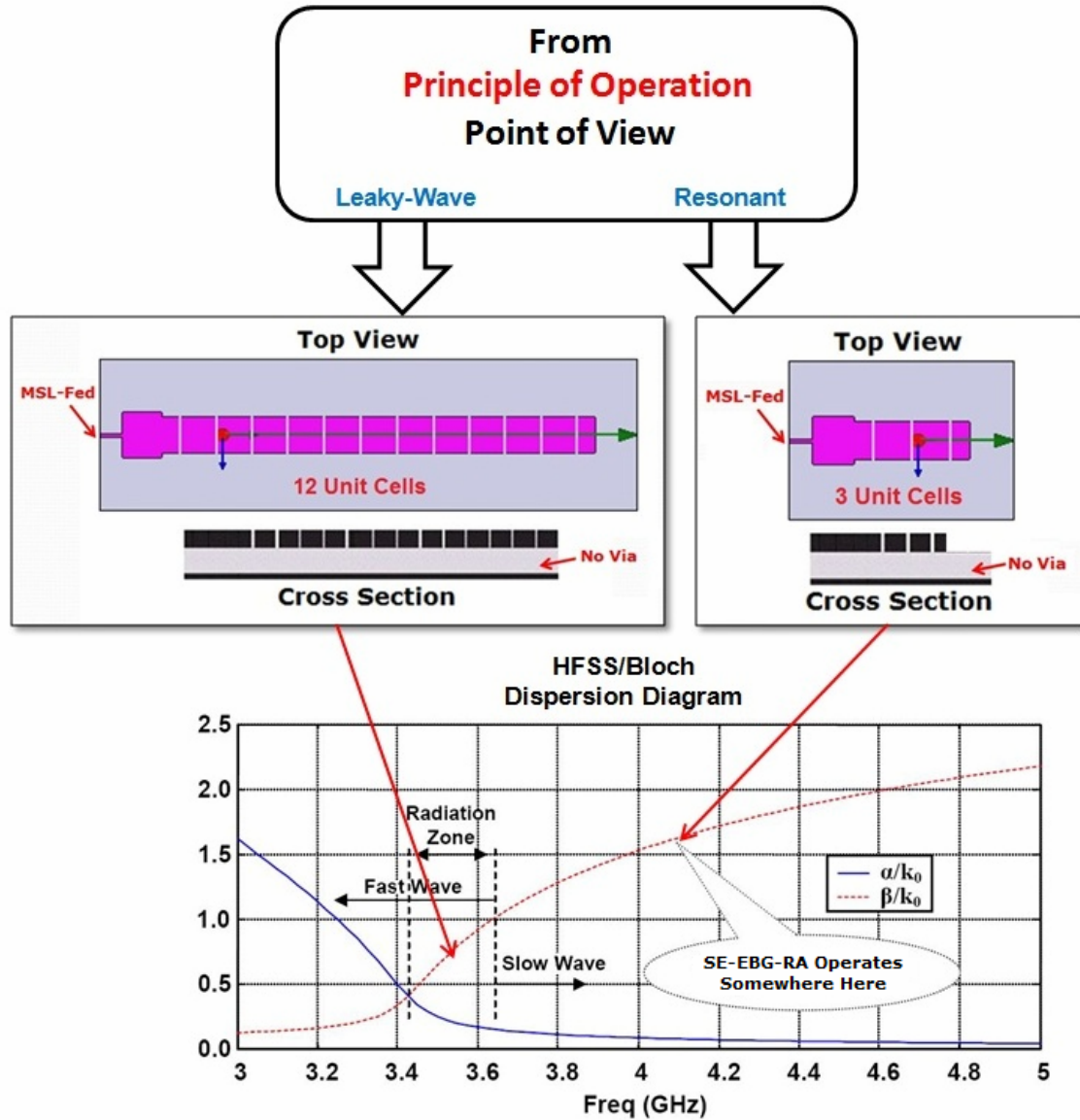


Fig. 3.4 Two fundamentally different antennas in this thesis developed using the HFSS/Bloch dispersion diagram.

Apart from the Bloch analysis, there are some analysis approaches in literature, which are usually applied to evaluate properties of periodic structures, including EBG surfaces. One of the most popular methods, usually preferred when tackling the EBG concept for antenna structures, is the reflection phase characterization method [5-8]. This method is based on illuminating the unit cell by plane waves and evaluating the phase of the reflection coefficient [8]. The curve created by this method is called reflection phase diagram (RPD) [9]. The frequency at which the phase is zero is the cell resonance frequency. At this resonance, the cell exactly behaves like a

perfect magnetic conductor (PMC). Usually, where the reflection phase is within  $\pm 90^\circ$ <sup>34</sup> [e.g. see 18] is considered the artificial magnetic conductor (AMC) zone. Fig. 3.5 shows an example of a RPD for the mushroom-like RBG cell [8]. This method will be used at the end of Sec. 4.1.

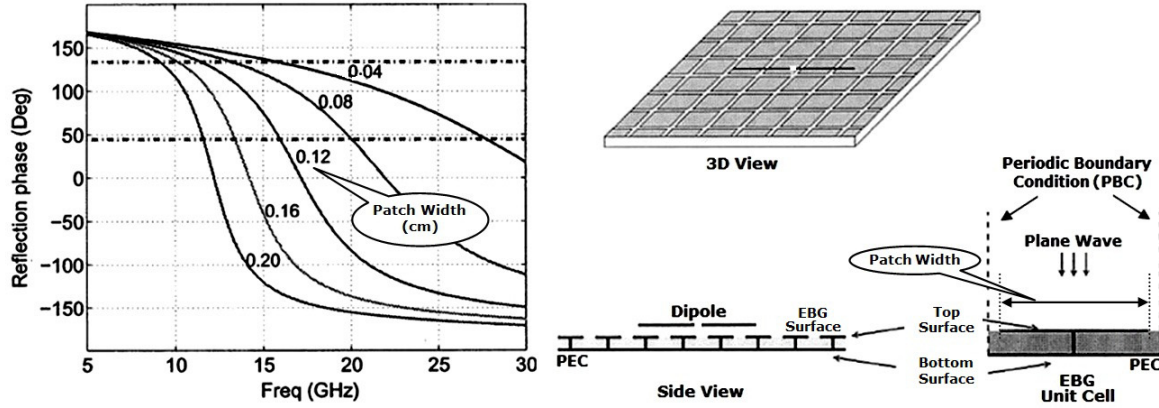


Fig. 3.5 An example of using RPD to analyze EBG grounded antennas [8] © 2003 IEEE; where the phase is zero (at cell resonance), the surface is imitating a PMC boundary; notice the resonance drops when  $W$  increases.

Another method which is naturally similar to the Bloch approach is using the dispersion curves known as Brillouin diagram [10-11]. Fig. 3.6 shows an example of such a diagram, which provides information about the propagation constant ( $\beta$ , the imaginary part of the complex propagation constant) as an indicator of the way waves propagate along the surface.

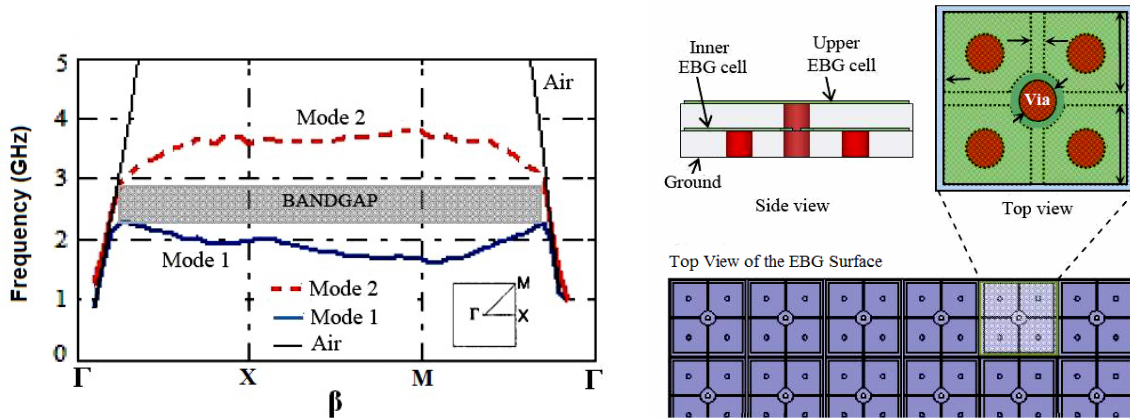


Fig. 3.6 An example of using Brillouin's dispersion diagram to evaluate surface wave suppression properties and bandgaps of EBG surfaces [10] © 2006 IEEE.

<sup>34</sup> Some other works consider the range  $\pm 45^\circ$  instead.

Using this diagram,  $\beta$  can be examined not only in lateral directions ( $\beta_x$  and  $\beta_y$ ) but also in the diagonal direction ( $\beta_{xy}$ ). The left section of the X-axis in Fig. 3.6 shows  $\beta$  when waves travel from the point  $\Gamma$  to the point X (see the small square cell inside the figure). At the center of the X-axis, the curve shows  $\beta$  when waves travel from the point X to the point M. Finally, on the right section of the X-axis,  $\beta$  is given when waves travel diagonally, from M to  $\Gamma$ . Therefore, the diagram can give a more profound view of propagation or suppression of surface waves in different frequencies and directions. For example, in Fig. 3.6, there is a frequency band somewhere between 2GHz and 3GHz for which  $\beta$  does not exist, thus this band is called a bandgap where no wave propagation is allowed. Because the power traveling along a planar structure is mainly guided in the form of surface currents and waves, this bandgap is ideal to suppress such surface waves where they are not desirable, e.g. in case of a planar antenna on a ground plane. Although this diagram is more popular in microwave community (originally used for photonic bandgap structures [12]), sometimes in antenna engineering it appears along with RPD to provide more profound views of the way the artificial surfaces operate [e.g. 5].

The next popular approach to find bandgaps of EBG surfaces is based on using the EBG surface as the ground plane of a 2-port MSL [13-16], as in Fig. 3.7. This stems from the fact that in very low or high frequencies, an EBG surface behaves like a PEC, and hence, the metal trace located on this PEC surface will be a normal MSL and is partially matched. Hence, in this case, the insertion loss,  $IL = -20\log|S_{21}|$ , is not too high. In contrast, over the bandgaps, the surface switches from PEC to PMC (better to say AMC), and the MSL impedance changes. In fact, a MSL on a PMC cannot guide power and tends to suppress surface current because tangential magnetic fields are not welcome on a PMC surface. This change deteriorates the matching condition severely ( $IL$  grows), and therefore, bandgap/stopband frequencies could be discriminated from others. It is noted that a similar approach will be used in the beginning of Sec. 4.1. Reviewing the literature shows that in some rare cases [2, 5], all three methods, including RPD, Brillouin's diagram, and  $IL$  are utilized and compared for further clarification.



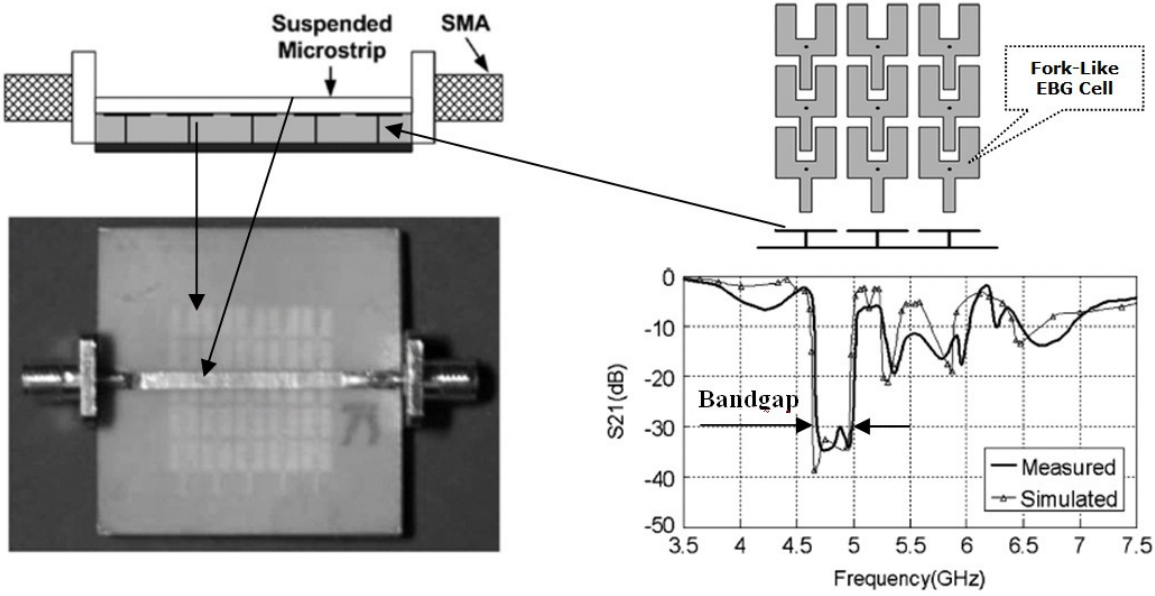


Fig. 3.7 An example of applying the insertion loss ( $\text{dB}|S_{21}|$ ) evaluation method [13] for deriving bandgaps of EBG surfaces. © 2006 IEEE.

The last method proposed to find the resonance of an EBG cell through simulation suggests modeling the cell similar to the RPD method, but it uses a different way to excite waves [17]. As seen in Fig. 3.8, instead of impinging the cell in the model by plane waves (see Fig. 3.5), the cell is excited by a waveport placed far from the surface of the cell. To model the periodicity, similar to the RPD method, walls parallel to waveport E-fields are assigned to be PMC and those perpendicular, will be considered PEC. This periodicity brings about a condition under which the cell is illuminated by normally incident<sup>35</sup> plane waves [17]. In this method, the effect of the distance between the waveport and the cell surface is also taken into account (is de-embedded) as it introduces a phase shift in addition to what the cell creates itself. In Sec. 4.1, this method will be applied to proposed HAR EBG cells and is compared to the HFSS/Bloch diagram to generate a deep insight about the exceptional performances of the antennas based on such cells.

<sup>35</sup> Oblique incidence case could also be studied, using other types of boundary conditions like Master/Slave. However, the modeling is more complicated and time consuming and requires a meticulous adjustment of analysis parameters.

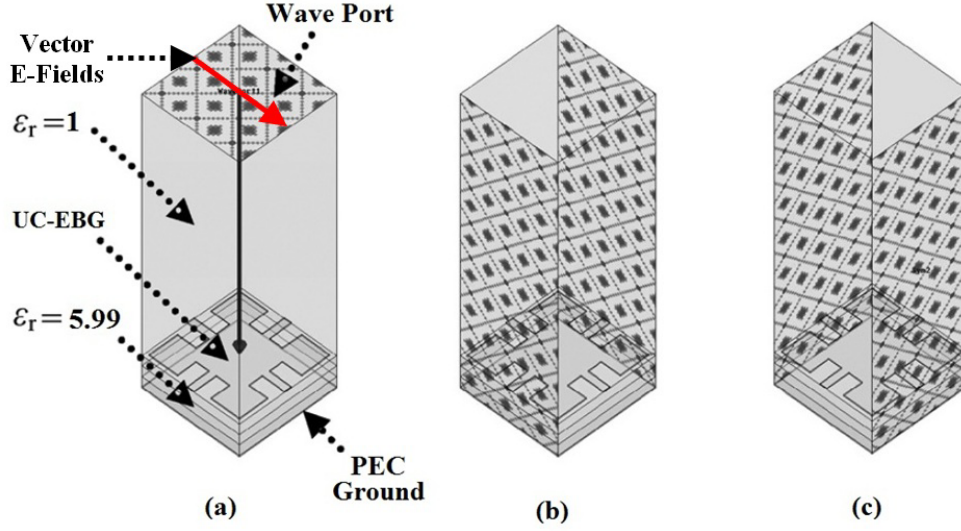


Fig. 3.8 a) Unit cell modeling in HFSS using waveport as proposed in [17] © 2009 IEEE, b) PEC symmetry planes, c) PMC symmetry planes.

### 3.1 Comparing Alternative Methods

In order to lend credibility to the analyses carried out and validate the designs based on those analyses, the results of at least two alternative methods are compared. In brief, three independent analysis methods are used throughout the thesis, which agree favorably. These methods include:

- HFSS/Bloch method proposed for the first time for such structures (described in Sec. 4.1 and used in later chapters)
- HFSS simulation as a full-wave analysis method (throughout the thesis)
- Prototyping and experimentation (used for some of the designs; Sec. 4.2, 4.4, 5.3, and Appendix C)

A circuit model is also proposed in Sec. 4.4, which is in fact a developed version of HFSS/Bloch method, thus not considered a fundamentally independent method. This model is the HFSS/Bloch method when its dependency on HFSS is deliberately removed (100% closed-form equations) using TL circuit theory.

### 3.2 Fabrication and Experimental Verification

As a traditional way of verification, a few prototypes are also fabricated and tested experimentally. For instance, one of the prototypes presented in Sec. 4.2 is first fabricated using CNC milling and then undergoes four different kinds of measurement to provide a complete verification on the performance. Fig. 3.9 describes such measurements in a whole view, which include input reflection measurement, efficiency measurement using the Wheeler cap method, radiation pattern measurement, and radiation gain measurement using the three-antenna-method. To measure the antenna radiation gain and pattern, it has been necessary to develop a test setup including a semi-anechoic condition (absorbers) and two extra antennas required for the process. Fig. 3.9 depicts a view of the antenna under test along with the two extra fabricated antennas. Details of the measurement processes are reflected in Sec. 4.2.

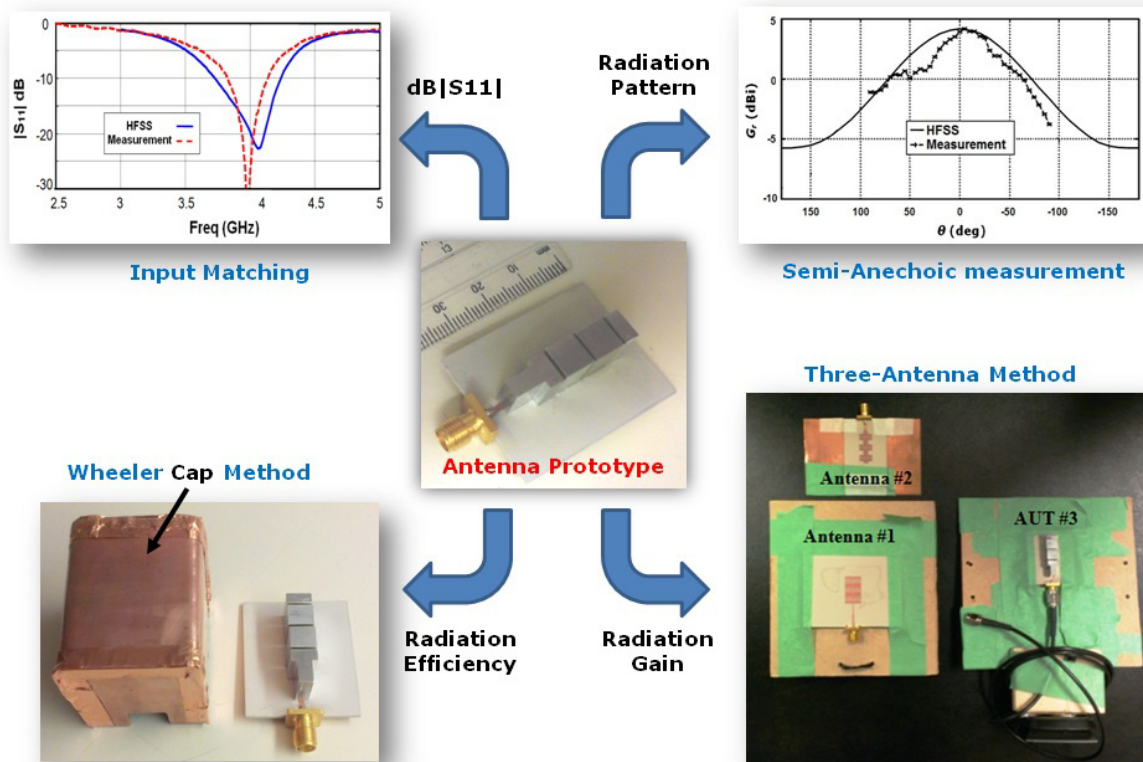


Fig. 3.9 a) The prototype to appear in Sec. 4.2, which undergoes a complete set of antenna measurements, as depicted.

Other prototypes fabricated during the research are briefly summarized here:

- A planar antenna with thin traces (4 $\mu$ m) made with UV-lithography using a Cr mask (Sec. 4.4).
- Some planar antennas with thin traces (30 $\mu$ m) made with UV-lithography, using a regular laser-printed mask (Sec. 4.4, Sec. 5.3, and two supplementary antennas in Fig. 3.9).
- Development of several process steps required for the fabrication of HAR antennas using X-ray lithography (Appendix C), including:
  - The design and fabrication of an in-house X-ray mask for such structures at SyLMAND laboratory of the Canadian Light Source.
  - Experimenting with X-ray exposure steps for future structures of such antennas.

## References

- [1] D.M. Pozar, *Microwave Engineering*, 2nd ed., John Wiley & Sons, 1998.
- [2] M. Rahman and M. A. Stuchly, "Transmission line-periodic circuit representation of planar microwave photonic bandgap structures," *Microwave and Optical Tech. Lett.*, vol. 30, no. 1, pp. 15–19, 2001.
- [3] Shawn D. Rogers, "Electromagnetic-Bandgap Layers for Broad-Band Suppression of TEM Modes in Power Planes," *IEEE Trans. Microwave Theory Tech.*, vol. 53, no. 8, pp. 2495–2505, Aug. 2005.
- [4] G.V. Eleftheriades, A.K. Iyer, and P.C. Kremer, "Planar Negative Refractive Index Media Using Periodically L-C Loaded Transmission Lines," *IEEE Trans. Microwave Theory Tech.*, vol. 50, no. 12, pp. 2709–2712, Dec. 2002.
- [5] D. Sievenpiper, L. Zhang, R.F. Jimenez Broas, N.G. Alexopolous, and E. Yablonovitch, "High-impedance electromagnetic surfaces with a forbidden frequency band," *IEEE Trans. Microwave Theory Tech.*, vol. 47, no. 11, pp. 2059–2074, Nov. 1999.
- [6] Lida Akhoondzadeh-Asl, Douglas J. Kern, Peter S. Hall, and Douglas H. Werner, "Wideband Dipoles on Electromagnetic Bandgap Ground Planes," *IEEE Trans. Antennas Propag.*, vol. 55, no. 9, Sep. 2007.
- [7] Mosallaei, H. and K. Sarabandi, "Antenna miniaturization and bandwidth enhancement using a reactive impedance substrate," *IEEE Trans. Antennas Propag.*, vol. 52, no. 9, pp. 2403–2414, Sep. 2004.
- [8] Yang, F. and Y. Rahmat-Samii, "Reflection phase characterizations of the EBG ground plane for low profile wire antenna applications," *IEEE Trans. Antennas Propag.*, vol. 51, no. 10, 2691–2703, 2003.
- [9] C.R. Simovski, P. de Maagt, and I.V. Melchakova, High-impedance surfaces having stable resonance with respect to polarization and incidence angle, *IEEE Trans. Antennas Propag.* vol. 53, no. 3, pp. 908–914, March 2005.
- [10] Soham Ghosh, Thanh-Ngon Tran, and Tho Le-Ngo, "A Dual-layer EBG-based Miniaturized Patch Multi-antenna Structure," *IEEE Int. Symp. Antennas and Propag.* (APS/URSI), 2011.

- [11] X. Mu, W. Jiang, S.-X. Gong, and F.-W. Wang, "Dual-band low profile directional antenna with high impedance surface reflector," *Progress In Electromagnetics Research Letters*, vol. 25, 67-75, 2011.
- [12] E. Yablonovitch, "Inhibited spontaneous emission in solid-state physics and electronics," *Physical Review Letters* 58 (20), pp. 2059-2062, May 1987.
- [13] Li Yang, Mingyan Fan, Fanglu Chen, Jingzhao She, and Zhenghe Feng, "A Novel Compact Electromagnetic-Bandgap (EBG) Structure and Its Applications for Microwave Circuits," *IEEE Trans. Microwave Theory Tech.*, Vol. 53, No. 1, Jan. 2005.
- [14] N. Sankaran, M. Swaminathan, and R. Tummala, "Synthesis of electromagnetic band gap structures using stepped impedance resonators," *Microwave and Optical Technology Letters*, vol. 53, no. 10, pp. 2378-2382, Oct. 2011.
- [15] Li Yang, Mingyan Fan, Fanglu Chen, Jingzhao She, and Zhenghe Feng, "A Novel Compact Electromagnetic-Bandgap (EBG) Structure and Its Applications for Microwave Circuits," *IEEE Trans. Microwave Theory Tech.*, vol. 53, no. 1, Jan. 2005.
- [16] M. F. Abedin, and M. Ali, "Effects of a Smaller Unit Cell Planar EBG Structure on the Mutual Coupling of a Printed Dipole Array," *IEEE Antenn. Wireless Propag. Lett.*, vol. 4, 2005.
- [17] Antti E. I. Lamminen, Antti R. Vimpri, and Jussi Säily, "UC-EBG on LTCC for 60-GHz Frequency Band Antenna Applications," *IEEE Trans. Antennas Propagat.*, vol. 57, no. 10, Oct. 2009.
- [18] D. J. Kern, D. H. Werner, A. Monorchio, L. Lanuzza, and M. J. Wilhelm, "The design synthesis of multiband artificial magnetic conductors using high impedance frequency selective surfaces," *IEEE Trans. Antennas Propagat.*, vol. 53, no. 1, pp. 8-17, Jan 2005.

# **Chapter 4**

## **Analysis and Design of Self-Excited EBG Resonator Antennas**

### **4 Analysis and Design of Self-Excited EBG Resonator Antennas**

In line with motivations and objectives sketched in previous sections, this chapter proposes a novel antenna structure called the Self-Excited EBG Resonator Antenna (SE-EBG-RA) together with a new method for its analysis and design. This fundamental method (referred to as HFSS/Bloch) is applicable to periodic structures such as the proposed periodic antennas, and will serve as the cornerstone of the thesis. Sec. 4.1 describes the development of the SE-EBG-RA and the HFSS/Bloch method. Then, Sec. 4.2 compares two different versions of the antenna, referred to as open- and short-circuited SE-EBG-RAs. After that, in Sec. 4.3, a scheme is presented to enhance the aperture gain of a SE-EBG-RA. Sec. 4.4 is dedicated to a mathematical approach to remove the dependency of HFSS/Bloch method on numerical analysis and to find a set of closed form equations for fast characterization of SE-EBG-RAs. Finally, Sec. 4.5 focuses on the periodicity of SE-EBG-RAs and the fact that by miniaturizing the antenna unit cell, electrically smaller SE-EBG-RAs are achievable.

#### **4.1 A Novel High-Performance Antenna: SE-EBG-RA**

In this section, radiation characteristics of an open-circuit electromagnetic band-gap (EBG) transmission line are employed to demonstrate a new low-profile antenna with high radiation efficiency. The self-excited EBG resonator antenna (SE-EBG-RA) presented is excited using a microstrip line, without requiring a separate probe. Tall metal traces enhance radiation while providing less loss, which results in better efficiency. Some desirable properties including radiation pattern, gain/efficiency, overall footprint, and resonance frequency are discussed.

##### **4.1.1 Introduction**

As discussed earlier, antennas with reduced size and higher radiation efficiency have long been targeted by researchers in the field of communications [1]-[5] and [7]-[8]. If the antenna footprint can be reduced while not sacrificing other parameters like bandwidth and radiated power efficiency ( $\eta$ ), lifetime, weight, cost, size, stability and biological harms of many communications systems can be ameliorated. To this end, many attempts have been made including: getting inspiration from fractal shaped objects [7], applying dielectric or magnetic materials around the original element [5], using optimization algorithms [5], utilizing lumped [5] or parasitic [4] elements, etc. Recently there is increased attention on incorporating electrically small periodic elements into the body of traditional structures [1]-[3], [8]-[9]. These elements, which can be metal, dielectrics, or a blend of both, are generally referred to as metamaterial [8]-[9], and some of them specifically as EBG structures [1]-[3]. The aptitudes of these structures in promoting size reduction, surface wave suppression, and loss mitigation are demonstrated [1-3], and were discussed in the previous chapters. This Chapter first incorporates EBG cells with some radiation properties into a transmission line (TL) structure, and then the TL is utilized to develop an antenna. The role of high aspect ratio (HAR) metal traces in enhancing  $\eta$  is also demonstrated.

##### **4.1.2 Periodically Deployed Patches as a Radiating EBG TL**

A well-known EBG surface is first considered. As seen in Fig. 4.1.1 (a), this EBG surface is the via-less version [2] of the mushroom-like structure [1]. To realize a TL composed of these EBG cells, a number of patches are deployed over a PEC-backed dielectric slab just in one direction. In Fig. 4.1.1 (a), the structure shown is made of 5 cells resembling a normal microstrip line (MSL), but with tiny sections periodically removed to discriminate between the adjacent patches (cell details are as in Fig. 4.1.3).

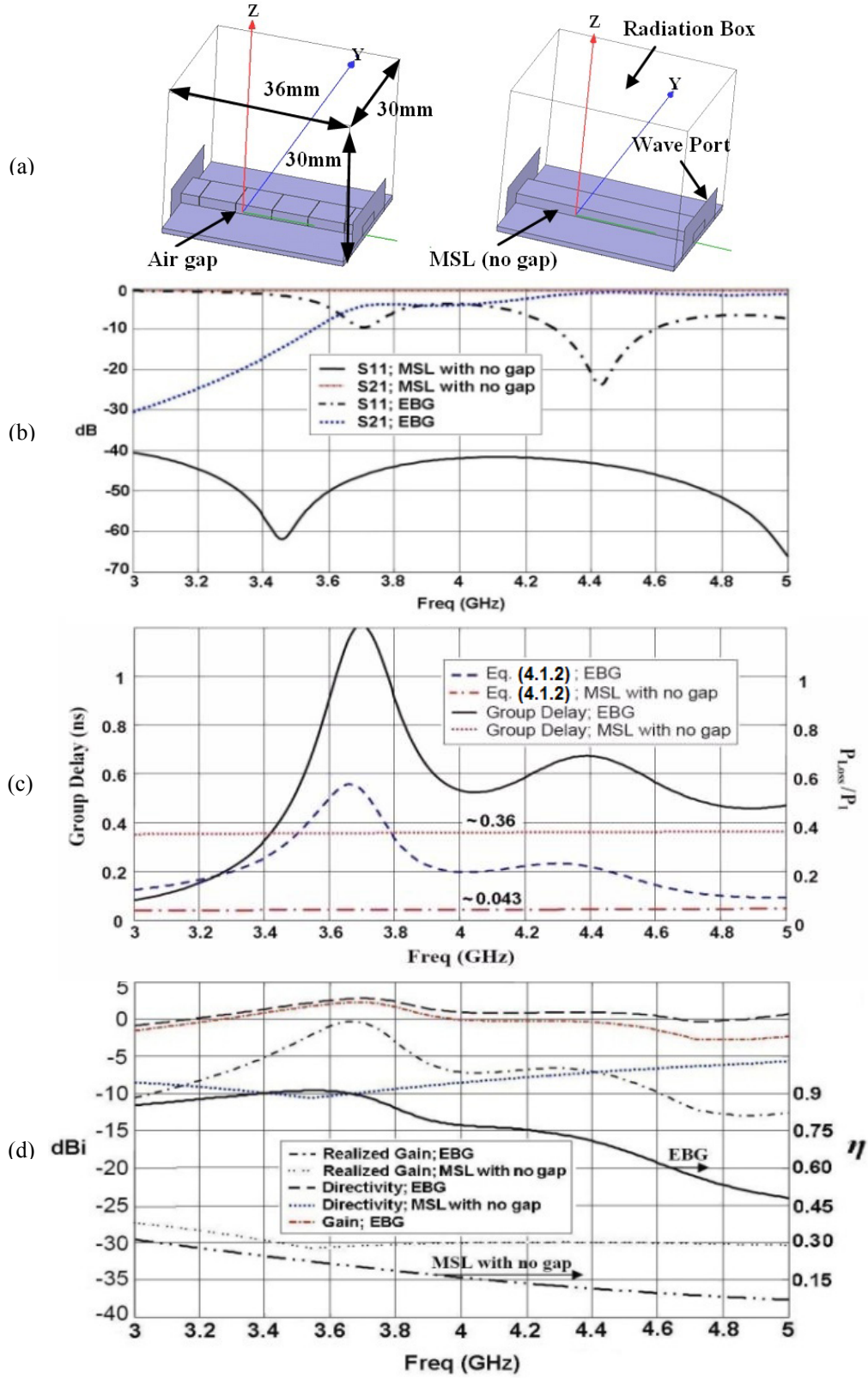


Fig. 4.1.1. 2-port analysis of the 5-cell EBG TL and its gap-less version [17] © 2012 IEEE, a) geometry and HFSS modeling, b) S<sub>11</sub> and S<sub>21</sub>, c) group delay and normalized loss in (4.1.2), d) realized gain, gain, directivity, and  $\eta$ ; detailed dimensions of the EBG cell are as in Fig. 4.1.3.



As seen, metallic traces project from the substrate surface to form a tall EBG woven TL. The importance of tallness will be explained in Sec. 4.1.5. Considering two wave ports on each side, the 2-port network behavior can be analyzed numerically. Fig. 4.1.1 renders the geometry and properties of this EBG TL over a wide frequency range. For comparison, properties of the gap-less version are also included in Fig. 4.1.1.

As shown in Fig. 4.1.1 (b), there are some bandgaps (around 3.7 GHz and 4.43GHz) at which the  $S_{11}$  is quite small meaning that nearly all the power coming to port 1 is delivered into the network.  $S_{21}$  is also reduced ( $< 0\text{dB}$ ) which shows not all the entering power can reach port 2 and indicates some form of loss. If the port impedance is the same as the reference impedance on which S-parameters are based, the power loss in the network can be written as:

$$P_{Loss} = P_{in} - P_2 = P_1(1 - |S_{11}|^2) - P_1|S_{21}|^2 \quad (4.1.1)$$

or the normalized loss can be expressed as [10] and [15]:

$$P_{Loss}/P_1 = 1 - |S_{11}|^2 - |S_{21}|^2 \quad (4.1.2)$$

where  $P_{in}$  is the power entering the network,  $P_1$  is power incident on port 1 ( $|V_1|^2/2Z_0$ ),  $P_2$  is power output from port 2, and  $Z_0$  is the reference impedance. It is well-known [10] that for a lossless 2-port network, (4.1.2) has to be zero. Therefore, (4.1.2) can be a proper criterion to evaluate radiation loss or other losses. Fig. 4.1.1 (c) shows (4.1.2) versus frequency. As observed, the loss is considerable meaning that if other loss mechanisms (i.e. conductor and dielectric loss) are negligible, the power must be radiating. For comparison, the group delay, which is the indicator of the electrical length, is also included in Fig. 4.1.1 (c). To have a correct analysis setup, the 2-port structure is placed in a radiation box, and all conditions required for analysis of a radiating structure are considered. For the structure of Fig. 4.1.1 (a), the gain and  $\eta$  are shown in Fig. 4.1.1 (d). In fact, this structure can be considered an antenna feeding from port 1, but terminated at port 2 by the port impedance (not open circuit, i.e. OC), which is also the idea utilized in [e.g. 14]. As in Fig. 4.1.1 (d),  $\eta$  of the EBG TL is generally high and tending to peak around a specific bandgap. It is obvious that around these bandgaps, group delay increases (longer electrical length), input matching and gain improve, and  $P_{Loss}/P_1$  is at its peak (peak radiation loss). Altogether, this simple analysis shows that this piece of TL is radiating a portion

of EM power and is capable of receiving the guided power from one port as a TL and radiating it from all over its structure as an antenna.

To provide an alternative analysis, the Bloch theory is employed which is an appropriate tool for analysis of periodic structures. Noting the general TEM solution of the differential equation ruling a TL [10] (in this case, Quasi-TEM for MSL), a complex propagation constant as  $\gamma = \alpha + j\beta$  can be assigned.  $\alpha$  adds a non-traveling, attenuation nature which might be attributed to the Ohmic loss, radiation loss, or the total reflection on the input port, similar to waveguide behavior below the first cut-off. On the other hand,  $\beta$  adds a traveling wave essence.  $\gamma$  is linked to network parameters using the equation given by the Bloch Theory [10]:

$$\cosh \gamma d = (A + D) / 2 \stackrel{\text{if symmetric}(A=D)}{=} A \quad (4.1.3)$$

in which  $A$  and  $D$  are the unit cell cascade parameters and  $d$  is the cell size. The cascade parameters can be derived from the S-parameters given by HFSS, and by using conversion tables in [10]. Moreover, an equivalent impedance can be assigned to the loaded TL, known as the Bloch impedance. For symmetric cells, this impedance is expressed by:

$$Z_B = B Z_0 / \sqrt{A^2 - 1} \quad (4.1.4)$$

in which  $Z_0$  is the impedance of the unloaded TL,  $B$  is the second cascade parameter. Thus, using (4.1.3) to (4.1.4),  $\gamma$  and  $Z_B$  of the loaded line can be found from scattering evaluation of the 2-port unit cell in HFSS.

#### 4.1.3 Open-Circuited TL and Its Radiation Characteristics

If a lossy fragment of TL is Open-Circuited, the input impedance can be written as [10]:

$$Z_{in} = Z_B \frac{Z_L + Z_B \tanh \gamma l}{Z_B + Z_L \tanh \gamma l} \stackrel{Z_L \rightarrow \infty}{\approx} \frac{Z_B}{\tanh \gamma l} \quad (4.1.5)$$

It is reminded that  $Z_B$  is a general complex value and dependent on the TL circuit components. Because  $Z_{in}$  is complex, in case the imaginary part vanishes, the real part can be matched to the generator. If at a specific electrical length, matching is provided and the radiation is simultaneously high enough, the OC TL can be regarded as a matched antenna with a high radiation resistance. This behavior is demonstrated later through numerical analysis and measurement. Fig. 4.1.2 shows the circuit model for the EBG cells.

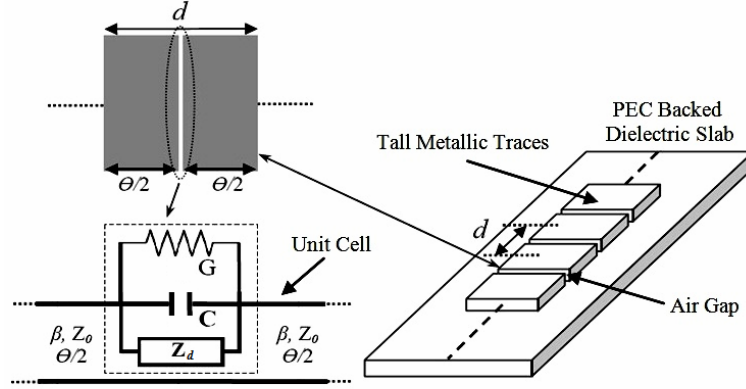


Fig. 4.1.2. Circuit model for the proposed EBG cells. The real power radiation is modeled as a conductance [17] © 2012 IEEE<sup>36</sup>.

This model is generally compatible with those used by the Bloch theory [9]-[10] and [13]. Specifically, the model is very similar to that in [13], except here the conductance  $G$  is added to model the radiation. As shown by [13],  $Z_d$  in Fig. 4.1.2, is related to the inductance provided by the PEC-backed dielectric slab given in [1]-[2] and [13]. If  $G$  is considerable, on the one hand, it causes more radiation and better  $\eta$  for the antenna made of this TL. On the other hand, by affecting the overall circuit model,  $G$  can affect  $\alpha$  and  $\beta$ . Because  $Z_{in}$  in (4.1.5) is a complex value dependent on  $\alpha$  and  $\beta$ ,  $G$  is able to affect the matching quality. It can be concluded that the size and  $\eta$  of the antenna made of this TL are dependent on  $G$ . To demonstrate the effect of  $G$ , two unit cells composed of small pieces of MSL are considered, one without any gap (Fig. 4.1.3 (a)), and the other with 0.1mm air gap at the center, i.e. EBG cell (Fig. 4.1.3 (b)). All other parameters are kept the same. The normalized  $\gamma$  in (4.1.3) is depicted versus frequency in Fig. 4.1.3 (c). Also, Table 4.1.1 compares  $\beta$ ,  $\alpha$ , and  $Z_B$  found by (4.1.3) to (4.1.4). Putting these parameters into (4.1.5), and considering a 3-cell OC section,  $Z_{in}$  and RL are found as in Table 4.1.1. As opposed to the gap-less unit cell, the EBG one is well matched to the 50Ω source, and its  $\eta$  is  $\sim 3.3$  times larger.

<sup>36</sup> Fig. 4.1.1 to 4.1.6, parts of Fig. 4.1.7, Fig. 4.1.8, Table 4.1.1 to 4.1.2 are published in [17] © 2012 IEEE.

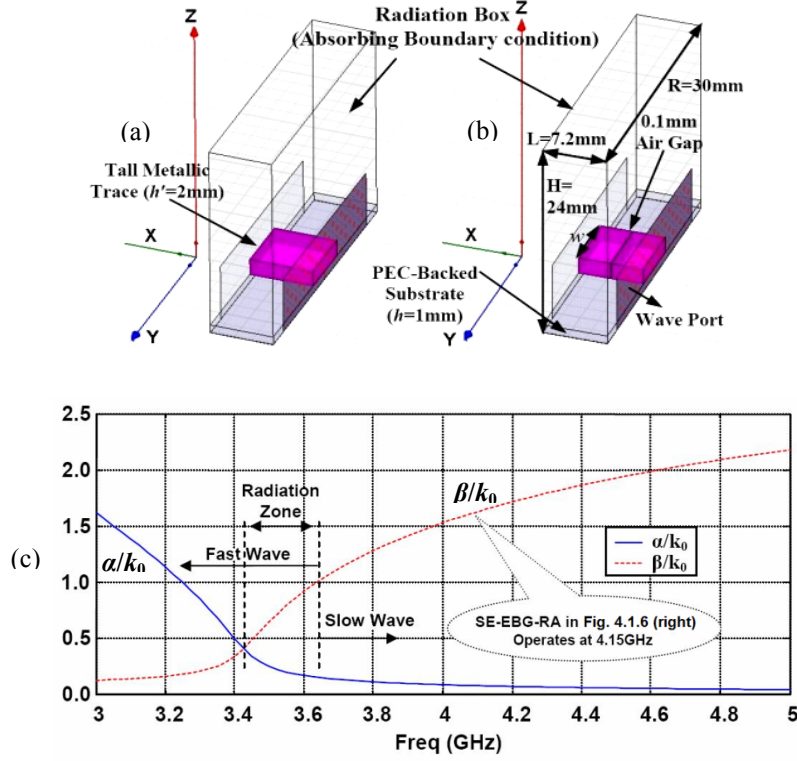


Fig. 4.1.3. Unit cell and the 3D model details for, a) the tall MSL, b) the gap loaded (EBG) tall MSL, c) normalized  $\gamma$  in (4.1.3);  $w=9$ ,  $\epsilon_r=9.9$ ,  $\tan\delta=0.003$ ,  $\sigma=5.8e7s/m$ .

Table 4.1.1 Performance comparison of 2 unit cells: low loss MSL, and EBG ( $Z_{in}$  and RL are given for a 3-cell OC piece of each case)

Freq (GHz)	$\beta/k_0$	$\alpha/k_0$	$Z_c$ ( $\Omega$ )	$\eta$	$Z_{in}$ ( $\Omega$ ) (3-cell OC piece)	Group Delay (ns)	RL (dB)
Gap-less version: $w=7.1mm$ , $L=7.2mm$							
4.15	2.88	0.009	12.3	22%	$0.32+j10.1$	0.072	-0.1
Gap-loaded (EBG) version: all the same except 0.1mm gap at center							
4.15	1.67	0.07	$5.64-j0.25$	73%	$41.85-j1.2$	0.09	-21.4

It is noted that before using (4.1.3) to (4.1.5), it is necessary to obtain  $Z_0$ , which can be found by numerically analyzing the gap-less unit cell, yielding  $Z_0=12.3\Omega$ . In fact, in HFSS, the port impedance is calculated from field components around the port. Taking a circuit approach, which means using (4.1.4), it is possible to evaluate  $Z_0$  by S-parameters instead of the fields. In this case,  $Z_B$  will be  $12.28\Omega$  which closely agrees with  $12.3\Omega$ . This clearly implies the soundness of modeling and the accuracy and convergence of the numerical analysis in HFSS. For comparison, closed form equations [e.g. 10] can also be employed to find  $Z_0$ . These formula give  $Z_0=11.9$

which is still close to  $12.3\Omega$  (error $<2.5\%$ ). Now the question is how to ensure that the structure is radiating sufficiently. To answer, it is noted that at some frequencies,  $\alpha$  grows while  $\beta$  is providing a large  $\text{Re}\{Z_{in}\}$  and a small  $\text{Im}\{Z_{in}\}$  in (4.1.5). In this case, the real power enters the 1-port OC fragment of TL with a good  $RL$ , and hence, it has to be consumed somewhere. If the consumption is mainly due to the radiation and not Ohmic loss, the structure is an antenna. Then, this radiation can be shown by a large radiation resistance ( $R_r$ ) while the Ohmic loss ( $R_{Loss}$ ) is relatively small, and this yields a large  $\eta = R_r/(R_r + R_{Loss})$ . This explanation is later confirmed by simulation and experiment. As known in antenna theory,  $R_r$  of a line with sinusoidal current is dependent on the electrical length [11]. For small antennas, the greater the electrical length, the higher  $R_r$  &  $\eta$ . Looking at Table 4.1.1 and comparing the group delay of unit cells, it is observed that the delay (electrical length) is larger for the EBG cell, and hence, with identical physical lengths, this cell has larger  $R_r$ .

#### 4.1.4 Concept of Self-Excited EBG Resonator Antenna

In Table 4.1.1, radiation by EBG cells was demonstrated. Now if considering a 3-cell OC EBG TL (1-port network), and analyzing it using (4.1.3) to (4.1.5), it is observed that at 4.15GHz, the  $RL$  is high meaning that this OC EBG network is a radiating structure around this frequency. Because this novel structure is woven by EBG cells, and it resonates only at around a specific frequency band (bandgap), it can be called an EBG Resonator Antenna (EBG-RA). The term “Self-Excited” is added to indicate that as opposed to other EBG cells usually used as the ground plane in antenna design [1]-[3], the SE-EBG-RA does not need an external EM probe like a dipole or patch antenna. Instead, it is simply excited from one side, in the same plane, by a MSL port. In section 4.1.5, it is shown that numerical analysis of this 3-cell OC EBG antenna totally done by HFSS (no Bloch) roughly results in the same 4.15GHz resonance predicted by (4.1.3) to (4.1.5). As in Table 4.1.1, the  $RL$  predicted by the Bloch method is -21.4dB while that of Fig. 4.1.6 (right) is -18.5dB (see Fig. 4.1.7), both resonances occurring at 4.15GHz, and demonstrating good agreement.

To show how the SE-EBG-RA radiates, the fields right above the EBG cell of Fig. 4.1.3 (b) are considered and the relevant real Poynting vectors are illustrated in Fig. 4.1.4. It is observed that vector components are pointing to the broadside direction implying that a portion of real power is radiating at the gaps. The important point is that E-fields are excited inside the gaps and

radiated out parallel to the ground, as opposed to the normal MSL in which E-fields are perpendicular. According to the Huygens' equivalence principle [11], the aperture E-fields can be replaced by their equivalent magnetic surface currents:

$$M_s = -2 \hat{n} \times E_a \quad (4.1.6)$$

where  $n$  is the unit vector normal to the surface, on the side of radiated fields. Based on (4.1.6), such E-fields can be represented by a magnetic current parallel to the ground. Because the image of  $M_s$  in a PEC is in phase, it constructively radiates. Fig. 4.1.5 illustrates the application of Huygen's principle to cells. To clarify, in [11], E-fields uniformly distributed on the open end of a parallel plate waveguide are considered, and an equivalent impedance is driven using the aperture theory with the assumption that the gap is surrounded by *infinite* PEC planes on each side. In fact, the field condition on the top surface of tall traces roughly satisfies this requirement. In Sec. 4.4, this is used to estimate the impedance at gap and develop the circuit model.

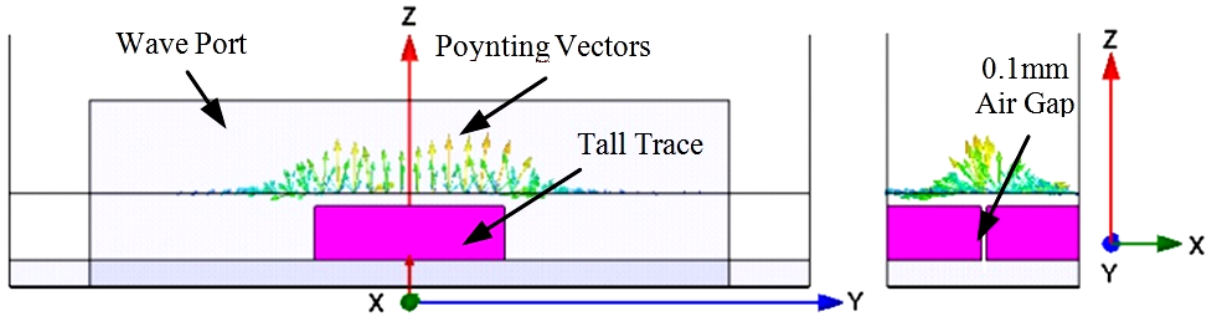


Fig. 4.1.4. Different views of the EBG unit cell of Fig. 4.1.3 (b) together with the distribution of real Poynting vectors adjacent to the cell aperture at 4.15GHz.

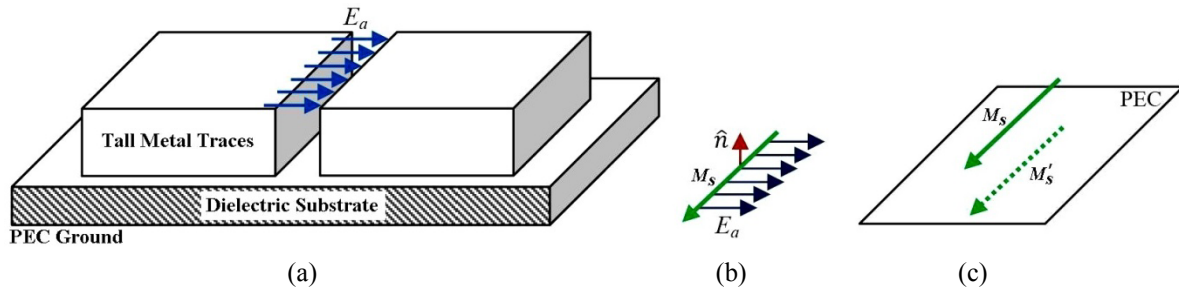


Fig. 4.1.5. General field distribution around the EBG cell gap: a) E-fields are parallel to the PEC ground, b) illustration of the equivalent magnetic current based on Huygen's principle, c) in phase image of  $M_s$  above a PEC (no field cancellation).

Fig. 4.1.5 could give the impression that the structure is a type of slot antenna or slotted antenna array, for which slots have been applied to a thick MSL. However, the fact that the slots are electrically small (typically  $< \lambda/10$ ) and that their periodicity is also small ( $< \lambda/10$ ) differentiates the antenna from those arrays which usually use large slots. The overall length of a typical 3-cell SE-EBG-RA is  $\sim 0.4\lambda$  while in later chapters, much smaller versions with 2 cells are also presented (down to  $\sim 0.22\lambda$  in length). Readers are urged to review the work in [16] because it has some similar aspects with the idea of this section.

#### 4.1.5 Advantages of Thick Unit Cells: Miniaturization and Efficiency

To show the effect of tallness, a 3mm portion of a non-tall (thin conductor) 50 $\Omega$  MSL is considered and its radiation is compared to that of a tall (thick conductor) 50 $\Omega$  version. The HFSS models for unit cells are like Fig. 4.1.3 (a), except for  $w$  and  $h'$  which are shown in Table 4.1.2, and  $H=20\text{mm}$  and  $L=3\text{mm}$ .

Table 4.1.2 Comparison of radiation properties of a tall and a non-tall 50 $\Omega$  MSL;  $Z_c$  is the characteristic impedance;  $\eta$  is for one cell, roughly calculated from the unit cell model in HFSS, to help as a baseline.

$\epsilon_r=9.9$ , $h=1\text{mm}$ , $\tan\delta=0.003$ , $\sigma=5.8\text{e}7\text{s/m}$ , $L=3\text{mm}$ $h$ is the dielectric thickness, $h'$ is the trace thickness, and $w$ is the trace width					
Freq (GHz)	$\beta/k_0$	$\alpha/k_0$	$\eta$ (%)	$Z_c$ ( $\Omega$ )	Group Delay (ns)
Tall Version ( $w=0.3\text{mm}$ , $h'=2\text{mm}$ )					
4.15	2.067	0.007	39.35	49.85	0.022
Non-Tall Version ( $w=0.92\text{mm}$ , $h'=0.03\text{mm}$ )					
4.15	2.584	0.007	8.32	49.45	0.026

As in Table 4.1.2, with identical  $Z_c$ ,  $\eta$  of the tall cell is 4.7 times higher. Although  $\eta$  is found for current distribution and loss on 2-port unit cells (not for the multi-cell structure), it is still a good figure to predict  $\eta$  of OC pieces of these TLs. It is noted that this is only a rough estimation, because for an accurate  $\eta$  commutation using HFSS, the boundary walls (radiation box) should be at least  $\lambda/4$  far from any point of the cell to allow them work properly. In light of observing mostly upward radiation from the cells (see Fig. 4.1.4), the radiation box is considered large enough on the top (Fig. 4.1.3), but not on the side. This causes some errors while at the same

time provides a quick insight on the  $\eta$  of the cells (comparatively) without the need to analyze the larger antenna structures.

The high  $\eta$  of the tall version can be attributed to less ohmic loss, yielding less  $R_{Loss}$  and more  $\eta$ . Another reason is that the amount and the distribution of fringing E-fields for the tall one are different which could yield more constructive radiation and less far-field cancelation. As in Table 4.1.2,  $\beta/k_0$  and delay are smaller for the tall one showing that fields infiltrating the air are larger. According to the Huygen's Principle, some parts of fringing E-fields which are parallel to the PEC ground, have in phase images (similar to Fig. 4.1.5), thus can radiate more effectively than those of a non-tall MSL. Non-tall MSL may also have such fringing fields, but they are comparatively smaller because the effective dielectric constant is higher in this case and fields are more bound inside the substrate, and less infiltrating the air (compare  $\beta/k_0$  in Table 4.1.2). This fact increases the  $R_r$  attributed to an OC piece of this TL, and hence,  $\eta$  enhances. Another advantage of tallness is that it can help realize a higher capacitance (Fig. 4.1.2) with the same lateral size as before. This helps the designer realize electrically smaller antennas. To demonstrate this feature, two SE-EBG-RAs are considered, which are identical with the exception of the height; one is 2mm tall (i.e. thick) and the other is 0.03mm (i.e. thin). These three EBG cells, depicted in Fig. 4.1.6, are fed by a 2.3mm long 50 $\Omega$  MSL on one side, and are open on the other side. To provide a logical comparison, while decreasing the height,  $w$  of the MSL feed line becomes laterally much larger, increasing from 0.3 to 0.92mm to keep the impedance fixed at 50 $\Omega$ . The analyses are entirely numerical and performed in HFSS to conduct an alternative to the results in Table 4.1.2.

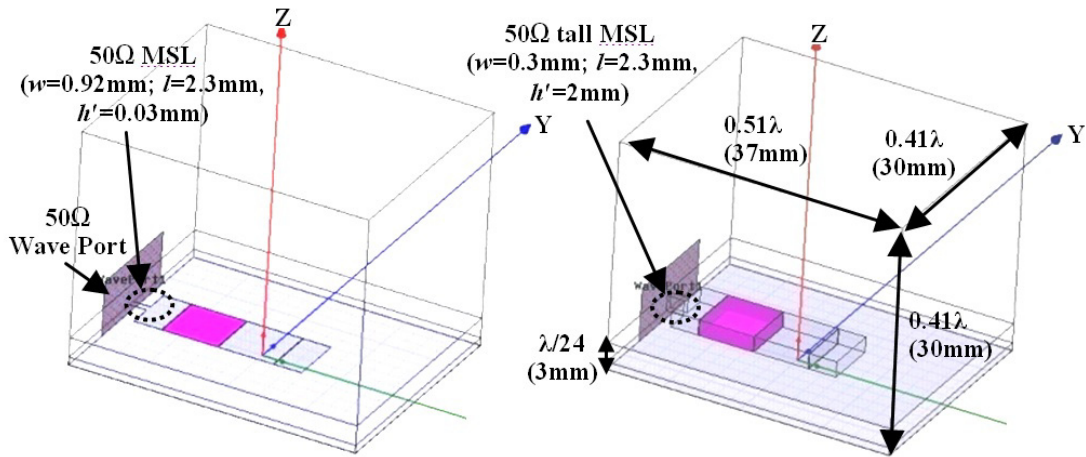


Fig. 4.1.6. 3D geometry of two SE-EBG-RAs which are identical with the exception of the trace height; right) 2mm tall (i.e. thick), left) 0.03mm tall (i.e. thin);  $\lambda$  is wavelength at 4.15GHz; unit cell details are rendered in Fig. 4.1.3.



As shown in Fig. 4.1.7, the tall version resonates at a lower frequency of 4.17GHz (~20%), and its matching quality is much higher (thickness serves as an extra parameter to achieve that). This frequency is close to 4.15GHz found by HFSS/Bloch, reported in Table 4.1.2. Also, as shown in Fig. 4.1.8, the gain and  $\eta$  of the tall version are much better. It is worth noting that SE-EBG-RA resonance of 4.17GHz is in the slow-wave region in Fig. 4.1.3 (c), and hence, the antenna does not belong to the leaky-wave family [9, 14], but to the resonating wave antennas [16].

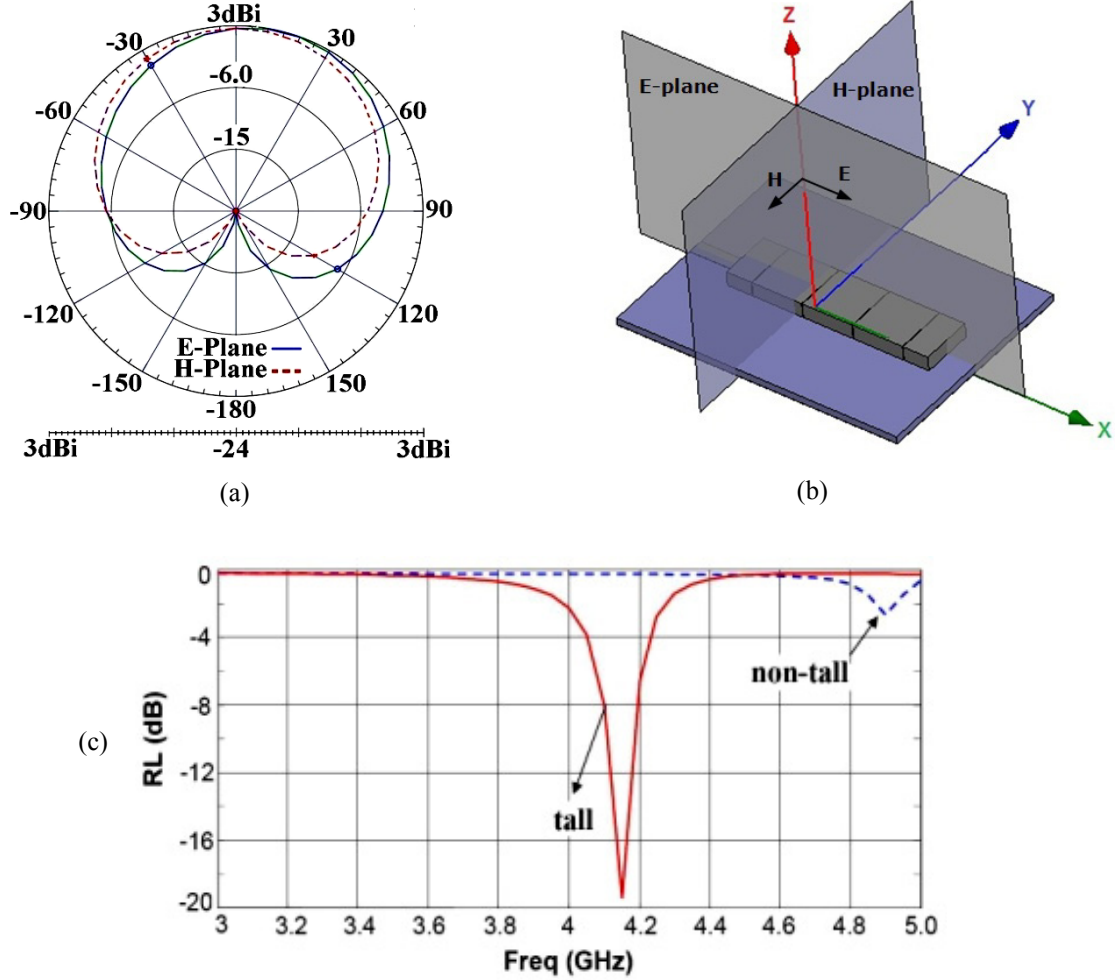


Fig. 4.1.7. a) radiation pattern of the tall SE-EBG-RA at 4.15GHz, b) antenna 3D view and the definition of major radiation planes, c) comparison of  $\text{dB}|S_{11}|$  of the tall (-18.5dB) and thin (-2.8dB) SE-EBG-RAs of Fig. 4.1.6.

The pattern in Fig. 4.1.7 (a) shows that, as usual for EBG antennas [2], Front-to-Back ratio is high while the ground plane is comparatively small ( $0.51\lambda \times 0.41\lambda$ ). Another common point is that the overall structure thickness is very small at  $\sim \lambda/24$ . Later, using the reflection phase analysis, it is shown that the antenna acts similar to EBG antennas. In fact, such an ideal pattern,  $\sim 3\text{dBi}$  gain

with this small size, and the simple feeding method discriminates this antenna from rivals. It is noted that this work intuitively shows that with different types of EBG cell, the radiation properties could be the same. Specifically, as demonstrated in coming chapters, by employing naturally smaller cells [e.g. 12], smaller versions of the proposed antenna could be achieved.

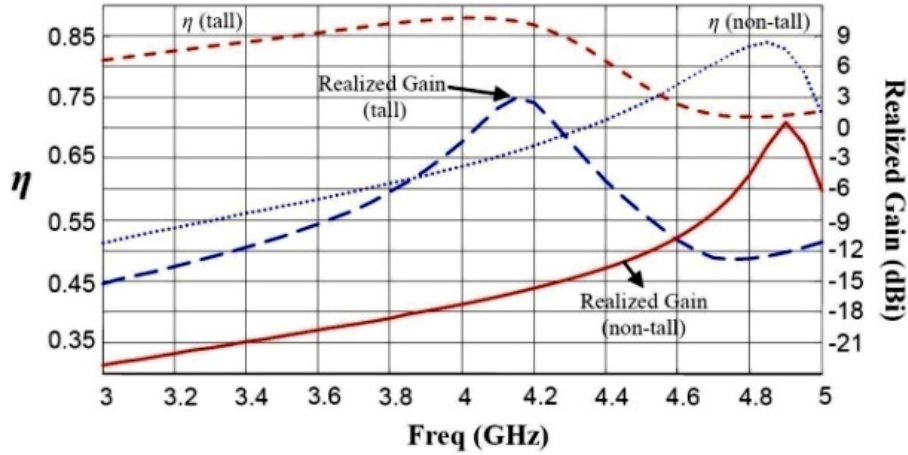


Fig. 4.1.8. Comparison between realized gain and  $\eta$  of the tall and non-tall SE-EBG-RAs; the gain is for the ground plane size (XY size in Fig. 4.1.6) of  $0.51\lambda \times 0.41\lambda$ .

#### 4.1.6 Soundness of the HFSS/Bloch Cell Modeling

To make sure that the effect of mutual coupling is sufficiently considered in the HFSS/Bloch method described before (see Fig. 4.1.3), a comparative study is arranged as follows. As in Fig. 4.1.9, three different Bloch-based models are considered in HFSS, the first of which with the regular 1-cell configuration (see Fig. 4.1.3 (b)), and the others comprising one and two more of the same unit cell. The idea is that if the mutual coupling for the first case is taken into account accurately (or is negligible), increasing the number of cells, as in Fig. 4.1.9, while accurately applying the Bloch theory, should not cause a noticeable difference in the Bloch dispersion diagrams. In that case, it can be concluded that the proposed Bloch cell modeling is reliable.

To provide a logical comparison, after extracting the S-parameters from the case with 2 cells, instead of considering  $d_{1\text{cell}}=7.2\text{mm}$  for the cell size,  $d$  must be doubled ( $d_{2\text{cell}}=2 \times 7.2\text{mm}$ ) in all equations presented in Sec. 4.1. In a similar fashion, for the 3-cell case in Fig. 4.1.9 (c),  $d_{3\text{cell}}=3 \times 7.2\text{mm}$ . This modification allows the Bloch theory to be applied exactly the same to all three cases in Fig. 4.1.9. Fig. 4.1.10 shows the Bloch dispersion diagrams associated with these cells. As observed, the curves correspond so closely that it is difficult to differentiate between

them. The error at cut-off is less than 0.3% and significantly less in other areas. It is reminded that the SE-EBG-RA described earlier is matched somewhere above the cut-off frequency as shown in Fig. 4.1.10. The cut-off is the frequency after which waves switch from an evanescent nature to a traveling nature and propagate (real power) along the TL. The definition of different zones of Fig. 4.1.10 is a convention used in literature [e.g. 22]. Such analysis demonstrates the soundness of HFSS/Bloch modeling, and that modeling only one cell provides accurate results.

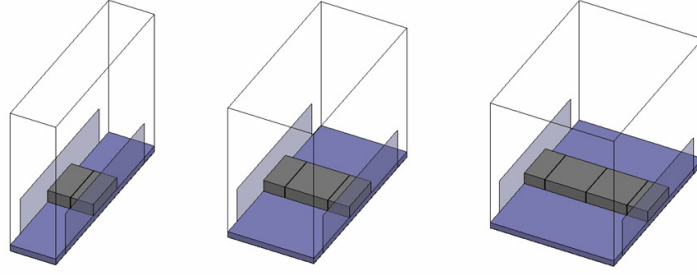


Fig. 4.1.9 HFSS/Bloch unit cell model for one (a), two (b), and three (c) identical unit cells; HFSS/Bloch method is applied to all cases to verify how close the dispersion diagrams are.

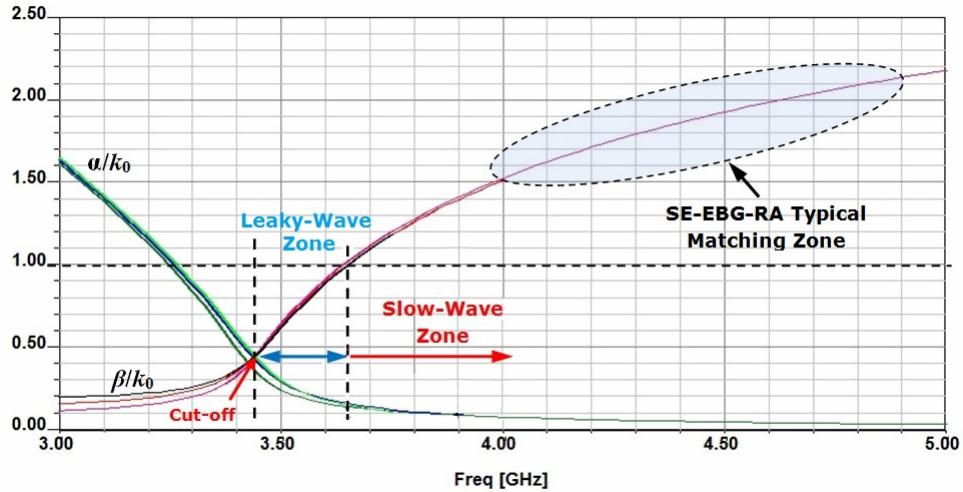


Fig. 4.1.10 Dispersion diagram by the HFSS/Bloch method for the three cells in Fig. 4.1.9. The curves agree closely and the difference in estimating the cut-off frequency is less than 0.3%.

Negligible mutual coupling allows truncation in the number of cells, while not significantly affecting the accuracy of HFSS/Bloch in estimating the behaviors of antennas made of the cells. In Sec. 4.2, SC and OC versions of the SE-EBG-RA antenna with different number of cells are studied, and it is shown that the difference between the resonance found by HFSS numerical analysis and HFSS/Bloch method is 0.8% for the 5-cell OC version and 0.5% for the 2-cell SC

version. Also, for the 3-cell structure of Fig. 4.1.6, this difference is as low as  $\sim 0.48\%$ . Such results are in agreement with the results reflected in Fig. 4.1.9. One explanation for negligible coupling is that according to the results in Sec. 4.4, fields are mainly trapped in the air-gaps and could only weakly couple in the substrate. In Sec. 4.4, it will be demonstrated that  $C_{pp}$ <sup>37</sup> (introduced by air-gaps) typically dominates  $C_{cp}$ <sup>38</sup> (dependent on dielectric material) and the *effective* dielectric constant along the structures of the designs is very low, at 2 to 4 (air is dominating the dielectric material).

#### 4.1.7 Reflection Phase Analysis of HAR EBG Cells

In this part, a new analysis method is presented which can supplement the HFSS/Bloch analysis of the HAR unit cells and provides more profound insight on how these cells operate. The method excites plane waves so that they normally impinge the surface of unit cells. This is as opposed to the HFSS/Bloch method in which waves travel along the surface inside the substrate. By observing the reflection coefficient of the surface in different frequencies and comparing the results with the dispersion diagram given by HFSS/Bloch, a new understanding of the EBG cells is obtainable. The UC-EBG<sup>39</sup> cell shown in Fig. 4.1.11 (a) was first introduced in [21]. It was also considered in [18] using the special cell modeling method shown in Fig. 4.1.11.

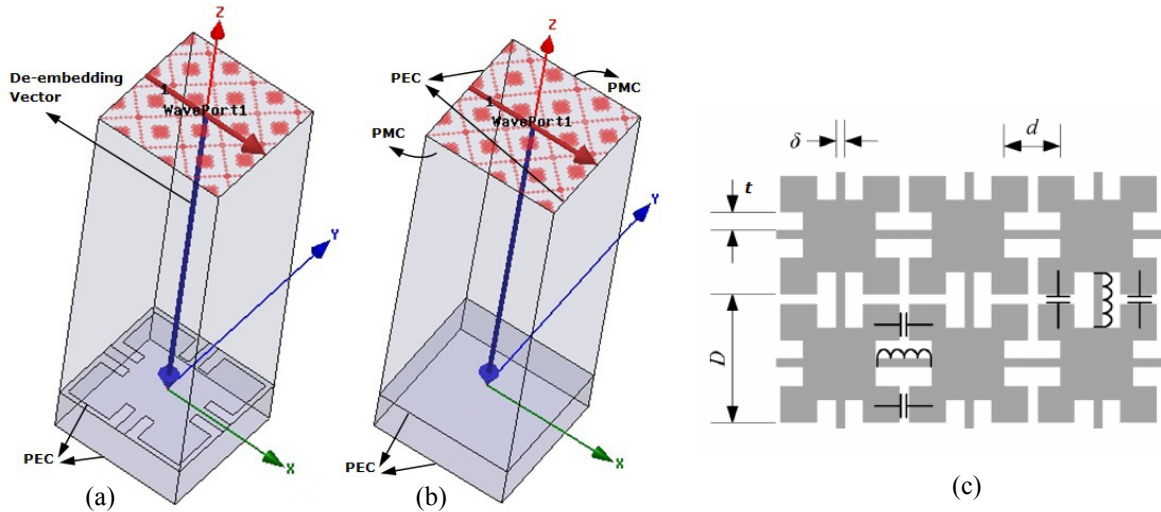


Fig. 4.1.11. HFSS model for a) the UC-EBG cell, b) the same cell with PEC on top layer, together with c) the geometry of the top metal layer and the definition of its physical parameters;  $D=0.9$ ,  $\delta=t=0.07$ ,  $d=0.4$ ,  $h=0.3$  (in mm), and  $\epsilon_r=5.99$ ; geometry, waveport (fields are along X-axis), and PEC/PMC symmetry planes are highlighted.

<sup>37</sup> Parallel plate capacitance at gaps

<sup>38</sup> Coplanar capacitance at gaps

<sup>39</sup> Uniplanar-compact electromagnetic bandgap

The modeling method considers parallel pairs of PEC and PMC as symmetry planes similar to other methods for modeling EBG cells [1-2, 19]. However, instead of using plane wave excitation, it utilizes a waveport as depicted in Fig. 4.1.11 (see the top face of the circumscribing box). The two faces parallel to XZ plane are PMC and those parallel to YZ plane are PEC. The bottom face is also set as a PEC. This way, the unit cell represents an infinite number of such cells deployed in X and Y directions.

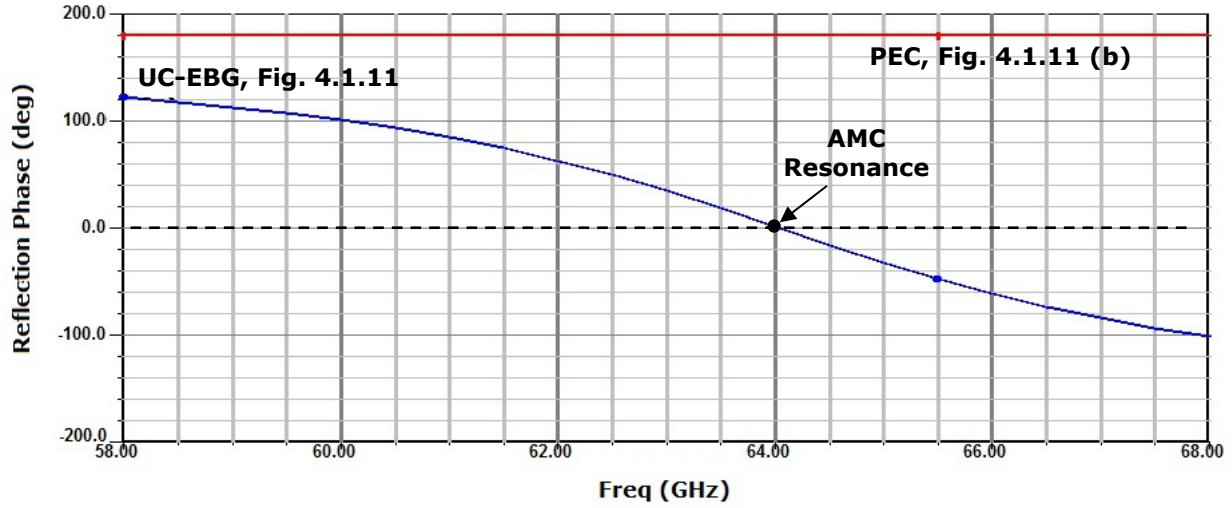


Fig. 4.1.12 Reflection phase diagram for the cells shown in Fig. 4.1.11.

This method of plane wave excitation is simpler to implement in HFSS than others [1-2, 19] and has proven accurate [18]. To assure that the HFSS modeling is seamless, the same cell in [18] is modeled here in HFSS, and the related reflection phase diagram (RPD) is rendered in Fig. 4.1.12. As seen in Fig. 4.1.11 (b), other than the main cell, another case is also considered which has a metal sheet totally covering the surface of EBG cell, playing the role of a PEC surface for which RPD is expected to be 180°. Fig. 4.1.12 shows that this expectation is fulfilled. For Fig. 4.1.11 (a) cell, the frequency at which phase is 0° is the resonance when the surface is acting like a PMC, and hence, the surface could be called an artificial magnetic conductor (AMC). In Fig. 4.1.12, the resonance happens at 64GHz and the one reported in [18] is 67GHz ( $\Delta < 4.5\%$ ) which provides some confidence in accuracy. This difference can be attributed to the fact that [18] does not indicate where the reference reflection plane is, whether on the top surface of EBG or on its PEC ground plane (thus,  $\Delta$  could be less). In this work, the reference is considered to be on the top surface. The vertical arrow inside the cell in Fig. 4.1.11 (a) or (b) touches the surface of the

substrate and shows that the phase shift caused by the distance between the waveport and this surface is de-embedded. Therefore, the RPD represents the phase difference only introduced by the substrate surface.

The next step is to use this method for the proposed HAR cells. Fig. 4.1.13 shows the associated unit cell. Because the proposed cell is 1D, i.e. in practice, it is not repeated in Y-direction, the radiation box in Fig. 4.1.13 is considered very wide to make images of the structure along the Y-axis very far from each other. Due to the effect of PMC symmetry planes, there are an infinite number of such images but the distance between them in Y-direction tends to sufficiently isolate them and cause the mutual coupling to be negligible. This isolation has been verified by increasing the cell width along Y-axis even more (twice what seen in Fig. 4.1.13) and observing that the shift in resonance is trivial. This strategy allows to apply the method described in Fig. 4.1.11 and analyze the resonant nature of the proposed cell with respect to *normal* plane waves. Fig. 4.1.14 shows the diagram and highlights the resonance frequency at 3.57GHz.

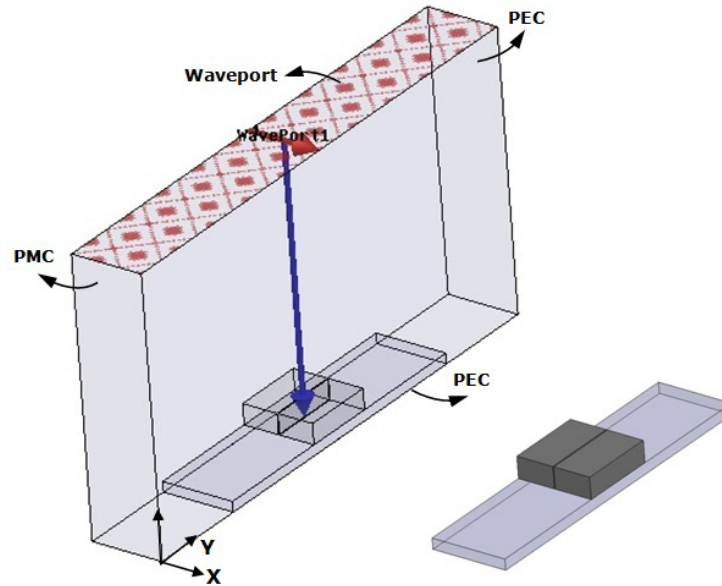


Fig. 4.1.13 The HFSS model for a the proposed EBG cell; the geometry and the wave-port excitation as well as the PEC and PMC symmetry planes are highlighted and are arranged the same as Fig. 4.1.11; the radiation box width is enlarged enough to make the images in Y-direction sufficiently far and suppress the mutual coupling.



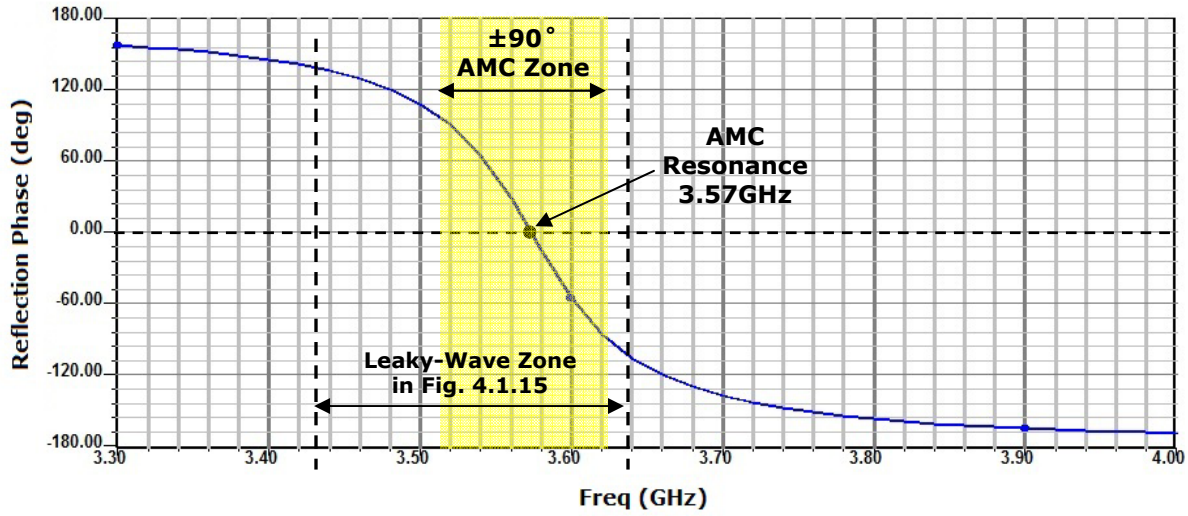


Fig. 4.1.14 Reflection phase diagram for the EBG cell shown in Fig. 4.1.13. The  $\pm 90^\circ$  phase range area is highlighted by a color box.

The dispersion diagram in Fig. 4.1.14 can be compared with the Bloch dispersion found by the Bloch cell modeling proposed earlier in Sec 4.1, as shown in Fig. 4.1.15 (over the same frequency range as Fig. 4.1.14). The comparison *interestingly* shows that the AMC condition in Fig. 4.1.14 occurs at a frequency, which lies somewhere inside the leaky-wave zone of Fig. 4.1.15. Because the SE-EBG-RA composed of such cells is typically operating above this zone, where  $\beta/k_0 > 1$  (e.g.  $\beta/k_0 \sim 1.65$  for Fig. 4.1.3 (c)) this antenna functions above the AMC resonance of the cell, but still close enough to the resonance to benefit from the high impedance (HI) behaviors of such cells. This is in contrast to the EBG antennas in [2] or [1] for which a dipole antenna on EBG ground is matched somewhere below the AMC resonance, and still benefits from the HI nature. It is worth mentioning that [2] calls its EBG surface a reactive impedance surface (RIS), but the surface is in fact an inductive impedance surface (IIS). In comparison, the body of the proposed SE-EBG-RA (which is based on the HAR EBG cells) can be regarded as a capacitive impedance surface (CIS) because the antenna is matched above the AMC resonance. To expand on this, it is noted that the typical circuit model for an EBG cell facing a normally incident plane-wave is a parallel  $LC$  tank [2, 20]. Accordingly, in frequencies above the AMC resonance ( $LC$  resonance), impinging waves view the surface impedance as a capacitor and below the resonance as an inductor [2, 20].

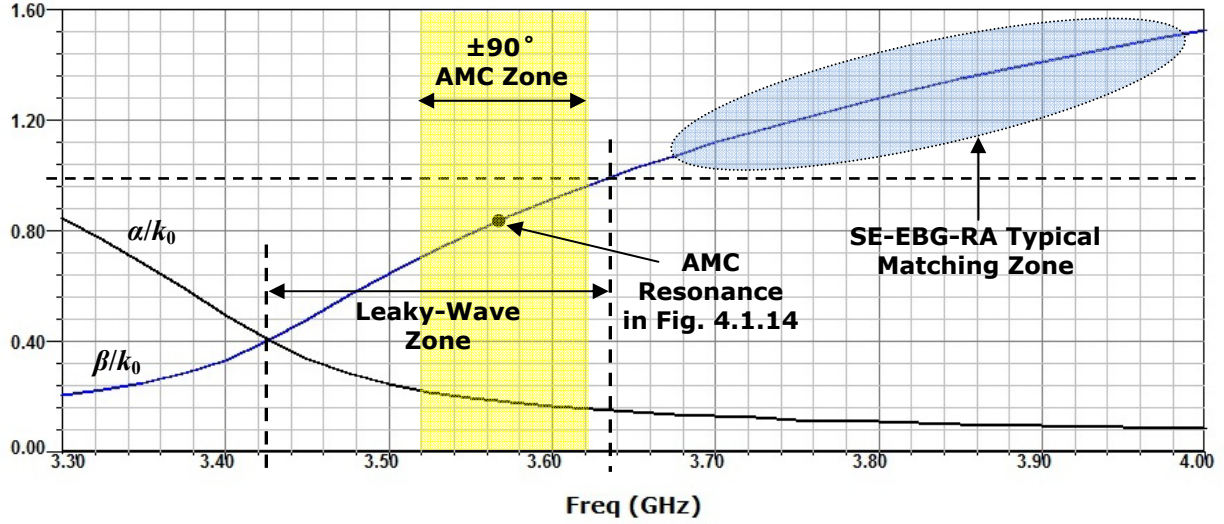


Fig. 4.1.15 Dispersion diagram calculated by the HFSS/Bloch method. The curves show the real and imaginary part of the normalized propagation constant ( $\gamma/k_0 = \alpha/k_0 + j\beta/k_0$ ). AMC zone is highlighted and overlaps the leaky zone.

#### 4.1.8 Conclusion

In this section, radiation characteristics and a tangible application of an EBG TL were investigated. The idea started by introducing the radiation properties of the TL. Then it was shown that although the radiation from this TL might not be desirable in TL realm, from a different standpoint, it could be useful to develop a novel antenna. The main feature of this antenna was the use of tall metal traces employed to mitigate loss and better excite EBG cells with a simple tall MSL. To form the antenna, a via-less version of mushroom-like EBG cells was first utilized to weave the EBG TL. Afterwards, by choosing a proper electrical length, an efficient antenna was achieved. The properties of the proposed antenna including radiation pattern, gain, overall footprint, and the input matching were rendered and discussed. The analysis of the EBG TL was based on the Bloch theory combined by numerical analysis (HFSS/Bloch). A dedicated study was arranged to demonstrate the soundness of the proposed HFSS/Bloch cell modeling. Finally, EBG unit cells were also characterized using the well-known reflection phase analysis method and the results were compared to results from HFSS/Bloch method. The comparison showed that the SE-EBG-RA is a type of EBG antenna, which is matched above, yet close to the high impedance resonance of its EBG cells.



## 4.2 SC versus OC SE-EBG-RA: Miniaturization by a Shorting Plate

In this part, a method is proposed to decrease the resonance frequency of the self-excited EBG resonator antenna (SE-EBG-RA) introduced in Sec. 4.1. The method is based on the application of a plate, which can short the open end of the antenna and make a short-circuited (SC) version with a reduced resonance. The antenna EBG cells are electrically much smaller than wavelength and are the same high aspect ratio (HAR) EBG cells described in Sec. 4.1. The set of EBG unit cells, which are arrayed only in one dimension (1D), are regarded as a fragment of EBG transmission line (TL), highly radiating from their apertures (as in Sec. 4.1). From a TL model perspective, this section shows how a few of these cells can be either open-circuited (OC) or SC on one end and behave like novel efficient antennas, while the SC version can be electrically smaller. As an extra step towards miniaturization, the effect of loading of HAR gaps of SE-EBG-RAs with dielectric slabs is also examined. Three different parametric studies are conducted on the antennas to demonstrate their particular features. Two proof-of-concept prototypes are fabricated and experimented to validate the idea and designs.

### 4.2.1 Introduction

By definition, an antenna is regarded as electrically small, if it meets  $ka < 1$  where  $a$  is the radius of the sphere circumscribing the antenna [27]. Moreover, in case the antenna is mounted on a PEC ground plane, the condition is much stricter and  $ka < 0.5$  is normally considered [26-28].

As described in Chap. 2, one way to achieve small antennas is to employ the EBG concept. Some published works focus on enforcing new boundary conditions by adding shorting pins [29], plates, or posts [30] along the structure of planar antennas. Similar efforts are also observed when an inverted-L antenna is turned into inverted-F antenna (IFA) or its planar version, Planar IFA with the aid of a shorting pin, a technique that brings about miniaturization [29] and flexibility in impedance matching [31].

Considering the potentials of shorting pins, and also noting exceptional rewards of the EBG concept, this section aims to exploit both ideas simultaneously. This feature results in novel planar EBG antennas with reduced ground plane size, which maintain a very high radiation efficiency and performance.

### 4.2.2 Expansion on the Theory of OC SE-EBG-RA

In Sec. 4.1 (also published in [17]), the concept of the OC EBG microstripline (MSL) with radiation properties was initiated, and a planar antenna with a small electrical footprint and high efficiency, called SE-EBG-RA, was introduced based on the concept. To elaborate on such an idea, this and the following sections scrutinize this antenna by expanding on its theory of operation, particularly finding its electrical length, setting parametric study on other versions of the antenna with different number of cells (as opposed to the version with only 3 cells in Sec. 4.1), and inspecting the effects of the ground plane size. Most significantly, the analytical view started here is used in the following section to develop the concept of SC SE-EBG-RA, which is the salient contribution of the current section. For a generally lossy fragment of TL, the input impedance was given by (4.1.5). This equation relates  $Z_{in}$  to  $Z_B$ , the line impedance,  $\gamma=\alpha+j\beta$ , the complex propagation constant associated with the waves traveling along the TL, and  $l$  is the fragment length. If this fragment is OC on one side, the input impedance can be written as [10]:

$$Z_{in}\Big|_{OC} = Z_B / \tanh \gamma l = Z_B \frac{1 + j \tanh \alpha l \tan \beta l}{\tanh \alpha l + j \tan \beta l} \quad (4.2.1)$$

If the TL is the EBG TL described in Sec. 4.1, which basically looks like a MSL periodically loaded by HAR gaps at electrically short distances, then  $Z_B$  is called the equivalent line impedance assigned to the loaded TL (known as the Bloch impedance). Fig. 4.2.1 shows the overall configuration of the EBG TL made by an array of patches on a PEC-backed substrate with tiny spacing. As in Sec. 4.1,  $\gamma$  and  $Z_B$  were analytically related to the cascade parameter of the Bloch unit cell, which were found by HFSS simulations of the cell and the Bloch theory (HFSS/Bloch method). At one specific electrical length,  $n\beta l=n\pi$  ( $l=n\lambda_g/2$ ), (4.2.1) can be simplified to:

$$Z_{in}\Big|_{OC} = R_{in} + jX_{in} = Z_B / \tanh \alpha l \quad (4.2.2)$$

Because  $Z_{in}$  is complex, in case  $X_{in}$  vanishes around a specific frequency,  $R_{in}$  can be matched to a 50Ω line. At this electrical length, the shortest possible  $l=\lambda_g/2$ , matching can be provided (an impedance transformer might be required) and the radiation is also high enough ( $\alpha$  is relatively high due to radiating gaps), and therefore, the OC EBG TL is regarded as a high efficiency antenna. The fact that SE-EBG-RA is a half-wavelength antenna like a microstrip patch antenna

is an important insight on top of the preliminary radiation effects introduced in Sec. 4.1 for a 3-cell OC antenna sample. Also, to ensure that regardless of the number of cells, the antenna still operates as expected with  $\lambda_g/2$  length, in Sec. 4.2.5, different versions with 2 to 6 cells will be presented and studied.

### 4.2.3 Concept of SC SE-EBG-RA

In a similar manner to Sec. 4.2.2, if a generally lossy fragment of TL is SC, the input impedance can be written as [10]

$$Z_{in} \Big|_{SC} = Z_B \tanh \gamma l = Z_B \frac{\tanh \alpha l + j \tan \beta l}{1 + j \tanh \alpha l \tan \beta l} \quad (4.2.3)$$

where at one specific electrical length, which is  $n\beta l = n\pi/2$  ( $l = n\lambda_g/4$ ), (4.2.3) is simplified to

$$Z_{in} \Big|_{SC} = Z_B / \tanh \alpha l \quad (4.2.4)$$

It is interesting that (4.2.4) is exactly the same as (4.2.2), but each one is valid for different electrical lengths, which means the resonance frequency ( $f_r$ ) at which each one can be matched to a  $50\Omega$  line are different. If a SC piece of the same EBG TL in Fig. 4.2.1 is specifically considered, then (4.2.4) shows that this piece can be matched (on the side opposite to the SC end), and at the same time due to the radiation from the gaps, the TL turns into a radiating SC planar antenna. However, the difference is that the electrical length of this new SC antenna is  $\lambda_g/4$  rather than  $\lambda_g/2$  for the OC case. To ensure that regardless of the number of cells, the SC version still operates with  $\lambda_g/4$  length, in Sec. 4.2.5, two SC antenna composed of 2 and 3 cells will be presented and studied. It is worth mentioning that if the gaps are removed (a thick MSL with no EBG cells),  $\alpha$  approaches zero as the line turns to a TL mostly guiding the power inside with very negligible radiation. Also,  $Z_B$  increases to  $Z_0$  (line impedance of a regular MSL with no gaps) because the series capacitances of the gaps, which naturally tend to drop the impedance ( $Z_B < Z_0$ ), are now removed.

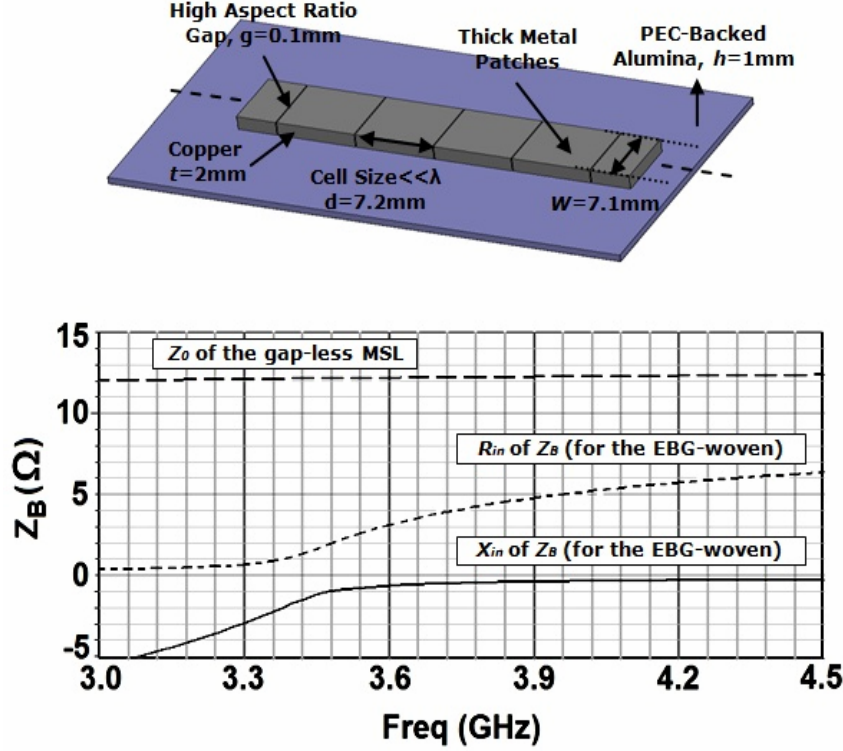


Fig. 4.2.1. 3D view of the EBG TL together with its Bloch line impedance,  $Z_B$  plotted versus frequency; for comparison, the line impedance of the same TL when gaps are removed is also included.

To show the effect of gaps on the line impedance, Fig. 4.2.1 compares the  $Z_B$  and  $Z_0$  for the unit cell dimensions depicted and shows the decrease in  $Z_B$ . Therefore, if there is no gap (no EBG cell), the increase in  $Z_B$  and the decrease in  $\alpha$  make (4.2.4) and (4.2.2) approach infinity which in turn makes matching the antenna to a  $50\Omega$  line impossible. This means that gaps are crucial to the expected operation of the SE-EBG-RA as they cause both radiation and allow matching. The related dispersion diagram is also given in Fig. 4.2.2.

To expand on the operation of SC and OC antennas from another perspective, it is noted that in general, a  $\lambda_g/2$  piece of TL images any load impedance exactly the same at its input. This means that if the piece is left open on one side, the input impedance should be infinity, while in case of the EBG TL, this infinite impedance is moderated by the effect of the radiation from gaps, as stated by (4.2.2). Similarly, a  $\lambda_g/4$  piece of TL will image any load impedance based on  $Z_0^2/Z_L$  (quarter-wave transformer). This means that a SC piece of TL should image the load  $Z_L=0$  again to infinity. Nonetheless, in case of the EBG TL, the effect of gaps modifies this high impedance and provides a finite impedance given by (4.2.4).

The fact that the SC version is  $\lambda_g/4$ , as opposed to the OC one with  $\lambda_g/2$ , demonstrates that the SC SE-EBG-RA brings about an antenna with considerably smaller size. Later on, in Table 4.2.1, where the SC/OC SE-EBG-RA performance is studied against the number of EBG cells, it will be shown that  $f_r$  of the SC version (with identical number of cells) is much lower compared to the OC counterpart. In Sec. 4.2.7, a 2-cell SC SE-EBG-RA is rendered which offers a matched antenna with a footprint as small as  $0.25\lambda \times 0.28\lambda$ , and at the same time, present a very high efficiency and maintained radiation.

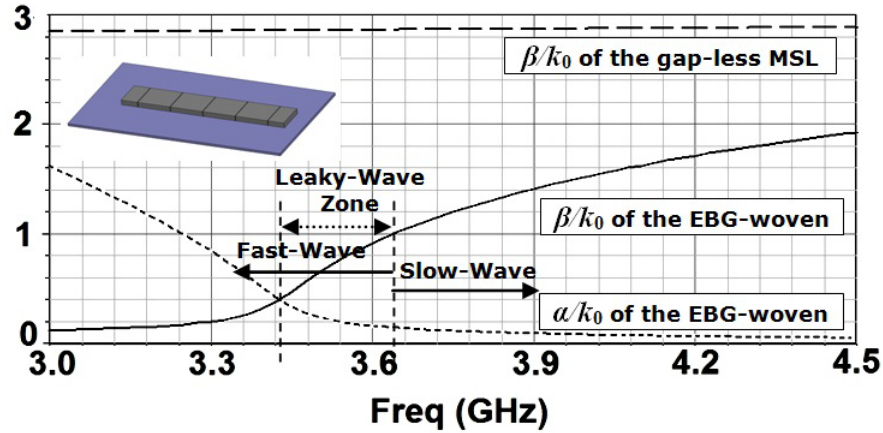


Fig. 4.2.2. The dispersion diagram by HFSS/Bloch method for the unit cell in Fig. 4.2.1, i.e. the normalized propagation constant ( $\alpha/k_0 + j\beta/k_0$ ) versus frequency ( $k_0$  is the free-space wavenumber); for comparison,  $\beta/k_0$  of the same cell with no gap is also included.

#### 4.2.4 Circuit Model for OC and SC SE-EBG-RAs

In chapter 6 of [10], it is shown that both SC  $\lambda_g/4$  long and OC  $\lambda_g/2$  long pieces of a generally lossy TL show a parallel  $RLC$  circuit behavior provided that BW is relatively low. In this case, the circuit elements and  $Q$  can be related to the line impedance,  $Z_0$ , resonance frequency,  $f_0$  ( $\omega_0 = 2\pi f_0$ ), the physical length,  $l$ , and  $\alpha$  along the TL:

$$R = Z_0 / (\alpha l) \quad (4.2.5)$$

$$C = \pi / (2m\omega_0 Z_0) \quad (4.2.6)$$

$$L = 1 / (\omega_0^2 C) \quad (4.2.7)$$

$$Q = \beta / (2\alpha) = \omega_0 RC = \pi / (2m\alpha l) \quad (4.2.8)$$

where  $m$  is 2 for the SC  $\lambda_g/4$  line and 1 for the OC  $\lambda_g/2$  one. Because the SC antenna is  $\lambda_g/4$  and the OC one is  $\lambda_g/2$ , (4.2.5) to (4.2.8) can be used to describe their resonance properties. In this

case,  $Z_0$  should be replaced by  $Z_B$ , the Bloch impedance associated with the EBG-TL line. In addition,  $l$  is the electrical length, which is  $\lambda_g/4$  for the SC case and  $\lambda_g/2$  for the OC case. It is deduced from (4.2.5) that  $\alpha$ , which represents the loss along the line, determines  $R$ , which will ultimately play the role of the antenna radiation resistance ( $R_r$ ). It should be noted that considering the ohmic efficiency, a small portion of  $R$  will be representing the ohmic loss ( $R_L$ ) before the input power is radiated totally, hence  $R=R_r+R_L$ . Moreover, (4.2.5) implies that to adjust  $R$  as close to as  $50\Omega$ ,  $Z_B$  and  $\alpha l$  should be adjusted deliberately. As for  $Q$ , (4.2.8) shows that  $\alpha l$  plays the main role, and the higher  $\alpha$  (the more radiation from gaps), the lower  $Q$ , which is equivalent to a higher BW. For example, for the 2-cell SC antenna in Table 4.2.1 and Fig. 4.2.4, (4.2.8) gives  $R=39.2\Omega$ ,  $C=7.17\text{pF}$ ,  $L=0.24\text{nH}$ , and  $Q=6.78$ . It is noted here that to find these values, first  $\alpha$  and  $Z_B$  have been found by the HFSS/Bloch.

#### 4.2.5 Number of Cells versus the Antenna Performance

Although the OC SE-EBG-RA introduced in Sec. 4.1 was based on three EBG cells, the antenna has the potential to be woven with different numbers of cells. Thus, this section is dedicated to gain knowledge on the performance of SC and OC SE-EBG-RAs with different numbers of cells. To perform this parametric study, two SE-EBG-RAs (OC and SC) with identical cells of Fig. 4.2.1 are considered, the number of cells is changed, and then antenna parameters are extracted by HFSS ( $\eta$  and  $f_r$ ) and HFSS/Bloch analysis (other parameters). Results are as in Table 4.2.1.

Table 4.2.1 Parametric study on characteristics of OC and SC SE-EBG-RA versus the number of unit cells in their structure (cells size as in Fig. 4.2.1); antennas are first matched to a  $50\Omega$  line by a  $\lambda_g/4$  transformer as  $R_m$  is not necessarily  $50\Omega$ .

# of Cells, $n$	$\beta/k_0$	$\alpha/k_0$	$\eta$ (%)	$R_m$ ( $\Omega$ )	$Q$ in (4.2.8)	$f_r$ (GHz)	Antenna Type
<b>OC SE-EBG-RA</b>							
2	2.13	0.04	82	105.5	26.63	4.88	Resonant
3	1.67	0.07	89	41.7	11.93	4.16	Resonant
4	1.35	0.1	89	19.75	6.75	3.84	Resonant
5	1.12	0.13	91	10.9	4.31	3.73	Resonant
6	0.98 <1	0.15	91	7.02	3.27	3.63	Leaky-Wave
<b>SC SE-EBG-RA</b>							
2	1.35	0.1	82	38.6	6.75	3.84	Resonant
3	0.96 <1	0.16	87	13.2	3	3.62	Leaky-Wave

As seen, for both SC and OC antennas, as  $n$  increases,  $f_r$  decreases,  $\eta$  slightly increases,  $R_{in}$  drops, and  $\alpha l$  increases. The last one is equivalent to an increased  $\eta$  with higher  $\alpha$ , and more radiation. In addition, it is observed that  $Q$ , which is calculated from (4.2.8), will decrease against increasing  $n$ . This behavior implies that the antenna, which is in fact a type of resonator, is capable to show a higher BW, if made out of more unit cells. Comparing  $Q$  in the OC and SC sections of Table 4.2.1, it is deduced that the SC versions have generally smaller  $Q$  (larger BW) although they have less cells. Specifically comparing the 3-cell SC antenna with the 6-cell OC one shows that they have roughly the same BW while  $f_r$  is about the same as well. This means that the one with fewer cells will become a smaller antenna with the same BW as the other. It is noted that, as in Table 4.2.1, this is a significant reward at the expense of only 4.4% less  $\eta$ .

Another important point reflected in Table 4.2.1 is that as  $n$  grows,  $\beta/k_0$  drops and approaches the boundary value of 1. As described in [32-33] and shown in Fig. 4.2.2, this is the point at which the cells are operating in leaky-wave mode, and therefore, the antenna belongs to the leaky-wave antennas family, as opposed to the resonant antennas family. An interesting observation with this condition is that the waves travel along the antenna axis faster than in the free-space above the antenna, which causes the fields to leak and the direction of the ensuing radiation to be dependent on the frequency. This fact makes the E-plane pattern (ZY plane in Fig. 4.2.3) squint towards the OC/SC end and scan with frequency as well. Obviously, in case the broadside radiation is desired, this condition should be avoided. Such “scanning” antennas based on the proposed HAR EBG cells are introduced and discussed in Sec. 5.1. As for other values of  $n$ , in case miniaturization is the main demand, the smallest  $n$  (defined in Table 4.2.1) should be used. On the contrary, if  $\eta$  and gain are the most important factors, and also, if there is no restriction on the ground plane, the size can be enlarged to obtain the most radiation, and then the largest possible  $n$  should be chosen. As an example, the 5-cell OC antenna in Table 4.2.1 is chosen and analyzed numerically. The corresponding radiation pattern, gain at broadside direction, and 3D view with detailed dimensions are rendered in Fig. 4.2.3. As observed, similar to the 3-cell antenna in Sec. 4.1, the radiation pattern is still broadside and the antenna is highly efficient. As seen in Table 4.2.1, the 5-cell version is even more efficient and more wideband than the 3-cell version (the one presented in Sec. 4.1) however at the expense of slightly longer physical length to accommodate two extra cells. The  $f_r$  found by HFSS is 3.73GHz which is only 0.8% different from 3.70GHz, found by (4.2.2), and reported in Table 4.2.1.

It is noted that comparing the 2-cell version for both OC and SC cases in Table 4.2.1 along with a look back at (4.2.8) reveals an interesting point. As seen,  $f_r$  of the SC one is by far lower while its  $al$  is  $\sim 2$  times bigger at resonance. As a rough estimate, (4.2.8) states that an increase in  $al$  can increase BW. This means that the 2-cell SC SE-EBG-RA (as compared to the 2-cell OC one) is a miniaturized antenna with a compensated and maintained BW due to having a bigger  $al$ .

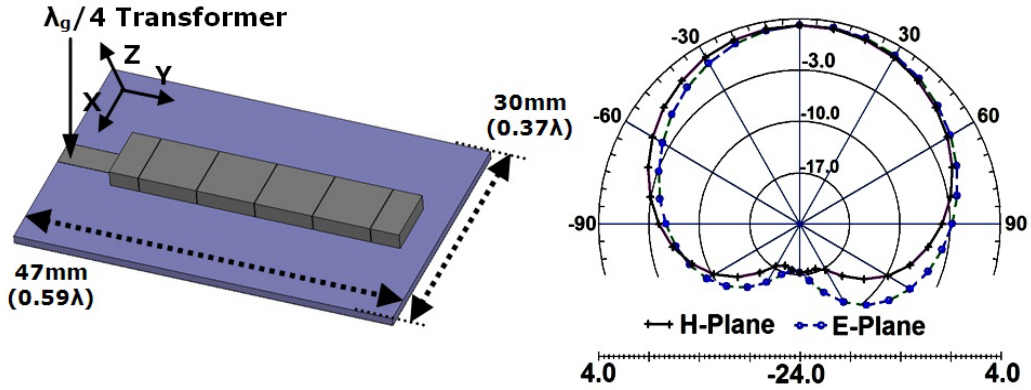


Fig. 4.2.3. 3D view of a 5-cell OC SE-EBG-RA and its radiation pattern; the input transformer is 3.3mm wide, 7.34mm long, and 30 $\mu$ m thick; cell dimensions are provided in Fig. 4.2.1; BW=2.6% and  $G_r$ =3.12dBi.

Another point deduced from Table 4.2.1 is that for all the antennas, regardless of the number of cells, the total electrical length is  $\lambda_g/2$  for OC versions and  $\lambda_g/4$  for SC ones, where the group wavelength,  $\lambda_g$ , is  $\lambda_0/(\beta/k_0)$  and  $\lambda_0$  is calculated at  $f_r$ . These results are in agreement with what was analytically predicted in Sec. 4.2.2 and Sec. 4.2.3. To verify, Fig. 4.2.4 plots the surface current distribution on the ground plane of 6-cell and 2-cell OC antennas and also a 3-cell SC antenna (candidates from Table 4.2.1). In Fig. 4.2.4 (a) and (b), the peak at center and minimum on both sides (symmetrical current) confirms that the antennas are  $\lambda_g/2$  long. Also, in Fig. 4.2.4 (c), the peak at SC point and minimum at the feed point confirms that the antenna is  $\lambda_g/4$  long.



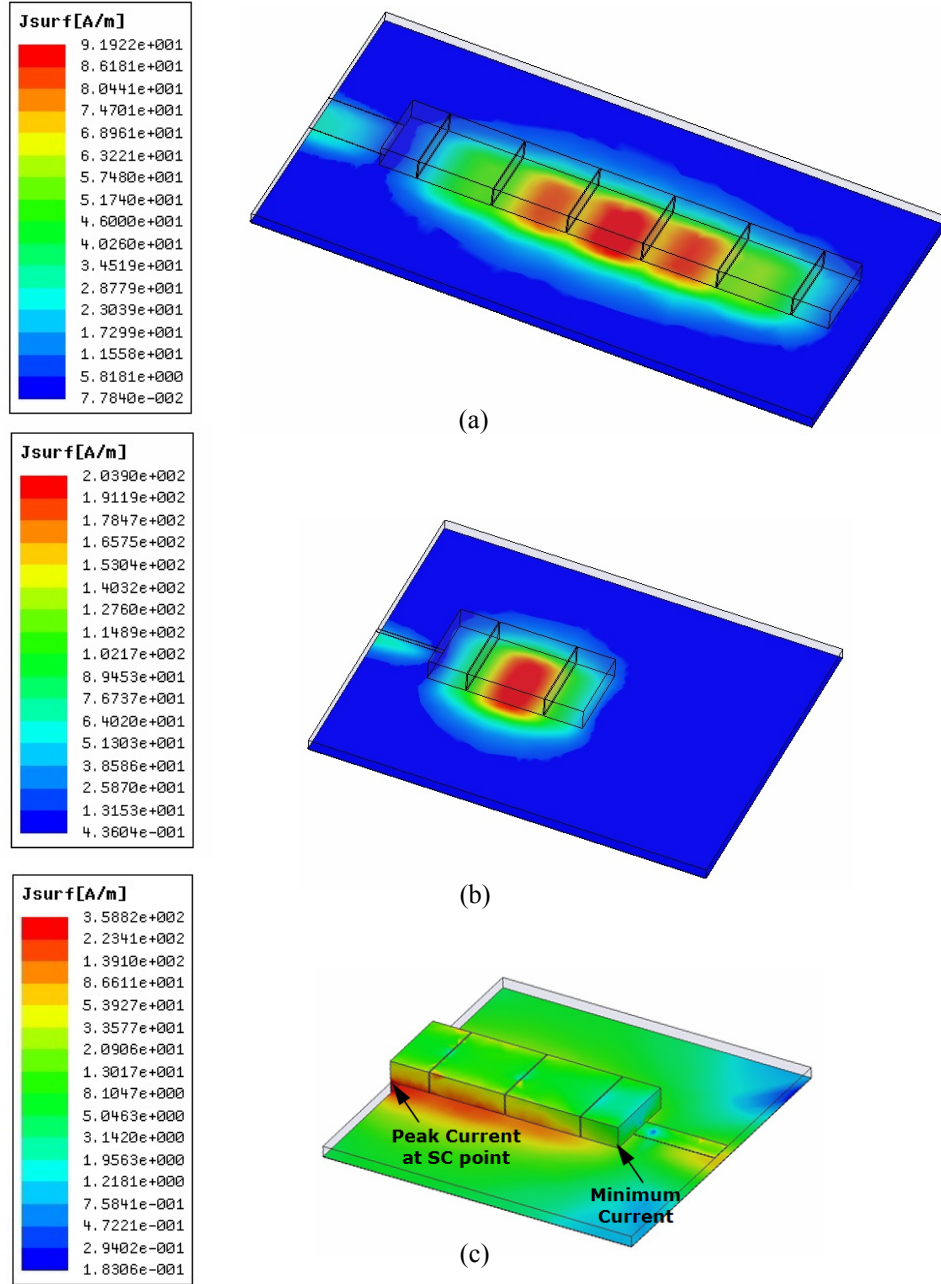


Fig. 4.2.4. Magnitude of the current on the ground plane, demonstrating the actual electrical length of the antenna, a) 6-cell OC SE-EBG-RA, b) 2-cell OC-SE-EBG-RA, c) 3-cell SC SE-EBG-RA; antennas are as in Table 4.2.1.

#### 4.2.6 Parametric Study on the Effect of Thickness

To highlight the advantages offered by thickening the metal top layer, a 3-cell OC SE-EBG-RA is considered and its properties are compared for a range of different thicknesses, as shown in Table 4.2.2. From one standpoint, shifting the resonance of an antenna to lower frequencies is

considered antenna size reduction [34]. According to Table 4.2.2, this reduction is exactly what is obtained by thickening the metal layer. Apart from this reward,  $\eta$  is maintained and even slightly enhanced while the antenna is shrinking. It is interesting to remind that in general, realization of electrically small antennas leads to degradation of both BW and  $\eta$  [27], while in case of SE-EBG-RA, this downside is compensated by the effect of thickness. As in Table 4.2.2, switching from aspect ratio (AR) of 1 to 40, the antenna electrical footprint (the physical footprint is fixed) decreases by half and  $\eta$  increases by  $\sim 10\%$ . A similar effect is expected to be observed for a SC SE-EBG-RA as well. The result implies that there is the possibility to exchange the vertical dimension (the thickness) for a smaller footprint and improved efficiency, while maintaining a relatively thin vertical profile. It is noted that even for the thickest metal layer in Table 4.2.2 (4mm), the overall antenna thickness does not exceed 5mm ( $\lambda/16.5$ ).

Table 4.2.2 Parametric study on properties of a 3-cell OC SE-EBG-RA versus the thickness of its top metal layer. Antennas are matched to a  $50\Omega$  line by a proper  $\lambda_g/4$  transformer. Parameters are found by HFSS; the ground plane size is 30mm $\times$ 40mm;  $G_r$  stands for the realized gain; unit cell is as in Fig. 4.2.1.

$t$ (mm)/AR	$\eta$ (%)	$G_r$ (dBi)	Electrical Footprint	Footprint Shrinkage (%)	Matching Freq (GHz)
4/40	88.5	2.37	$0.49\lambda \times 0.37\lambda$	51.1	3.65
3.5/35	88.5	2.65	$0.5\lambda \times 0.38\lambda$	48.8	3.75
3/30	87.7	2.69	$0.52\lambda \times 0.39\lambda$	45.3	3.89
2.5/25	87.2	3.09	$0.53\lambda \times 0.40\lambda$	42.9	4.00
2/20	87.0	3.45	$0.55\lambda \times 0.42\lambda$	37.7	4.16
1.5/15	85.1	3.87	$0.58\lambda \times 0.44\lambda$	31.2	4.33
1/10	82.7	4.29	$0.61\lambda \times 0.46\lambda$	24.4	4.55
0.5/5	82.7	4.97	$0.66\lambda \times 0.49\lambda$	12.8	4.89
0.1/1	80.8	5.18	$0.70\lambda \times 0.53\lambda$	0.0	5.22

Another important point indicated in Table 4.2.2 is that the increase in  $\eta$  occurs simultaneous with the decrease in  $G_r$ . This decrease shows that as the thickness is growing, the radiation from antenna aperture ( $R_r$ ) is reducing, a behavior which can be related to the fact that the electrical size of the whole antenna aperture is dropping. However, to explain why  $\eta$  does not deteriorate with less radiation, it is reminded that  $\eta$  is not only dependent on the  $R_r$ , but also on the loss ( $R_L$ ) so that for small antennas  $\eta = R_r / (R_r + R_L)$  holds. From this relation, it can be concluded that to simultaneously have an increasing  $\eta$  and decreasing  $R_r$ ,  $R_L$  must be decreasing when the thickness is growing.

The last two studies demonstrate the high efficiency nature of the OC and SC versions, which can be attributed to the concurrent performance of the EBG cells (able to enhance radiation) and the thick metal traces (able to mitigate loss). In addition, it is observed that the thickness has an extra contribution, that is to provide very narrow gaps with very tall sidewalls, i.e. HAR gaps, introducing a lot of parallel plate capacitance and therefore reducing  $f_r$  considerably. It is demonstrated that thick traces and HAR gaps bring about two simultaneous advantages of reducing the loss and reducing the resonance frequency. Moreover, the thickness can serve as an extra adjustable parameter, which can provide additional degrees of freedom during the antenna design process. It is emphasized that the term "gain" used throughout the thesis refers to the realized gain ( $G_r$ ), which includes the effect of efficiency, directivity, and input matching quality.

#### 4.2.7 Ground Plane Size versus Performance

In this section, the performance of the SC SE-EBG-RA is studied against the size of the ground plane. To form such a study, a 2-cell SC SE-EBG-RA with the cells used in Fig. 4.2.1 is considered and the size of its ground plane is changed over a range, in two different dimensions. Afterwards, each ensuing antenna is numerically analyzed by HFSS to find its  $\eta$  and  $G_r$ . The results are listed in Table 4.2.3.

Table 4.2.3 Parametric study on  $G_r$  and  $\eta$  of a 2-cell SC SE-EBG-RA versus its ground plane size in XY dimensions. All antennas are matched to a 50 $\Omega$  line by  $\lambda_g/4$  transformers; cell dimensions are as in Fig. 4.2.1.

$L$ (mm)	$W$ (mm)	$\eta$ (%)	$G_r$ (dBi)	Matching Freq (GHz)
$W$ is fixed at 30mm				<div><math>\sim 3.80</math> with negligible change (<math>\Delta &lt; 1\%</math>)</div>
22.17	30	88.4	1.5	
27.17		88.4	2.14	
32.17		87.5	2.48	
42.17		87.2	3.78	
55.17		79.1	4.32	
70.17		77	4.33	
$L$ is fixed at 22.17mm				
22.17	20	83	0.68	
	30	82	1.5	
	50	79	2.23	
	70	79	2.95	
$L$ & $W$ are fixed at $\sim 0.88\lambda \times 0.88\lambda$				
70.17	70	76	4.89	

As observed, as the ground plane enlarges, the resonance frequency remains almost fixed and  $\eta$  drops. It is also seen that  $G_r$  increases (to some extent), but the rate of this increase gradually drops and is ultimately limited at a certain level. For example, the antenna shown in Fig. 4.2.5 (a) is the same antenna in Fig. 4.2.5 (b) with a relatively large ground plane of  $0.58\lambda \times 0.58\lambda$ , which shows a  $G_r=4.47\text{dBi}$  as compared to  $G_r=0.68\text{dBi}$  for  $0.25\lambda \times 0.28\lambda$  ground size. However, simulations show that beyond this size, the increase in  $G_r$  will be negligible. This is connected to the fact that metal edges of the plane are not illuminated enough by the fields excited on gap apertures. To demonstrate this situation further, in the section 3 of the Table 4.2.3, the same antenna in Fig. 4.2.5 (a), with even much larger ground plane of  $0.88\lambda \times 0.88\lambda$  is considered, for which the associated  $G_r$  is 4.89dBi. As seen, although a considerable size change is applied to ground plane, (from  $0.58\lambda$  to  $0.88\lambda$ ), the enhancement in  $G_r$  is only 0.42dB.

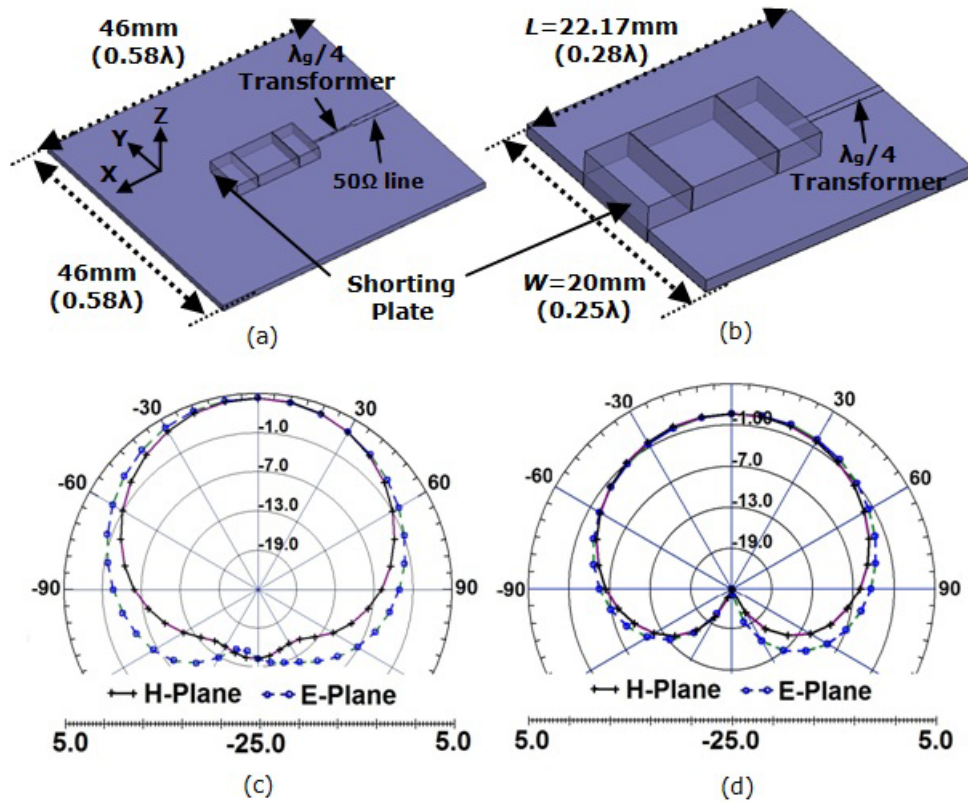


Fig. 4.2.5 A 2-cell SC SE-EBG-RA a) with a relatively large ground plane of  $0.58\lambda \times 0.58\lambda$ , b) with highly truncated ground plane of  $0.25\lambda \times 0.28\lambda$ , c) radiation pattern for Fig. 4.2.5 (a), d) radiation pattern for Fig. 4.2.5 (b); the transformer dimensions for both antennas are 0.35mm and 8mm; the 50Ω feedline is 0.92mm wide and 8mm long; all thin traces are 30μm thick MSL; cell dimensions are as in Fig. 4.2.1.

It is noted that the proposed 2-cell SC SE-EBG-RA in Fig. 4.2.5 (b) has a very truncated ground plane of  $0.25\lambda \times 0.28\lambda$ , and simultaneously, its resonance frequency, efficiency, and radiation properties are maintained. Such features are typically offered by planar antennas like patch, when placed on an EBG ground plane [e.g. 30]. However, the situation is slightly different for the proposed EBG structures because, as in Fig. 4.2.5 or Fig. 4.2.6 (b), the top metal layer is woven by EBG cells so that it seems that the planar antenna (as the main radiator) and the EBG ground plane are both integrated into a single-layer easy-to-excite structure. Another similarity with most EBG antennas is that the thickness, including the substrate and metal layer, is electrically thin (at  $\sim \lambda/27$ ). As seen in Fig. 4.2.5 (b), for a small volume of  $0.25\lambda \times 0.28\lambda \times \lambda/27$ , the front-to-back ratio (F/B) is satisfactory and the radiation pattern remains broadside (Fig. 4.2.5 (d)). This small size, BW of 1.34%, realized gain of 0.68dBi, and the simple feeding method are of distinguishing features of the antenna in Fig. 4.2.5 (b). The HFSS-simulated  $f_r$  of 3.84GHz for Fig. 4.2.5 (b) is only 0.5% different from 3.82GHz, which is found by (4.2.4) (see Table 4.2.1). This is estimate an accurate, considering the severe truncation of the cells to *only two*, while  $Z_B$  and  $\alpha$  in (4.2.4) are found by HFSS/Bloch methods, requiring an infinite number of cells.

#### 4.2.8 SE-EBG-RA versus Rectangular Microstrip Antenna

In an effort to highlight benefits of proposed antennas, in this section, performances of a SE-EBG-RA and a microstrip patch antenna are compared. Fig. 4.2.6 shows a 5-cell OC SE-EBG-RA and a microstrip antenna, both matched to a  $50\Omega$  line using quarter-wave transformers. To provide a logical comparison, the substrate material (alumina) and thickness (1mm or  $\lambda/80$ ) and the ground plane footprint ( $50 \times 50$ mm or  $0.62\lambda \times 0.62\lambda$ ) are set to be the same, as in Fig. 4.2.6.

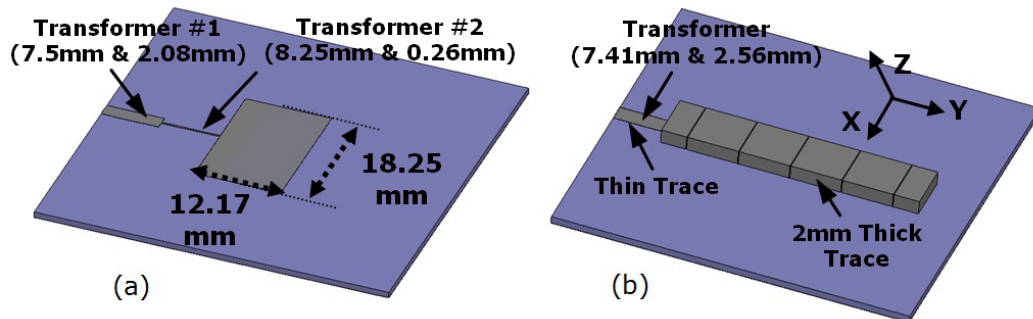


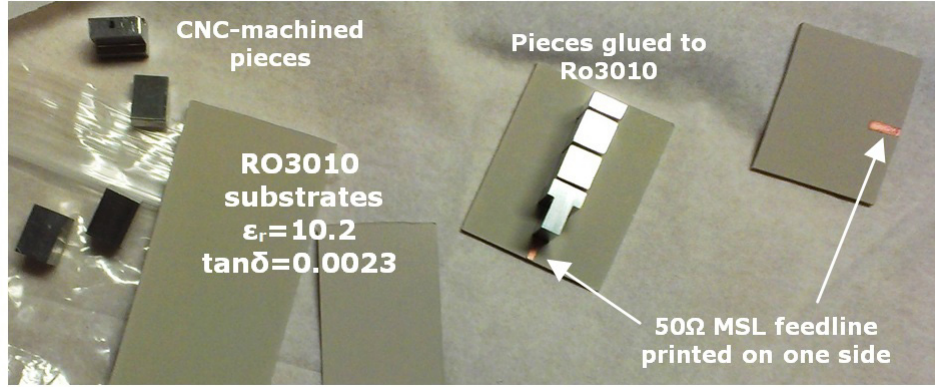
Fig. 4.2.6 Comparison between the performance of a microstrip patch antenna and an OC SE-EBG-RA with 5 cells, both matched at 3.73GHz; ground planes are both 50mm $\times$ 50mm; substrate material and thickness for both antennas and the unit cell of Fig. 4.2.6 (b) are given in Fig. 4.2.1; thin traces are 30 $\mu$ m thick MSL.

The unit cell is the one considered in Table 4.2.1 and depicted in Fig. 4.2.1. Considering that  $f_r$  for Fig. 4.2.6 (b) is 3.73GHz, the patch in Fig. 4.2.6 (a) is given the typical width-to-length ratio of 1.5 [35] so that it shows a reasonable  $Q$  and then is adjusted in length so that it resonates at 3.73GHz. The related dimensions are given in Fig. 4.2.6 (a). The associated patch edge resistance is  $\sim 315\Omega$ , which is relatively high due to the low bandwidth nature of patch antennas. In order to have this impedance matched to a  $50\Omega$  line, at least two  $\lambda_g/4$  transformers with the dimension in Fig. 4.2.6 (a) are required. The BW,  $\eta$ , and gain calculated by numerical analysis are 0.8%, 66%, and 4.58dBi, respectively. On the contrary, the 5-cell OC SE-EBG-RA requires only one transformer (as the edge impedance is  $10.9\Omega$ ), and the associated parameters are BW=1.9%,  $G_r=5.3\text{dBi}$ ,  $\eta=91\%$ . Therefore, by comparison, for the SE-EBG-RA, BW is  $\sim 240\%$  larger, the realized gain is 0.72dB more, and the ohmic efficiency is 38% better. It is worth noting that these rewards are offered while the electrical footprint and substrate thickness, and also the dielectric material are identical. Another advantage of the SE-EBG-RA is that the width of its top metal layer is by far smaller than the width of the patch in Fig. 4.2.6 (a). As observed, the unit cell used in Fig. 4.2. (b) and Fig. 4.2.1 is 7.1mm wide, which is significantly smaller than 18.25mm in Fig. 4.2.6 (a).

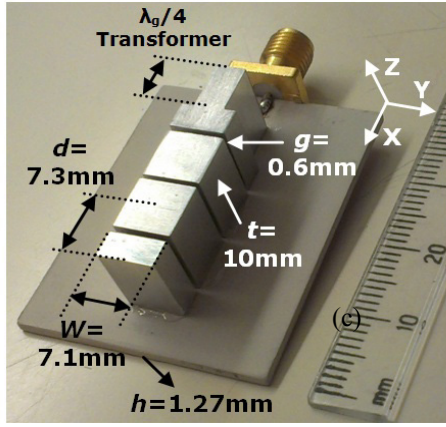
#### 4.2.9 Prototyping and Experimental Verification

In order to validate the theory and designs presented in previous sections, in this section two antenna samples are designed and fabricated to serve as proof-of-concept prototypes. The unit cells of these prototypes are deliberately thickened to 10mm so that with 0.6mm gaps, the aspect ratio remains high ( $AR=10/0.6=16.67$ ), but not unnecessarily restricting. This strategy simplifies the fabrication process for the HAR gaps of the antenna prototypes. Fig. 4.2.7 (b) shows the first antenna, which is a 3-cell OC SE-EBG-RA. Also, as in Fig. 4.2.7 (d) and (e), the second antenna is a 2-cell SC SE-EBG-RA.

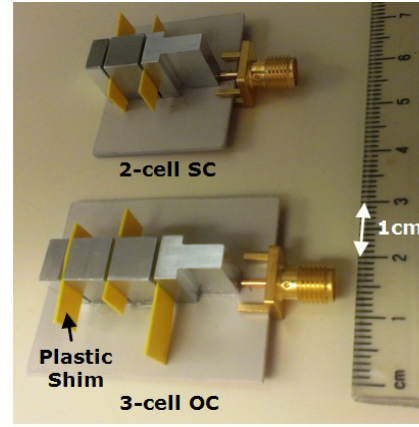




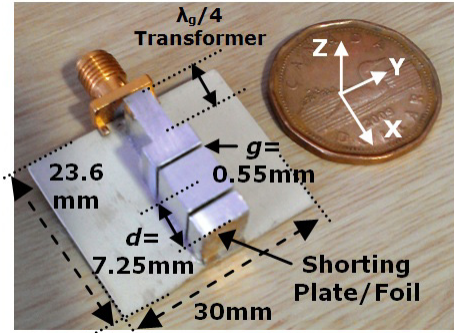
(a)



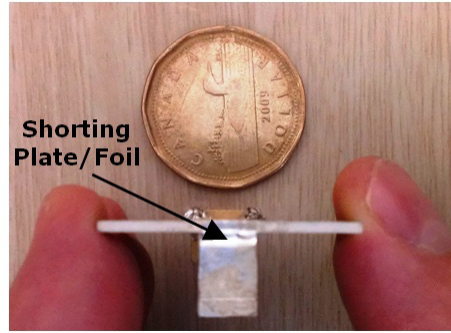
(b)



(c)



(d)



(e)

Fig. 4.2.7. Fabrication process of SC and OC SE-EBG-RAs serving as proof-of-principle prototypes; dimensions of  $\lambda_g/4$  transformers are 6.68mm & 3.9mm for the OC antenna and 7.4mm & 3.7mm for the SC one.

As observed, both antennas have a  $\lambda_g/4$  impedance transformer at the input, with the same thickness as the cells, but with adjusted width to provide the desired transformation ratio. The dimensions of transformers and the unit cell are given in Fig. 4.2.7 (b) and (d). As depicted in Fig. 4.2.7 (a), in order to realize the antennas, thick metal pieces of the top layer are first CNC-

machined to size, and then are glued on the top of a RO3010 Rogers substrate (the copper layer on one side of the substrate is already etched). As in Fig. 4.2.7 (c), plastic shims of 0.5mm thickness provide the spacing needed between pieces and are removed when the glue is hardened. In practice, after removing the shims, the measured gap sizes achieved are 0.55mm for the SC antenna and 0.6mm for the OC one. It is noted that as shown in Fig. 4.2.7 (d) and (e), the SC condition for the first prototype is realized by a piece of metal foil, shorting the end of the last cell to the ground.

After preparing the prototypes, the realized gain,  $G_r$ , at broadside for the 3-cell OC SE-EBG-RA has been measured by the three-antenna-measurement (TAM) method [36]. The TAM is explained in more detail in Appendix A. The method is used to measure the gain of the antenna under test (AUT) when there is no standard calibrated antenna available. However, to carry out such a method, two extra antennas with unknown gains are required that must be able to operate at the same frequency of the AUT. For this purpose, two different planar antennas with broadside radiation pattern have been designed by HFSS and fabricated. Fig. 4.2.8 shows the AUT and the extra antennas. In addition, Fig. 4.2.9 shows a photo of the test setup used for the TAM process.

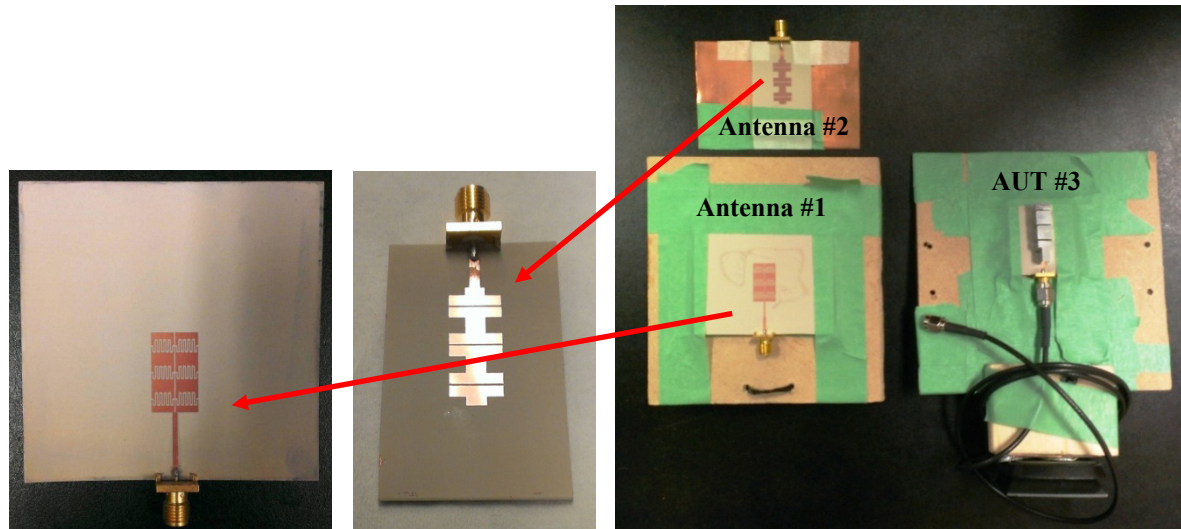


Fig. 4.2.8. AUT (Fig. 4.2.7 (b)) and the two extra fabricated antennas, mounted on thin plywood sheets, and prepared for the radiation pattern and three-antenna measurement implementation.



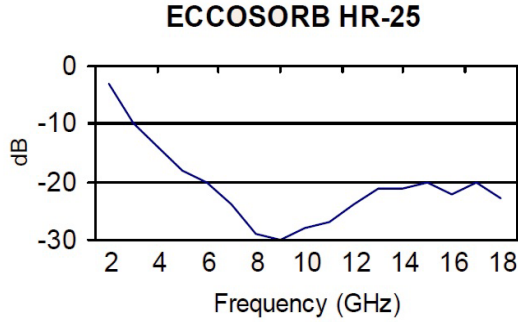


Fig. 4.2.9. Absorbers and stands in use during the measurement.

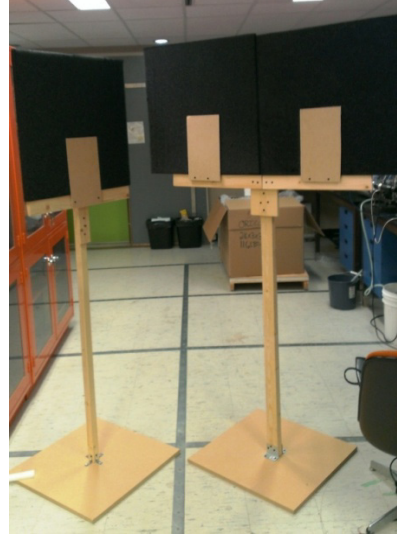
Another condition for the TAM method is that the measurement must occur in an anechoic condition. In the absence of a standard anechoic chamber, attempts have been made to control the echoes by a number of microwave absorbers surrounding the test setup. Fig. 4.2.10 shows the absorbers used during the measurement. Also, the wooden stand used to hold and position the absorbers and the typical reflectivity of the EM waves from the absorbers is reflected in Fig. 4.2.11.



Fig. 4.2.10. ECCOSORB® HR should be bonded to a metal surface for optimal performance; aluminum foil is applied on the backside.



(a)



(b)

Fig. 4.2.11. a) Typical reflectivity of ECCOSORB®HR-25 absorbers supplied by Emerson & Cuming Microwave Products Inc (<http://www.eccosorb.com>); results may vary depending on application, b) absorbers mounted on custom made wooden stands with adjustable heights.

The outcome of the measurement is listed in Table 4.2.4, where measured gains (by TAM) and simulated gains (by HFSS) are compared. As seen, the gain difference ( $\Delta$ ) for all antennas is satisfactorily less than 0.88dB. In addition to  $G_r$  at broadside, the radiation pattern for the 3-cell OC prototype is also measured, as shown in Fig. 4.2.12. The simulated E- and H-plane patterns are also included in Fig. 4.2.12 for better comparison. The  $\text{dB}|S_{11}|$  for both fabricated samples of Fig. 4.2.7 (SC and OC) will also be included in Fig. 4.2.15 later.

It has been observed that at broadside direction, both antennas behave as expected due to the effective application of absorbers in suppressing echoes. As a result, as seen in Table 4.2.4, gain results, which are measured when none of the antennas are rotated, are satisfactory. However, during the test, it is observed that as the AUT is rotated, uncalibrated reflections gradually become significant. As seen in Fig. 4.2.12, especially beyond  $\pm 25^\circ$  from the main lobe, echoes start causing cancellations/nulls.

Table 4.2.4 Comparison between the gain obtained by the Three-Antenna-Measurement method and HFSS at 3.99GHz for the AUT and the two other antennas fabricated as reference antennas.

Antennas	$G_r$ (dBi)		
	HFSS	TAM	$\Delta$ (dB)
Planar Antenna #1	5.35	4.47	-0.88
Planar Antenna #2	4.06	3.77	-0.29
SE-EBG-RA, AUT #3	3.9	3.17	-0.73

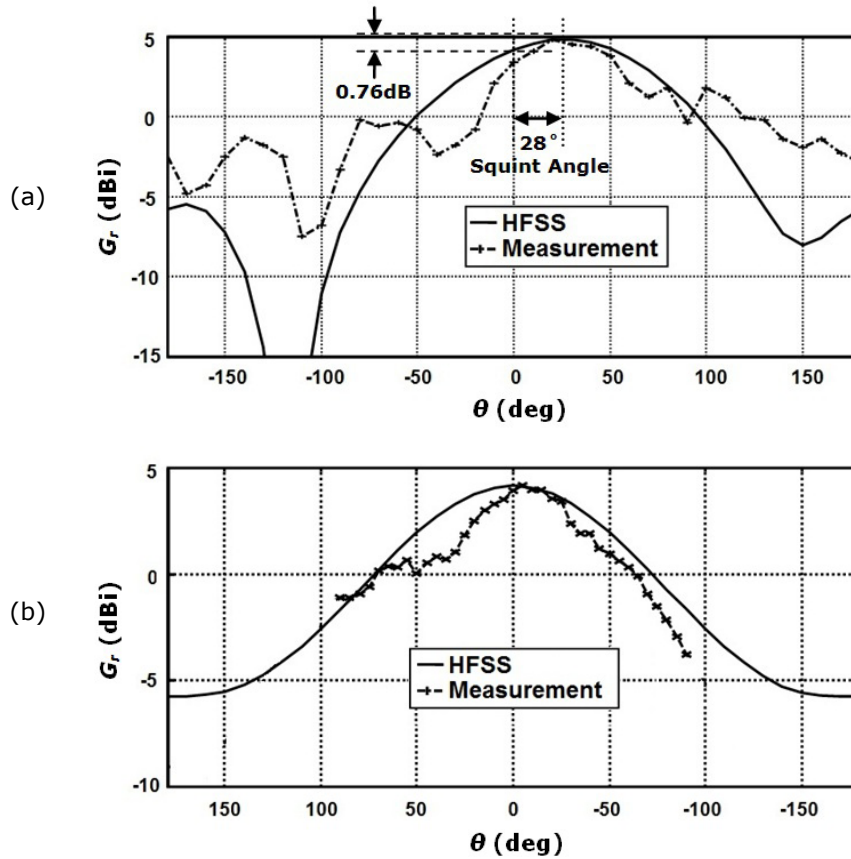


Fig. 4.2.12. Measured and simulated radiation patterns for the fabricated 3-cell OC SE-EBG-RA; a) E-plane, i.e.  $\phi=0^\circ$ , b) H-plane, i.e.  $\phi=90^\circ$  (XYZ axes are as in Fig. 4.2.7 (b));  $f_r=3.99$ GHz.

The fact that the gains measured for all three antennas involved in TAM agree with the full-wave simulations, the fact that the measured E-plane pattern is  $28^\circ$  squinted like the simulated pattern (see Fig. 4.2.12 (a)), and also that the measured E-plane pattern has a null (at  $105^\circ$ ) quite close to what HFSS reports (at  $120^\circ$ ) are evidences that demonstrate the success of

measurements, and therefore, the credibility of the HFSS modeling/simulations. Another measurement performed on one of the prototypes is to estimate  $\eta$  using the Wheeler cap method [37], which is described in more detail in Appendix B. As in Fig. 4.2.13, a rectangular Wheeler cap is made and mounted on the 3-cell SE-EBG-RA.

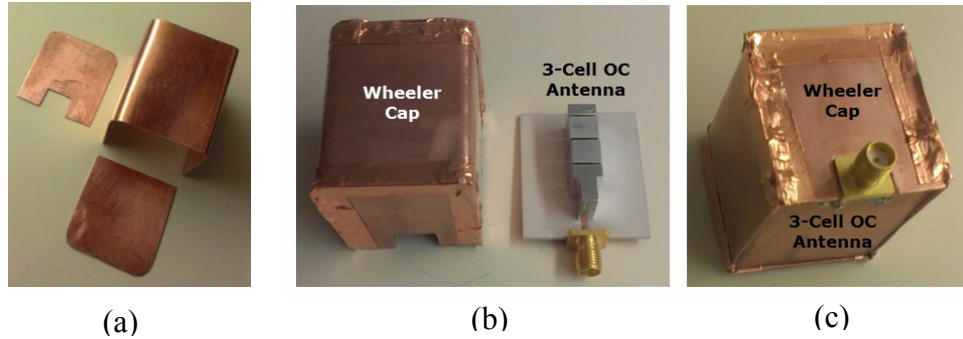


Fig. 4.2.13. Antenna efficiency measurement using Wheeler cap method, a) the parts cut out of a copper sheet, b) assembled cap and the SE-EBG-RA prototype, c) the cap mounted on the antenna and sealed using metal foil.

The efficiency calculated by HFSS at resonance (4.07GHz) is 94% and the one measured by the Wheeler cap method is  $\sim 87\%$ . It is noted that when repeating the measurement 10 times, the uncertainty observed has been within  $\pm 5\%$ . It should be noted that although the Wheeler method is generally accurate for most antennas, its accuracy could be dependent on the AUT circuit model. As described in Appendix B, this method is applicable to small antennas with a series model in which radiation resistance is in series with the loss resistance. As described before, the SE-EBG-RA has a parallel  $RLC$  model; however as the measured antenna has a  $\lambda/4$  impedance transformer, the circuit model at the antenna feed point (after transformation) become series.

As seen, the measured efficiency is 8% lower than the simulated one. This can be first attributed to the  $\sim 6\mu\text{m}$  roughness on the surface of machined metal pieces, and second to the fact that HFSS simulation usually results in higher efficiency than expected.

#### 4.2.10 Effects of Dielectric Slab Loading of HAR Gaps

To demonstrate further miniaturization, here HAR gaps of the SC and OC prototypes in Fig. 4.2.7 are loaded by thin dielectric slabs. The slabs material is the same RO3010 used as substrate with 0.25mm thickness and are inserted in the gaps as demonstrated in Fig. 4.2.14. Fig. 4.2.15 compares the matching quality of the two antennas with and without the slabs and shows a

significant drop in resonance frequencies due to dielectric loading. This electrical size reduction occurs while efficiencies are well maintained, as shown by the results in Table 4.2.5. As seen, for SC and OC cases, respectively, loading introduces  $\sim 13\%$  and  $\sim 15\%$  reduction in  $f_r$  without deteriorating the radiation pattern and  $\eta$ , while the matching quality is also retained well. There is relatively more difference ( $\sim 8\%$ ) between the measured and simulated results in the unloaded SC case, which could be due to the tolerance in gap sizes when fabrication the antenna.

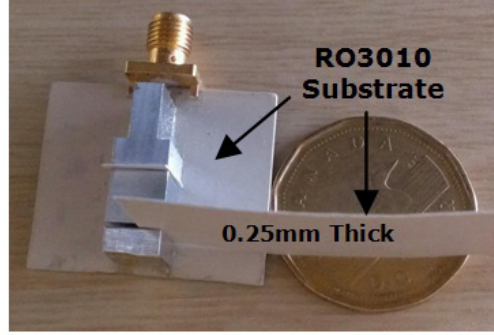


Fig. 4.2.14 Demonstration of dielectric slab loading of the SC SE-EBG-RA.

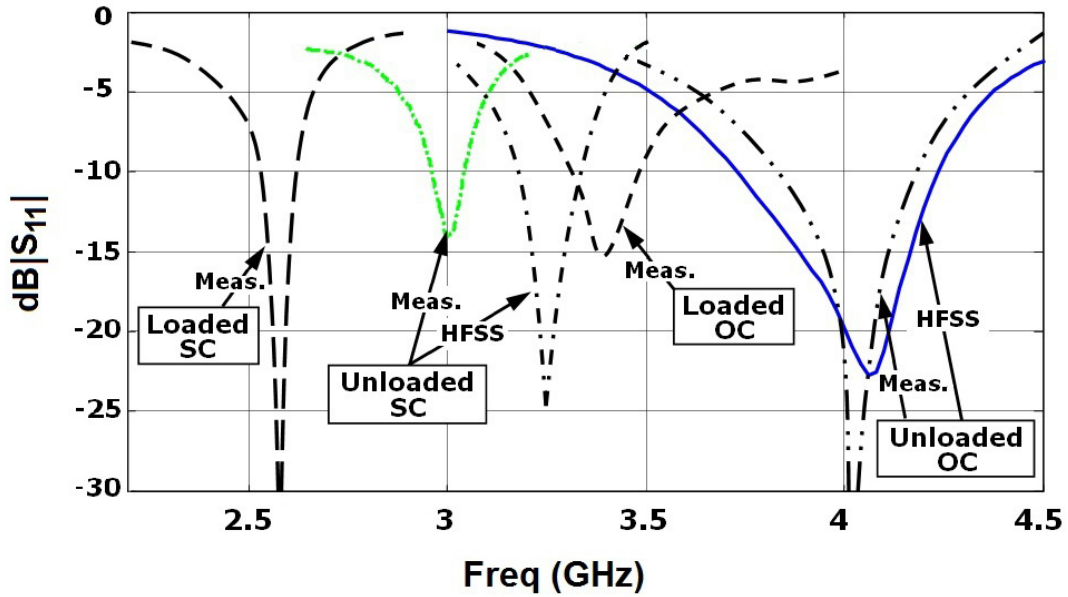


Fig. 4.2.15 Comparison of  $\text{dB}|S_{11}|$  for the fabricated 3-cell OC and 2-cell SC SE-EBG-RAs with and without RO3010 slabs ( $\epsilon_r=10.2$ ).

Fig. 4.2.16 compares the simulated radiation patterns of prototypes in the E-plane. As seen, not only do the radiation patterns roughly remain similar to unloaded versions (broadside



radiation), but also the F/B slightly increases for the OC antenna. Moreover, the slight squinting angle, i.e. the  $28^\circ$  orientation of E-plane pattern to the right in Fig. 4.2.8 (a) and Fig. 4.2.16, is reduced to  $9.5^\circ$ , as addressed in Table 4.2.5.

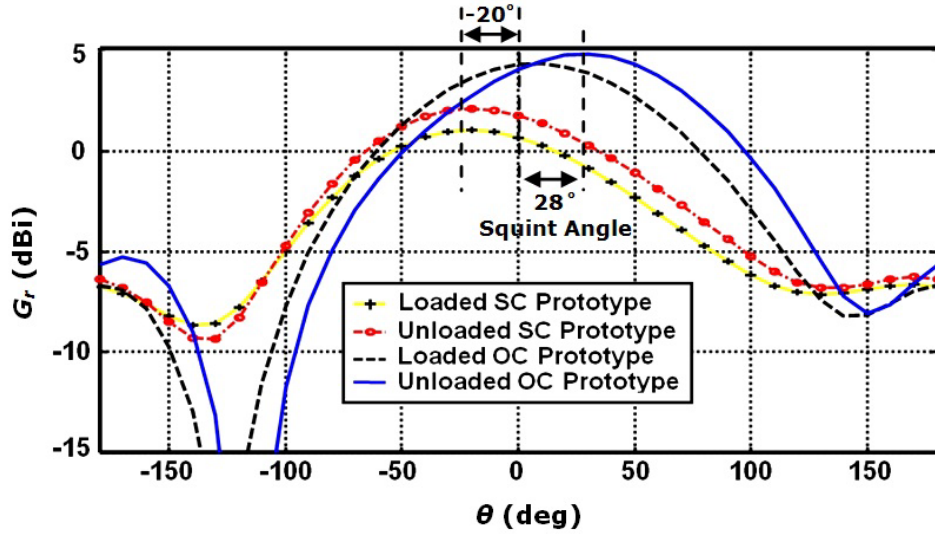


Fig. 4.2.16 Comparison between E-plane radiation patterns of the fabricated antennas in Fig. 4.2.7, with and without slabs in the gaps; H-plane radiation patterns are all symmetrical and similar to the HFSS result in Fig. 4.2.8 (b).

Table 4.2.5 Properties of antenna prototypes in Fig. 4.2.7, with and without slabs in the gaps, as demonstrated in Fig. 4.2.14. Results are based on HFSS simulation.

OC antenna XY size is 37.5mm×30mm & SC antenna XY size is 23.6mm×30mm						
F/B (dB)	$G_r$ (dBi)		$\eta$ (%)	BW (%)	$f_r$ (GHz)	Antenna Electrical Size XYZ
	Broadside ( $\theta=0^\circ$ )	Squinted From Broadside ( $\theta\neq0^\circ$ )				
Unloaded 3-Cell OC Prototype						
9.8	4.03	4.83 ( $\theta=28^\circ$ )	94	12.8	4.07	0.50 $\lambda$ ×0.39 $\lambda$ ×0.15 $\lambda$
Loaded 3-Cell OC Prototype						
11	4.33	4.37 ( $\theta=9.5^\circ$ )	93	7.5	3.45	0.43 $\lambda$ ×0.35 $\lambda$ ×0.13 $\lambda$
Unloaded 2-Cell SC Prototype						
8.1	1.80	2.15 ( $\theta=-20^\circ$ )	96	4.9	3.25	0.26 $\lambda$ ×0.33 $\lambda$ ×0.12 $\lambda$
Loaded 2-Cell SC Prototype						
7.5	0.70	1.09 ( $\theta=-20^\circ$ )	96	3.5	2.84	0.22 $\lambda$ ×0.28 $\lambda$ ×0.10 $\lambda$

#### 4.2.11 Conclusion

This section puts forward a method to miniaturize the open-circuited (OC) 3-cell EBG antenna introduced in Sec. 4.1. The cells are electrically small thick metal patches on top of a PEC-backed substrate separated with tiny high aspect ratio gaps. The idea is to connect the last cell to the ground plane with a shorting plate and reduce the size of the radiating structure as compared to the OC case described in Sec. 4.1. An analytical TL model is presented for the EBG antenna as a tool to compare electrical length and radiation for both OC and short-circuited (SC) antenna versions. Three different parametric studies are also conducted on the antennas to demonstrate how the number of unit cells in the structure, the thickness of the top metal layer, and the ground plane size can affect antennas properties. It is shown that one of the SC designs with two EBG cells possesses a very small size of  $0.25\lambda \times 0.28\lambda \times \lambda/27$  with a high efficiency of 83%. In addition to the shorting method, the miniaturization effect obtained by dielectric loading of gaps is also demonstrated. It is shown that simple loading introduces an extra  $\sim 15\%$  reduction of resonance without deteriorating the radiation pattern and efficiency. Two prototypes are fabricated and experimented. The simulated efficiency and footprint of the smallest gap-loaded prototype, the 2-cell SC SE-EBG-RA, are 96% and  $0.22\lambda \times 0.28\lambda \times 0.10\lambda$ , respectively. For one of the prototypes, efficiency, input matching, radiation patterns, and gain are measured and compared with simulations to validate the soundness of the idea and numerical analyses.

### **4.3 Aperture Efficiency Enhancement for Electrically Large SE-EBG-RAs**

In sections 4.1 and 4.2, the high-performance nature of the SE-EBG-RA, whether the SC or OC version, was demonstrated. The results showed that simultaneous rewards of EBG cells on the one hand and the benefits of cells thickened on the top layer on the other hand result in high efficiency (low loss) antennas. These antennas had the potential to be very compact and low-profile radiating elements, ideal for applications with stringent requirements especially on size (device form factor). However, in practice these are not the only applications, which can benefit from high-performance nature of such elements. There are some important applications which require medium to high radiation gains, i.e. electrically larger apertures (in terms of wavelength), and at the same time, demand efficient and high-performance antennas. This section is focused on a technique to achieve SE-EBG-RAs with larger apertures.

#### **4.3.1 Introduction**

In radar systems, satellite communications, in space exploration programs [43], and the like, in which the transmitter and receivers are located very far apart, the SNR is severely degraded in the link budget, requiring high gain antennas with large apertures. Apart from this feature, in some cases, it is ideally desired to have an antenna with high power handling capacity, as it is necessary to increase the effective isotropic radiated power (EIRP: gain times the input power) by increasing the antenna input power. With a large array antenna, poor element efficiencies result in high power dissipation that not only wastes power resources, but also generates heat which can be a secondary problem to practical, compact, and highly reliable system/RF solutions. Although planar high gain antennas can be based on elements like microstrip patch antennas, the inherent inefficiency of these elements could result in a huge ohmic loss dissipated as heat in the thin structure. Another problem is the loss in the feed network that begins to cancel out and dominate the added gain the elements introduce, when the number of elements increases beyond a threshold. These points emphasize the importance of high efficiency array antenna elements. By employing such high efficiency elements, the idea of flat high gain antennas replacing parabolic antennas which are sometimes hard to integrate, deploy, and handle in practice would be realizable. Although many methods have been put forward to achieve these goals, like the idea of reflectarray antennas [38] (flat reflector antennas), Fresnel zone plate antennas [41] or using superstrate EBG resonator antennas [39-40], each of these ideas has its



own limitations and complexities in the design process and fabrication stage. Therefore, for some applications, using the conventional planar arraying approaches, while employing high efficiency elements is an attractive solution. To exemplify, in [42], a relatively efficient  $16 \times 8$  array of microstrip patches at 18GHz demonstrates 28dBi gain with only 57% overall efficiency, which was even improved thanks to a special feeding topology utilized.

In this part, an example design from the previous section is chosen and the ground plane is enlarged to achieve a higher gain. In addition, parasitic elements on the antenna aperture are introduced, with the objective of increasing the single element gain while simultaneously suppressing the surface currents between array elements. It is noted that when enlarging the ground plane of planar antennas, the rate of increase in the radiation gradually drops. This behavior originates from the fact that with an enlarged ground, radiating fields excited by the antenna at the center begin tapering/sinking over the aperture with distance away from the source. The outcome of this tapering would be a non-uniform illumination of the aperture in terms of both phase and magnitude, each of which deteriorates the radiation based on the aperture theory [11]. This effect was demonstrated in Sec. 4.2 for one of the designs. To compensate this inherent deficiency, a technique is examined to help maintain or improve the efficiency ( $\eta$ ) and gain.

#### 4.3.2 HI Parasitic Elements Applied to the SE-EBG-RA Structure

Fig. 4.3.1 shows a SC 2-cell SE-EBG-RA designed in Sec. 4.2 (dimensions and substrate material are the same). The magnitude of the surface current on the ground plane is visualized using standard Colorkey graph in HFSS. In order to stop the surface current, a number of  $\lambda/2$  parasitic elements are deployed around the antenna, as in Fig. 4.3.2. A wire version of such high impedance (HI) elements was successfully applied to a dipole antenna to reach a low-profile efficient periodic antenna [45] (see Fig. 2.9). HI elements are suggested to be a little smaller than  $\lambda/2$  ( $\lambda$  is group wavelength). Such HI elements also have shown successful effects in the design of a new CP version [44] of the same structure in [45]. Although these elements resemble the director elements of a Yagi antenna, it is important to note that they are repeated at electrically smaller intervals ( $< \lambda_0/10$ ) and are only  $\sim \lambda_0/80$  spaced from the ground plane ( $\lambda_0$  is wavelength at the resonance frequency). This implies that HI elements cannot radiate themselves (image in the

PEC ground cancels the radiation), but can change the boundary condition, thus suppress the surface waves, and improve the radiation from the SC SE-EBG-RA.

The design process begins with the design of the center element according to Sec. 4.2 (HFSS/Bloch method or alternatively using the circuit model in Sec. 4.4). Then a 2mm thick trace of 3mm width and 12.5mm length is repeated roughly at the same electrical length as in [45]. The situation is slightly different here as this case deals with thick traces on high dielectric material and to know the electrical length, it is necessary to know the group wavelength along each thick trace. This could be done by modeling a small section of this trace in a unit cell, similar to the HFSS/Bloch cell already discussed, and applying the equations to extract effective dielectric constant that defines the electrical length. Following this procedure and using the approximations described, the first dimensions obtained (as  $\lambda/2$  HI elements) have been directly used in the proposed structures (see Fig. 4.3.1) and have yielded satisfactory results. It is important that no optimization process has been employed to achieve such designs.

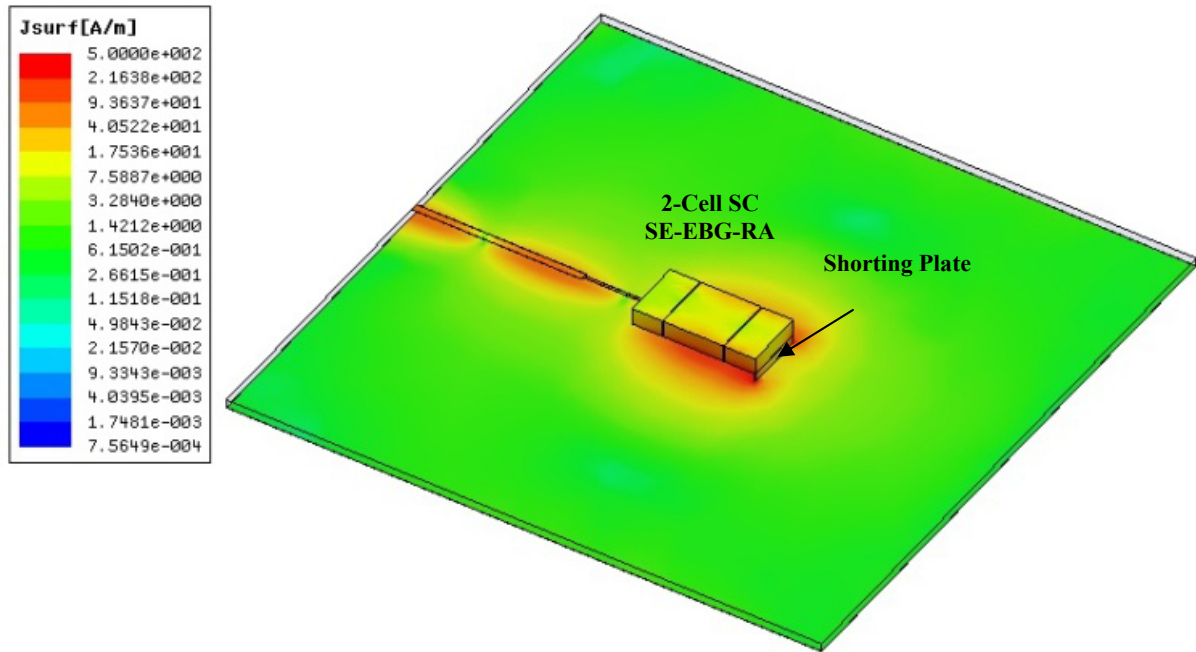


Fig. 4.3.1 A 2-cell SC EBGRA on a relatively large ground plane;  $\eta=76\%$ ,  $D=6.3\text{dBi}$ ,  $f=3.75\text{GHz}$ ; the XY size is  $70.17\text{mm} \times 70\text{mm}$ ; this design has already presented in Fig. 4.2.5, but with smaller ground plane; the thick HI elements are 12.5mm long and 3mm wide, and the first one has 9mm offset form the center.

Because the top layer of the main antenna in Fig. 4.3.2 is formed of a thick metal layer, HI elements are made of the same thickness (2mm). This condition provides a design with uniform thickness, which could be fabricated by (e.g.) a single-stage DXRL process. As shown in Fig. 4.3.2 and 4.3.3, two versions supported with 4 and 8 HI elements are considered. It is noted that the maximum current in all figures is the same so that the current distribution could be visually compared. Because of adding  $\lambda/2$  parasitic elements in Fig. 4.3.2, without mismatch or mistuning,  $\eta$  increases from 76% to 82% and 0.55dB improvement happens to the realized gain as well. As for the 8-element case, the antenna improves even more. This means  $\eta$  increases from 76% to 84% and the design renders  $\sim 1.4$ dB more realized gain than the one without HI elements.

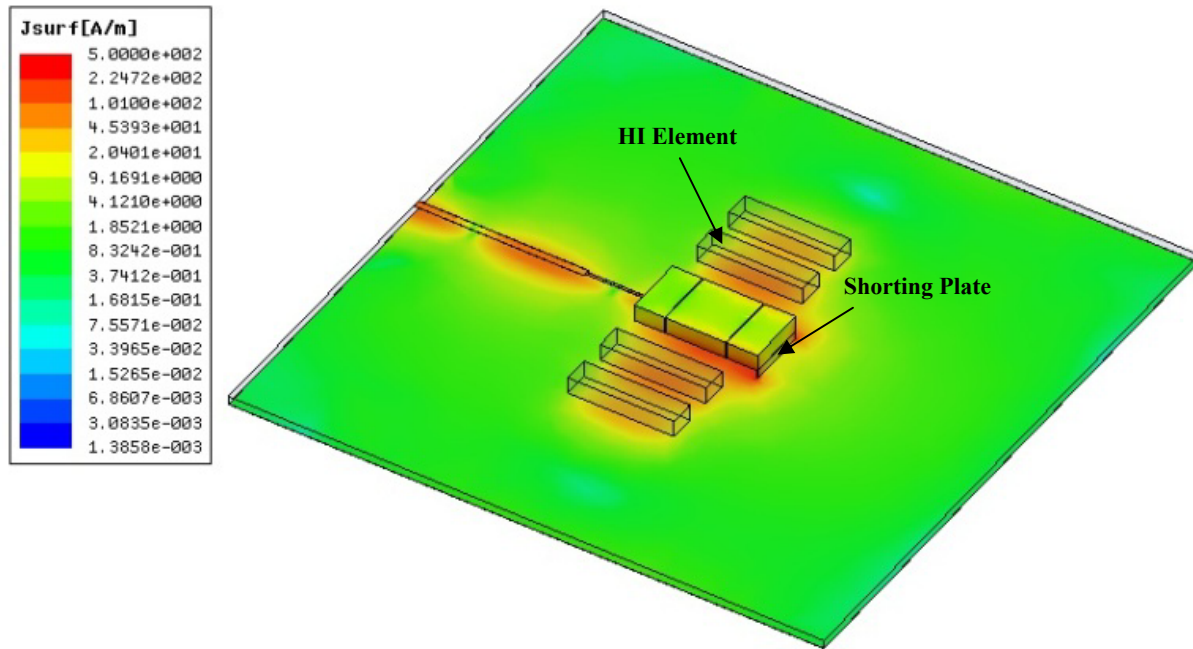


Fig. 4.3.2 The antenna in Fig. 4.3.1 supported with 4 HI resonating elements around the main radiator;  $\eta=82\%$ ,  $D=6.85$ dB,  $f=3.72$ GHz; Ground plane size is the same as Fig. 4.3.1.

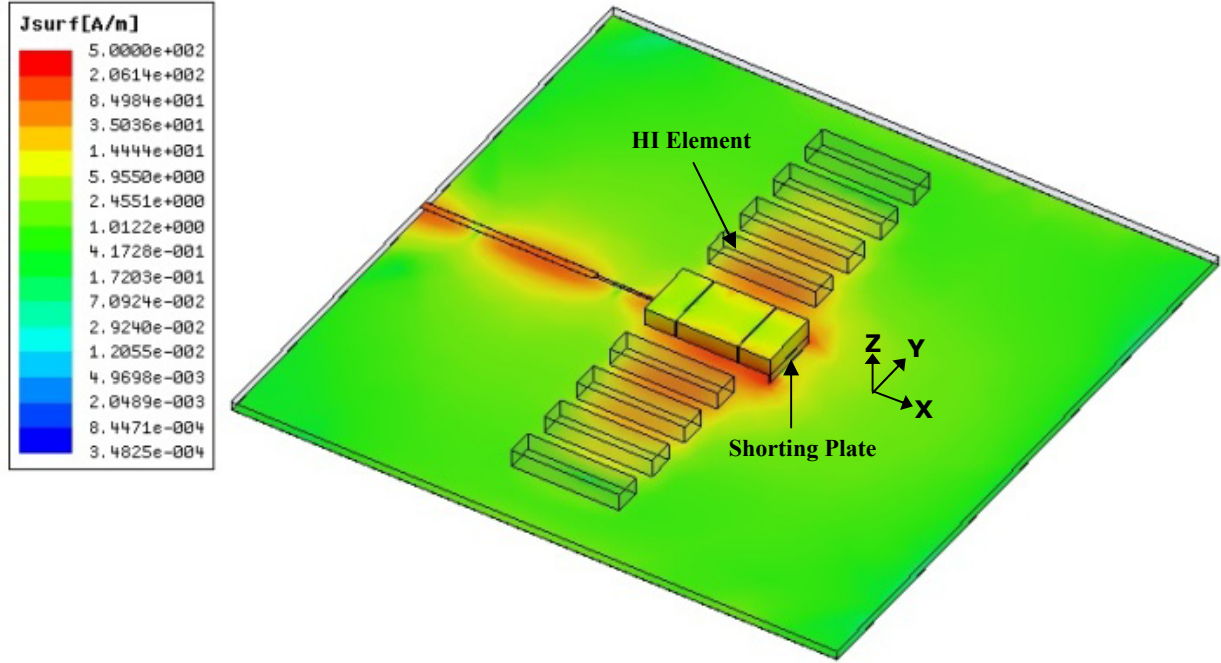


Fig. 4.3.3 The antenna in Fig. 4.3.1 supported with 8 HI resonating elements around the main radiator;  $\eta=84\%$ ,  $D=7.31\text{dBi}$ ,  $f=3.71\text{GHz}$ ; Ground plane size is the same as Fig. 4.3.1.

It is noted that if the ground planar of Fig. 4.3.1 is considered as a rectangular aperture, under the best scenario for which the distribution of fields are uniform (phase and amplitude), the maximum directivity will be found from  $D=4\pi ab/\lambda^2$ . Here  $a$  and  $b$  are physical sizes of the aperture and  $\lambda$  should be the matching frequency, thus  $D=9.82\text{dBi}$ . This means that the antenna has the potential to achieve this directivity, while is rendering only  $6.3\text{dBi}$ . We demonstrated that deploying 8 HI element could bring the directivity to  $7.31\text{dBi}$ . On the other hand, efficiency has also improved that causes some extra improvement to the overall realized gain.

In the same manner, the surface could be filled with more HI elements and this could help make better use of the space available towards constructive radiation and turning the surface waves into real radiated power. It is observed that the deviation in resonance occurring due to adding HI elements even for the 8-HI version is tolerable (difference  $< 1.6\%$ ). Fig. 4.3.4 compares  $\text{dB}|S_{11}|$  of antennas in Fig.4.3.1 to 4.3.3.

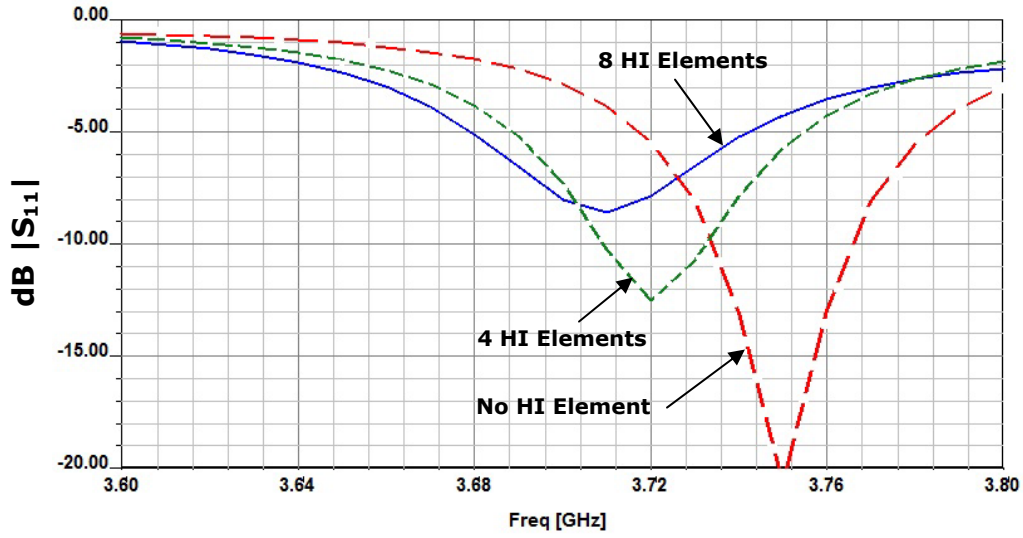


Fig. 4.3.4 Comparison of the input matching quality if antennas in Fig. 4.3.1 to 4.3.3.

As seen, the minimum  $\text{dB}|S_{11}|$  for the 4-HI version is still low enough, but that of the 8-HI version is a slightly deteriorated (-8.5dB at the matching frequency), yet close to -10dB. In addition, it is observed that the frequency shift is downward for the two cases. This deviation is small, and hence, a slight fine-tuning could compensate it with reduced computational load. The observation that the mistuning and mismatch are tolerable allows the designer to design the main 2-cell SE-EBG-RA separately, based on the HFSS/Bloch method, and then deploy the HI elements, and expect that the resulting structure does not severely lose its matched condition. Radiation patterns of all three antennas are also very similar, thus only the directivity of the version with 8 HI elements is rendered in Fig. 4.3.5.

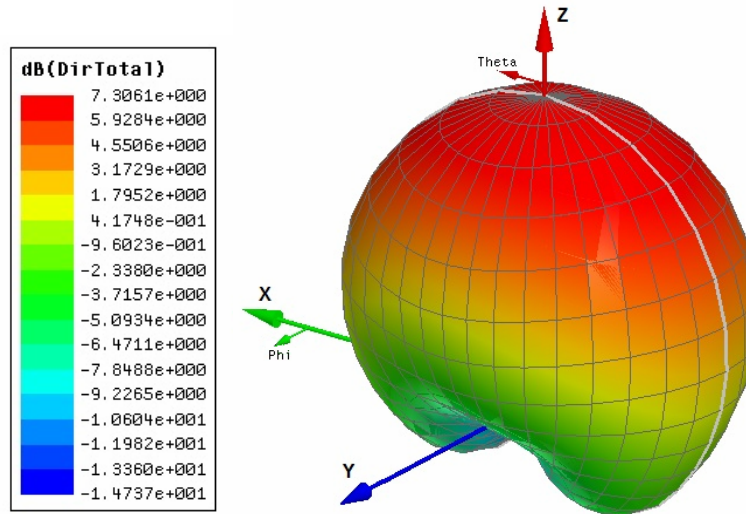


Fig. 4.3.5 3D plot of the directivity of the antenna in Fig. 4.3.3.

### 4.3.3 Conclusion

This study in this section presents a technique to trap the surface waves excited around the proposed planar antennas and turn them into radiation. The result is increasing the overall radiation of the antenna even beyond what can be obtained by thickening the top layer. The technique involves adding resonating HI elements around the main radiator which, as demonstrated, do not significantly disturb the radiation mechanism of the main radiator. As a result, the input impedance and the corresponding matching condition remain reasonably stable. This desirable stability is obtained without any retuning, and hence, using a fine-tuning process (or an optimization process) the directivity and efficiency could improve even more. In brief, the study shows that modified versions of SE-EBG-RAs shown in Fig. 4.3.3 offer a high-performance antenna design with the following special characteristics:

- The antenna is a single-layer planar antenna with a very simple feeding method, and hence, it is very suitable for deployment and realization of an array topology.
- It features a projected top metal layer, which as demonstrated in Sec. 4.2, could significantly reduce the loss in the antenna body and in the array feedlines.
- The antenna is based on EBG cells, which as demonstrated before introduces enhanced radiation and alleviated loss.
- As the design employs thick top metal traces, if utilized in an array fed by thick MSL with the same thickness (with relatively low loss), it could result in new planar array antennas with enhanced efficiencies.
- Due to using an alumina substrate and having no vias in the ground plane, it is considered quite compatible with single metal layer micro-fabrication processes, like DXRL (See Appendix C).

#### **4.4 TL Circuit Model for HAR EBG Cells and SE-EBG-RAs**

In this section, a circuit model based on Bloch theory is introduced to simplify analysis and design of antennas composed of thick metal electromagnetic bandgap (EBG) cells with large intercell coupling capacitance (thick EBG cells described before). Two versions of cells are presented which provide large intercell capacitance, one with narrow high aspect ratio (HAR) gaps between cells, as described in Sec. 4.1, and the other with interdigitated gaps between cells. This large capacitance reduces the antenna resonance and dramatically miniaturizes the EBG cells. Three cascaded unit cells are used to demonstrate the applicability of the circuit model to characterize the self-excited EBG resonator antenna introduced in Sec. 4.1. Full-wave numerical analysis and experimentation validate the robustness and accuracy of the model over large variations in electrical/physical cell dimensions.

##### **4.4.1 Introduction**

Accurate circuit models can be powerful tools for characterizing challenging electromagnetic (EM) structures such as microwave antennas. Circuit-based analysis can offer a good set of initial values for time-consuming computer-aided parametric design optimization, while also offering a quick insight into the relationships between performance and structural parameters. A good circuit model should be able to predict both input impedance and radiation properties of antennas [46]. Although prevalent for passive microwave components like transmission lines (TL) [47] and filters [48], such models are less common for radiating structures which are not completely bound EM problems and have extra complexities. Most published circuit models are applicable to antennas with a planar configuration [e.g. 49-50], which can be represented using TL theory. The best examples of model-based antennas are planar leaky-wave antennas [49], which belong to the traveling wave family and exhibit both TL and radiating behaviors. Another similar example is a TL model for a broadband spiral antenna and the circuit miniaturization achieved [50]. Furthermore, the very recent study in [51] proposes a broadband circuit approach to model the impedance and fields of antennas using characteristic eigenmodes. Among these, perhaps one of the most successful contributions of circuit models to antenna technology has been made to antennas with periodic structures [49-50, 17], most popular and promising of which are metamaterial-based antennas [49], and specifically EBG-based antennas [20]. Periodicity allows the designer to focus on the antenna building block, the so-called unit cell,

characterize it separately [34], and then use the result along with theories like Floquet-Bloch [52] to describe the performance of the structure. As indicated in [53], models are sometimes solely based on lumped elements [47, 34] or based on TLs and embedded lumped elements [50, 52-53]. Most models for periodic structures only focus on reactive behaviors [47, 53] and ignore real powers while some also include the effects of radiation and loss [50], which is also the goal of the current section.

Specifically, this section presents a (lumped/TL-based) model suitable for describing unit cells with high capacitance gaps, which can be realized using narrow, high-aspect-ratio and/or interdigitated metal structures. Such unit cells can be applied to the self-excited EBG resonator antenna (SE-EBG-RA) structure presented in Sec. 4.1. More importantly, in addition to the basic cell proposed in Sec. 4.1, the model is generalized to include cells with high capacitance interdigitated gaps.

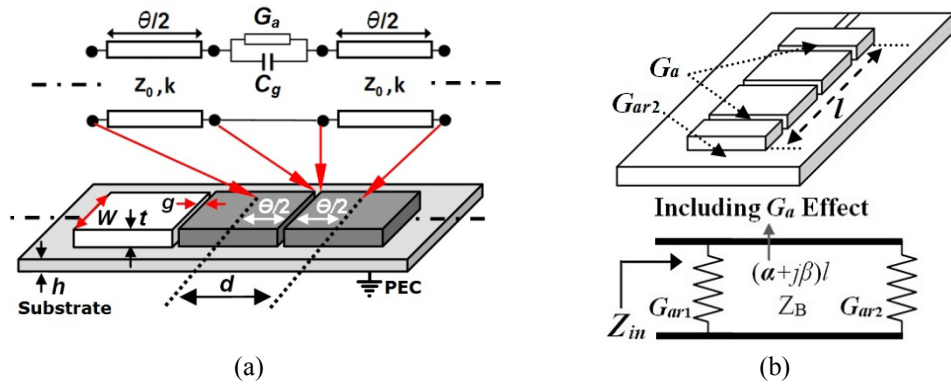


Fig. 4.4.1. a) Bloch unit cell and circuit model representation for a cascade of small thick metal patches on a PEC-backed substrate; b) circuit model for the SE-EBG-RA composed of three EBG cells.

#### 4.4.2 Equivalent Circuit Model for Basic Unit Cells

In Sec. 4.1, HFSS/Bloch model was proposed to analyze cascaded thick metal unit cells of the general form shown in Fig. 4.4.1. This method, though promising, was practically limiting since it was dependent on computer full-wave numerical analysis to extract the cascade network parameters of the unit cell, which were then fed to the Bloch equations. The model presented here retains the overall simplicity of the approach, however removes the requirement for *any* numerical analysis because the cascade parameters are determined directly from the physical parameters. The equivalent circuit model in Fig. 4.4.1 is composed of a gap impedance,  $Z_g$ , with two  $\theta/2$ -long MSLs on each side.  $Z_g$  is comprised of the parallel combination of gap



conductance,  $G_a$ , and gap capacitance,  $C_g$ . The Bloch dispersion relation of this symmetrical cell (in  $ABCD$  matrix,  $A=D$ ) can be expressed as [52]:

$$\cosh \gamma d = A = \cos \theta + j \frac{Z_g}{2Z_0} \sin \theta \quad (4.4.1)$$

where  $A$  is the first cascade parameter of the cell in Fig. 4.4.1,  $\gamma=\alpha+j\beta$  is the complex propagation constant along the cell,  $Z_0$  is the line impedance of the unloaded line (without periodic gap loading),  $d$  is the cell length,  $\theta=kd$ , and  $k$  is the wavenumber of the unloaded MSL expressed as:

$$k = \omega \sqrt{\mu_0 \epsilon_0} \sqrt{\epsilon_{\text{reff}}} \quad (4.4.2)$$

In (4.4.2),  $\epsilon_{\text{reff}}$  is the effective relative permittivity given by (4.4.7), and  $\epsilon_0$  and  $\mu_0$  are free-space permittivity and permeability, respectively. If  $d \ll \lambda$ , where  $\lambda$  is the free-space wavelength, then  $\gamma d \ll 1$  and  $\theta \ll 1$ , and  $\cos \theta$  and  $\cosh \gamma d$  can be replaced by the first two terms of their Taylor series expansions [52], and  $\sin \theta \approx \theta$ . Thus, (4.4.1) is simplified to

$$\gamma^2 = -k^2 + j \frac{kZ_g}{dZ_0} \quad (4.4.3)$$

Neglecting the radiation represented by  $G_a$  in Fig. 4.4.1,  $Z_g \approx 1/j\omega C_g$ . In this case,  $\gamma=0+j\beta$  ( $\alpha=0$ ) and (4.4.3) becomes

$$\beta^2 = k^2 - j \frac{kZ_g}{dZ_0} \quad (4.4.4)$$

The cut-off frequency ( $f_c$ ) can be found by setting  $\beta=0$ :

$$\omega_c^2 = \frac{c}{Z_0 d C_g \sqrt{\epsilon_{\text{reff}}}} \quad (4.4.5)$$

where  $c$  is  $(\epsilon_0 \mu_0)^{-1/2}$ .  $Z_0$  can also be found using the following equation [34], with an accuracy of  $\pm 0.25\%$  for  $1 < W/h < 10$ :

$$Z_0 = \frac{\eta_0}{\sqrt{\epsilon_{\text{reff}}}} \left[ \frac{W}{h} + 2.42 - 0.44 \frac{h}{W} + \left( 1 - \frac{h}{W} \right)^6 \right]^{-1} \quad (4.4.6)$$

where  $\eta_0$  is the free-space impedance. It is noted that in (4.4.6), the thickness of metal traces is neglected. As for  $\epsilon_{\text{reff}}$  in (4.4.6), [54] provides an equation which includes the effect of  $t/h$  for a MSL with a finite thickness:

$$\varepsilon_{\text{reff}} = \frac{\varepsilon_r + 1}{2} + \frac{\varepsilon_r - 1}{2} \left( 1 + 12 \frac{h}{W} \right)^{-1/2} - \frac{\varepsilon_r - 1}{4.6} \frac{t/h}{\sqrt{W/h}} \quad (4.4.7)$$

where  $0.1 < w/h < 20$  and  $t/h < 0.2$ . An interesting observation from (4.4.5) is that  $\varepsilon_{\text{reff}}^{1/2}$  is cancelled by the same term introduced by  $Z_0$  in (4.4.6). Therefore, under certain conditions, the model does not require a particularly accurate estimation of  $\varepsilon_{\text{reff}}$ , which can be difficult to determine for thick metal structures. In fact, (4.4.7) which is most accurate for comparatively small  $t/h$ , when applied to the model, is found to produce good results, even for  $t/h$  up to 2-3. The  $C_g$  in Fig. 4.4.1 is attributed to the coplanar coupling on the top of the adjacent cells ( $C_{cp}$ ) plus the parallel plate coupling between the high aspect ratio (HAR) gap in the middle ( $C_{pp}$ ), i.e.  $C_g = C_{pp} + C_{cp}$ . The static approach in [20] gives  $C_{cp}$  as ( $d \gg g$ )

$$C_{cp} = \frac{2W}{\pi} \varepsilon_0 \varepsilon_{\text{reff}} \cosh^{-1}(d/g) \quad (4.4.8)$$

Also,  $C_{pp}$  is found by the following well-known relation:

$$C_{pp} = \varepsilon_0 t W / g \quad (4.4.9)$$

Under this circumstance, the only dependency of  $\omega_c$  on  $\varepsilon_{\text{reff}}$  occurs because  $C_g$  is still partially dependent on  $\varepsilon_{\text{reff}}$  as seen in (4.4.8). However, if  $C_{pp} \gg C_{cp}$ , then  $C_g \approx C_{pp}$ , which according to (4.4.9), eliminates the dependency of  $C_g$  on  $\varepsilon_{\text{reff}}$ . Parallel plate coupling will typically dominate coplanar coupling for most relevant thick metal structures, meaning that fields will be *mostly* constrained inside the narrow air-filled gaps and have negligible dependency on the substrate material. To include the gap effect in the model, the gap surface is regarded as a radiating aperture with a radiation conductance,  $G_a$ . In [11], E-fields uniformly distributed on the open end of a parallel plate waveguide are considered, and an equivalent impedance is driven using the aperture theory with the assumption that the open gap is surrounded by infinite PEC planes on each side. In fact, the field condition on the top surface of tall traces (adjacent patches in Fig. 4.4.1) roughly satisfies this requirement. Thus,  $G_a$  is expressed as

$$G_a = \frac{W\pi}{\lambda\eta_0} \left[ 1 - \frac{(k_0 g)^2}{24} \right] \stackrel{g \ll \lambda}{\approx} \frac{W\pi}{\lambda\eta_0} \quad (4.4.10)$$

where  $k_0$  is the free-space wavenumber. Although  $G_a$  can model the antenna radiation, it is still a rough estimate since thick MSLs can radiate themselves as shown in Sec. 4.1. Also, thick traces

can cause the gap apertures to be slightly further spaced from the PEC ground and affect  $G_a$ . However, this inaccuracy does not weaken the model in predicting the zero-crossing in the reactive part of the input impedance (as in Sec. 4.4.4).

#### 4.4.3 Capacitance for the Interdigitated Unit Cell

The circuit model in Sec. 4.4.2 can be directly applied to characterize the basic unit cell with a high capacitance narrow HAR gap shown in Fig. 4.4.2 (a). Next, the model is extended to describe a modified version of the unit cell, which employs interdigitated gaps to increase the gap capacitance, either in thick metal configuration of Fig. 4.4.2 (b) or a more conventional thin metal configuration.

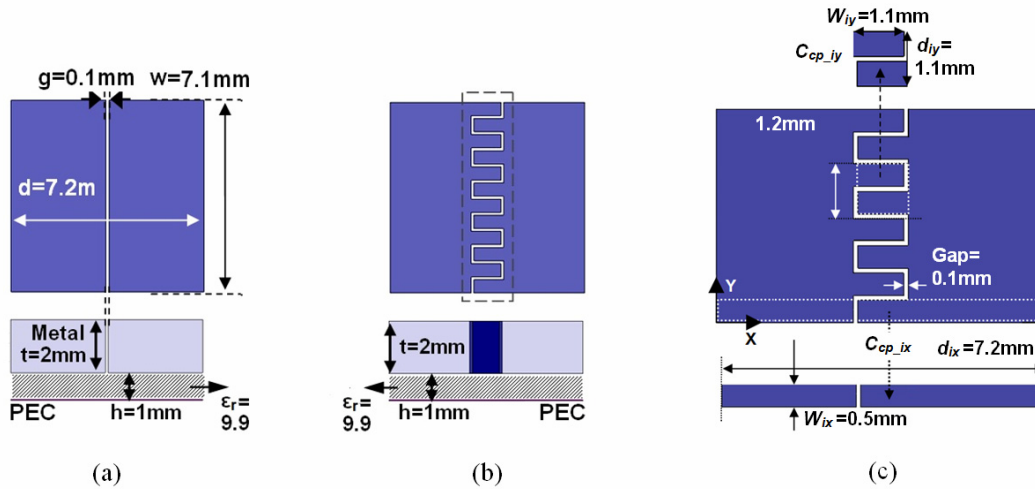


Fig. 4.4.2. Side and top views of EBG unit cells with a thick metal layer and high gap capacitance; (a) cell with narrow HAR gap; (b) cell with interdigitated gap; (c) detailed dimensions of the interdigits in Fig. 4.4.2 (b).

Considering the geometry and parameters depicted, the cumulative coplanar capacitance can be expressed by the summation of capacitances in Y-axis-oriented gaps ( $C_{cp\_iy}$ ) and also X-axis-oriented gaps ( $C_{cp\_ix}$ ):

$$C_{cp\_i} = 2mC_{cp\_ix} + (2m-1)C_{cp\_iy} \quad (4.4.11)$$

where  $m$  is the number of the periods in Fig. 4.4.2 (b) (for the case shown,  $m=6$ ). Here  $C_{cp\_iy}$  is calculated from (4.4.8) when  $W$  is replaced by  $W_{iy}$  and  $d$  by  $d_{iy}$ , respectively. Similarly,  $C_{cp\_ix}$  is calculated from (4.4.8) when  $W$  is replaced by  $W_{ix}$  and  $d$  is replaced by  $d_{ix}$  ( $d_{ix}$ ,  $d_{iy}$ ,  $W_{ix}$ , and  $W_{iy}$  are denoted in Fig. 4.4.2 (c)).

Table 4.4.1 Dimensions and characteristics of the four SE-EBG-RA samples based on four different unit cells;  $\lambda_r$  is wavelength at  $f_r$ , and  $\Delta$  is the difference between  $f_r$  given by the model and HFSS, divided by the HFSS value; dimensions are in millimeters.

	Sample 1 $\epsilon_r=9.9$ , $\tan\delta=0.003$ (alumina), $w=7.1$ , $d=7.2$ , $t=2$ , $g=0.1$ (AR=20), $h=1$			Sample 2 $\epsilon_r=6$ , $\tan\delta=0.0023$ (Rogers TMM 6), $w=10$ , $d=7.2$ , $t=0.4$ , $g=0.02$ (AR=20), $h=1$			Sample 3 $\epsilon_r=6$ , $\tan\delta=0.0023$ (Rogers TMM 6), $w=8$ , $d=8$ , $t=3$ , $g=0.1$ (AR=30), $h=1.27$			Sample 4 $\epsilon_r=3.78$ , $\tan\delta=0.0003$ (glass), $w=4$ , $d=4$ , $t=0.8$ , $g=0.04$ (AR=20), $h=0.5$		
	Model	HFSS	$\Delta$ (%)	Model	HFSS	$\Delta$ (%)	Model	HFSS	$\Delta$ (%)	Model	HFSS	$\Delta$ (%)
Thickness ( $h+t$ )	3 ( $\lambda_r/24$ )			1.4 ( $\lambda_r/48$ )			4.27 ( $\lambda_r/17.5$ )			1.3 ( $\lambda_r/23.6$ )		
Cell Size ( $d$ )	7.2 ( $\lambda_r/10$ )			7.2 ( $\lambda_r/9.4$ )			8 ( $\lambda_r/9.4$ )			4 ( $\lambda_r/7.66$ )		
$f_r$ (GHz)	4.01	4.17	3.8	4.25	4.43	4.1	4.04	4	1.0	9.87	9.79	0.8

Similar to (4.4.8) for which  $d \gg g$ , here  $d_{ix} \gg g$  and  $d_{iy} \gg g$  are two necessary conditions for the coplanar capacitance equation by [20]. Also, the parallel plate capacitance,  $C_{pp\_i}$ , can be calculated from (4.4.9) when  $W$  is replaced by

$$W_{eff} = (2m-1)W_{iy} + m(d_{iy} + g) \quad (4.4.12)$$

It is noted that similarly,  $W$  in (4.4.10) can be replaced by  $W_{eff}$  to find the effective  $G_a$  at the interdigitated gap. In the next section, the accuracy of (4.4.11) and (4.4.12) is demonstrated.

#### 4.4.4 Verification of the Circuit Model

This section presents several examples to compare the circuit model predictions to results obtained through full-wave simulations. To this end, cells are used to structure several example SE-EBG-RAs. All antenna examples comprise three EBG cells ( $d \ll \lambda$ ) forming a piece of EBG-woven TL, left open on one side and fed by a MSL from the other side. The configuration is shown in Fig. 4.4.1 (b). As seen, in addition to  $G_a$  at each gap, there are two more radiating apertures at the feed ( $G_{ra1}$ ) and open ( $G_{ra2}$ ) sides of the antenna, very similar to radiating apertures of a regular patch antenna [11, 55]. Using the lossy TL theory [10], and considering Fig. 4.4.1 (b), the input impedance can be derived as

$$Z_{in} = R_{in} + jX_{in} = G_{ra1}^{-1} \parallel Z_B \frac{G_{ra2}^{-1} + Z_B \tanh \gamma l}{Z_B + G_{ra2}^{-1} \tanh \gamma l} \quad (4.4.13)$$

When  $\beta l = n\pi/2$  ( $n=0,1,2,\dots$  and for  $n=1$ , a half-wavelength antenna like a patch antenna is achieved)  $X_{in}$  vanishes and  $Z_{in}$  becomes resistive, and hence, in a similar fashion to patch antennas [11, 55]  $G_{ra1}=G_{ra2}$ . In [55],  $G_{ra1}$  is found by Harington's Equation and applied to patch antennas. The equation is identical to (4.4.10), except that  $g$  is replaced by  $h$ . Also, the Bloch line impedance,  $Z_B = BZ_0/\sqrt{A^2-1}$ , is already given in Sec. 4.1, i.e. (4.1.4). In (4.1.4),  $A$  is given by (4.4.1) and  $B$ , the second cascade parameter, is extracted as (based on the Bloch theory in [55])

$$B = Z_g (\cos \theta + 1) / 2 + jZ_0 \sin \theta \quad (4.4.14)$$

In (4.4.13),  $l$  is the total length of the EBG TL. Because the antenna has 3 cells,  $l=3d$  where  $d$  is depicted in Fig. 4.4.1 (a). For this antenna, the zero-crossing ( $X_{in}=0$ ) can be found either from (4.4.1) to (4.4.13), i.e. entirely based on the circuit model, or from the HFSS full-wave analysis. By putting  $\beta l = \pi/2$  ( $n=1$ ) into (4.4.4), this resonance can be expressed by  $\omega_r^2 = \omega_c^2 + \omega_p^2$  where  $\omega_c$  is given by (4.4.5) and  $\omega_p$  is

$$\omega_p = 0.5 c \pi \epsilon_{\text{reff}}^{-1/2} / l \quad (4.4.15)$$

The radiation from each resonator gap is embedded in the total radiation losses of the propagating waves along the antenna. The radiation from each gap is included in  $\alpha$  and  $Z_B$ , and the radiation from both sides of the antenna is modeled by  $G_{ra1}$  and  $G_{ra2}$ , as expressed by (4.4.13). In Sec. 4.1, the behavior of the antenna body as a radiating EBG TL was described in more details, using the HFSS/Bloch dispersion diagram.

In Table 4.4.1, four sample SE-EBG-RAs with considerably different EBG cells are considered to demonstrate the applicability and generality of the circuit model. The properties obtained from the model (using the dispersion relation (4.4.1), rather than the simplified relation (4.4.4)), are compared to those obtained from HFSS full-wave analysis. This approach provides two different evaluations of the antenna resonance frequency ( $f_r$  at which  $X_{in}=0$ ). In Table 4.4.1, the difference between the predicted  $f_r$  ( $\Delta$ ) for all samples ranges from 0.8% to 4.1%, implying a satisfactory agreement for design purposes which is consistent with or better than other analytical circuit models presented for EBG cells with uncertainties as high as 6.5% [34]. It is important to note that such an agreement occurs while all different antennas in this table are truncated to only 3 cells. This fact is a supplementary demonstration (in addition to Fig. 4.1.10)

that mutual coupling is typically negligible, the truncation is not problematic, and the Bloch theory can be accurately applied to the proposed antennas.

In Table 4.4.1, samples are chosen to have high aspect ratio (AR) capacitance gaps, ranging from 20 to 30, where  $AR=t/g$  as shown in Fig. 4.4.1 (a). One more verification is to examine the accuracy of (4.4.11) and (4.4.12). Table 4.4.2 uses the interdigitated cell in Fig. 4.4.2 (b) in a 3-cell SE-EBG-RA and compares its  $f_r$  found by the circuit model and HFSS. As seen,  $\Delta < 1.8\%$ , which is quite low considering the complexity of features added to the cell. For comparison,  $f_r$  of the non-interdigitated cell in Fig. 4.4.2 (a) is included as well. As seen,  $f_r$  of the interdigitated cell has significantly dropped while both cells have identical physical sizes. It is also observed that interdigitation enhances  $C_{pp}/C_{cp}$ , causing  $C_{pp}$  to dominate  $C_{cp}$ . Obviously, this trend continues as the order and depth of interdigitation increases.

Table 4.4.2  $f_r$  of SE-EBG-RAs composed of cells in Fig. 4.4.2 (a) and (b), given by the model and HFSS.  $C_{pp}$  and  $C_{cp}$  are also calculated by the model;  $\Delta$  is the difference between  $f_r$  by the model and HFSS, divided by the HFSS value.

Cell Type	$C_{cp}$ (pF)	$C_{pp}$ (pF)	$C_{pp}/C_{cp}$	$\Delta$ (%)	$f_r$ (GHz)	
					Model	HFSS
Interdigitated	2.54	4.96	1.95	1.8	3.26	3.32
Basic	1.33	1.26	0.95	3.4	4.01	4.15

It can be concluded that the model proves relatively accurate in estimation of resonance (where  $X_{in}=0$ ), provided that  $g \ll \lambda$ ,  $g \ll d$ ,  $d \ll \lambda$ ,  $g \ll d_{ix}$ ,  $g \ll d_{iy}$ . Also, although (4.4.6) does not include the effect of thickness and (4.4.7) only roughly includes that effect, the accuracy as demonstrated ( $\Delta < 4.1\%$ ), is not drastically affected, especially in the case of these structures where  $C_{pp}$  dominates  $C_{cp}$ . The model also (to some extent) includes the effect of radiation, and thereby, (4.4.13) can estimate  $R_{in}$ , but not as accurately as  $X_{in}$ .

#### 4.4.5 Verification through Prototyping

In this section, the effectiveness of the circuit model in design is demonstrated through experimental measurement of two fabricated antenna prototypes. The first prototype is shown in Fig. 4.4.3. The antenna features  $27\mu\text{m}$  gaps and is made by electroplating  $4\mu\text{m}$  Ni on an alumina substrate. The unit cells are as shown in Fig. 4.4.1, with dimensions given in Fig. 4.4.3.

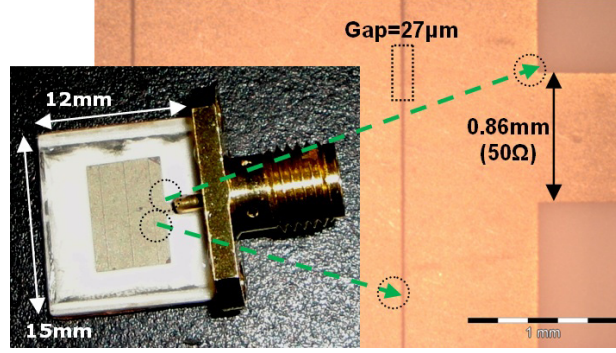


Fig. 4.4.3. The fabricated thin 3-cell antenna with micron-scale gaps; metal traces are  $4\mu\text{m}$  thick plated Ni; cells are as in Fig. 4.4.1 with  $d=1.81\text{mm}$ ;  $W=7.8\text{mm}$ ,  $h=1\text{mm}$ ,  $g=27\mu\text{m}$ ;  $\epsilon_r=9.9$ ,  $\tan\delta=0.003$ .

The input reflection ( $\text{dB}|S_{11}|$ ) of the antenna is shown in Fig. 4.4.4 (a). The measured resonance frequency ( $f_r$ ) from Fig 4.4.4 is  $12.43\text{GHz}$ , compared to an  $f_r$  predicted by HFSS simulation of  $11.54\text{GHz}$ . The circuit model predicted  $f_r$  of  $12.25\text{GHz}$  is comparable to the HFSS simulation ( $\Delta=6.1\%$ ), and quite respectable considering the high operating frequency ( $>12\text{GHz}$ ) of the partially lumped model. Also with micron scale features, even small discontinuities, for instance in the launch, can introduce uncertainty at higher frequencies. As seen, the difference between the model and experimental results is less than  $1.5\%$ .

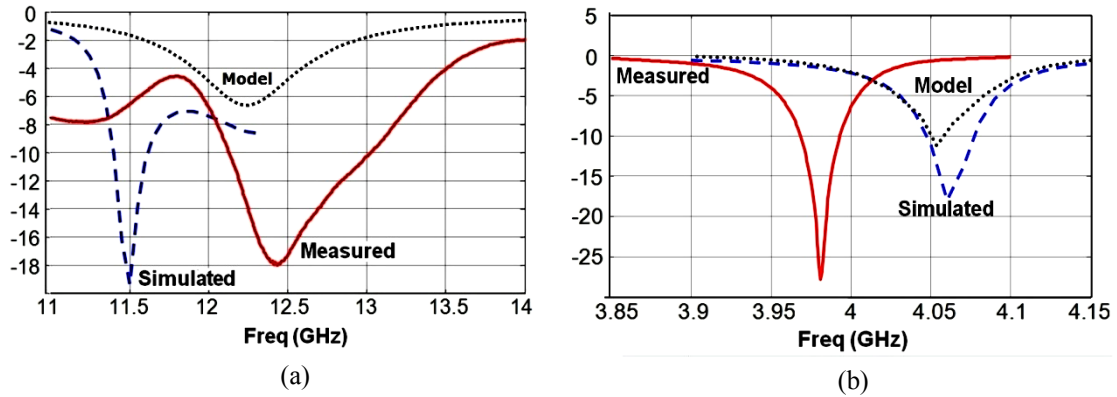


Fig. 4.4.4. Measured, HFSS-simulated, and modeled input reflections for a) the antenna in Fig. 4.4.3, b) the antenna in Fig. 4.4.5; both Y-axes show  $\text{dB}|S_{11}|$ .

The second prototype and its input reflection are shown in Fig. 4.4.5 and Fig. 4.4.4 (b), respectively. The simulated radiation pattern of this antenna at its resonance ( $4.06\text{GHz}$ ) is shown in Fig. 4.4.6 as well. As seen, the *realized* gain at broadside is  $2.85\text{dB}$ . In Fig. 4.4.5, the cell

differs from Fig. 4.4.1 in that some metal sections have been removed (indented), forming a dog-bone-like cell. The circuit model in Sec. 4.4.2 was developed for rectangular unit cells as shown in Fig. 4.4.1. However, with some considerations, it can also be effectively applied to the cell in Fig. 4.4.5 (a).

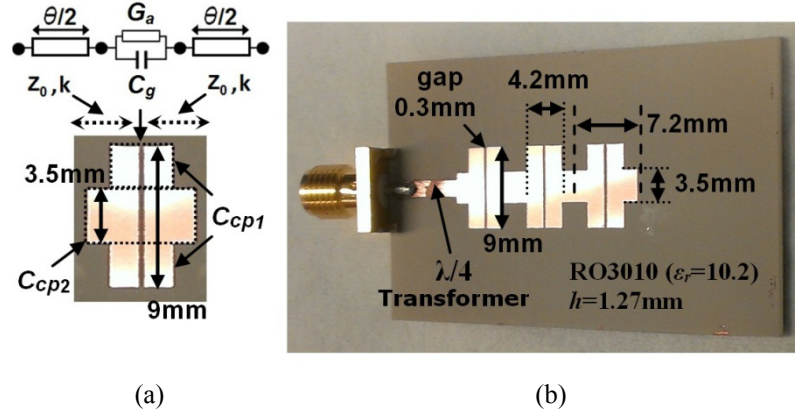


Fig. 4.4.5. The fabricated 3-cell antenna; the metal traces are made of 30 $\mu$ m thick copper; the  $\lambda/4$  transformer is 1.94mm wide and 6.96mm long.

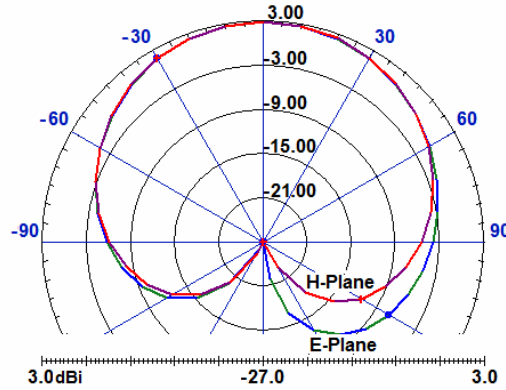


Fig. 4.4.6. HFSS-simulated radiation pattern of the 2nd prototype at 4.06GHz for 30mm×38mm ground plane size.

As shown in Fig. 4.4.5 (a),  $C_{cp}$  associated with the cell is composed of different capacitances,  $C_{cp}=2C_{cp1}+C_{cp2}$  where  $C_{cp1}$  and  $C_{cp2}$  can be calculated using (4.4.8), considering the depicted  $d$  and  $W$  in Fig. 4.4.5 (a) for each coplanar capacitance. Also,  $Z_0$  of the TL in Fig. 4.4.1 varies along the length due to the width discontinuities. Therefore two widths of 3.5mm and 9mm can be considered, each introducing a different  $Z_0$  to the model. In Table 4.4.3, these two cases are separately considered and the associated  $f_r$  is calculated. As  $d \ll \lambda$ , for the third case, the average of the trace widths in Case 1 and Case 2 is considered as an estimate. As seen, for Case 3,  $Z_0$  falls



somewhere between  $Z_0$  of the Case 1 and 2, and its estimate for  $f_r$  is the best ( $\Delta$  is the least at 2%). Even at the worst case (Case 2),  $\Delta < 8.3\%$  which is still tolerable.

Table 4.4.3 Properties of the antenna in Fig. 4.4.5 calculated by the model;  $\Delta$  is the difference between  $f_r$  given by the model and experiment, divided by the experimental value.

$f_r$ found by experiment (for Fig. 4.4.5) is 3.98GHz					
	Trace width (mm)	$Z_0 (\Omega)$	$\epsilon_{\text{reff}}$	$\Delta (\%)$	$f_r$ (GHz) by Model
Case 1	3.5	26.97	7.56	6.0	3.74
Case 2	9	13.22	8.38	8.3	4.31
Case 3	$(9+3.5)/2$	17.7	8.07	2.0	4.06

#### 4.4.6 Conclusion

A TL circuit model is proposed for describing thick radiating EBG unit cells. To demonstrate its effectiveness, this model is applied to the design of SE-EBG-RA presented in Sec. 4.1. Two kinds of EBG cells are considered for the antenna, including basic rectangular-shaped cells with narrow high-capacitance gaps, and an alternative version with high-capacitance interdigitated gaps. To ensure that the model is reliable, it is also applied to the design of four SE-EBG-RAs composed of cells with various physical and electrical properties. The antenna resonance found by the model compares favorably with that predicted by HFSS numerical analysis (typically  $< 4.1\%$  difference). Two different SE-EBG-RA prototypes are fabricated and measured, one of which features narrow gaps of  $27\mu\text{m}$ . Again, it is observed that the model and experimental results are very similar, differing by only 1.5% and 2%. This demonstrates the ability of the simple equation-based circuit model for accurately predicting the resonance frequency of radiating EBG unit cells.

## 4.5 Unit Cell Miniaturization and Applications to SE-EBG-RAs Design

This section focuses on thick EBG cells presented in Sec. 4.1 and discusses cell miniaturization and its applications to antenna size reduction. Miniaturization techniques to reduce the resonance frequency of the basic unit cell using the HFSS/Bloch approach are presented. Improved, compact EBG cells are applied to the structure of SE-EBG-RA, presented in Sec. 4.1. The original SE-EBG-RA with the basic EBG cell is compared to the new version developed here with improved cells.

### 4.5.1 EBG Cell Development and Miniaturization

The progression towards a miniaturized thick-metal EBG unit cell is shown in Fig. 4.5.1. The basic cell in Fig. 4.5.1 (a) can be considered a type of via-less version [2] of the mushroom-like cell [11], composed of electrically small thin metal patches on top of a PEC-backed dielectric substrate.

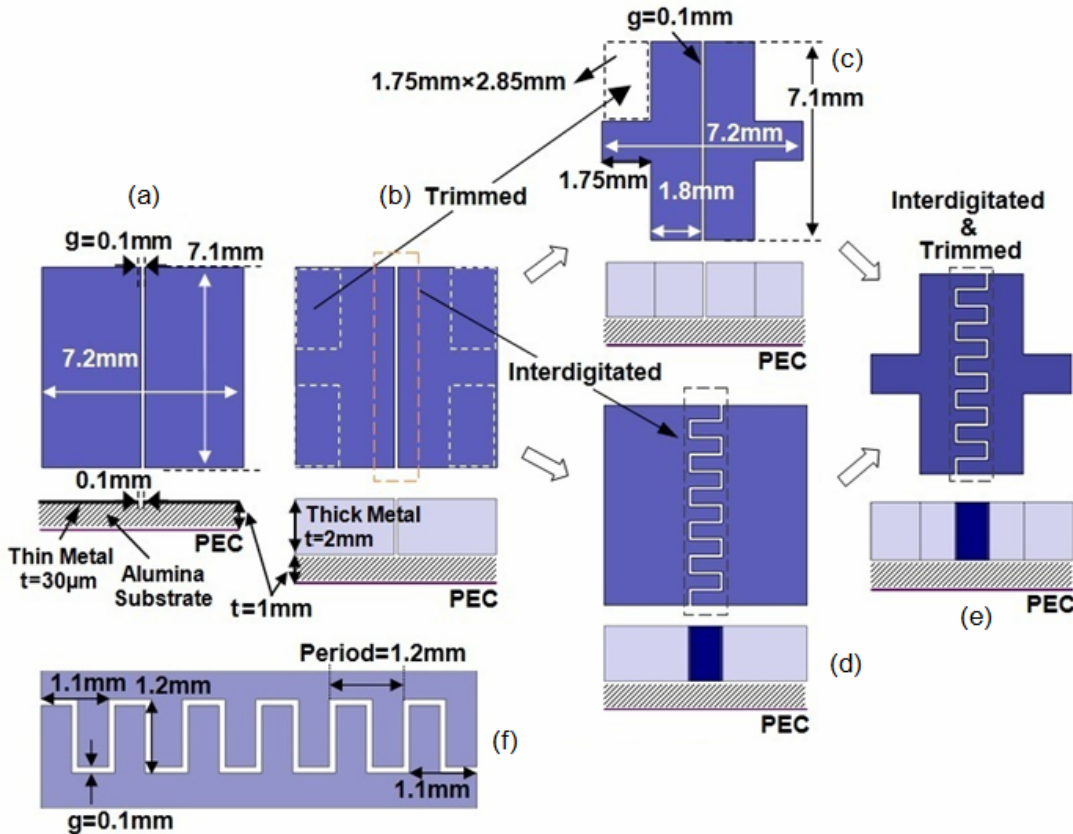


Fig. 4.5.1. Step-by-step development and miniaturization of the thick metal EBG unit cell (side/top views depicted); the substrate in this example is alumina with  $\epsilon_r=9.9$  and  $\tan\delta=0.003$ ; the aspect ratio, AR, is  $t/g$ .

The idea to attain new cells is to thicken the top metal layer considerably, while manipulating the lateral metal pattern to reduce the cell resonance frequency. The ensuing EBG structures proposed in this study (the antennas in Sec. 4.5.2) comprise a number of these thick patches deployed periodically in one dimension (1D EBG structure), and with very tiny gaps between cells. The gaps typically have very high aspect ratios (HAR) (Fig. 4.5.1 (b) example has  $AR=2\text{mm}/0.1\text{mm}=20$ ), and therefore introduce a high capacitive coupling effect that significantly reduces the cell electrical size.

#### ***A. Thickening, Interdigitation, and Trimming***

There are a number of methods proposed to tailor the properties of EBG cells such as interdigitation [56-57, 9], trimming [58], and much less commonly, thickening [17, 32, 59]. In this section, these methods are applied to the thin via-less mushroom-like EBG cell in Fig. 4.5.1 (a), both separately and in combination, with the objective to develop a new type of EBG cell with dramatically reduced electrical size.

First, the thickness of the metal layer of the thin EBG cell in Fig. 4.5.1 (a) is increased considerably, in this example to 2mm while the gap remains constant at 0.1mm. This turns the cell into a very thick EBG cell with a HAR gap ( $AR=20$ ), as shown in Fig. 4.5.1 (b). Fig. 4.5.2 and Table 4.5.1 compare the cell properties in the progression from cell 4.5.1(a) to 4.5.1(b), showing that the cut-off frequency ( $f_c$ ) decreases from 4.83GHz to 3.43GHz (29% drop).

Fig. 4.5.2 (down) shows the cell dispersion diagram generated by the HFSS/Bloch method described before. The method renders two curves for each cell, which are the real ( $\alpha$ ) and imaginary part ( $\beta$ ) of the complex propagation constant ( $\gamma$ ) along a 1D array (in the Y direction shown in Fig. 4.5.2 (a)) made of an infinite number of cells. In this method, the array in Fig. 4.5.2 (a) is considered a transmission line (TL), composed of EBG cells (EBG TL). The  $f_c$  reported in Table 4.5.1 is where these two curves intersect as highlighted in Fig. 4.5.2 (b).

The next method applied is to trim some rectangular pieces of the thick metal layer shown in Fig. 4.5.1 (b), to obtain the cell in Fig. 4.5.1 (c). This modification turns the cell into a 1D dogbone-like cell, the 2D version of which is known as Jerusalem cross cell [34]. As in Table 4.5.1 and Fig. 4.5.2, this change decreases  $f_c$  again, from 3.43GHz to 2.58GHz (25% drop). The next attempt is to apply interdigitation rather than trimming. To do this, the cell in Fig. 4.5.1 (b) is considered and its HAR gap is interdigitated towards increasing the gap capacitance, as shown

in Fig. 4.5.1 (d). The details of the example interdigitation are given in Fig. 4.5.1 (f). As seen in Fig. 4.5.2 and Table 4.5.1, this reduces  $f_c$  from 3.43GHz to 2.34GHz (32% drop).

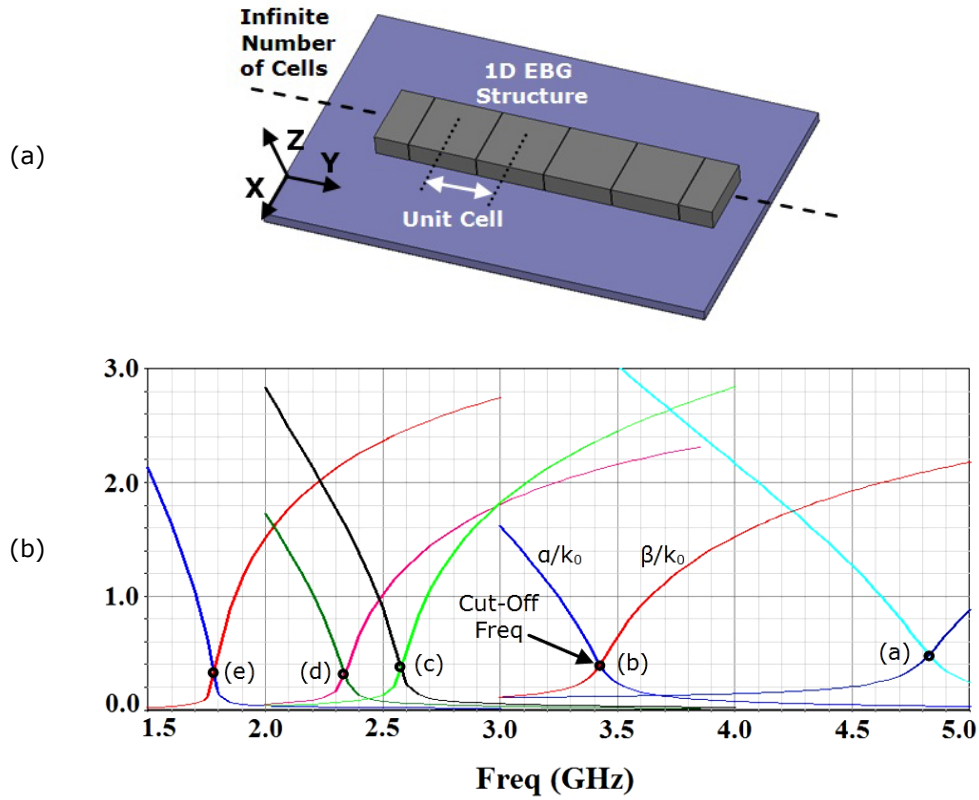


Fig. 4.5.2. a) 1D array structure of the EBG cell in Fig. 4.5.1 (b), b) the complex propagation constant ( $\gamma=\alpha+j\beta$ ) along Y-axis normalized by free-space wavenumber ( $k_0$ ) for EBG cells described in Fig. 4.5.1/Table 4.5.1; the twin curves (a) to (e) are related to Fig. 4.5.1 (a) to (e) and Result 1 to 5 in Table 4.5.1.

Table 4.5.1 Electrical and physical properties of the EBG cells in Fig. 4.5.1;  $\lambda_c$  is the wavelength at  $f_c$

	Thin EBG	Thick/Tall EBG			
	Result 1 Fig. 4.5.1 (a)	Result 2 Fig. 4.5.1 (b)	Result 3 Fig. 4.5.1 (c)	Result 4 Fig. 4.5.1 (d)	Result 5 Fig. 4.5.1 (e)
<b>Cut-off Freq (GHz)</b>	4.83	3.43	2.58	2.34	1.78
<b>Cell Size (mm)</b>	7.2 ( $\lambda_c/8.6$ )	7.2 $\lambda_c/12.15$	7.2 $\lambda_c/16.15$	7.2 $\lambda_c/17.8$	7.2 $\lambda_c/23.5$
<b>Overall Thickness (mm)</b>	1 $\lambda_c/62$	3 $\lambda_c/29.2$	3 $\lambda_c/38.8$	3 $\lambda_c/42.7$	3 $\lambda_c/56$
<b>Cell Size Shrinkage (times)</b>	1	1.41	1.87	2.06	2.7
<b>Footprint Shrinkage (times)</b>	1	2	3.5	4.25	7.3

### B. HAR Interdigitated Dogbone EBG Cell

The next step after separately demonstrating the miniaturization effects rendered by trimming and interdigitation is to combine and simultaneously apply them to the cell in Fig. 4.5.1 (b). Figure 4.5.1 (e) shows what the ensuing cell resembles and that this combination reduces  $f_c$  from 3.43GHz for Fig. 4.5.1 (b), to 1.78GHz for Fig. 4.5.1 (e) (48% drop). Table 4.5.1 compares the electrical and physical properties of all five EBG cells depicted in Fig. 4.5.1. The results clearly demonstrate a gradual and remarkable reduction in  $f_c$  of the cells. It is worth noting that by switching from Result 1 ( $f_c=4.83$ GHz) to Result 5 ( $f_c=1.78$ GHz),  $f_c$  dramatically drops by 63%, i.e. 2.7 times lower. Since the cell is spread two dimensionally, this is approximately equal to the shrinkage achieved in both the X and Y directions of the 1D array, resulting in an array footprint which is 7.3 ( $2.7^2$ ) times smaller, in terms of the new  $\lambda_c$  (at the new  $f_c$ ). It is worthwhile to note that starting from the cell in Fig. 4.5.1 (a) and ending with the cell in Fig. 4.5.1 (e), the lateral physical dimensions and the substrate material are unchanged, and the only modification is to increase the metal layer thickness and manipulate the lateral pattern.

### C. Physical Comparison of Presented Cells

To show the actual size reduction potential, the cells in Fig. 4.5.1 (b) and (e) are scaled down in size, and designed to operate at the same  $f_c$  as the basic cell (Fig. 4.5.1 (a)), all with the same substrate permittivity. Therefore, all cells shown in Fig. 4.5.3 resonate at 4.83GHz (identical  $\lambda_c$ ), however their physical dimensions are considerably different, and easy to compare visually.

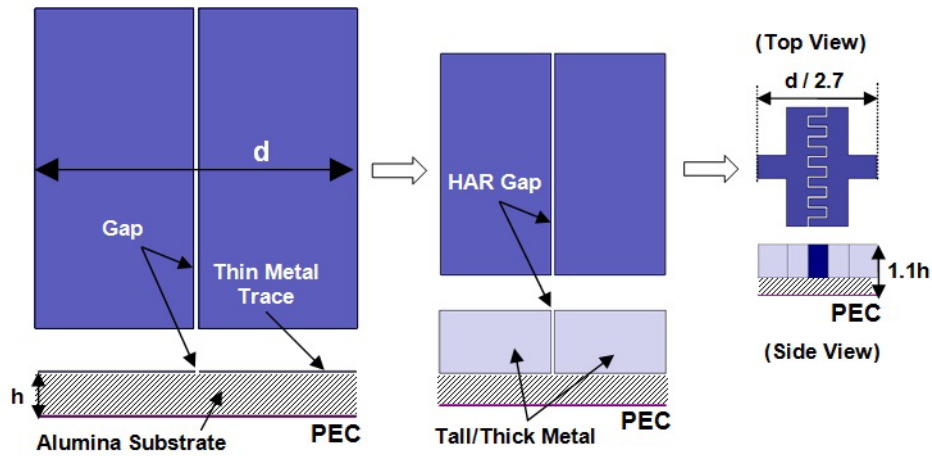


Fig. 4.5.3. Visual comparison between size, thickness, and footprint of the EBG cells in Table 4.5.1. Dimensions of cells (b) and (e) in Fig. 4.5.1 are scaled to operate at the same resonance ( $f_c=4.83$ GHz) of the basic thin EBG cell (a).

As shown in Fig. 4.5.3, the overall thickness of the last cell, i.e. from the PEC ground to the top of the metal layer, is only 1.1 times larger ( $h$  increases to  $1.1h$  in Fig. 4.5.3) than the first (roughly the same) while its cell size is 2.7 times smaller than the first cell. It is worth noting that the footprint is noticeably smaller as it is reduced two dimensionally (by  $2.7^2$  or 7.3 times). This means that the application of interdigitation and trimming causes the ensuing cell to only occupy 13.7% of the surface area taken by the basic thin EBG cell (with identical  $f_c$ ).

It is noted that as expressed by (4.4.10),  $G_a$  is proportional to  $W/\lambda$ . This means that when trying to miniaturize the cell by thickening (compare Fig. 4.5.1 (a) and (b)),  $W$  is fixed while the new resonance is lower (new  $\lambda \uparrow$ ). This fact reduces  $W/\lambda$  and  $G_a$ , which is the typical cost paid to achieve miniaturization. However, as demonstrated in Table 4.2.2, at the same time with the drop in  $G_a$ , loss in the structure drops (due to thickening), which for the proposed antenna under study in Table 4.2.2, favorably yields an increase in efficiency. Therefore, both miniaturization and efficiency enhancement are simultaneously achieved.

#### ***D. The Advantage of Thick Interdigitated Gaps***

When creating an interdigitated capacitor with gaps in thin metal layer (Fig. 4.5.1 (a)), the couplings between interdigits are largely coplanar, occurring outside the gap. This practically limits the number of possible interdigitated arms because using more interdigits reduces the width of each, and lowers the coplanar coupling. In contrast, with HAR gaps (Fig. 4.5.1 (d) and (e)), the dominant coupling mechanism is parallel plate capacitance. In this case, gap capacitance is relatively high, electric fields are contained mainly within the HAR gaps, and the number of interdigits can be increased considerably, up to minimum feature size and maximum AR limitations of the fabrication process. Deep X-ray lithography (DXRL) with metal electroforming, for instance, has been used to realize ARs of  $> 50$  for metal microwave devices [60], and with very smooth sidewalls. Such HAR microfabrication methods allow the designer to reach considerable degrees of freedom to trade-off the number and length of interdigits with metal thickness to drastically reduce the cell size and the size of antennas incorporating these cells, while at the same time improving other antenna characteristics such as radiation efficiency. In addition, the via-less nature of the proposed thick metal cells can considerably simplify the fabrication process. Appendix C describes some of the efforts on prototyping of the proposed antennas using DXRL.

### 4.5.2 Application of Miniaturized EBG Cells to Antenna Design

This section demonstrates the potential for miniaturizing antennas using the proposed cells, by applying them to the novel antenna presented in Sec. 4.1, the self-excited EBG resonator antenna (SE-EBG-RA). The SE-EBG-RA in this case is made of three cascaded thick metal EBG unit cells (cell size  $\ll \lambda_r$ , at the matching/resonance frequency,  $f_r$ ) forming an open circuit microstrip-fed EBG TL. The antenna configurations for two types of cells are shown in Fig. 4.5.5 (a) and (b). The SE-EBG-RA input impedance can be found from (4.1.5),  $Z_{in} = Z_B / \tanh \gamma l$ , where  $Z_B$ , the Bloch line impedance, and  $\gamma$  of the EBG TL (both along Y-axis in Fig. 4.5.2 (a)) can be found using the HFSS/Bloch method in Sec. 4.1.

In (4.1.5),  $l$  is the total antenna length, which in case of the 3-cell antenna structures considered here is 3 times the cell size ( $l = 3 \times 7.2\text{mm}$  for all cells). Using (4.1.5),  $\text{dB}|S_{11}|$  of different versions of SE-EBG-RA with cells shown in Figs. 4.5.1 (c), 4.5.1 (d), and 4.5.1 (e) are calculated and compared in Fig. 4.5.4. The results show a gradual reduction in  $f_r$ . As expected, this behavior corresponds to the gradual decrease in  $f_c$  ( $f_c \neq f_r$ ) already observed in Fig. 4.5.2 (b) and Table 4.5.1.

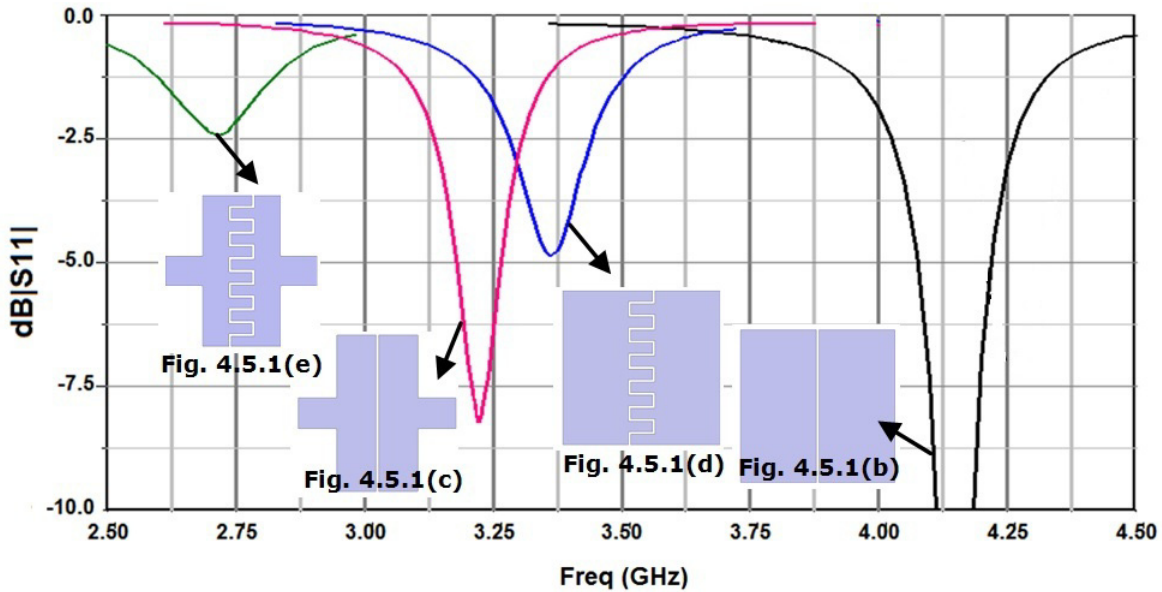


Fig. 4.5.4. Comparison of the input matching of SE-EBG-RAs composed of different EBG cells in Fig. 4.5.1; results are based on HFSS/Bloch method.

For comparison, two of four cases in Fig. 4.5.4 are modeled in HFSS and analyzed completely numerically. This provides independent results that can be compared with the result in Fig. 4.5.4

obtained by HFSS/Bloch method. The antennas in Figs. 4.5.5 (a), and 4.5.5 (b) with identical substrate and physical size are compared, and the radiation patterns are depicted in Figs. 4.5.5 (c) and 4.5.5 (d), respectively (realized gains). The related  $\text{dB}|S_{11}|$  and efficiency are also compared in Fig. 4.5.6. As observed,  $f_r$  in both cases agrees very well with the results shown in Fig. 4.5.4.

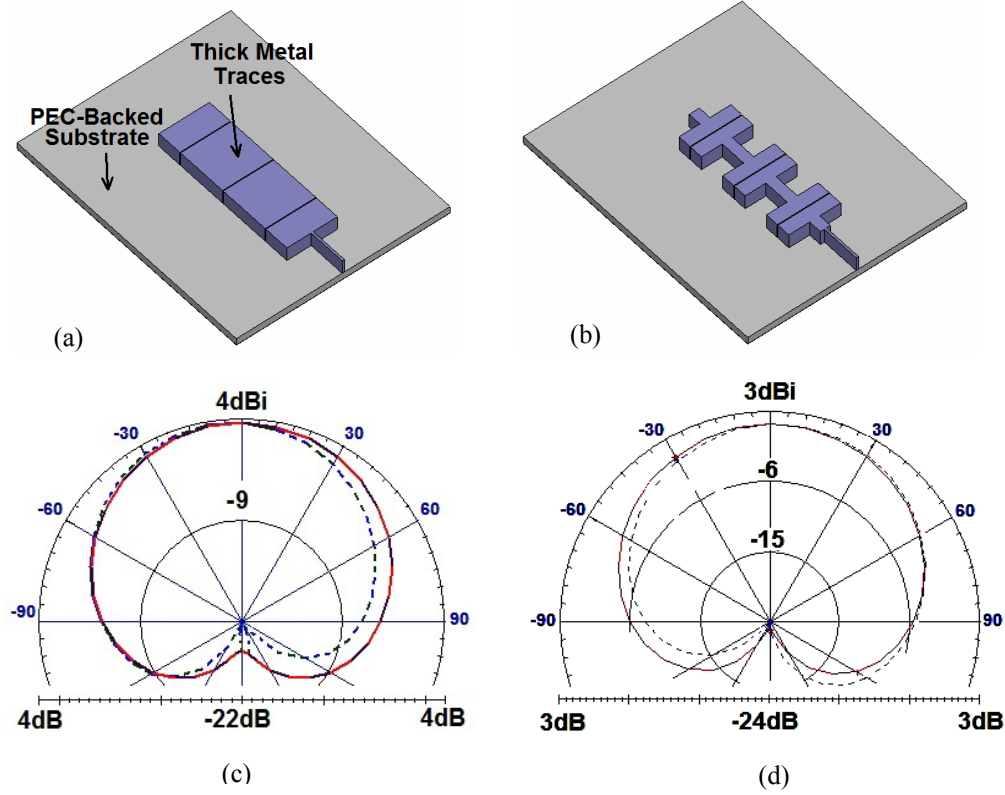


Fig. 4.5.5. 3D view of SE-EBG-RAs composed of EBG cells in Fig. 4.5.1 (b) and (c); Radiation pattern (c)/(d) corresponds to the antennas in (a)/(b); Dashed/solid line is the E/H-plane pattern; ground plane size is  $30 \times 37 \text{ mm}$ ; input  $50\Omega$  MSLs are  $0.3 \text{ mm}$  wide,  $5.25 \text{ mm}$  long, and  $2 \text{ mm}$  tall (same as cells); the cell size is given in Fig. 4.5.1.



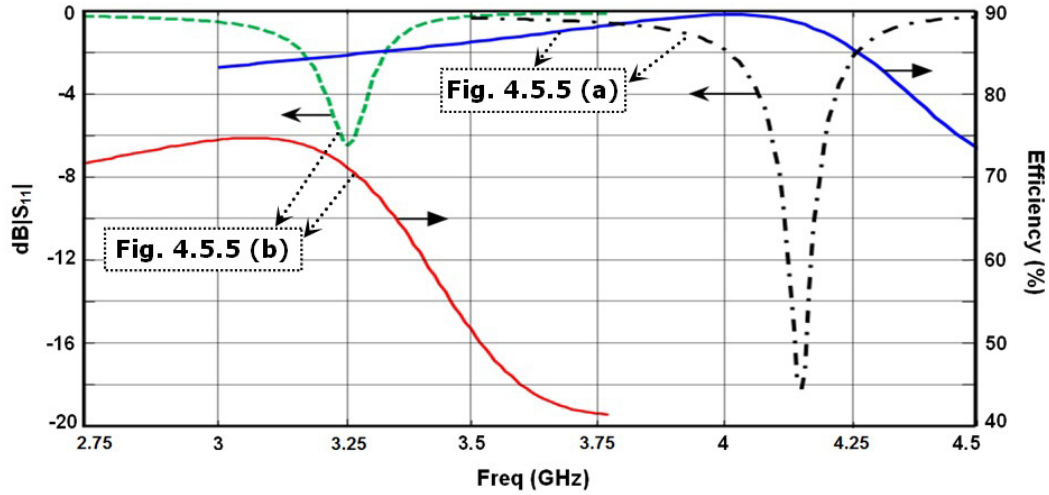


Fig. 4.5.6. Comparison of the resonance frequency and efficiency for the SE-EBG-RAs in Fig. 4.5.5; based on full-wave analysis.

Although the antennas in Fig. 4.5.4 do not target any specific frequency band and are only rendered for demonstration, as observed, they are operating close to some popular bands like unlicensed ISM 2.4GHz [61] or WLAN (2.4/5GHz). Therefore, in case a designer is interested in such miniaturized designs, it is possible to use either scaling or a computationally affordable fine-tuning approach to adjust  $f_r$  to the desired frequency. Specifically indicating the left cell in Fig. 4.5.4, it is observed that the 3-cell SE-EBG-RA based on the cell is matched at 2.7GHz which is very close to 2.4GHz ISM band. It should also be noted that when using different cells in Fig. 4.5.4, to keep comparisons easy and reasonable, the antenna feedline has not changed (at the same size used for the cell on the right, to have  $50\Omega$ ). This condition causes the other three antennas to resonate (the reactive part of  $Z_{in}$  crosses zero), but not exactly be matched to  $50\Omega$ . A  $\lambda/4$  transformer can then be designed and added to each antenna to match them to  $50\Omega$ . Due to the high permittivity of the substrate ( $\epsilon_r=9.9$ ), the physical length added by the transformer will be very small.

### 4.5.3 Conclusion

A methodology is presented to miniaturize an EBG antenna using unit cells with thick metallization and narrow gaps. The effects of several modifications to the metal layer such as trimming, and interdigitating, both separately and simultaneously are demonstrated. The result is a remarkable decline in the resonance frequency while the physical size remains constant. A miniaturized unit cell occupying only 13.7% of the surface area of the basic unit cell demonstrates the potential of the approach for size reduction. Such cells were applied in the structure of a self-excited EBG resonator antenna, demonstrating a drastic reduction in the resonance frequency while maintaining the same physical size.

### References

- [1] F. Yang and Y. Rahmat-Samii, "Reflection phase characterizations of the EBG ground plane for low profile wire antenna applications," *IEEE Trans. Antennas Propagat.*, vol. 51, no. 10, pp. 2691-2703, 2003.
- [2] H. Mosallaei and K. Sarabandi, "Antenna miniaturization and bandwidth enhancement using a reactive impedance substrate," *IEEE Trans. Antennas Propagat.*, vol. 52, no. 9, pp. 2403-2414, Sep. 2004.
- [3] M. Hosseini, A. Pirhadi, and M. Hakkak, "Design of a Non-Uniform High Impedance Surface for a Low Profile Antenna," *J. of Electromag. Waves and Appl.*, vol. 20, no. 11, pp. 1454-1464, 2006.
- [4] S. Collins and Y.M.M. Antar, "Antenna size reduction using Yagi-Uda loops and shorted circular patches," *IEEE Trans. Antennas Propagat.*, vol. 52, no. 3, pp. 855-864, March 2004.
- [5] A. K. Skriverervik, J. F. Zurcher, O. Staub, and J. R. Mosig, "PCS antenna design: the challenge of miniaturization" *IEEE Antennas and Propagation Magazine*, vol. 43, no. 4, pp. 12-27, Mar 2002.
- [6] W. Xia, K. Saito, M. Takahashi, and K. Ito, "Performances of an implanted cavity slot antenna embedded in the human arm," *IEEE Trans. Antennas Propagat.*, vol. 57, no. 4, pp.894-899, Apr. 2009.
- [7] Steven R. Best and Jarrett D. Morrow, "The effectiveness of space filling fractal geometry in lowering resonant frequency," *IEEE Antennas and Wireless propagation letters*, vol. 1, pp. 112-115, Jan 2002.
- [8] G. V. Eleftheriades, and R. Islam, "Miniaturized microwave components and antennas using negative-refractive-index transmission-line (NRI-TL) metamaterials," *Metamaterials*, vol. 1, no. 2, pp. 53-61, Dec 2007.
- [9] M. A. Antoniades and G.V. Eleftheriades, "A CPS leaky-wave antenna with reduced beam squinting using NRI-TL metamaterials," *IEEE Trans. Antennas Propag.*, vol. 56, no.3, pp.708-721, Mar. 2008.
- [10] D. M. Pozar, *Microwave Engineering*, 2nd ed., John Wiley & Sons, 1998.
- [11] C.A. Balanis, *Antenna Theory: Analysis and Design*, 3rd Ed., NJ: Wiley, 2005.
- [12] M. Hosseini, A. Pirhadi, and M. Hakkak, "Compact Angularly Stable AMCs Utilizing Skewed Cross-Shaped FSSs," *Microwave and Optical Technology Letters*, vol. 49, no. 4, pp. 781-786, Apr. 2007.
- [13] M. Rahman and M. A. Stuchly, "Transmission line-periodic circuit representation of planar microwave photonic bandgap structures," *Microwave and Optical Technology Letters*, vol. 30, no. 1, pp. 14-19, 2001.

- [14] Amit M. Patel, and Anthony Grbic, "A Printed Leaky-Wave Antenna Based on a Sinusoidally-Modulated Reactance Surface," *IEEE Trans. Antennas Propag.*, vol. 59, no. 6, pp. 2087–2096, June 2011.
- [15] K. C. Chen, C. K. C. Tzuang, Y. Qian and T. Itoh, "Leaky Properties of Microstrip above a Perforated Ground Plane," *IEEE International Microwave Symposium Digest*, Anaheim, CA, USA, June 1999.
- [16] Park, J. H., Y. H. Ryu, J. G. Lee, and J. H. Lee, "Epsilon negative zeroth-order resonator antenna," *IEEE Trans. Antennas Propag.*, vol. 55, no. 12, pp. 3710-3712, 2007.
- [17] M. Hosseini and D. M. Klymyshyn, "Radiation Properties of EBG Textured Tall Transmission Lines and Applications: A Low Profile Self-Excited EBG Resonator Antenna," *IEEE Antenn. Wireless Propag. Lett.*, vol. 11, pp. 276-280, 2012.
- [18] Lamminen, A.E.I., Vimpari, A.R., Saily, J. "UC-EBG on LTCC for 60-GHz Frequency Band Antenna Application," *IEEE Trans. Antennas Propag.*, vol. 57, no. 10, pp. 2904-2912, Oct. 2009.
- [19] D. Sievenpiper, L. Zhang, R.F. Jimenez Broas, N.G. Alexopolous, and E. Yablonovitch, "High-impedance electromagnetic surfaces with a forbidden frequency band," *IEEE Trans. Microwave Theory Tech.*, vol. 47, no. 11, pp. 2059–2074, Nov. 1999.
- [20] D.F. Sievenpiper, High-impedance electromagnetic surfaces, PhD thesis, Univ. Calif., LA, USA, 1999.
- [21] F. R. Yang, K. P. Ma, Y. Qian, and T. Itoh, "A uniplanar compact photonic-bandgap (UC-PBG) structure and its applications for microwave circuits," *IEEE Trans. Microw. Theory Tech.*, vol. 47, no. 8, pp. 1509–1514, Aug. 1999.
- [22] J. W. Wu, C. F. Jou, and C. J. Wang, "A compact wideband leaky-wave antenna with etched slot elements and tapered structure," *IEEE Trans. Antennas and Propag.*, vol. 58, no. 7, pp. 2176-2183, July 2010.
- [23] H. A. Wheeler, "Fundamental Limitations of Small Antennas," *Proc. of the IRE*, vol. 35, no. 12, pp. 1479-1484, Dec. 1947.
- [24] W. Geyi, "Physical Limitations of Antenna," *IEEE Trans. Antennas Propag.*, vol. 51, no. 8, Aug. 2003.
- [25] Sentucq, B.; Sharaiha, A.; Collardey, S., "Superdirective metamaterial-inspired electrically small antenna arrays," *7th European Conference on Antennas and Propagation (EuCAP)*, Gothenburg, April 2013.
- [26] J. S. McLean, "A re-examination of the fundamental limits on the radiation Q of electrically small antennas," *IEEE Trans. Antennas Propag.*, vol. 44, pp. 672-676, May 1996.
- [27] B. Ghosh, S. M. Haque, D. Mitra, and S. Ghosh, "A Loop Loading Technique for the Miniaturization of Non-Planar and Planar Antennas," *IEEE Trans. Antennas Propag.*, vol.58, no.6, pp.2116-2121, Jun. 2010.
- [28] A. Erentok and R. W. Ziolkowski, "Metamaterial-inspired efficient electrically small antennas," *IEEE Trans. Antennas Propag.*, vol. 56, pp. 691-707, Mar. 2008.
- [29] Y. L. Chow and K. L. Wan, "Miniaturizing patch antenna by adding a shorting pin near the feed probe—a folded monopole equivalent," *the IEEE Antennas and Propag. Society Inter. Symp.*, vol. 4, pp. 6-9, June 2002.
- [30] R. B. Waterhouse, S. D. Targonski, and D. M. Kokotoff, "Design and performance of small printed antennas," *IEEE Trans. Antennas Propag.*, vol. 46, no. 11, pp. 1629–1633, Nov. 1998.
- [31] K.R. Boyle and L. P. Ligthart, "Radiating and balanced mode analysis of PIFA antennas," *IEEE Trans. Antennas Propag.*, vol. 54, no. 1, pp. 231-237, Jan. 2006.

- [32] M. Hosseini and D. M. Klymyshyn, "A Low Profile Efficient Leaky-Wave Antenna Composed of High Aspect Ratio EBG Unit Cells," *IEEE Radio and Wireless Symp.*, Austin, TX, USA, Jan 20-23, 2013.
- [33] D. R. Jackson, C. Caloz, and T. Itoh, "Leaky-Wave Antennas," *Proc. of the IEEE*, vol. 100, no. 7, pp. 2194-2206, July 2012.
- [34] M. Hosseini, M. Hakkak, "Characteristics estimation for jerusalem cross based artificial magnetic conductors," *IEEE Antenna and Wireless Propagation Letters*, vol. 7, pp. 58-61, 2008.
- [35] J. L. Volakis, *Antenna Engineering Handbook*, 4th ed., McGraw Hill Professional, 2007.
- [36] W. H. Kummer and E. S. Gillespie, "Antenna measurements-1978," *IEEE Proc.*, vol. 66, no. 4, pp. 483-507, Apr. 1978.
- [37] D. M. Pozar and B. Kaufman, "Comparison of Three Methods for the Measurement of Printed Antenna Efficiency," *IEEE Trans. Antennas and Propag.*, vol. 36, no. 1, pp. 136-139, Jan. 1988.
- [38] P. Nayeri, F. Yang, and A. Z. Elsherbeni, "Bifocal Design and Aperture Phase Optimizations of Reflectarray Antennas for Wide-Angle Beam Scanning Performance," *IEEE Trans. Antennas Propag.*, vol. 61, no. 9, Sep. 2013.
- [39] J. C. Iriarte, I. Ederra, R. Gonzalo, Y. Brand, A. Fourmault, Y. Demers, L. Salgetti-Drioli, and P. de Maagt, "EBG Superstrate Array Configuration for the WAAS Space Segment," *IEEE Trans. Antennas Propag.*, vol. 57, no. 1, Jan. 2009.
- [40] R. Alkhatib and M. Drissi, "Improvement of bandwidth and efficiency for directive superstrate EBG antenna," *Electronics Letters*, vol. 43, no. 13, June 2007.
- [41] D. R. Reid and G. S. Smith, "A Full Electromagnetic Analysis of Grooved-Dielectric Fresnel Zone Plate Antennas for Microwave and Millimeter-Wave Applications," *IEEE Trans. Antennas Propag.*, vol. 55, no. 8, Aug. 2007.
- [42] M. Yousefbeigi, A. Enayati, M. Shahabadi and D. Busuioc, "Parallel-series feed network with improved G/T performance for high-gain microstrip antenna arrays," *Electronics Letters*, vol. 44, No. 3, Jan. 2008.
- [43] Atef Z. Elsherbeni, Payam Nayeri, and Fan Yang, "Reflectarray Antennas for Space Applications," *IEEE International Conference on Ultra-Wideband*, Sept. 2012.
- [44] M. Hosseini and S. Bashir, "A novel circularly polarized antenna based on an artificial ground plane," *Progress In Electromagnetics Research Letters*, vol. 5, pp. 13-22, 2008.
- [45] M. Hosseini, A. Pirhadi, and M. Hakkak, "Design of a Non-uniform High-Impedance Surface for a Low Profile Antenna," *J. of Electromagnetic Waves and Applications*, vol. 20, no. 11, pp. 1454-1464, 2006.
- [46] David M. Pozar, "Microstrip Antennas," *Proc. IEEE*, vol. 80, no. 1, pp. 79-91, Jan 1992.
- [47] C. Caloz and T. Itoh, "Transmission line approach of left-handed (LH) materials and microstrip implementation of an artificial LH transmission line," *IEEE Trans. Antennas Propag.*, vol. 52, no. 5, pp. 1159-1166, May 2004.
- [48] M.F. Karim, A.Q. Liu, A. Alphones, X.J. Zhang and A.B. Yu, "CPW band-stop filter using unloaded and loaded EBG structures," *IEE Proc. Microw. Antennas Propag.*, vol. 152, no. 6, pp. 434-440, Dec. 2005.

- [49] J. S. Gomez-Diaz, A. Álvarez-Melcon, and T. Bertuch, "A Modal-Based Iterative Circuit Model for the Analysis of CRLH Leaky-Wave Antennas Comprising Periodically Loaded PPW," *IEEE Trans. Antennas and Propaga.*, vol. 59, no. 4, pp. 1101-1112, Jan 2011.
- [50] M. Lee, B.A. Kramer, C. Chen, and J. L. Volakis, "Distributed Lumped Loads and Lossy Transmission Line Model for Wideband Spiral Antenna Miniaturization and Characterization," *IEEE Trans. Antennas and Propaga.*, vol. 55, no. 10, pp. 2671-2678, Oct. 2007.
- [51] J. J. Adams and J.T. Bernhard, "Broadband Equivalent Circuit Models for Antenna Impedances and Fields Using Characteristic Modes," *IEEE Trans. Antennas and Propaga.*, vol. 61, no. 8, Aug. 2013.
- [52] G.V. Eleftheriades, A.K. Iyer, and P.C. Kremer, "Planar Negative Refractive Index Media Using Periodically L-C Loaded Transmission Lines," *IEEE Trans. Microwave Theory Tech.*, vol. 50, no. 12, pp. 2709-2712, Dec. 2002.
- [53] B. Mohajer-Iravani and O.M. Ramahi, "Wideband Circuit Model for Planar EBG Structures," *IEEE Transactions on Advanced Packaging*, vol. 33, no. 1, pp. 169-179, Feb. 2010.
- [54] I. J. Bahl and R. Garg, "Simple and accurate formulas for a microstrip with finite strip thickness," *Proceedings of the IEEE*, vol. 65, no. 11, pp. 1611-1612, Nov. 1977.
- [55] Thomas A. Milligan, *Modern Antenna Design*, 2nd ed. John Wiley & Sons, 2005.
- [56] A. Alphones and J. Cheng, "Compact interdigitated microstrip bandpass filter with meandered EBGs," *European Microwave Conference*, Singapore, 2009.
- [57] B.Q. Lin, J. Liang, Y.S. Zeng, and H. M. Zhang, "A novel compact and wide-band uni-planar EBG structure," *Progress In Electromagnetics Research C*, vol. 1, pp. 37-43, 2008.
- [58] S. Jahani, J. Rashed-Mohassel, and M. Shahabadi, "Miniaturization of Circular Patch Antennas Using MNG Metamaterials," *IEEE Antenn. Wireless Propag. Lett.*, vol. 9, pp., 2010.
- [59] M. Coulombe, S. Farzaneh Koodiani, and C. Caloz, "Compact Elongated Mushroom (EM)-EBG Structure for Enhancement of Patch Antenna Array Performances," *IEEE Trans. Antennas and Propaga.*, vol. 58, no. 4, April 2010.
- [60] D. M. Klymyshyn, M. Börner, D. Haluzan, E. Gono Santosa, M. Schaffer, S. Achenbach, J. Mohr, "Vertical High-Q RF-MEMS Devices for Reactive Lumped Element Circuits," *IEEE Trans. Microwave Theory Tech.*, vol. 58, no. 11, pp. 2976-2986, Nov. 2010.
- [61] F. Merli, L. Bolomey, J. Zurcher, G. Corradini, E. Meurville, A.K. Skrivervik, "Design, Realization and Measurements of a Miniature Antenna for Implantable Wireless Communication Systems," *IEEE Trans. Antennas and Propaga.*, vol. 59, no. 10, pp. 3544-3555, Oct 2011.

# Chapter 5

## Extended Ideas and Designs

### 5 Extended Ideas and Designs

This chapter extends the ideas developed in Chap. 4, while orienting the extension towards different applications or demands. Sec. 5.1 introduces a HAR leaky-wave antenna, in contrast to the resonant antennas presented in Chap. 4, however based on the same HAR EBG cells and dispersion diagram (HFSS/Bloch). Sec. 5.2 presents a series-fed array antenna based on the proposed cells. In Sec. 5.3, a novel EBG microstrip antenna is studied which shows fast-wave behaviors and better performance, as compared to the conventional patch antenna. Finally, in Sec. 5.4, a very small and efficient version of the SE-EBG-RA (introduced in Chap. 4) is presented which is able to radiate circular polarization.

## **5.1 Low-Profile Efficient Leaky-Wave Antennas with Proposed EBG Cells**

This section proposes a very efficient low profile leaky-wave antenna (LWA) made of high aspect ratio (HAR) electromagnetic bandgap (EBG) unit cells. As described in Chap. 3 (see Fig. 3.4), the proposed HAR unit cells can be used within either the leaky-zone of the cell dispersion diagram or the slow-wave zone, resulting in either a LWA or a resonant antenna, respectively. On the contrary to the previous sections, this section focuses on LWAs and proposes a high performance HAR LWA. The idea is the first attempt to incorporate HAR EBG cells into the structure of LWAs. To develop the idea, a LW transmission line (LW TL) is introduced, which is textured of HAR EBG cells, and then, an open circuit piece of such a LW TL is utilized as a LWA. The results show that the simultaneous contribution of EBG cells and HAR metal traces yields maintained efficiency while reducing the structure resonance.

### **5.1.1 Introduction**

LWAs are found to be inexpensive low profile but effective candidates satisfying the demands for easy to integrate, flat, high gain antennas for many communication systems such as those mounted on vehicles (most well-known automotive radars, as described in Fig. 5.1.1) or other platforms [1-2]. Generally speaking, a planar LWA is like a planar TL which is leaking a portion of the power while guiding the other portion along its structure so that the parts located farther can be simply fed sequentially, with no separate feed lines or components. Such LWAs are typically characterized by a phase and leakage constant along their radiating structure [1]. The analysis approach in this section is based on the HFSS/Bloch method described in Sec. 4.1, however the closed-form equations developed in Sec. 4.4 could also be applied to the design of such LWAs. In addition to the analysis, a synthesis and design process is also suggested for the proposed LWA.

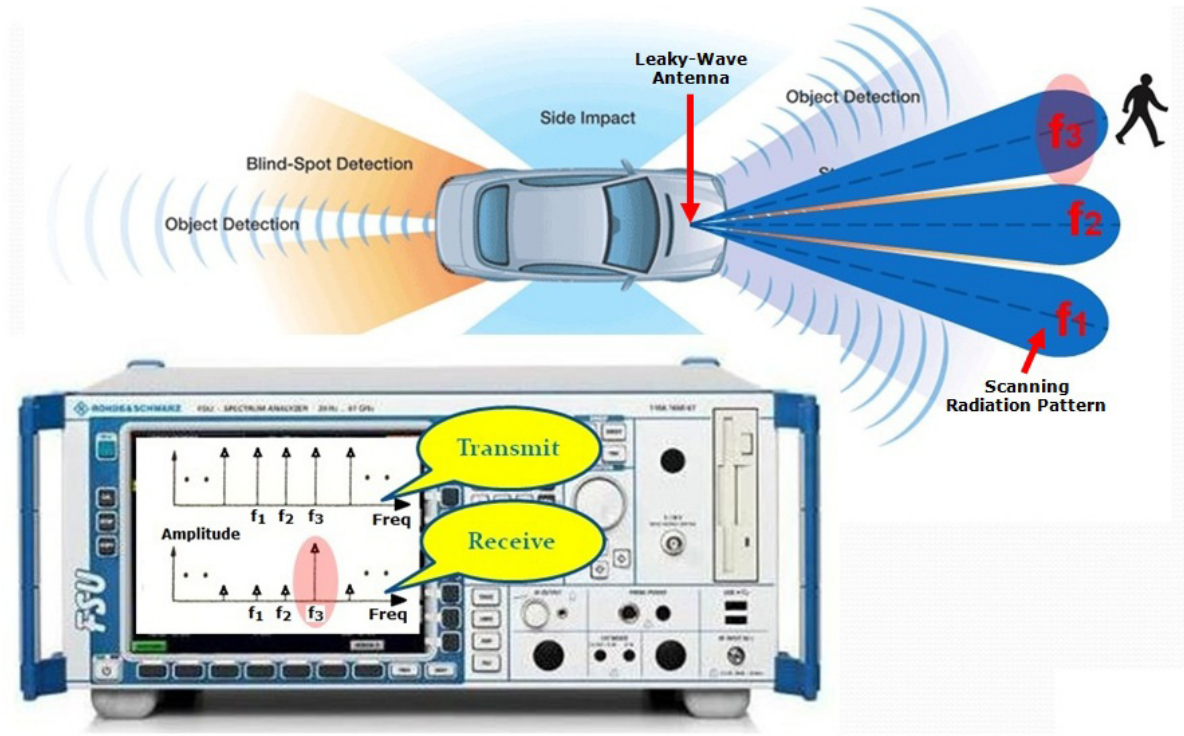


Fig. 5.1.1. General description of an automotive radar system with a frequency scanning LWA antenna on the car front. The transmit frequency is swept continuously over the leaky range, making the pattern scan. The receive signal is then inspected for possible frequency components returned from the object (every component represents a unique angle).

### 5.1.2 Proposed LWA Structure

An EBG unit cell with dimensions given in Fig. 5.1.2 (a) is considered, which is the same cell proposed in Sec. 4.1. However in this section, the cell is utilized in the leaky-wave frequency zone rather than the slow-wave zone (see Fig. 5.1.2 (b)), which is the key to achieve a scanning radiation pattern [1], [3].

The analysis is initiated by regarding the unit cell as a HAR microstripline (MSL), periodically loaded at the center by a narrow gap (see Fig. 5.1.2 (a)). For such a cell, the HFSS/Bloch method (see Sec. 4.1 or [4-5]) provides an equivalent line impedance and propagation constant ( $\alpha + j\beta$ ). Fig. 5.1.2 (b) shows  $\alpha$  and  $\beta$  versus frequency, which describe the dispersive behaviors of the loaded TL textured by repeating such a unit cell. To characterize the leaky and bound modes of the EBG textured TL, LW, fast, and slow-wave regions are indicated in Fig. 5.1.2 (b). These regions are differentiated in the same manner in [e.g. 3].



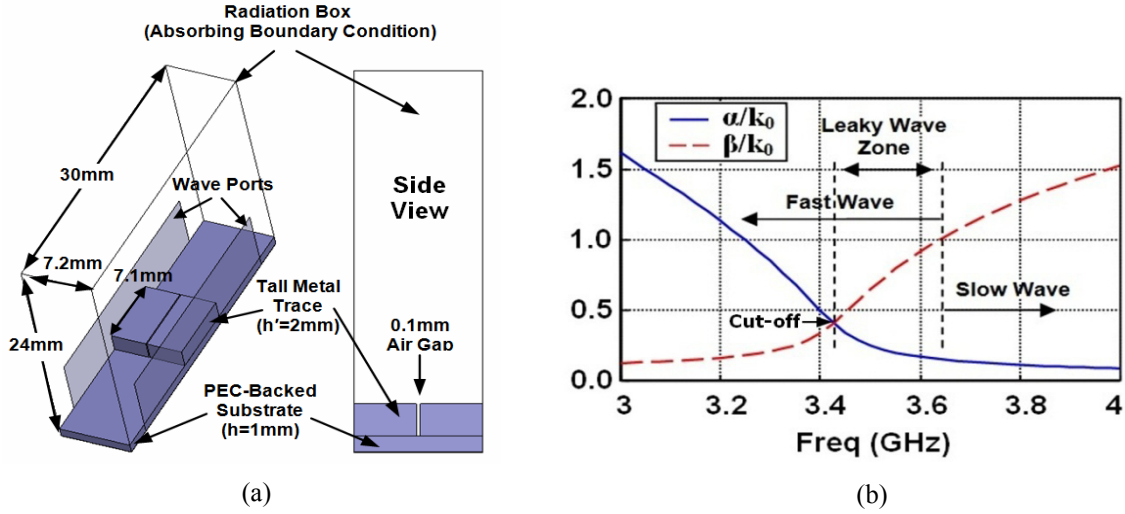


Fig. 5.1.2. a) The unit cell and HFSS model for the HAR EBG cell (size  $\sim \lambda/11 \times \lambda/11 \times \lambda/28$ ), b) dispersion behavior expressed by the normalized propagation constant versus frequency; the substrate is Alumina with  $\epsilon_r=9.9$ ,  $\tan\delta=0.003$ , and metal is copper,  $\sigma=5.8e7s/m$ .

For a LWA made out of a large number of EBG cells (here 12), the antenna demonstrates a traveling wave behavior [1] and the signal reflected towards the input port can be assumed negligible (the proposed LWA is open one side, with no matched load). This feature causes the LWA (see Fig. 5.1.3) to show an input impedance roughly equal to the line impedance. The Bloch line impedance,  $Z_B$ , can be calculated as described in Sec. 4.1 (also in [4-5]), the value of which at the center of the LW zone of Fig. 5.1.2 (b) (i.e. 3.54GHz) is  $2.64\Omega - j0.81\Omega \approx 2.64\Omega$ . Although this impedance is very low, it will be shown later that the EBG LWA possesses a high efficiency ( $\eta$ ) of  $\sim 90\%$ . It is reminded that as opposed to small antennas, for electrically large antennas like this LWA, radiation resistance ( $R_r$ ) is *not necessarily* close to the input resistance and could be its transformed version. This is one reason for  $R_r$  and hence  $\eta$  to remain high. Fig. 5.1.13 plots this impedance versus frequency. Then, as illustrated in Fig. 5.1.3, a  $\lambda/4$  HAR MSL matching section ( $Z_{match}^2 \sim 50 \times 2.64$ ) roughly transforms this low impedance to the standard  $50\Omega$  value. The ensuing structure is the HAR LWA shown in Fig. 5.1.3 made of 12 HAR EBG cells and the matching circuit. Because the antenna operates within the LW zone of Fig. 5.1.2 (b), it is expected to have a scanning pattern (i.e. the main lobe radiation direction changes with frequency). This behavior is expressed by [3, 6]

$$\theta_m = \arcsin(\beta/k_0) \quad (5.1.1)$$

(5.1.1) gives the angle of the main lobe from the broadside direction (Z-axis). The scanning occurs in the XZ plane in Fig. 5.1.3. As seen, for the case in Fig. 5.1.2 (b),  $\beta/k_0$  ranges from  $\sim 0.44$  to 1 over LW zone which, according to (5.1.1), means the antenna should be ideally able to scan over  $26^\circ < \theta_m < 90^\circ$ .

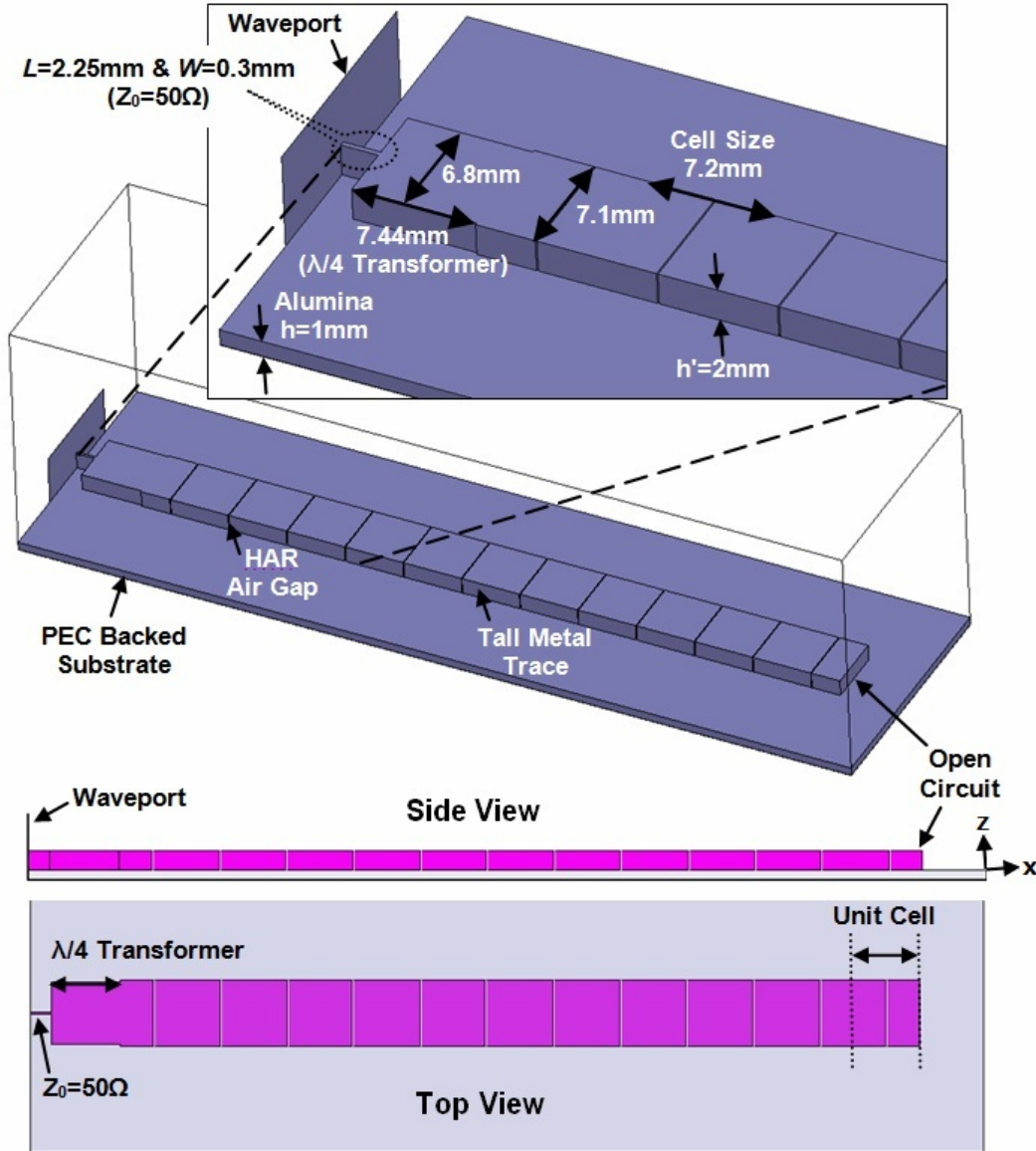
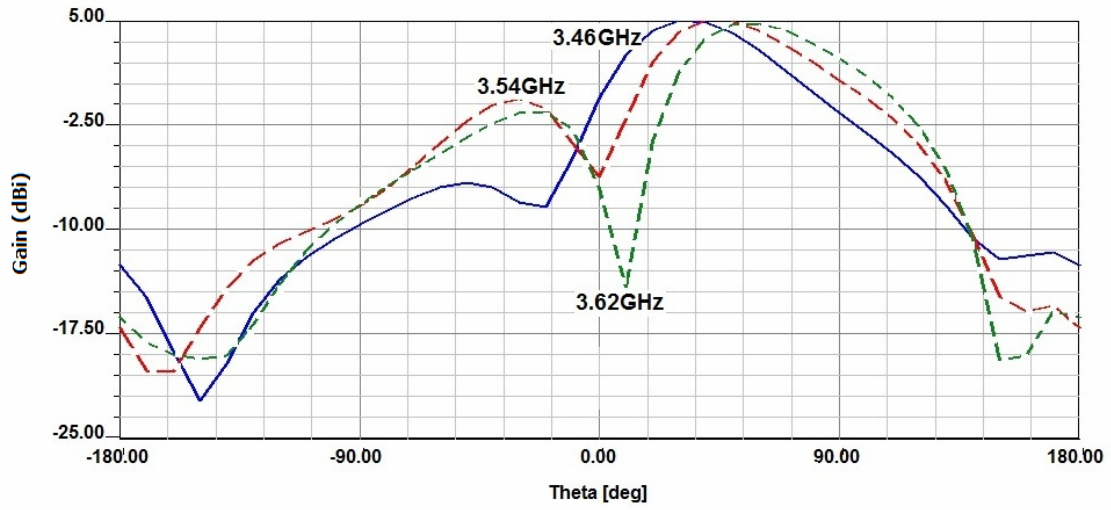


Fig. 5.1.3. HFSS model of the proposed LWA with 12 EBG cells. A  $\lambda/4$  transformer with the same thickness as the antenna matches the antenna to a 50Ω line; ground plane size is 30mm×103mm ( $1.24\lambda \times 0.36\lambda$ ); cell Size is  $\sim \lambda/11 \times \lambda/11 \times \lambda/28$ ;  $\lambda$  is the wavelength at matching frequency.

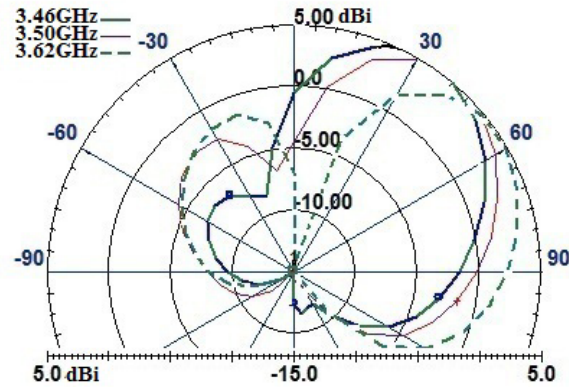
In practice however, due primarily to the limited size of the antenna and deviation from the theoretical condition for validity of (5.1.1),  $\theta_m$  has an upper limit much lower than  $90^\circ$ . Table 5.1.2 presented later shows that the upper limit is  $65^\circ$  and  $67^\circ$  for two different LWAs.

### 5.1.3 Simulation Results

The HFSS simulation results including gain/radiation pattern, input matching, and efficiency are shown in Fig. 5.1.4 and Fig. 5.1.5. As seen, the input is matched over the LW zone (see Fig. 5.1.2 (b)) which justifies the assumption of the traveling wave nature. The natural beam scanning behavior of a LWA is also obvious in Fig. 5.1.4.



(a)



(b)

Fig. 5.1.4. The realized gain of the HAR EBG LWA at three different frequencies, showing the typical beam scanning of LWAs, a) rectangular radiation pattern ( $\phi=0$ ), b) polar radiation pattern at ZX plane ( $\phi=0$ ).

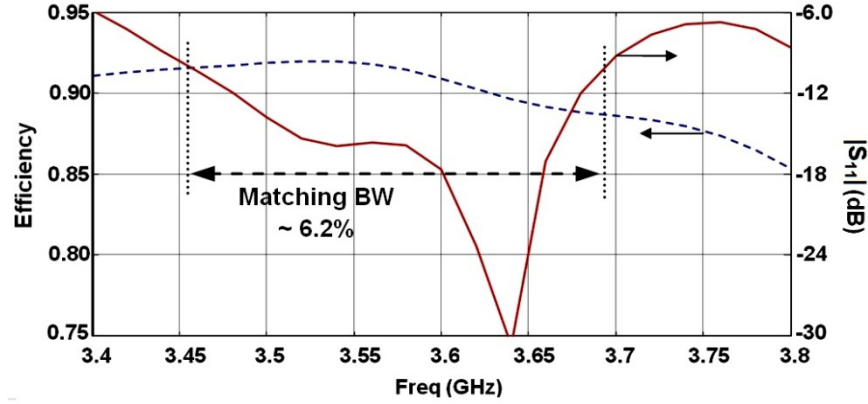


Fig. 5.1.5. Radiation efficiency and return loss of the HAR EBG LWA around the LW zone in Fig. 5.1.2 (b).

Having the total electrical length of  $1.24\lambda$  (XYZ:  $1.24\lambda \times 0.36\lambda \times \lambda/28$ ) which is much smaller than  $\sim 4\lambda$  for traditional MSL LWA [3] and still maintaining a high efficiency of  $\sim 90\%$  with  $\sim 5\text{dBi}$  gain are distinguishing properties of the proposed LWA.

#### 5.1.4 Comparison with Similar LWAs

To highlight the advantages of the proposed HAR EBG LWA, two published LWAs are reviewed and their physical and electrical properties are discussed. The first antenna is shown in Fig. 5.1.6 [6].

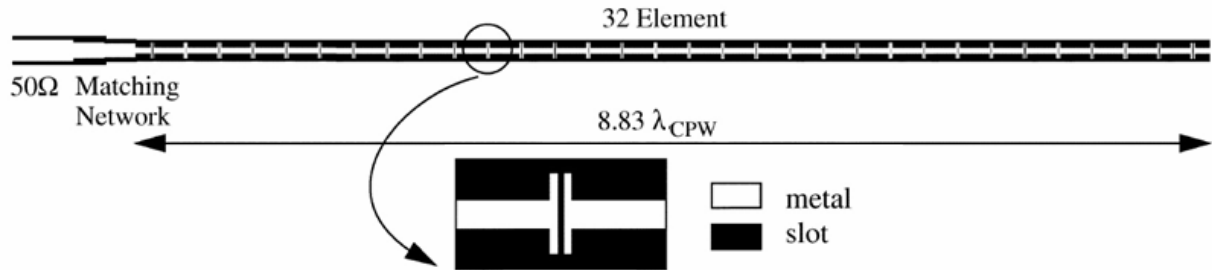


Fig. 5.1.6. Top layer view of the periodic planar LWA presented in [6], which is designed employing coplanar waveguides; © IEEE 2002.

This planar antenna resonates at 30GHz, and is comprised of 32 cells, each  $\lambda/5$  ( $\lambda$  at 30GHz) long. The effective reported gain is  $\sim 9\text{dBi}$  and the efficiency is 95%. As seen, this antenna is highly efficient at the expense of being very long at  $\sim 8\lambda$ . Typically, LWAs have to be at least  $4\lambda$  [3] to be able to have the cumulative radiation large enough to dominate the loss and result a

high efficiency. To resolve this problem, [3] presents an electrically small LWA with a periodic feature on both ground plane and top metal layer, as in Fig. 5.1.7. The design can reach a length as small as  $1.15\lambda$  but at the expense of poor radiation efficiency ( $\sim 30\%$ ) and hence deteriorated radiation gain. Although such a design can reduce the size unconventionally ( $\ll 4\lambda$ ), due to missing the cumulative radiating aperture, the radiation cannot effectively dominate the loss. Another issue with such a design is the complexity of the design process because the performance is dependent on the size of so many features on both sides of the ground plane. For instance, Fig. 5.1.7 shows the tapered nature and complexity of the traces on the top layer.

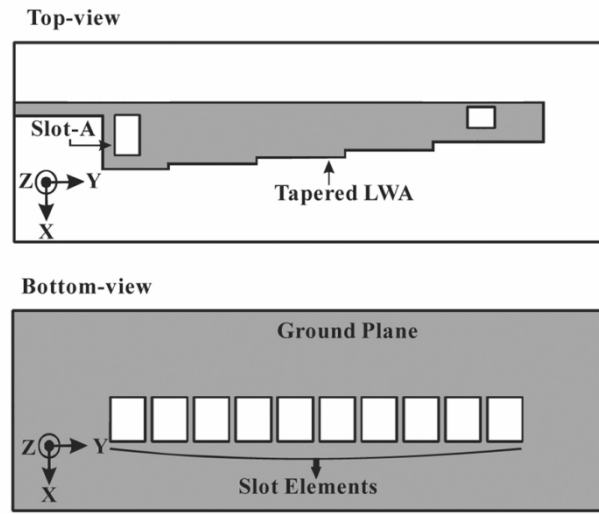


Fig. 5.1.7. The top and bottom views of the periodic planar LWA presented in [3]; © IEEE 2010.

Comparing the proposed HAR EBG LWA to these two examples, not only is it electrically small ( $1.24\lambda \times 0.36\lambda \times \lambda/28$ ) due the special characteristics that its periodic unit cell provides, but also it successfully maintains the radiation efficiency at a very high level of at least 88% over the operating range. This outstanding performance is obtained thanks to the simultaneous application of the EBG concept and trace thickening strategy, while purposefully keeping the aspect ratio of the gaps as high as  $\sim 20$  (the gap size is kept much smaller than the thickness).

### 5.1.5 Array of the Proposed LWAs

In this part, two of the proposed HAR EBG LWAs are arrayed to investigate the possibility of providing a higher aperture gain, while maintaining the scanning nature. Fig. 5.1.8 shows the array configuration for which the element spacing is set to be relatively small at  $\sim 0.35\lambda$ . The

dimensions of each element are given in Fig. 5.1.3, while details of the feed lines are provided in Fig. 5.1.8. As seen, similar to the antennas, all feedlines are also composed of HAR MSLs to cause a uniform integrated top metal layer that could be possibly fabricated by a single exposure, for instance, using fabrication methods like UV-LIGA or Deep X-ray LIGA (Appendix C).

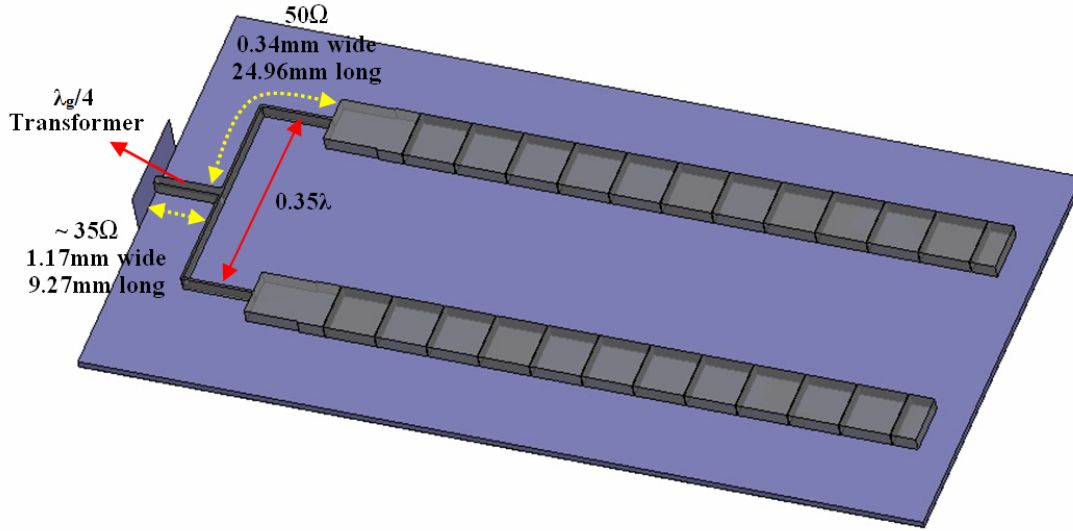


Fig. 5.1.8. 3D view of a 2-element array of the HAR LWA shown in Fig. 5.1.3; ground plane is 118mm×60mm ( $0.72\lambda \times 1.38\lambda$ );  $\lambda$  is the wavelength at matching frequency; the transformer provides 50Ω input impedance.

Fig. 5.1.9 shows the rectangular plot of the realized gain at the scanning plane and demonstrates that the antenna has retained its scanning nature satisfactorily. This robustness is very noticeable when reminded that the array spacing is relatively small at  $0.35\lambda$ .

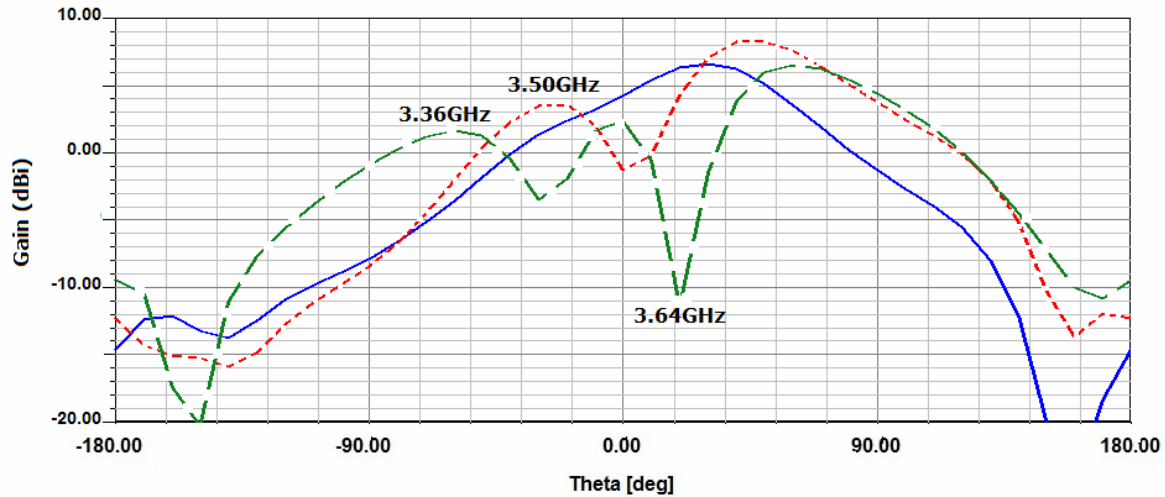


Fig. 5.1.9. Rectangular plot of the realized gain at scanning plane ( $\phi=0$ ) for the 2-element HAR LWA array.

Reduced electrical spacing could bring about mutual coupling in regular arrays and not only could cause mismatch, but also could deteriorate the LW behavior of cells. The fact that such a tight arraying does not change the LW behavior of the antenna highlights the role that EBG cells play in suppressing the surface waves and that the proposed EBG LWA elements have the potential to form high-efficiency high-gain LWA arrays.

Table 5.1.1 compares the physical, electrical, and radiation properties of both 1- and 2-element antennas. As seen, the 2-element outweighs the 1-element in almost any feature except for the maximum F/B radiation ratio over the specified frequency range. Specifically, it is observed that the realized gain is 1.51dBi more for the 2-element case. It is noted that if the decrease in  $G_r$  could be tolerated down to 4dBi (with F/B>5dB), then 1-element antenna can offer even a wider scanning range of  $25^\circ < \theta < 65^\circ$  (see Table 5.1.2 for details). The same situation is expected to occur for the 2-element array.

Table 5.1.1. Comparison between physical, electrical, and radiation properties of both 1- and 2-element LW antennas;  $\lambda$  is the wavelength at matching frequency;  $G_r$  is the realized gain.

	Max F/B (dB)	All Over Frequency Range		Frequency Range (GHz)	Frequency Mistuning (%)	$\eta$ at Center Freq (%)	Scanning Range (deg)	Array Electrical Size
		Min $G_r$ (dBi)	Max $G_r$ (dBi)					
1-Element	6.9	5.0	5.1	3.46 to 3.62	0	92	30 to 58	$0.35\lambda \times 1.22\lambda$
2-Element	4.1	6.51	8.3	3.36 to 3.64	< 1.1	92	30 to 60	$0.72\lambda \times 1.38\lambda$

### 5.1.6 Applying the Scaling Principle

In order to show that the LWA design of Fig. 5.1.3 could be useful in other frequencies as well, the unit cell is downsized and then the antenna LW performance is scrutinized. The idea is to divide all physical features by 3 (as an example) and expect to have the antenna resonate at approximately 3 times higher frequency. However, scaling could result in dimensions, which are not round or might not be feasible in practice, and hence, after scaling, the dimensions are modified. For example, scaling turns the 100 $\mu$ m gap to 100/3, which is rounded to 38 $\mu$ m, and turns the 2mm thickness to 2mm/3, which is again rounded to 0.7mm. Most importantly, due to the availability of 0.5mm alumina substrates, the 1mm thickness is rounded to 0.5mm rather than 1mm/3. Table 5.1.2 compares the original design (#1) and the scaled one (#2) along with

dimensions and electrical properties of the antennas simulated in HFSS. As seen, the scanning properties of the antenna #2 are all retained and its frequency of operation is increased from 3.6GHz to 8.8GHz. The increase is 2.45 times (less than the expected 3) which is attributed mainly to the rounding applied, especially on the thickness of the dielectric substrate.

Table 5.1.2. Comparison between the physical, electrical, and radiation properties of the LWA in Fig. 5.1.3 and its scaled version;  $\lambda$  is the wavelength at matching frequency;  $G_r$  is the realized gain.

	Design #1	Design #2 (Scaled)
<b>Aspect Ratio</b>	2mm/0.1mm or 20	700 $\mu$ m/38 $\mu$ m or 18
<b>Substrate</b>	Alumina ( $\epsilon_r=9.9$ ), 1mm	Alumina ( $\epsilon_r=9.9$ ), 0.5mm
<b>Metal Thickness</b>	2mm	700 $\mu$ m
<b>Metal Material</b>	Copper	Nickel
<b>Realized Gain, <math>G_r</math></b>	> 4dBi with F/B>5dB	3.5dBi< $G_r$ <6.3dBi with F/B>4.5dB
<b>Scanning Range</b>	$25^\circ < \theta < 65^\circ$	$31^\circ < \theta < 67^\circ$
<b>Minimum Efficiency, <math>\eta</math></b>	88%	85% (with Nickel)
<b>Center Frequency</b>	$\sim 3.6$ GHz	$\sim 8.8$ GHz
<b>Bandwidth, BW</b>	$\sim 6.2\%$	$\sim 7\%$
<b>Electrical dimensions: XYZ</b>	$1.25\lambda \times 0.36\lambda \times \lambda/28$	$1.45\lambda \times 0.38\lambda \times \lambda/25$
<b>Number of Unit Cells</b>	12	12
<b>Unit Cell Size XY</b>	7.2mm $\times$ 7.1mm	2.738mm $\times$ 2.7mm
<b>Gap Size</b>	100 $\mu$ m	38 $\mu$ m
<b>Dimensions of Transformer Section</b>	Fig. 5.1.3, XY: 7.44mm $\times$ 6.8mm	Fig. 5.1.11, XY: 3mm $\times$ 3.44mm
<b>Ground Plane Size: XY</b>	103mm $\times$ 30mm	40.7mm $\times$ 12.8mm

For the design #2 in Table 5.1.2, a numerical comparison is set to assure the soundness of port modeling. To do this, rather than a rectangular waveport in HFSS, as in Fig. 5.1.10 (a), this port is replaced with a SMA connector excited by a circular waveport. The dimensions and the insulator material of the coaxial core of the SMA connector are chosen to be very close to a practical SMA connector with 50 $\Omega$  impedance.



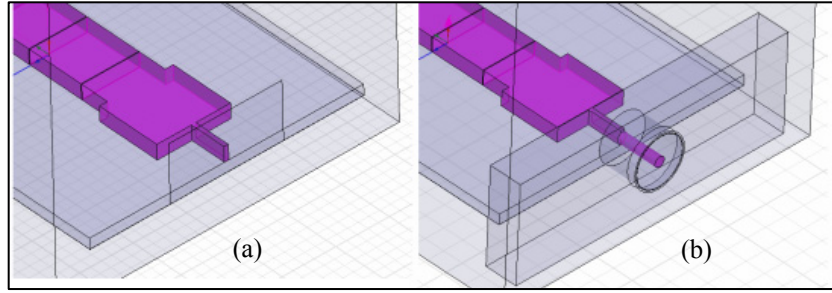


Fig. 5.1.10. The scaled LWA, a) modeled by rectangular a waveport, as assumed for design #1 in Table 5.1.2, b) modeled when replacing the rectangular waveport with a 50Ω SMA connector excited by a circular waveport.

Fig. 5.1.11 compares the input matching of the design #2 in Table 5.1.2 with and without this connector. As observed, the BW is maintained at  $\sim 7\%$  for both cases, and the SMA connector modeling only introduces a *negligible* upward shift.

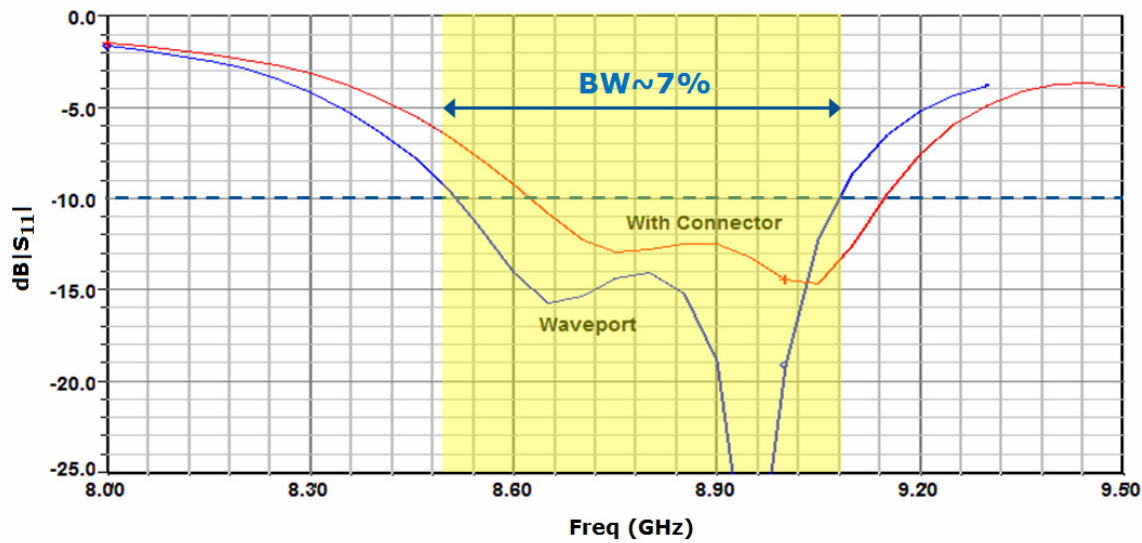


Fig. 5.1.11. Comparison between the simulated input matching of the design #2 in Table 5.1.2 with and without the SMA connector.

Fig. 5.1.12 (a) shows the related HFSS 3D model. Two large views of the connector and the antenna transformer section are also included in Fig. 5.1.12 (b) and (c) with an emphasis on the connector 3D configuration and the insulator, respectively. The port impedance calculated by HFSS at the circular waveport is  $53\Omega$ , which is very close to the expected  $50\Omega$ .

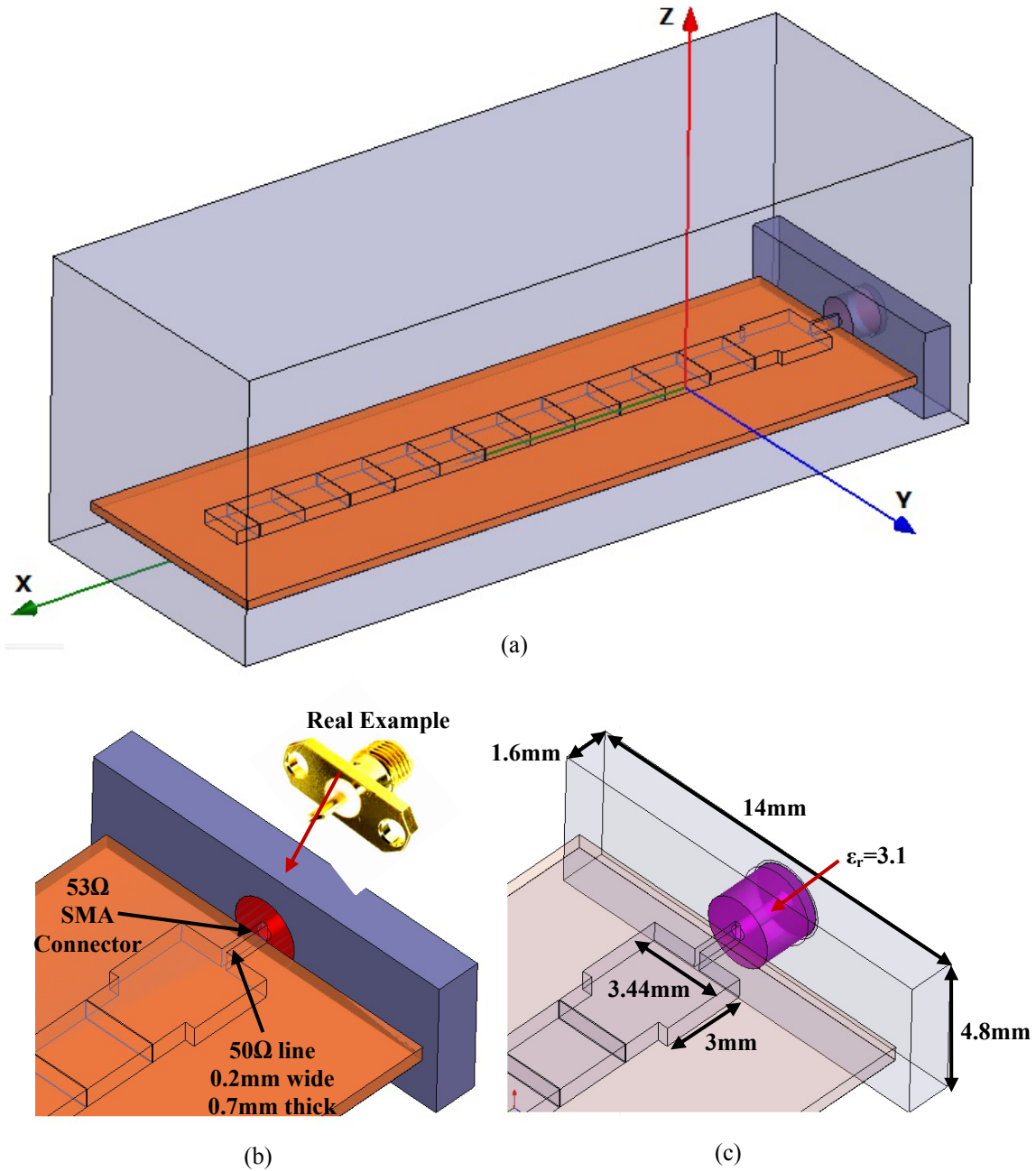


Fig. 5.1.12. a) 3D view of the scaled LWA modeled when replacing the rectangular waveport with a 50Ω SMA connector excited by a circular waveport (design #2 in Table 5.1.2); for clarification, two different enlarged views of the connector and feed point section are rendered as well.

### 5.1.7 Design Process

Up to this step, the analysis of an EBG cell with known dimensions and substrate material, using the HFSS/Bloch method, was described. Two sample HAR EBG LWAs were rendered based on such cells, and simulation results were presented. To supplement those studies, this part is dedicated to the design/synthesis (as opposed to the analysis) of the HAR EBG LWA. The goal is to practically apply the knowledge gained on such an antenna to the design of real-life antennas requiring specific frequency bands. To meet this goal, the design process can be broken down into the following steps:

- 1- Choose the substrate material/thickness and a feasible range of the aspect ratio for gaps (i.e. gap size).
- 2- Use the circuit model (Sec 4.4, equ. (4.4.5)) to find a set of initial dimensions for the cell so that its cut-off frequency is roughly close the design frequency<sup>40</sup>.
- 3- For these initial dimensions, sketch the dispersion diagram by HFSS/Bloch method over an adequately wide frequency range.
- 4- Sketch the related Bloch equivalent impedance,  $Z_B$  (Fig. 5.1.13) over the same range.
- 5- Assume a large number of cells to have a traveling wave, and therefore,  $Z_{in} \approx Z_B$ .
- 6- Find the leaky-wave zone in the dispersion diagram and pick an average  $Z_B$  ( $Z_{Bav}$ ) in the middle of this zone from the  $Z_B$  curve (e.g.  $2.7\Omega$  in Fig. 5.1.13). Assume  $Z_{in} \approx Z_{Bav}$ .
- 7- Design a quarter-wave transformer to match this typically low  $Z_{in}$  to  $50\Omega$  line.
- 8- Model the whole LWA including the transformer and a large number of cells (typically 10 to 15) in HFSS and numerically find the matching range.
- 9- Inspect the scanning feature of the simulated pattern, ideally over the matching range.
- 10- Inspect the common frequency range where matching and scanning are both desirable.
- 11- If the common range is small and the scanning range, gain, or F/B are not maintained well in this range, return to the initial values in Step 2, slightly adjust them, and repeat the process.
- 12- Repeat the whole process until the desired scanning range, gain, F/B, and efficiency are achieved.

---

<sup>40</sup> It is noted that (4.4.5) estimates the cut-off frequency, which is the lower limit of the LW zone (see Fig. 4.6.2 (b)), and hence, the center of the zone is slightly above this estimated frequency. In fact, the design frequency should be placed roughly at the center of the LW zone not at the cut-off.

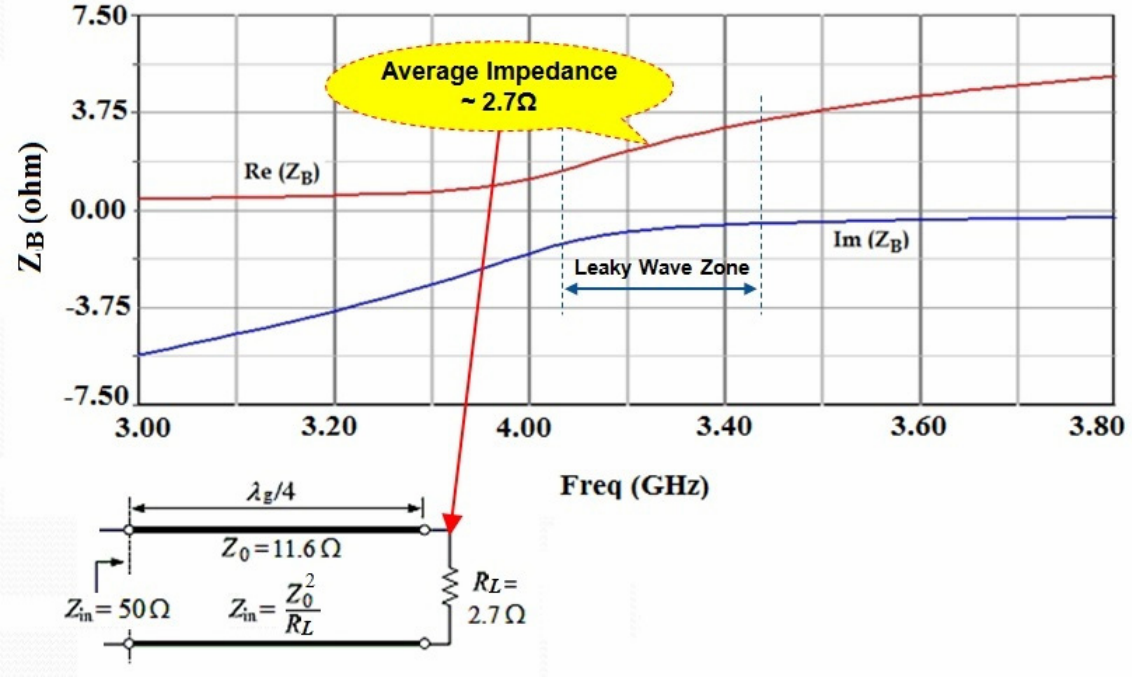


Fig. 5.1.13. Bloch line impedance versus frequency generated by HFSS/Bloch method, associated with the dispersion diagram of Fig. 5.1.2, and the description of how the curve is used to design a matching network for the proposed LWA.

### 5.1.8 Conclusion

A very efficient low profile leaky-wave antenna made of high aspect ratio EBG unit cells is proposed. The antenna is based on an open circuit piece of a tall MSL, composed of twelve HAR EBG cells presented in Sec. 4.1. The simulation results, including gain/radiation pattern, input matching, and efficiency are presented and discussed. Such results show that the simultaneous contribution of EBG cells and HAR metal traces brings about a relatively high efficiency of approximately 90% while the overall electrical length is very short for LWA antennas at  $1.24\lambda$ . The compact footprint ( $1.24\lambda \times 0.36\lambda$ ) and the small overall thickness ( $\lambda/28$ ) are of other distinguishing features offered by the proposed LWA. Furthermore, the applicability of scaling technique and the possibility of easily arraying the proposed antenna without disturbing the LW behavior are demonstrated.

## 5.2 Series-Fed Array Antennas with Proposed EBG Cells

This section presents an efficient planar array antenna composed of “separate groups” of thick electromagnetic bandgap (EBG) cells. The basic element, the SE-EBG-RA, is the same antenna introduced in Sec. 4.1 containing several EBG cells. The array comprises equally-spaced series-fed elements (i.e. groups of several EBG cells) designed to have broadside radiation. A computationally efficient approach is presented to form the array in series with negligible mutual coupling between elements. To this end, first the terminated version of SE-EBG-RA element is introduced. Then, it is shown how such elements can structure the series array effectively. Results show that the application of EBG cells and thick traces yields high efficiency, alleviated mutual coupling, and a symmetrical broadside pattern with reduced numerical computation load.

### 5.2.1 Introduction

Array antennas have long been under study as a way to achieve high-gain apertures demanded by many communications and radar systems. The notion of attaining cost-effective low-profile monolithic arrays has drawn much attention to array structure based on planar elements, most popular of which is the microstrip antenna. Therefore, many efforts have been made to develop topologies and techniques to effectively array these elements. The classical way to do this is to use corporate feeding networks [e.g. 7]. This method provides a large bandwidth (BW) and desirable phase difference at the expense of long feed-lines, yielding relatively high dissipation loss [8] and low efficiency ( $\eta$ ) [9]. A remedy to mitigate this loss is to employ a series feeding method [e.g. 10-11], which has reduced feed-line lengths and reduced line radiation [9]. As an array element, microstrip antennas suffer from inherent weaknesses like low BW and low power handling capability [12]. In some applications like automotive radar at 77GHz [13], even a small BW percentage can accommodate a sufficiently high data rate. However, especially at high frequencies, the increased loss in microstrip structures [13] can deteriorate  $\eta$ . This fact emphasizes the importance of series-fed arrays under such conditions. To combat the loss issue, this section applies two parallel schemes. The first is to replace the microstrip antenna with the high-efficiency planar element described in Sec. 4.1, the self-excited EBG resonator antenna (SE-EBG-RA). The second scheme is to utilize the series-feeding method to efficiently excite elements. Another feature of the idea is an approach to deploy successive elements so that the design process is not dependent on full-wave analysis of the whole array, but rather on the design

of each element separately. The idea is that employing the SE-EBG-RA yields reduced mutual coupling between elements, a condition that is the core of the computationally efficient array design process to be described. In fact, this notion stems from advantages of periodic EBG structures [5, 14-17, et al.], such as bandwidth and gain enhancement, size reduction, surface wave suppression, and loss mitigation. Among these, as investigated in [16], suppressing surface waves is the key to isolating the adjacent elements, and is utilized in this section. The analysis method employed is the HFSS/Bloch method described in Sec. 4.1.

### 5.2.2 Main Idea

In Sec. 4.1, the concept of open-circuited (OC) SE-EBG-RA textured by three EBG cells was introduced. The concept can be generalized by considering a finite real load impedance replacing the OC end (infinite impedance) of the antenna. As described in Sec. 4.1, to develop the OC version, a 1D EBG-woven TL was introduced, and then, using the HFSS/Bloch method, the dispersive behavior of the TL was fully extracted. The results were an equivalent line impedance called Bloch impedance, and a complex propagation constant ( $\gamma=\alpha+j\beta$ ), both available versus frequency. Having access to these two parameters, a new version with a finite load (here  $50\Omega$ ) can be designed in a similar manner (referred to as the terminated SE-EBG-RA). The idea is that a matched OC SE-EBG-RA (like the design in Sec. 4.1) can play the role of a  $50\Omega$  load for the second antenna element, which is the terminated SE-EBG-RA. Because the terminated antenna is designed to operate with a  $50\Omega$  load, introducing the OC antenna element as its load will not disturb its operation, provided that the mutual coupling is negligible. The idea can be extended by noting that now these two arrayed elements can be regarded as a new matched planar antenna with  $50\Omega$  input impedance, a module which can be a  $50\Omega$  load for a third terminated SE-EBG-RA. This approach allows us to cascade additional elements to the series arrays while there is no need for corporate feed-line systems. Fig. 5.2.1 renders an overview of the described idea. From this point on, the rest of the design process will be to adjust the distance between the antenna elements so that they have the appropriate phase at the input port, providing the desired radiation pattern. The deviation caused by the mutual coupling is also a factor to consider, but it is expected (demonstrated later) to be negligible due to the role of EBG cells in suppressing surface waves [16].

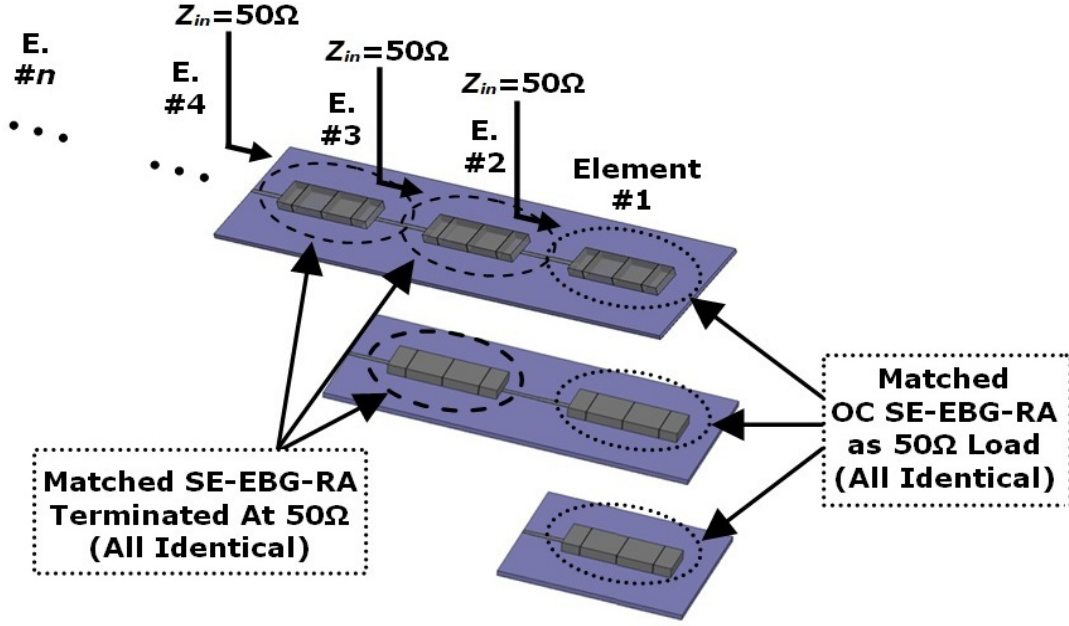


Fig. 5.2.1. Generalization of a  $n$ -element series array of SE-EBG-RA antennas; the first element is OC-SE-EBG-RA and the rest are identical and classified as terminated SE-EBG-RA due to being loaded at the end.

### 5.2.3 Concept of Terminated SE-EBG-RAs

To expand on how a terminated SE-EBG-RA functions, it is noted that the theory presented in Sec. 4.2 for the open- or short-circuited SE-EBG-RAs can be generalized by terminating the antenna by an arbitrary load. This is as opposed to using short ( $Z_L=0$ ) or open ( $Z_L=\infty$ ) loads described in Sec 4.2. A simple case of termination, which is used in this section (Fig. 5.2.1 and 5.2.2), is to consider an ohmic load like  $Z_L=50\Omega$ . Accordingly, the problem is simplified to analyzing a piece of TL composed of a cascade of EBG cells (3 cells in this case) which is terminated on one side by a  $50\Omega$  load and is fed from the other side. Using the HFSS/Bloch method presented in Sec. 4.1, the propagation constant,  $\gamma=\alpha+j\beta$ , and the equivalent line impedance,  $Z_B$ , can be extracted for this EBG TL. Using these parameters and referring to the lossy TL theory, the input impedance of such terminated piece of TL can be obtained. It can be shown that at  $l=n\lambda_g/2$  (the electrical length of the piece of EBG TL), the terms containing  $\beta$  vanish in the equations, and the input impedance is simplified to

$$Z_{in} = Z_B \frac{Z_B \tanh \alpha l + Z_L}{Z_B + Z_L \tanh \alpha l} \quad (5.2.1)$$



Because in this case  $Z_L$  is real ( $50\Omega$ ) and  $Z_B$  is also approximately real, (this is shown in the last figure of Sec. 5.1 where  $Z_B$  is plotted for the EBG cells),  $Z_{in}$  will be a real impedance capable of being matched to a  $50\Omega$  line.

#### 5.2.4 Simulation Results

To demonstrate the idea through an example, the 3-cell OC SE-EBG-RA of Sec. 4.1 is considered as the OC element on the right side of Fig. 5.2.2. The same 3-cell structure is also considered for the terminated element on the left. The input impedance of each element is found *separately*, i.e. in single element mode, by HFSS/Bloch method (see Sec. 4.1 and [5]). The comparison shows that a  $50\Omega$  load is imaged by the piece of 3-cell EBG TL to  $23.2\Omega$  while an infinite load is imaged to  $42.1\Omega$ . Both antennas resonate (imaginary part of input impedance is zero) at identical resonance ( $f_r$ ) of 4.15GHz. One way to bring these impedances back to  $50\Omega$  is to add quarter-wave transformers, as shown in Fig. 5.2.2.

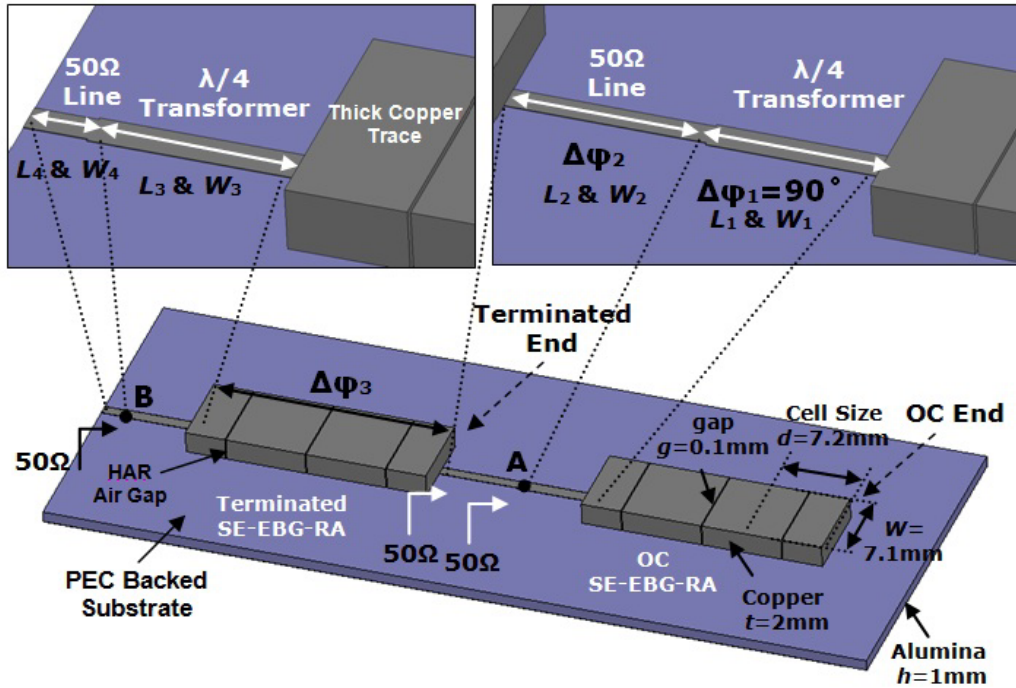


Fig. 5.2.2. A 2-element series array of SE-EBG-RA; the substrate is alumina with  $\epsilon_r=9.9$  and  $\tan\delta=0.003$ ; the ground plane size is  $72\times 30$ ;  $W_1=1.1$ ,  $W_2\&W_4=0.912$ ,  $W_3=1.05$  ( $30\mu\text{m}$  thick),  $g=0.1$ ,  $L_1=6.92$ ,  $L_2=7.04$ ,  $L_3=6.9$ ,  $L_4=1.86$ ; the array spacing is  $35.56$ ; all dimensions are in mm.



As a result, the impedances seen at points A and B in Fig. 5.2.2 become  $50\Omega$ . It is noted that all these design steps are carried out without analyzing the two elements at the same time while it is expected that the whole 2-element array will resonate roughly at the same  $f_r$  of 4.15GHz. To corroborate this expectation, in the next step, the whole array in Fig. 5.2.2 is numerically analyzed in HFSS. As seen, a piece of  $50\Omega$  line in the middle connects the two antennas and is adjusted in length ( $\Delta\phi_2$  in Fig. 5.2.2) to provide the total  $360^\circ$  phase difference needed for a broadside array ( $\Delta\phi_1+\Delta\phi_2+\Delta\phi_3=360^\circ$ ). It is noted that  $\Delta\phi_1=90^\circ$  as it is created by a quarter-wave transformer.  $\Delta\phi_3$  is also fixed for the given geometry of the cells and is found from  $\beta$  of the EBG TL, obtained by HFSS/Bloch method. For the array in Fig. 5.2.2, the radiation pattern in E- and H-planes are shown in Fig. 5.2.3, and the related parameters are  $BW=1.25\%$ ,  $f_r=4.13\text{GHz}$ ,  $\eta=84\%$ , and  $G_r=7.24\text{dBi}$  (realized gain). As seen, the array is still matched to a  $50\Omega$  line at 4.13GHz. This frequency is only 0.5% deviated from 4.15GHz at which each element has been designed to operate separately. The array parameters are comparable to  $\eta=89\%$ , and  $G_r=3.0\text{dBi}$  for the single element 3-cell OC SE-EBG RA. The frequency stability observed after deploying the two antennas on such a high dielectric substrate, at a relatively close distance (array spacing is  $0.48\lambda$ ), demonstrates that the mutual coupling between elements is negligible.

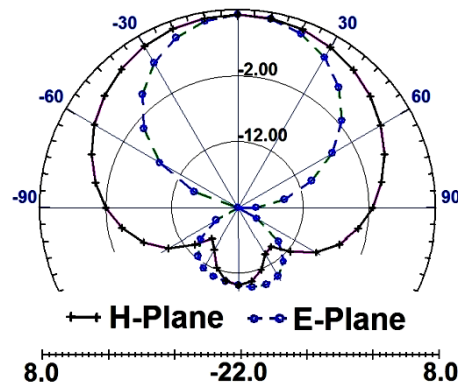


Fig. 5.2.3. Radiation pattern of the 2-element series array in Fig. 5.2.2.

Fig. 5.2.4 also shows a 3-element array comparable to Fig. 5.2.2. The associated parameters are  $\eta=83\%$ ,  $G_r=8.5\text{dBi}$ ,  $f=4.09\text{GHz}$ , which means the matching (resonance) frequency only has 1.4% shift from 4.15GHz for the single-element. Rectangular and 3D radiation patterns are shown in Figs. 5.2.5 and 5.2.6. Moreover, Fig. 5.2.7 compares the return loss of one-, two-, and three-element arrays shown in Fig. 5.2.1.

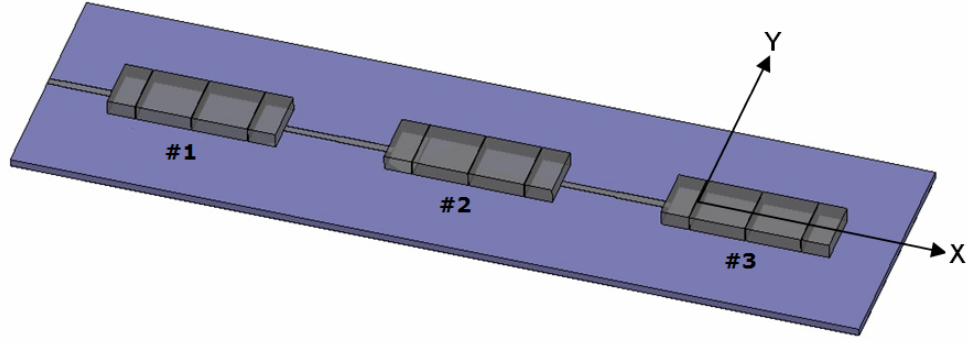


Fig. 5.2.4 A 3-element series-fed array of SE-EBG-RA; the substrate material and dimensions are like Fig. 5.2.2; the ground plane size is 109mm×30mm; elements #2 and #3 are the same as the second element in Fig. 5.2.2.

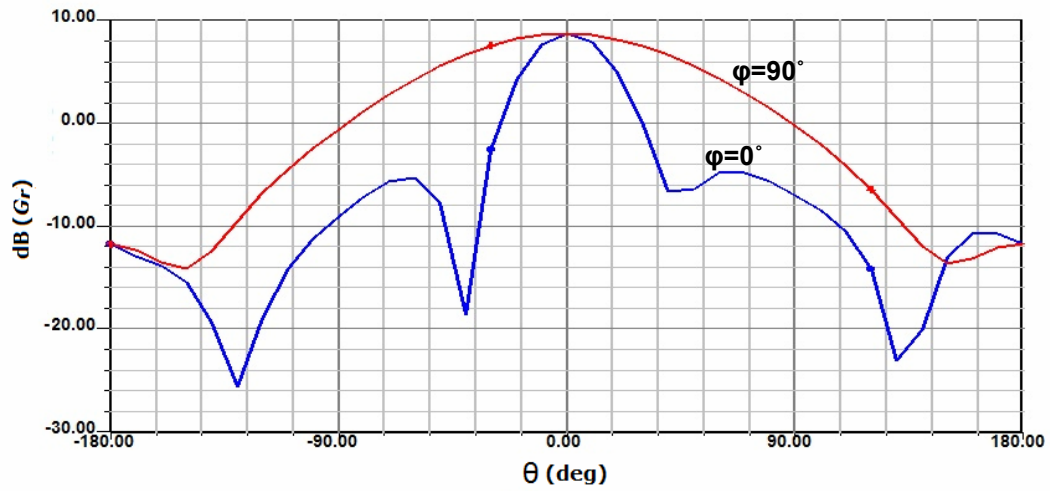


Fig. 5.2.5. Rectangular radiation pattern of the 3-element array of Fig. 5.2.4 (realized gain plotted).

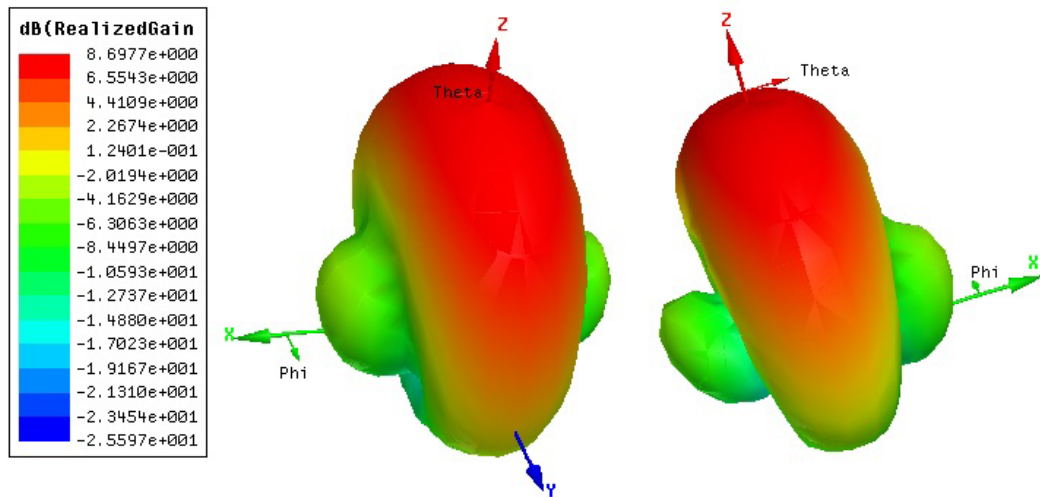


Fig. 5.2.6. Two different views of the 3D radiation pattern of the 3-element array of Fig. 5.2.4 (realized gain plotted).

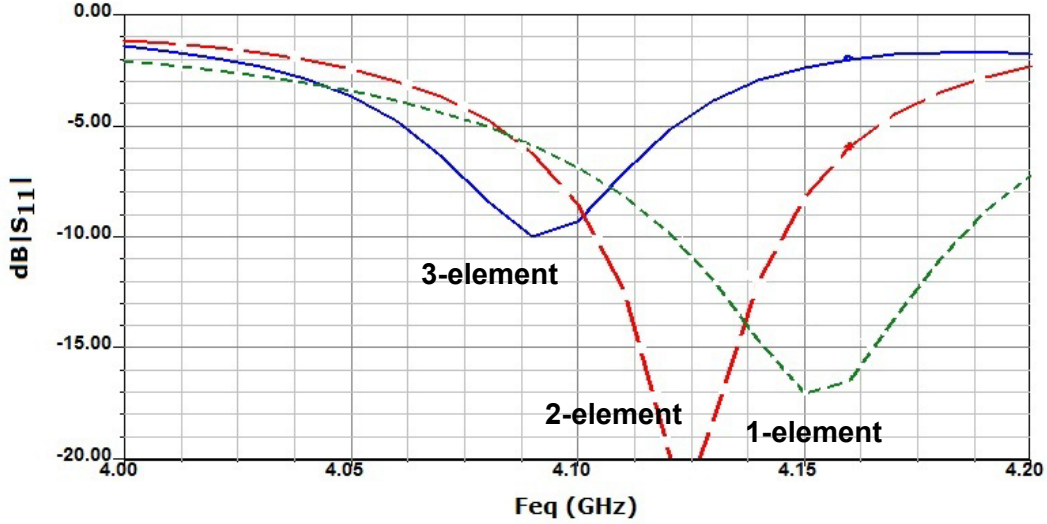


Fig. 5.2.7. Comparing the return loss of one-, two-, and three-element arrays shown in Fig. 5.2.1.

It is noted that an array of (for instance) three SE-EBG-RAs, as in Fig. 5.2.4, has  $3 \times 3$  unit cells. One conceivable way for increasing the aperture size and its gain is to use one SE-EBG-RA element with more cells than 3 (e.g. 9 cells). However, the effect of the number of cells was discussed in Sec. 4.2 and the conclusion was that after increasing this number beyond a certain limit (six cells in case of the example in Sec.4.2), the antenna changes its nature from being resonant to being leaky-wave and the radiation pattern begins to scan. Therefore, in the case of requiring a high gain antenna with broadside radiation, the solution is to turn to the array structures like the efficient series-fed topology described here.

It is worth noting here that in addition to their undesired radiation, the feedlines of an array antenna generate thermal noise due to the ohmic loss. This noise is uncorrelated with other noise sources in the system. The available noise power of a low loss transmission (TL) can be expressed as [18]

$$P_{n,available} = kT\Delta f (e^{2\alpha l} - 1)(e^{2\alpha l} + |\Gamma_g|^2)(e^{4\alpha l} - |\Gamma_g|^2)^{-1} \quad (5.2.2)$$

where  $\Gamma_g$  is the source reflection coefficient,  $k$  is the Boltzmann constant,  $T$  is the ambient temperature, and  $\Delta f$  is the bandwidth, respectively. Also,  $\alpha$  is the attenuation constant, and  $l$  is the length of the TL. Accordingly, it can be easily shown that, for a given mismatch factor, this power increases with increasing  $l$ . Hence, the total length of the feed network plays an important role in controlling the noise [19] when the array antenna is used as a receive antenna. This is a

fact that further highlights the advantages of the proposed series-fed HAR EBG array antenna, as its series-fed topology minimizes the length of the feed networks.

### **5.2.5 Conclusion**

An equally-spaced series-fed array antenna with efficient EBG antenna elements is presented. A computationally efficient approach is presented to form the array in series with negligible mutual coupling between elements. The idea of the terminated SE-EBG-RA as opposed to short or open circuit SE-EBG-RAs is described and is applied to the efficient design of the proposed array. Full-wave simulation results show that compared to the resonance frequency of 4.15GHz for the 1-element antenna, the matching mistuning is only 0.5% and 1.4% (downward shift) for the 2- and 3-element arrays, respectively. Also as compared to efficiency of 89% and gain of 3.0dBi for the single element antenna, the parameters are 84%/7.24dBi and 83%/8.5dBi for the 2- and 3-element arrays, respectively. Such results demonstrates that an array antenna with large aperture, and hence, higher gain is achieved, for which, the efficiency is maintained satisfactorily.

### 5.3 A Novel EBG Microstrip Antenna with Fast-Wave Behavior

This part of the study presents a compact patch antenna, which is periodically loaded by air gaps. The gaps are arranged to create EBG cells, which affect the dispersive behaviors of the patch (as a transmission line). This causes waves to travel faster along the patch, and increases the cumulative radiation from the structure. The proposed antenna is compared with its conventional counterpart, considering efficiency, electrical/physical size, and the potential to achieve an electrically small footprint. Experimental results validate the analyses.

#### 5.3.1 Introduction

As described earlier, microstrip antennas suffer from inherent weaknesses like low bandwidth (BW) [20] and vulnerability to surface wave excitation and the associated loss, especially on high permittivity dielectric substrates [21]. Also, relatively large ground planes are typically required to counter surface wave diffraction at the ground plane edges and reduce front-to-back radiation ratio. An effective remedy to many of these issues is to place the patch on an EBG ground plane rather than a PEC one [e.g. 22]. Some designs offer a single-layer structure, deploying EBG cells around the patch on the same layer [23], while others require at least two layers, sometimes with different permittivities. Another interesting trend has been to weave the patch itself using EBG cells and achieve a reduced resonance [24]. The radiation properties of such structures can be improved by thickening the metal layer of its small EBG cells as in Sec. 4.1 and [5]. Following such efforts, this section considers a single layer conventional patch antenna, then divides the patch into small unit cells created by periodic air gaps to demonstrate the advantages achieved.

#### 5.3.2 Concept

Fig. 5.3.1 shows the proposed small unit cell made of a metal strip on a PEC-backed substrate. As seen, there is a narrow (0.25mm) interdigitated gap dividing the cell at the center. This cell can be cascaded to realize the gap-loaded patch antenna shown in Fig. 5.3.2 (a). Using the HFSS/Bloch analysis described in Sec. 4.1, the equivalent line impedance,  $Z_c$ , the complex propagation constant along Y-axis in Fig. 5.3.1,  $\gamma=\alpha+j\beta$ , and the effective relative permittivity,  $\epsilon_{reff}$ , are calculated as in the left section of the Table 5.3.1. For comparison, in Table 5.3.1, the same cell with gaps removed is also analyzed using HFSS/Bloch analysis (Sec. 4.1) to provide

the dispersive TL behaviors of the conventional patch antenna in Fig. 5.3.2 (b). Because this gap-less cell is in fact a wide microstripline (MSL), its TL parameters can also be calculated using well-known closed-form equations [e.g. 4]. The results are  $\epsilon_{\text{reff}}=9.28$ ,  $Z_c=10.76$ , and  $\beta/k_0=3.05$  and agree very well with the HFSS/Bloch results in Table 5.3.1. Apart from the unit cell analysis, both antennas in Fig. 5.3.2 are modeled in HFSS and are analyzed entirely numerically. The related properties are listed in the right section of Table 5.3.1. As the antenna in Fig. 5.3.2 (a) operates at 4GHz,  $L_r$  in Fig. 5.3.2 (b) is adjusted so as to have the antenna resonate at the same frequency, while  $W_r$  and  $W_g$  remain the same to keep both antennas identical in width.

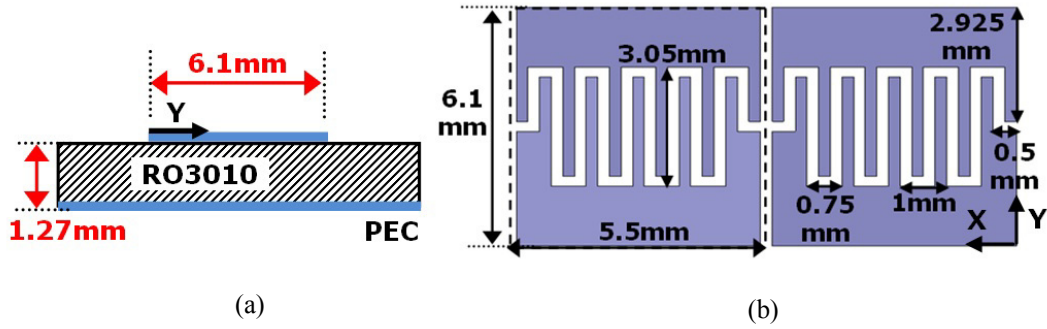


Fig. 5.3.1 Side (a) and top (b) views of the Bloch unit cell of the antenna in Fig. 5.3.2 (a); all gaps are 0.25mm; the Bloch cell size is  $\lambda/7 \times \lambda/12.3 \times \lambda/59$ , and the cell is composed of two smaller identical portions (EBG cells) of size  $\lambda/14 \times \lambda/12.3 \times \lambda/59$  ( $\lambda$  at 4GHz).

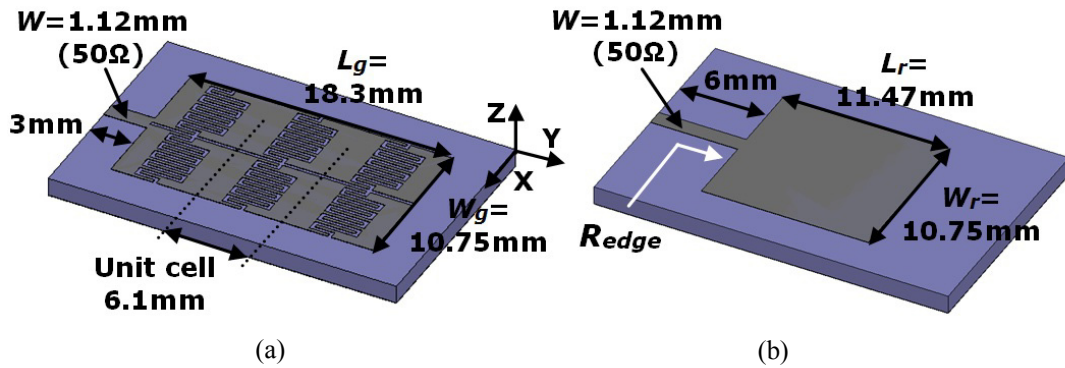


Fig. 5.3.2 Microstrip antenna versus its gap-loaded version both resonating at 4GHz; both ground planes are 16mm×24.3mm; both substrates are 1.27mm thick RO3010 ( $\epsilon_r=10.2$ ,  $\tan\delta=0.0023$ ); the unit cell of Fig. 5.3.2 (a) is given in Fig. 5.3.1; metal traces are 30μm thick copper.

Table 5.3.1 HFSS/Bloch analysis of the unit cell in Fig. 5.3.1 with and without gaps and simulated parameters of patch antennas based on them in Fig. 5.3.2;  $G_r$  is the realized gain including the  $\text{dB}|S_{11}|$  effect;  $\eta$  is found by HFSS simulation.

Properties at 4GHz; $k_0$ is the free-space wavenumber								
Unit Cell (HFSS/Bloch)				Antenna (HFSS)				
$\epsilon_{\text{reff}}$	$Z_c (\Omega)$	$\beta/k_0$	$\alpha/k_0$	$R_{\text{edge}} (\Omega)$	Gain (dBi)	$G_r$ (dBi)	$\eta$ (%)	$\text{dB} S_{11} $
Regular patch; patch size as in Fig. 5.3.2 (b) ( $W_r$ and $L_r$ )								
9.18	10.98	3.03	0.01	312	1.48	-1.97	75	-2.5
The gap-loaded patch; patch size as in Fig. 5.3.2 (a) ( $W_g$ and $L_g$ )								
4.16	6.26	2.04	0.04	37.4	1.95	1.9	84	-19

Table 5.3.1 compares properties of the antennas in Fig. 5.3.2 and their unit cells. As seen,  $\epsilon_{\text{reff}}$  of the proposed gap-loaded patch is much lower as a result of field interaction with air at the gaps. Similarly,  $Z_c$  is also much lower for Fig. 5.3.2 (a) than Fig. 5.3.2 (b). More importantly, applying gaps has *reduced*  $\beta/k_0$  by  $\sim 1.5$  times, which is a clear indication of *fast-wave* behavior of the structure compared to the regular patch. As seen, such effects introduced by loading, result in a low patch edge impedance,  $R_{\text{edge}}$ , of  $37.4\Omega$ , much less than  $312\Omega$  for the conventional patch and desirably close to  $50\Omega$ . This means the gap-loaded patch can be effectively fed directly by a  $50\Omega$  line (19 dB return loss compared to 2.5 dB for the conventional patch) without requiring a (large) multi-section matching transformer. For the conventional patch,  $W_r$ , can be increased to reduce  $R_{\text{edge}}$ ; however, a typical  $W_r/L_r$  of 1.5 [21] is required, which is much wider than the gap-loaded structure in Fig. 5.3.2 (a). With interdigitated gaps, there is the opportunity to exploit the number, length, and the width of interdigits as extra parameters to achieve the desired  $R_{\text{edge}}$ , without the need to increase the patch width, i.e.  $W_g$  in Fig. 5.3.2 (a). Furthermore, as in Table 5.3.1, the efficiency ( $\eta$ ) of the gap-loaded patch is 12% higher, leading to a higher antenna gain. One more informative parameter in Table 5.3.1 is  $\alpha/k_0$ , which is 4 times higher for the gap-loaded patch.  $\alpha/k_0$  represents the enhanced radiation leakage of the structure, caused by applying gaps, and explains the enhancement in  $\eta$ . The radiation patterns of antennas in Fig. 5.3.2 are shown in Fig. 5.3.3.

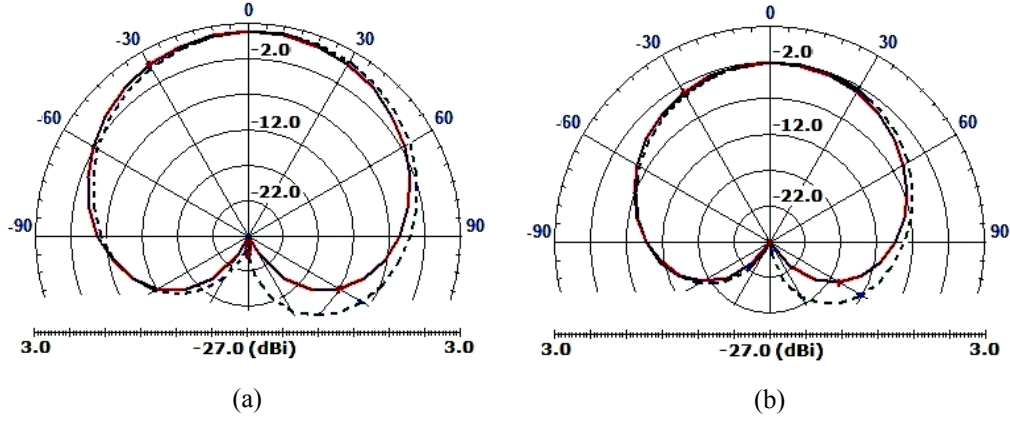


Fig. 5.3.3 Simulated realized gains of antennas in Fig. 5.3.2 (a) and Fig. 5.3.2 (b); the dashed/solid line is related to E-/H-plane.

### 5.3.3 Discussion

Reference [24] compares a similar EBG-textured patch antenna with a slow-wave nature to a conventional patch. The antenna requires two separate low permittivity substrates ( $\epsilon_r$  of 2.2 and 2.55), is excited through a MSL-fed slot, and has an overall volume of  $\sim 0.43\lambda \times 0.43\lambda \times \lambda/28$ . By comparison, the proposed gap-loaded patch of Fig. 5.3.2 (a) is similarly EBG-woven, however can be simply fed by a MSL on a single-layer high permittivity substrate ( $\epsilon_r=10.2$ ), and has a significantly smaller electrical volume of  $0.21\lambda \times 0.32\lambda \times \lambda/59$ . Also, as shown in Table 5.3.1, waves travel faster along this loaded patch compared to the conventional patch.

### 5.3.4 Experimental Verification

The antenna in Fig. 5.3.2 (a) is fabricated with a large ground plane of 63mm $\times$ 60mm. The prototype is shown in Fig. 5.3.4. Fig. 5.3.5 compares simulated and measured  $\text{dB}|S_{11}|$ , showing satisfactory agreement. In addition, the gain in the broadside direction measured by the three-antenna-method [25] is 4.47dBi which is only 0.88dB lower than the HFSS result. However, as the SMA connector has not been simulated,  $\sim 0.2$ -0.4dB out of 0.88dB can be attributed to the SMA loss, and the actual gain uncertainty ranges from 0.48dB to 0.68dB.



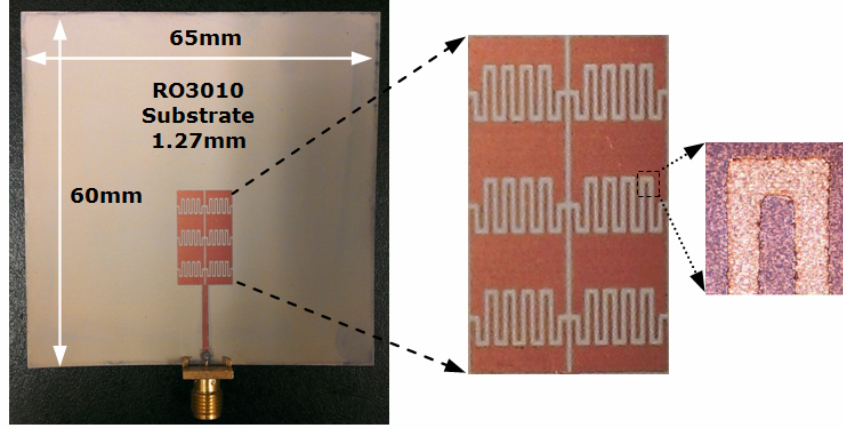


Fig. 5.3.4 Fabricated gap-loaded patch antenna of Fig. 5.3.2 (a) with a large ground plane.

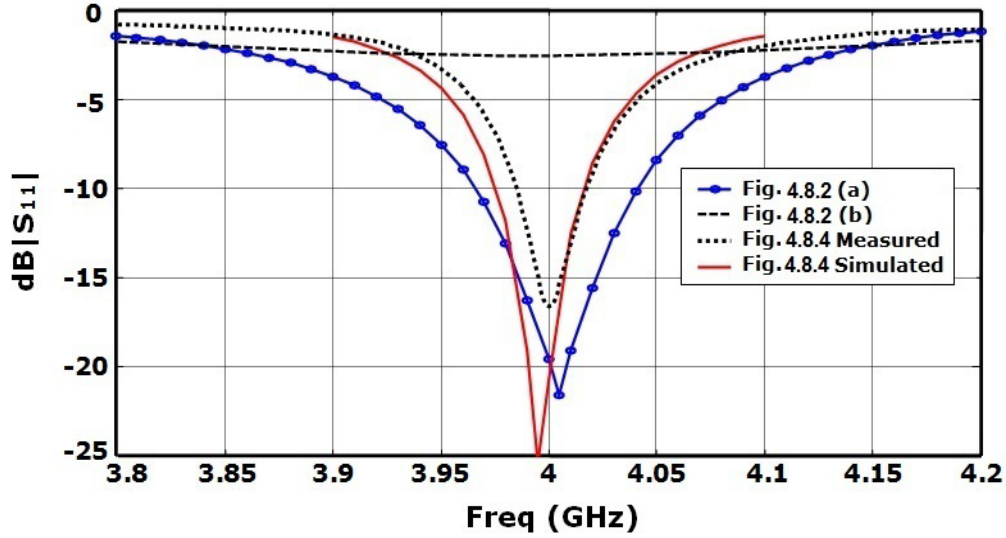


Fig. 5.3.5  $\text{dB}|S_{11}|$  of the antennas in Fig. 5.3.2 and Fig. 5.3.4.

### 5.3.5 Conclusion

This section presents an improved microstrip patch antenna, which is textured by  $2 \times 3$  small EBG cells of size  $\lambda/14 \times \lambda/12.3 \times \lambda/59$ . A comparative study shows that the patch body acts as a piece of periodically-loaded MSL with radiation properties which guides the waves at a faster speed as compared to a normal MSL. An antenna design example is rendered which has a high efficiency of 84%, BW of 1.75%, realized gain of 1.9dBi, and a small volume of  $0.21\lambda \times 0.32\lambda \times \lambda/59$ . It is demonstrated that a conventional patch counterpart cannot compete to reach this degree of compactness.

## 5.4 Compact Circularly Polarized SE-EBG-RAs

This section presents a highly efficient and miniature planar electromagnetic bandgap (EBG) antenna with circularly polarized (CP) radiation. The antenna building blocks are the high aspect ratio (HAR) EBG cells introduced in Sec. 4.1, nine of which are deployed in both lateral dimensions ( $3 \times 3$ ). Because the top metal layer of this EBG surface is symmetrical, it can simultaneously accommodate two orthogonal E-field components. These fields are excited by two microstriplines attached to the corners. A compact simplified shifter/power divider provides quadrature phase difference and equal magnitudes at feed points, enabling the structure to generate a broadside CP radiation pattern. Thanks to the natural capability of EBG cells, the low loss nature of HAR metal traces, and high capacitive coupling of gaps, this section features a planar CP antenna with a footprint as small as  $0.26\lambda \times 0.29\lambda$  and efficiency as high as 94%.

### 5.4.1 Introduction

In mobile communications systems, mobile devices happen to be in a variety of positions, movements, and directions so that a linearly polarized (LP) antenna may not always be an optimum solution. Under such circumstances, it is very difficult to effectively match the polarization of the antenna with the polarization of the incoming signal. One remedy is to use circularly polarized (CP) waves [26-27] to improve the polarization diversity and reduce impacts of multi-path environments on performance. As a result, many modern communications systems adopt or desire CP waves [28]. For example, in body area networks applications [26], global positioning systems [29], mobile RFID readers [30], and in some satellite-to-earth communications links, small CP antennas for mobile terminals involved are desirable, not only to improve the signal quality, but also to meet the requirements on the overall weight and size [31]. Although there are some miniaturization techniques special to CP antennas [32-33], most techniques are only applied to LP antennas. A reason is that very small antennas are so challenging to design that enforcing extra requirements for CP radiation complicates the design and optimization process. For instance, it is difficult to realize an electrically small antenna with maintained bandwidth (BW) and efficiency ( $\eta$ ) [34]. Therefore, achieving a planar CP antenna, which is highly efficient, small in footprint, and simple in terms of feeding method remains a demanding, yet challenging area. In light of this, this section puts forward an idea to fill the gap sketched. The antenna proposed has a structure similar to a square patch antenna, the metal patch

of which is divided by periodically applied tiny gaps at electrically short intervals. This way the patch body is textured of small EBG unit cells (small square patches on a PEC-backed substrate), which are thickened until the gaps become very high aspect ratio (HAR) (thickness/gap=20). The motivation for thickening is to reduce the conduction loss while increasing the capacitive coupling between the EBG cells (inside the gaps). There are also other scarce works like [35-36] utilizing structures with projected metal layers. To the best of our investigation, this idea is the first attempt to utilize EBG antennas with thick metal layers radiating CP waves.

#### 5.4.2 Approach to Providing CP Radiation

The idea is initiated with considering a regular square patch antenna fed by two microstriplines (MSL) from two adjacent corners. Two modifications are applied to the structure which include thickening the top metal layer ( $t=2\text{mm}$ ) and adding narrow gaps of 0.1 mm at short intervals. This way, as in Fig. 5.4.1, a thick sectioned EBG patch antenna is obtained. The gaps are very HAR as their thickness over gap size is 20. This high value is purposefully chosen to increase the side coupling between adjacent gaps and drop the resonance. It is noted that in Sec. 4.1, a one dimensional (1D) version of this 2D EBG antenna with only three cells was presented, which operated as a high-efficiency LP antenna.

The next step is to excite two orthogonal E-field components with  $90^\circ$  phase difference, inside the structure in Fig. 5.4.1. A conventional way to achieve this condition is to apply cross-feeding topology shown in Fig. 5.4.2. As depicted, this topology requires a power divider with different arm lengths ( $l_1$  &  $l_2$ ) to equally divide the power and provide  $90^\circ$  phase shift simultaneously. The downside of this feeding method however is that it occupies much space because it needs two extra quarter-wave transformers to compensate the impedance mismatch after power division. In addition, the total feeding section will be relatively long (and hence lossy) in order to accommodate such impedance transformers.

To circumvent this issue, the  $3 \times 3$ -cell patch antenna is designed to have  $80\Omega$  input impedance at each corner at the desired frequency, as shown in Fig. 5.4.1 (a). For a given dielectric material and thickness, adjusting parameters like gap and patch size can provide this condition. After this impedance is obtained, two  $80\Omega$  MSLs can feed the corners with no mismatch.

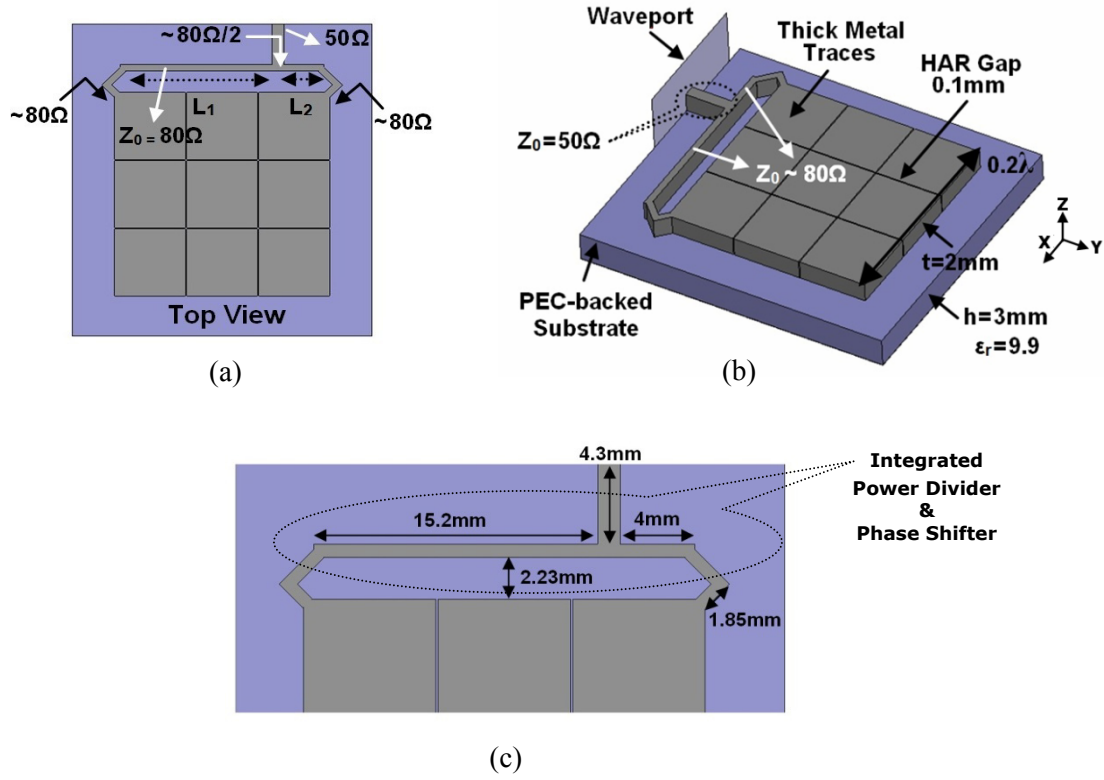


Fig. 5.4.1. Top (a) and 3D (b) views of the CP HAR EBG antenna along with detailed dimensions of the feed section (c); the cell size is  $\sim \lambda/16 \times \lambda/16 \times \lambda/23$ ; the substrate is alumina with  $\epsilon_r = 9.9$  and  $\tan\delta = 0.003$ ; the metal is copper with  $\sigma = 5.8e7\text{s/m}$ ; the ground plane size is  $33\text{mm} \times 30\text{mm}$ ; the trace width for the  $50\Omega$  line is  $1.2\text{mm}$  and for  $80\Omega$  line is  $0.7\text{mm}$ .

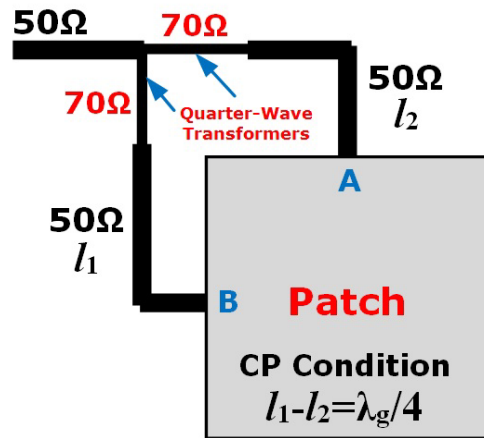


Fig. 5.4.2. A regular square patch antenna, traditionally fed by two cross MSLs at the center of two adjacent sides; to provide the condition for CP radiation, feedlines must be in the right size, as described.

As in Fig. 5.4.1 (a), these MSLs have different lengths to provide the required phase shift and they meet where a  $50\Omega$  line feeds them. As both MSLs have  $80\Omega$  impedance, they provide a  $40\Omega$  ( $80\Omega/2$ ) input impedance at the fork, which is matched well enough to the  $50\Omega$  line. Although, the ideal impedance for MSLs is  $100\Omega$  rather than  $80\Omega$ , realization of such a high impedance, especially with thick traces, puts some pressure on the design, and hence, is avoided. This strategy enables the antenna to generate two orthogonal E-field components (i.e. degenerate modes) with roughly the same magnitude and quadrature phase shift, turning the antenna into a CP radiator. As seen in Fig. 5.4.1, the power divider/shifter is very compact and appears a part of the antenna structure.

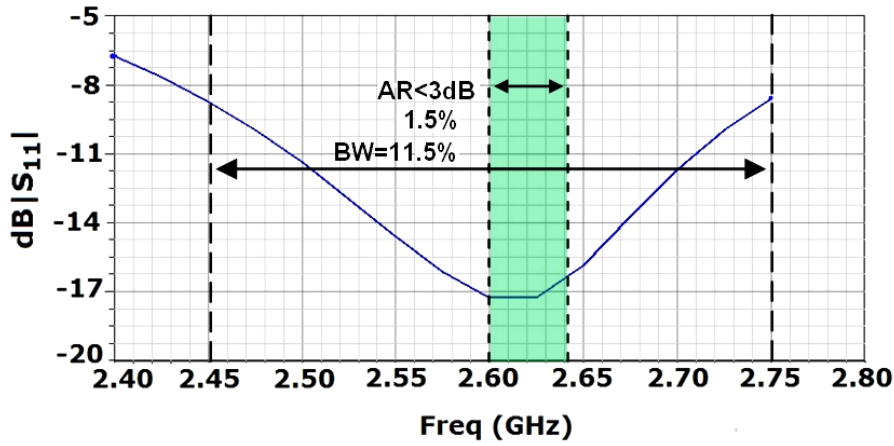


Fig. 5.4.3.  $\text{dB}|S_{11}|$  for the antenna in Fig. 5.4.1.

### 5.4.3 Simulation Results

HFSS simulation results for the antenna in Fig. 5.4.1, including the input matching and gain/radiation pattern, are shown in Fig. 5.4.3 and Fig. 5.4.4, respectively. The antenna offers very small electrical dimensions of  $0.26\lambda \times 0.29\lambda \times \lambda/23$ , remarkable  $\eta$  of 94.3% (from 2.4 GHz to 2.75GHz), realized gain of 0.13dBi, and matching BW of 11.5%. The axial ratio (AR) bandwidth (where  $\text{AR} < 3\text{dB}$ ) is also 1.5% as shown in Fig. 5.4.3. Moreover, Fig. 5.4.5 shows the antenna 3D radiation pattern. As seen, Fig. 5.4.4 indicates that the AR is maintained over about  $\pm 70^\circ$  angular range. To provide more details on how CP is generated, Fig. 5.4.6 renders the rectangular plots of the AR as well as the magnitude and phase of  $E_\theta$  in two orthogonal planes.

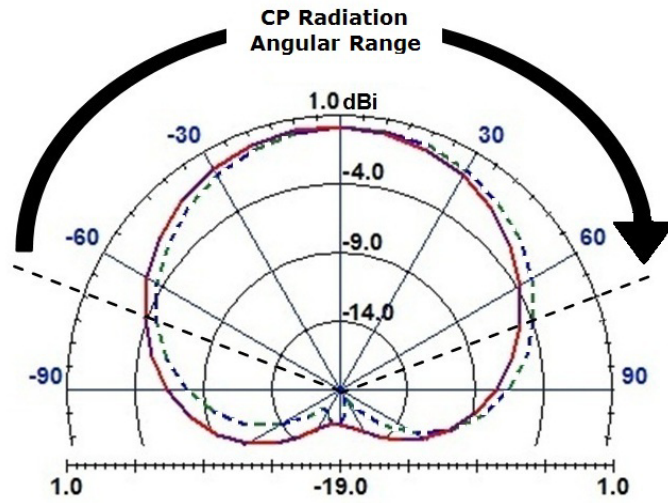


Fig. 5.4.4. Realized gain of the CP EBG antenna; the dashed/solid line is for  $\phi=90^\circ/\phi=0^\circ$  plane.

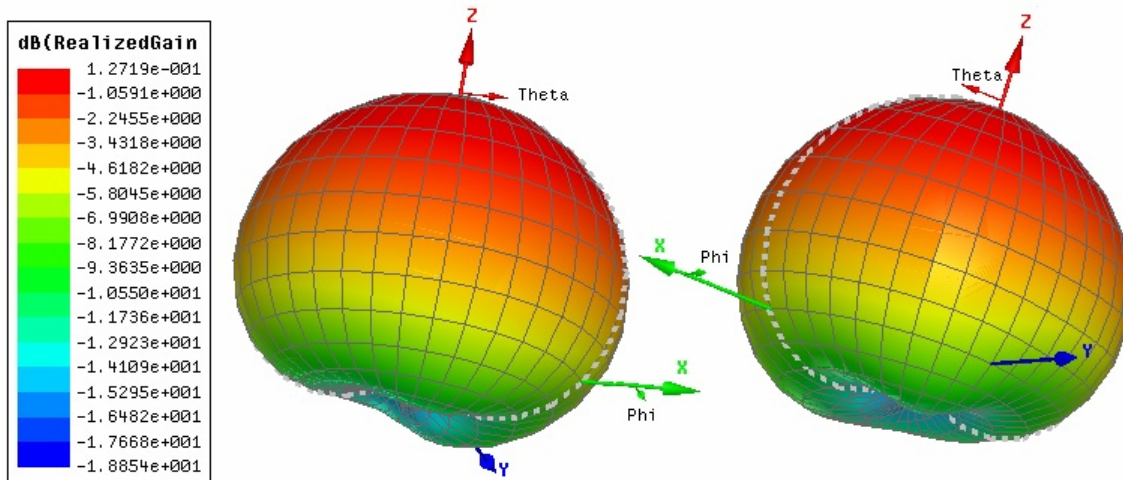


Fig. 5.4.5. 3D plot of the realized gain for the CP antenna in Fig. 5.4.1, at the matching frequency of 2.62GHz.

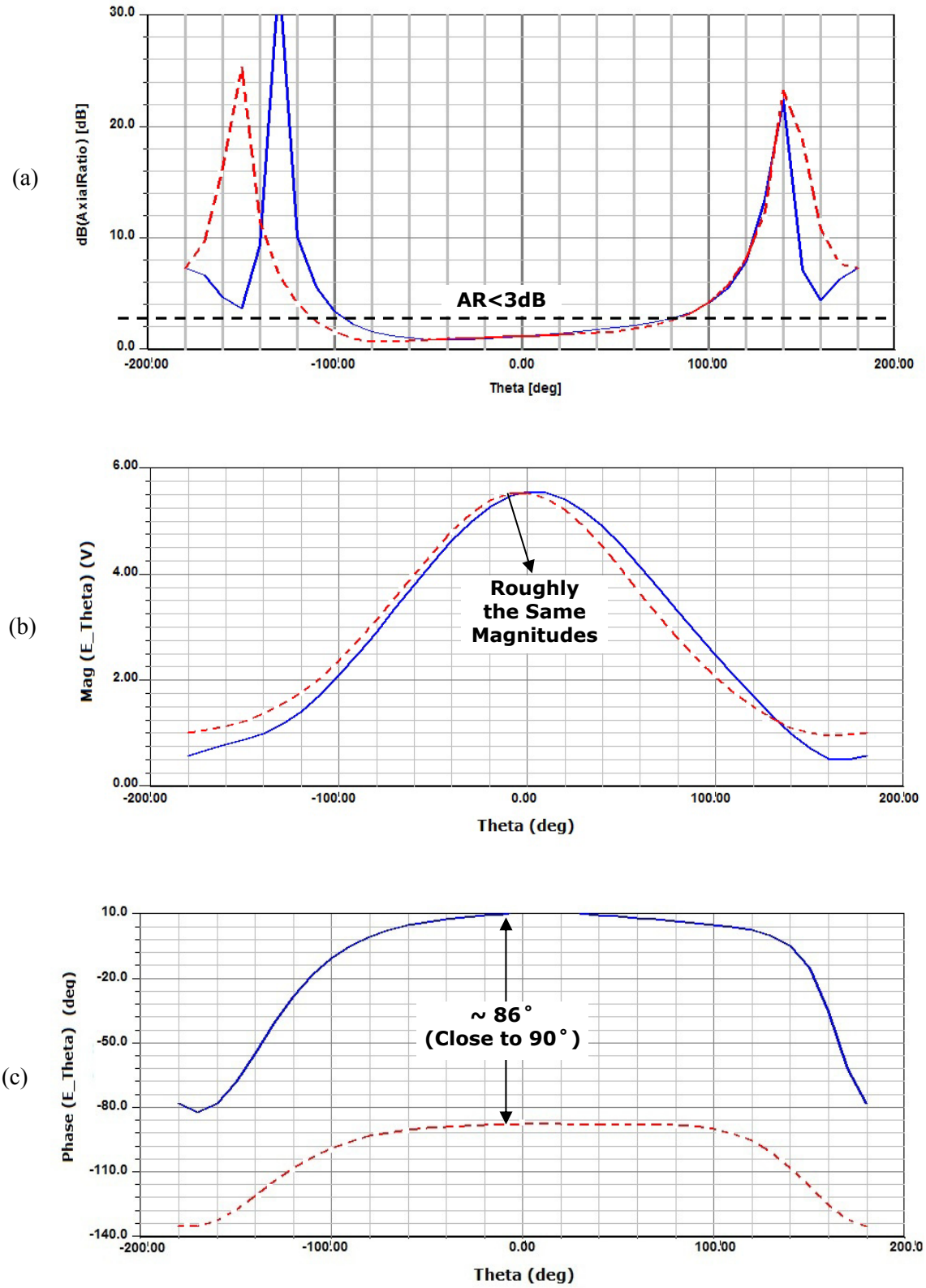


Fig. 5.4.6. AR (a) together with the magnitude (b) and phase (c) of  $E_\theta$  for the CP antenna in Fig. 5.4.1; curves are plotted at the matching frequency of 2.62GHz; the dashed/solid line is for  $\phi=90^\circ/\phi=0^\circ$  plane.

While noting the small antenna size of  $0.26\lambda \times 0.29\lambda \times \lambda/23$ , it is worth reminding that in general, realization of electrically small antennas leads to severe degradation of both BW and  $\eta$  [34]. However, for the proposed CP HAR EBG antenna, such degradations are overcome due to the simultaneous application of the EBG concept and trace thickening.

#### 5.4.4 Conclusion

A design methodology is presented for the design of an efficient miniature EBG antenna with CP radiation. The antenna is composed of  $3 \times 3$  EBG cells with projected top metal layer and HAR gaps in the layer. The symmetry of the patch structure is utilized and two degenerate modes with orthogonal E-field components are excited in the structure using a compact simplified shifter/power divider. The proposed antenna renders a symmetrical broadside CP radiation pattern, a footprint as small as  $0.26\lambda \times 0.29\lambda$ , and efficiency as high as 94%.

#### References

- [1] Amit M. Patel and Anthony Grbic, "A printed leaky-wave antenna based on a sinusoidally-modulated reactance surface," *IEEE Trans. Antennas Propag.*, vol. 59, no. 6, pp. 2087-2096, June 2011.
- [2] K. C. Chen, C. K. C. Tzuang, Y. Qian, and T. Itoh, "Leaky properties of microstrip above a perforated ground plane," *IEEE International Microwave Symposium Digest*, Anaheim, 13-19 June 1999.
- [3] J. W. Wu, C. F. Jou, and C. J. Wang, "A compact wideband leaky-wave antenna with etched slot elements and tapered structure," *IEEE Trans. Antennas and Propagat.*, vol. 58, no. 7, pp. 2176-2183, July 2010.
- [4] D. M. Pozar, *Microwave Engineering*, 2nd ed., John Wiley & Sons, 1998.
- [5] M. Hosseini, and D. M. Klymyshyn, "Radiation properties of EBG textured tall transmission lines and applications: A low profile self-excited EBG resonator antenna," *IEEE Antennas and Wireless Propagation Letters*, vol. 11, pp. 276-280, 2012.
- [6] A. Grbic and G. V. Eleftheriades, "Leaky CPW-Based Slot Antenna Arrays for Millimeter-Wave Applications," *IEEE Trans. Antennas Propag.*, vol. 50, no. 11, pp. 1494-1504, Nov. 2002.
- [7] M.F.B Ain, U. Ullah, S.S. Olokede, Z. Ahmad, "Dual-segment corporate feed four elements array antenna for broadband application," *IEEE Asia-Pacific Conf. on Antennas and Propaga.*, Aug. 2012.
- [8] I. Slomian, K. Wincza, S. Gruszczynski, "Series-Fed Microstrip Antenna Array With Inclined-Slot Couplers as Three-Way Power Dividers," *IEEE Antenn. Wireless Propag. Lett.*, vol. 12, pp. 62-64, 2013.
- [9] T. Metzler, "Microstrip series arrays," *IEEE Trans. Antennas Propag.*, vol. AP-29, no. 1, pp. 174-178, Jan. 1981.
- [10] S. Sengupta, D. R. Jackson, and S. A. Long, "Analysis of a Linear Series-Fed Rectangular Microstrip Antenna Array," *IEEE Int. Symp. Antennas and Propaga.*, Chicago, IL, July 2012.



- [11] T. Kokkinos, A. M. Katsounaros, and A.P. Feresidis, "Series-Fed Microstrip Patch Arrays Employing Metamaterial Transmission Lines: A Comparative Study," 2nd *European Conf. on Antennas and Propaga. (EuCAp)*, Edinburgh, UK, Nov. 2007.
- [12] R. Mailloux, et al., "Microstrip array technology," *IEEE Trans. Antennas Propag.*, vol. 29, pp. 25-37, 1981.
- [13] Y. Chong and D. Wenbin, "Microstrip Series Fed antenna Array for Millimeter Wave Automotive Radar Applications," *IEEE MTT-S Int. Microwave Workshop Series on Millimeter Wave Wireless Tech. and Applications*, Nanjing, China, Sep. 2012
- [14] D. Sievenpiper, L. Zhang, R. F. Jimenez Broas, N. G. Alexopolous, and E. Yablonovitch, "High-impedance electromagnetic surfaces with a forbidden frequency band," *IEEE Trans. Microwave Theory Tech.*, vol. 47, no. 11, pp. 2059-2074, Nov. 1999.
- [15] F. Yang and Y. Rahmat-Samii, "Reflection phase characterizations of the EBG ground plane for low profile wire antenna applications," *IEEE Trans. Antennas Propag.*, vol.51, no.10, pp. 2691-2703, 2003.
- [16] F. Yang, and Y. Rahmat-Samii, "Microstrip Antennas Integrated With Electromagnetic Band-Gap (EBG) Structures: A Low Mutual Coupling Design for Array Applications," *IEEE Trans. Antennas Propag.*, vol. 51, no. 10, pp. 2936-2946, Oct. 2003.
- [17] M. Hosseini, A. Pirhadi, and M. Hakkak, "Design of a non-uniform high impedance surface for a low profile antenna," *J. of Electromag. Waves and Appl.*, vol. 20, no. 11, pp. 1454-1464, 2006.
- [18] S. Demir and C. Toker, "Optimum design of feed structures for high G/T passive and active antenna," *IEEE Trans. Antennas Propag.*, vol. 47, no. 3, pp. 443-452. March 1999.
- [19] M. Yousefbeiigi, A. Enayati, M. Shahabadi and D. Busuioc, "Parallel-series feed network with improved G/T performance for high-gain microstrip antenna arrays," *Electronics Letters*, vol. 44, no. 3, Jan. 2008.
- [20] J. S. Kula, D. Psychoudakis, W. J. Liao, C.C. Chen, J.L. Volakis, J.W. Halloran, "Patch antenna miniaturization using recently available ceramic substrates," *IEEE Antennas Propag. Mag.*, vol. 48, no. 6, pp. 13-20, 2006.
- [21] J. L. Volakis, *Antenna Engineering Handbook*, 4th ed., McGraw Hill Professional, 2007.
- [22] H. Mosallaei and K. Sarabandi, "Antenna miniaturization and bandwidth enhancement using a reactive impedance substrate," *IEEE Trans. Antennas Propag.*, vol. 52, no. 9, pp. 2403-2414, Sep. 2004.
- [23] M. Fallah-Rad and L. Shafai, "Enhanced Performance of a Microstrip Patch Antenna using a High Impedance EBG Structure," *IEEE AP-S Int. Symp.*, Columbus, OH, USA, June 2003.
- [24] S. Pioch and J. M. Laheurte, "Size reduction of microstrip antennas by means of periodic metallic patterns," *Electronics Letters*, vol. 39, no. 13, pp. 959-961, June 2003,
- [25] W. H. Kummer and E. S. Gillespie, "Antenna measurements-1978," *IEEE Proc.*, vol. 66, no. 4, pp. 483-507, Apr. 1978.
- [26] S.A. Rezaeieh, A. Abbosh, "Broadband CPW-fed slot antenna with circular polarization for on-body applications at ISM band," *Asia-Pacific Microwave Conference*, Taiwan, Dec. 2012.
- [27] S. Rezaeieh, "Dual band dual sense circularly polarised monopole antenna for GPS and WLAN applications," *Electronics Lett*, vol. 47, no. 22, pp. 1212-1214, Oct. 2011.

- [28] B. Y. Toh, R. Cahill, and V. F. Fusco, "Understanding and measuring circular polarization," *IEEE Trans. Education*, vol. 46, pp. 313, 2003.
- [29] D. M. Pozar, S. M. Duffy, "A dual-band circularly polarized aperture coupled stacked microstrip antenna for global positioning satellite," *IEEE Trans. Antennas and Propag.*, vol. 45, pp. 1618-1625, 1997.
- [30] T. Wu, H., L. Gan, H. Chen, J. Huang, H. Zhang, "A Compact and Broadband Microstrip Stacked Patch Antenna with Circular Polarization for 2.45-GHz Mobile RFID Reader," *IEEE Antenn. Wireless Propag. Lett.*, vol. 12, pp. 623-626, 2013.
- [31] H. Wong, K.K. So, K.B. Ng, K.M. Luk, C.H. Chan, Q. Xue, "Virtually Shorted Patch Antenna for Circular Polarization," *IEEE Antenn. Wireless Propag. Lett.*, vol. 9, pp. 1213-1216, 2010.
- [32] K. L. Wong and Y.F. Lin, "Circularly-polarised microstrip antenna with tuning stub," *Electron. Lett.*, vol. 34, no. 9, pp. 831-832, 1998.
- [33] W. S. Chen, C. K. Wu, and K. L. Wong, "Novel Compact Circularly Polarized Square Microstrip Antenna," *IEEE Trans. Antennas and Propag.*, vol. 49, pp. 340-342, Mar. 2001.
- [34] B. Ghosh, S. M. Haque, D. Mitra, S. Ghosh, "A Loop Loading Technique for the Miniaturization of Non-Planar and Planar Antennas," *IEEE Trans. Antennas Propag.*, vol. 58, no. 6, pp. 2116-2121, 2010.
- [35] M. T. Aligodarz, D. M. Klymyshyn, and A. Rashidian, "Air-gap standing parallel strips waveguide for X-ray lithography fabrication: characteristics and antenna application," *5th Eur. Conf. on Antennas and Propag.*, Italy, April 2011.
- [36] T. L. Willke and S. S. Gearhart, "Micromachined thick-metal TSAs for high-permittivity substrates," *IEEE Antennas and Propag. Society Inter. Symp.*, Atlanta, GA, USA, June 1998.

# Chapter 6

## Conclusions and Recommendations for Future Work

### 6 Conclusions and Recommendations for Future Work

To conclude the thesis, in this section, a synopsis of the research carried out is presented and the contributions of the study and its outcomes are outlined. The dissertation is then closed by a list of potential future works, which are in line with the current outcomes and could yield improved or new ideas and contributions.

#### 6.1 Research Summary

In brief, the research carried out in this thesis can be outlined as follows:

- A new periodic TL<sup>41</sup> composed of HAR<sup>42</sup> EBG<sup>43</sup> cells with radiation properties is proposed, its dispersive nature is studied, and its radiation properties are demonstrated.
- Two types of novel antennas are proposed based on such a TL: short- and open-circuited SE-EBG-RA.

---

<sup>41</sup> Transmission Line

<sup>42</sup> High Aspect Ratio

<sup>43</sup> Electromagnetic Bandgap

- A novel analysis method based on the Bloch theory is proposed to efficiently analyze such periodic structures (called HFSS/Bloch).
- The HFSS/Bloch method is further developed to become independent of numerical analysis and be 100% closed-form.
- The basic HAR EBG cell is modified to develop miniaturized cells, which are then applied to the design of miniaturized versions of the proposed antenna.
- Some highly miniaturized antenna designs are presented, applicable to real-life space-limited communication systems.
- A new LWA<sup>44</sup> is presented based on the proposed HAR EBG cells.
- The proposed EBG antenna element is arrayed based on series-feeding topology, which yields a novel large aperture. A design process is rendered for this array, which improves the computational efficiency.
- A gap-loaded microstrip antenna with improved performance and fast-wave characteristics is introduced.
- A compact CP version of the proposed EBG antenna is presented.
- A technique based on parasitic HI<sup>45</sup> elements is investigated to better utilize the available physical aperture of the proposed antenna and enhance the overall aperture efficiency.
- The possibility of antenna measurement (efficiency, gain, and pattern) in semi-anechoic condition is demonstrated.
- DXRL fabrication steps are reviewed and partially developed to demonstrate the possibility of realizing HAR features for antennas like the proposed SE-EBG-RA. UV-lithography is used to fabricate various thin-metal antenna samples, and CNC milling was used to fabricate representative HAR samples for validating the various antennas through experimentation.

## 6.2 Conclusions and Contributions

In conclusion, the research offers the following scientific contributions:

- An analysis method based on Bloch theory for characterizing periodic antennas similar to the proposed ones, which uses a new way to model the unit cells, yielding new advantages.

---

<sup>44</sup> Leaky-Wave Antenna

<sup>45</sup> High Impedance

- Novel miniaturized EBG antennas with maintained performance applicable to modern mobile communications system with restricted power and form factor.
- A new circuit model yielding computational efficiency in the design process of the proposed antennas. This feature makes the method fast and easy to use without intensive numerical analyses and could be included in commercial CADs<sup>46</sup>.
- High-performance planar array antennas based on proposed EBG antennas, which is applicable to communication systems demanding high-gain low-loss flat antennas.
- Compact high-performance LWAs with scanning radiation pattern applicable to automotive radar systems.
- New theoretical insights on the relationship between antennas and TLs, generated by dedicated analyses and discussions.
- Antenna structures which are compatible (see Fig. 6.1) with emerging HAR microfabrication techniques like DXRL (see Appendix C), and hence, are able to be designed at higher frequencies with alleviated dielectric and conduction loss.

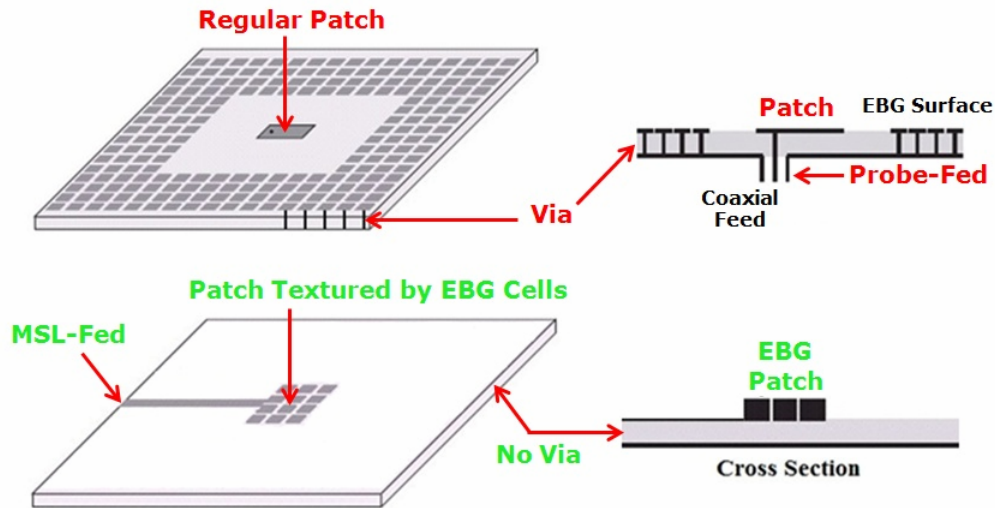


Fig. 6.1 Description of one of the novel antenna designs in the thesis (e.g. Sec. 5.4); to provide a DXRL-friendly design, the structure is simply fed by MSL, no via is considered, the substrate is alumina (friendly to X-ray scanner), and the top metal layer is thickened to accommodate HAR gaps.

Fig. 6.2 provides a concise overview of different classes of antennas proposed throughout the thesis and lists some of the potential applications of each one.

<sup>46</sup> Computer Aided Designs

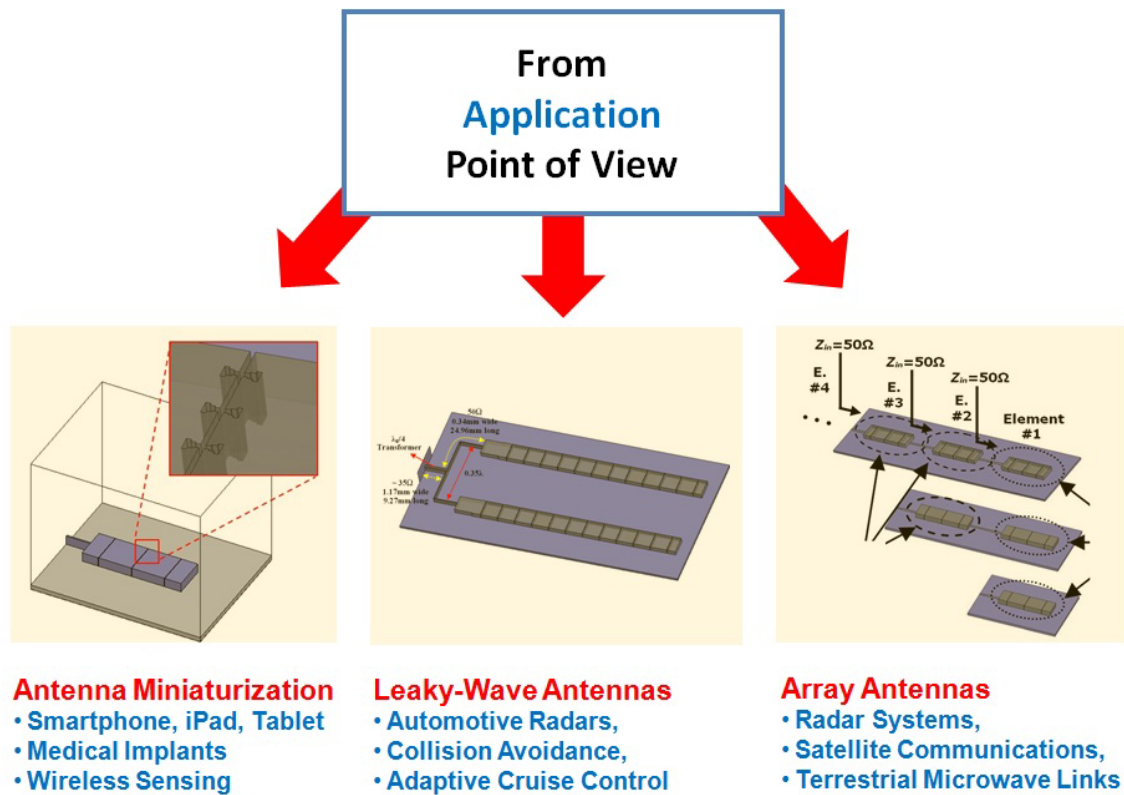


Fig. 6.2 Overview of different sorts of antennas introduced in this thesis and some of their potential applications.

### 6.2.1 Publications Based on the Thesis Material

- [1] M. Hosseini and D. M. Klymyshyn, "Radiation Properties of EBG Textured Tall Transmission Lines and Applications: A Low Profile Self-Excited EBG Resonator Antenna," *IEEE Antenna and Wireless Propagation Letters*, vol. 11, 2012; *Based on the material in Sec. 4.1.*
- [2] M. Hosseini and D. M. Klymyshyn, "A Low Profile Efficient Leaky-Wave Antenna Composed of High Aspect Ratio EBG Unit Cells," *Presented in the IEEE Radio and Wireless Symposium*, Austin, TX, USA, Jan 20-23, 2013; *Based on the material in Sec. 5.1.*
- [3] M. Hosseini and D. M. Klymyshyn, "Thick Metal EBG Cells with Narrow Gaps and Application to The Design of Miniaturized Planar Antennas," *Progress In Electromagnetics Research-PIER 64*, page 43-51, April 2014; *Based on the material in Sec. 4.5.*
- [4] M. Hosseini and D. M. Klymyshyn, "A High-Efficiency Planar Series-Fed Array Antenna Based on Thick EBG Resonator Elements," *Presented in the 16th Inter. Symp. on Antenna Technology and Applied Electromagnetics*, Victoria, BC, Canada, July 13-17, 2014; *Based on the material in Sec. 5.2.*
- [5] M. Hosseini and D. M. Klymyshyn, "A Circuit Model for the Design of Self-Excited EBG Resonator Antennas with Miniaturized Unit Cells," *IEEE Antenna and Wireless Propagation Letters*, vol. 13, June 2014; *Based on the material in Sec. 4.4.*
- [6] M. Hosseini and D. M. Klymyshyn, "Properties of Small Gap-Loaded Patch Antenna with Fast-Wave Behaviours," *Electronics Letters*, vol. 50, no. 18, Aug. 2014; *Based on the material in Sec. 5.3.*
- [7] M. Hosseini and D. M. Klymyshyn, "Miniaturization of the HAR Self-Excited EBG Resonator Antenna with a Shorting Plate: the Concept of Terminated, Short, and Open Circuited EBG Resonator Antenna," submitted to the *IEEE Trans. Antennas Propag.*, Sep. 2014; *Based on the material in Sec. 4.2.*
- [8] M. Hosseini and D. M. Klymyshyn, "A Compact Circularly Polarized Self-Excited EBG Resonator Antenna with High Radiation Efficiency," to be submitted, *Based on the material in Sec. 5.4.*

### 6.3 Future Works

A list of possible future works in line with or supplementary to the research outcomes is as follows:

- A CPW<sup>47</sup> version of the proposed HAR EBG cells (currently based on MSL<sup>48</sup>) could be developed.
- A CPW version of the proposed EBG antennas (SE-EBG-RA) could be sought, which are anticipated to exhibit higher BW.
- The circuit model for unit cells could be improved to work more accurately, especially for gaps with extremely high aspect ratios ( $30 < AR < 100$  within the feasible range for fabrication).
- The proposed antennas with thick EBG cells could be investigated for new designs on High Resistivity Silicon wafers (as opposed to alumina substrate or the like) to achieve compatibilities with Si microelectronics processes.
- Different kinds of feeding methods, like probe-feeding or proximity coupling, could be investigated for the SE-EBG-RA (currently MSL-fed).
- A cost-effective fabrication process based on UV lithography or simplified X-ray lithography could be developed to affordably and rapidly fabricate the proposed HAR EBG antennas.
- The efforts on DXRL processes initiated in Appendix C could be followed up to fabricate some of HAR EBG antennas proposed.
- A high gain flat array antenna (comparable to reflector-array antennas) based on the SE-EBG-RA elements could be designed for a particular application, such as direct satellite TV on vehicles, to further demonstrate the effectiveness of the designs.

---

<sup>47</sup> Coplanar Waveguide

<sup>48</sup> Microstripline



# **APPENDICES**

# Appendix A

## Three-Antenna Measurement Method

### A1 Friis Transmission Equation

The well-known Friis transmission equation [1] governing wireless communication links is as follows

$$P_r = \left( \frac{\lambda}{4\pi d} \right)^2 G_r G_t P_t = L_{FS} G_r G_t P_t \quad (\text{A1})$$

where  $P_r$  is the power received by the receiving antenna and  $P_t$  is the transmitted power. Fig. A.1 depicts how (A1) is applied to a typical communication links. (A1) describes the relation between the link performance and the parameters such as antenna performance (gain, etc.), wavelength ( $\lambda$ ), and the physical distance from transmitter to the receiver ( $d$ ). The term  $L_{FS}$  is known as free space loss. In practice, another term  $L_{other}$  has to be added considering the channel losses:

$$P_r = L_{FS} L_{other} G_r G_t P_t \quad (\text{A2})$$

where  $L_{other}$  includes any kinds of loss in the channel between transmitter and receivers such as those caused by diffraction, multiple reflection/refraction, effects of the earth surface, scattering by fog/rain, etc. Also, in (A1), the terms  $G_r$  or  $G_t$  are the realized gains of transmitter and receiver antennas as defined below:

$$G_{Realized} = (1 - |S_{11}|^2) \eta_{ohmic} D \quad (\text{A3})$$

where  $D$  is the antenna directivity.

### A2 Three-Antenna Method

The three-antenna measurement technique described in [2-3] is a method to measure the gain of an antenna under test (AUT) when there is a second standard calibrated antenna is not available. However, to carry out such a method, two extra antennas with unknown gains are required while they have to be able to operate at the same frequency of the ATU. The distinguished feature of

the method, which makes it quite appealing, is that it does not require any prior knowledge on the gain of any of the three antennas involved [4].

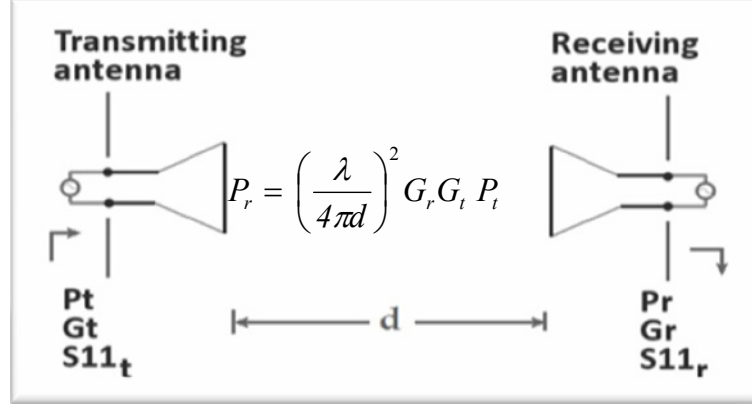


Fig. A.1. A typical communications link and the Friis transmission equation [1] governing the system.

This method starts with performing three measurements based on (A1). This leads to the following system of equations describing all three experiments:

$$G_1 \text{ dB} + G_2 \text{ dB} = 20\log_{10}\left(\frac{4\pi d}{\lambda}\right) + 10\log_{10}\left(\frac{P_r}{P_t}\right)^{(1)} = A \quad (\text{A5})$$

$$G_1 \text{ dB} + G_3 \text{ dB} = 20\log_{10}\left(\frac{4\pi d}{\lambda}\right) + 10\log_{10}\left(\frac{P_r}{P_t}\right)^{(2)} = B \quad (\text{A6})$$

$$G_3 \text{ dB} + G_2 \text{ dB} = 20\log_{10}\left(\frac{4\pi d}{\lambda}\right) + 10\log_{10}\left(\frac{P_r}{P_t}\right)^{(3)} = A \quad (\text{A7})$$

If the distance,  $d$ , the wavelength,  $\lambda$ , and the ratios of the received to transmitted power ( $P_r/P_t$ ) are known, the right-hand sides of the equations will all be known. The ratio  $P_r/P_t$  is in fact  $S_{21}$  in dB (i.e.  $20\log|S_{21}|$ ) measured by the network analyzer during the test. (A5) to (A7) is a system of three equations with three unknowns, and the solution to this system is simply as

$$G_1 \text{ dB} = \frac{A + B - C}{2} \quad (\text{A8})$$

$$G_2 \text{ dB} = \frac{A - B + C}{2} \quad (\text{A9})$$

$$G_3 \text{ dB} = \frac{-A + B + C}{2} \quad (\text{A10})$$

## Reference

- [1] C.A. Balanis, *Antenna Theory: Analysis and Design*, 3rd Ed., NJ: Wiley, 2005.
- [2] IEEE Standard Test Procedures for Antennas, ANSI/IEEE Std, 149–1979, Dec. 1979.
- [3] Kummer, W. H. and E. S. Gillespie, “Antenna measurements–1978,” *IEEE Proc.*, vol. 66, no. 4, pp. 483–507, Apr. 1978.
- [4] K. T. Selvan, “A modified three-antenna gain-measurement method to simplify uncertainty estimation,” *Progress In Electromagnetics Research*, PIER 57, 197–208, 2006.

# Appendix B

## Wheeler Cap Method

For a small antenna with a series circuit model around resonance, the efficiency can be calculated using [1-2]:

$$\eta = \frac{P_{\text{rad}}}{P_{\text{in}}} = \frac{P_{\text{rad}}}{P_{\text{rad}} + P_{\text{Loss}}} = \frac{R_1 - R_2}{R_1} \quad (\text{B1})$$

To be able to calculate  $\eta$ , first, the input resistance of the antenna under test (AUT) is measured without the cap and the value is called  $R_1$ . Second, the same resistance, with the cap mounted on the antenna is measured and is called  $R_2$ . This is described in Fig. B.1.

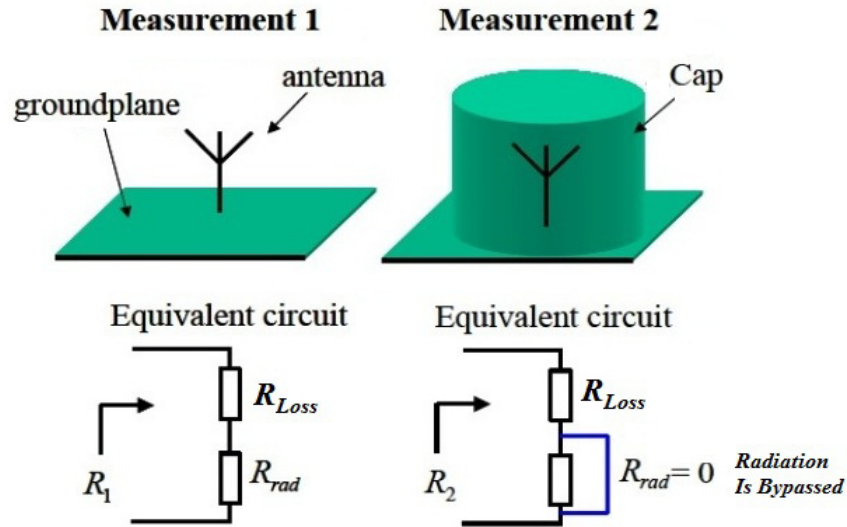


Fig. B.1 Description of the Wheeler Cap method and the related equivalent circuit model [3]

Even for antennas with parallel  $RLC$  model, sometimes experiments show that the series model assumption is sufficiently accurate. For example, although the patch antenna has a parallel  $RLC$  model, the series model, described by (B1), has resulted accurate experimental outcomes [4]. This could be attributed to the fact that each antenna comes with a piece of MSL feedline

and the loss in this line dominates the loss in antenna structure [4]. The parallel *RLC* model recommends using the following equation [2]:

$$\eta = \frac{G_R}{G_R + G_L} = \frac{G_{\text{no cap}} - G_{\text{cap}}}{G_{\text{no cap}}} \quad (\text{B2})$$

It is noted that if the antenna has multiple resonances which are located closely, the simple parallel or series *RLC* model is not able to accurately predict the efficiency and more complicated equations than (B1) or (B2) might be needed [e.g. 5]. The experiments carried out in [6] (and restated in [4]) show that the cap size and shape is not so critical. Other attempts like [7] also demonstrate the applicability of cubic or rectangular caps. Many researchers have used rectangular caps and have shown that this cap functions like the spherical one assumed by the theory. It is also discovered in [6] that the cap conductivity (and hence the type of metal) do not significantly change the result. However, it is observed that a good electrical contact between the cap and the ground plane is very important. Another important factor to consider is to place the antenna at the center of the cap [4]. This work shows that the Wheeler method is repeatable and provides high accuracy. It is also deduced from [4] that the method is not difficult to implement, as the cap shape and material are arbitrary (to some extent).

## References

- [1] E.H. Newman, P. Bohley, C.H. Walter, "Two Methods for the Measurement of Antenna Efficiency," *IEEE Trans. Antennas Propag.*, vol. AP-23, no. 4, July 1975.
- [2] H. Choo, R. Rogers, and H. Ling, "On the Wheeler Cap Measurement of the Efficiency of Microstrip Antennas," *IEEE Trans. Antennas Propag.*, vol. 53, no. 7, pp. 2328-2332, July 2005.
- [3] O. Litschke, M. Geissler, D. Heberling, P. Waldow and I. Wolff, "Adaption of the Wheeler-Cap Method for Measuring the Efficiency of Mobile Handset Antennas", IMST GmbH, Itg Fachbericht, Germany, 2003.
- [4] D. M. Pozar and B. Kaufman, "Comparison of Three Methods for the Measurement of Printed Antenna Efficiency," *IEEE Trans. Antennas Propag.*, vol. 36, no. 1, Jan. 1988.
- [5] C. Cho, I. Park, and H. Choo, "A Modified Wheeler Cap Method for Efficiency Measurements of Probe-Fed Patch Antennas With Multiple Resonances," *IEEE Trans. Antennas Propag.*, vol. 58, no. 9, pp. 3074-3078, Sep. 2010.
- [6] E. H. Newman, P. Bohley, C. H. Walter, "Two Methods for the Measurement of Antenna Efficiency," *IEEE Trans. Antennas Propag.*, vol. 23, no.4, pp. 457 - 461, July 1975.
- [7] Y. Huangl , R. M. Narayananl , and G. R. Kadambi, "On Wheeler's Method for Efficiency Measurement of Small Antennas," *IEEE Antennas and Propagation Society International Symposium*, Boston, MA, USA, July 2001.

# Appendix C

## Antenna Prototyping Employing DXRL Process

A sample HAR SE-EBG-RA was fabricated using a process based on assembly of CNC milled parts and was successfully tested (Sec. 4.2). However, this process was somewhat limiting in providing small structures with very high aspect ratio (HAR) features required for high performance at higher microwave frequencies, and was also not suitable for batch fabrication. The assembly process realized gaps by inserting shims, and favorably resulted in AR of 16 (gap=0.6mm). This could be compared to AR of 14, stated by Table C.1, if using CNC machining to realize the gaps. From Table C.1, the associated roughness by the CNC method is typically as high as 3-5 $\mu$ m, which was also confirmed by inspection of the machined metal pieces of the aforementioned prototype (~6 $\mu$ m). Therefore, CNC machining is not the best choice for high frequency designs for which roughness could cause undesirable loss.

As an alternative to CNC machining, we attempt to prototype one sample of the proposed HAR antennas to *demonstrate the possibility* of future fabrication via deep X-ray lithography (DXRL) processes. These process steps have been primarily conducted at the Canadian Light Source (CLS, SyLMAND lab), and have not previously been specifically applied to such antenna structures. The efforts undertaken here include assessing several of the process steps required to fabricate an X-ray mask incorporating the antenna layout, and then using the mask to perform first X-ray lithography exposures of representative antenna structures.

### C.1 Introduction to DXRL

Nowadays, a number of micromachining techniques are available which are capable of fabricating very fine 2D or 3D micro-systems and micro-structures. These techniques include (but not limited to) mechanical micromachining (e.g. CNC machining/milling), laser-based micromachining (e.g. laser ablation), surface/bulk micromachining (mostly used with silicon wafers), X-ray lithography-based techniques (such as LIGA), UV-based techniques (such as UV-

LIGA), Deep Reactive Ion Etching, and Electro-Discharge machining. These are the same methods used to fabricate MEMS<sup>49</sup> except that MEMS devices usually have moving parts. Among these, LIGA which is a German acronym for Lithographie (deep X-ray lithography), Galvanoformung (electroforming), and Abformung (plastic molding) [1-2] is a micromachining process specializing in realization of tall micro-structures (up to few millimeters [3-4]), with relatively high aspect ratio (up to 100, see Table C.1), with highly accurate sub-micron feature sizes [4], and with nearly optical sidewall quality (see Table C.1). Starting from 1975 [5], LIGA has been used in a variety of applications in various realms including Micro-fluidics, Photonics, Micro-mechanics, and more recently Microwave Engineering. DXRL is the part of the complete LIGA process which is immediately applicable to the antennas in this thesis. Although the initial cost of mask making, X-ray exposure, and all other stages is relatively high, the process could be much cheaper thanks to the potential of replication using DXRL fabricated molds. Table C.1 compares DXRL with some other microfabrication techniques in terms of five different parameters.

Table C.1 Comparison between properties of some microfabrication techniques, which are available for realization of HAR features [6].

Parameters	CNC Machining	Deep Ultra Violet	Deep Reactive Ion Etching	Electro Discharge Machining	X-ray Lithography	Laser
Aspect Ratio	14	22	10-25	<100	100	<10
Accuracy	3-5 $\mu$ m	2-3 $\mu$ m	<1 $\mu$ m	1-3 $\mu$ m	<1 $\mu$ m	3-5 $\mu$ m
Roughness	3-5 $\mu$ m	1 $\mu$ m	2 $\mu$ m	0.3-1 $\mu$ m	<20nm	0.1-1 $\mu$ m
Maximum height	Unlimited	300 $\mu$ m	300 $\mu$ m	3-5mm	<10mm	300 $\mu$ m
Mask required?	No	Yes	Yes	No	Yes	No

It is deduced from Table C.1 that Electro-Discharge and DXRL micromachining methods are the most qualified candidates to employ for direct fabrication of the HAR features required for these antenna structures. However, Electro-Discharge machining (electrode/wire-based carving) is not suitable for HAR features of the proposed antennas because it could require separate fabrication of the top HAR metal layer structures and then separate assembly and mounting onto the microwave substrate. Also, when comparing the tolerance and sidewall roughness in Table

<sup>49</sup> Micro-Electro-Mechanical Systems



C.1, DXRL stands out. The distinguishing features of DXRL stem from the use of highly penetrating X-rays able to expose not only the impinged outer surface but also the other side of the thick layer of resist (mostly PMMA<sup>50</sup>) used in the process. Fig. C.1 describes different steps of the LIGA process (excluding the molding step).

As seen, first a thick X-ray sensitive resist is glued onto a substrate with a proper thin adhesion layer and plating base in between (Cr/Au or Ti/TiOx). For most RF circuits, the substrate is a grounded dielectric slab made of alumina, quartz, GaAs, etc. Then, an X-ray compatible working mask is required. As seen in Fig. C.1 (b), the mask is made of a thin X-ray transparent membrane (e.g. Be, Ti, or Graphite) and an absorber (typically gold). As the absorber is of a high atomic number, negligible X-ray passes through it. After obtaining the mask, as in Fig. C.1 (c), it is placed adjacent to the substrate/resist and some parts of the resist are irradiated by X-rays, based on the desired layout patterned on the mask. Then, the exposed areas of PMMA can be (very selectively) dissolved in a proper developer. As in Fig. C.1 (d), utilizing the plating base, it is now possible to electroplate a metal (typically Ni or Au) filling the voids in the resist. After that, as in Fig. C.1 (e), the remaining unexposed resist is removed (so-called stripping), and finally using a proper etchant, the plating and adhesion layer is etched away to provide electrical isolation (only needed for some special applications like antennas) between the thick metal traces on the top of the microwave substrate. At this point, the metal traces, which included tiny gaps with tall sidewalls (HAR gaps), are successfully grown on the substrate. Considering that the substrate is either already backed by a metal (ground plane) or could be backed at this point, the antenna will be ready for being diced off the wafer and passed onto the measurement stage.

As opposed to the considerable works on the DXRL-based MEMS technology, DXRL is still young with the fabrication of micro-scale RF components. The review shows that serious attention to DXRL-based RF components dates back to the 1990s [e.g. 7-10]. The lack of published resources, however, has become an incentive to explore the possibility of realizing complex 2D/3D RF components, especially for very high frequency applications [11-12] in which  $\lambda$  severely shrinks, and hence, minimum feature sizes enter the micro-scale regime. Some aspects of MEMS and DXRL technology have also been applied to microwave passive elements where the realization of inductances [13] and tunable capacitances are investigated. References [14-18] provide some other efforts recently made on DXRL-based RF technology. Altogether, it

---

<sup>50</sup> Polymethyl-methacrylate

can be concluded from such studies that utilizing the vertical dimension may provide one or a combination of these features: more flexibility in design (an extra parameter), higher power handling (higher breakdown point), less dispersion, reduced power consumption, smaller size, increased side coupling, and reduced cost of batch fabrication.

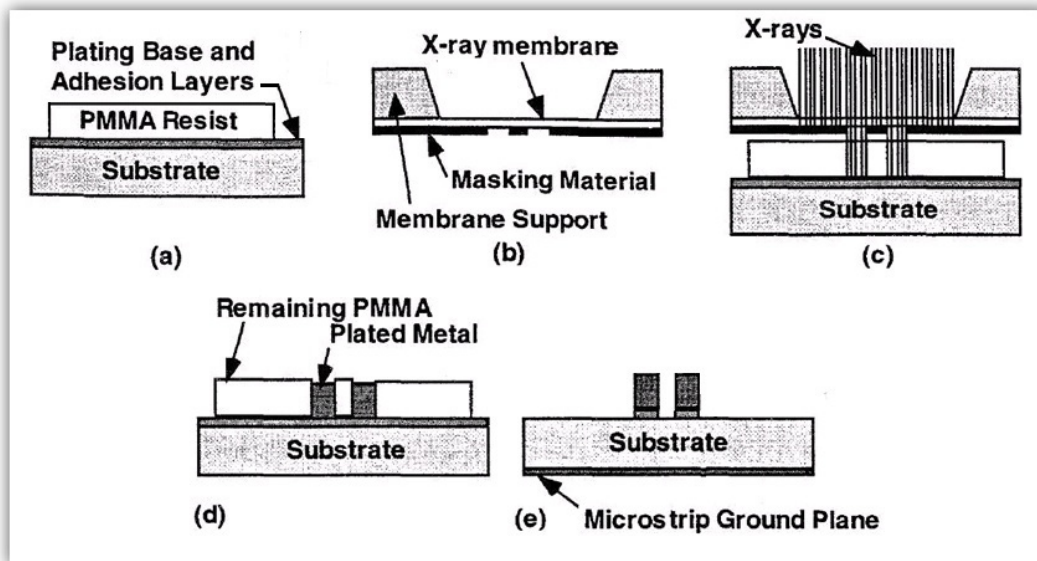


Fig. C.1 Illustration of DXRL fabrication process [19] © 1998 IEEE.

Inspecting the literature more narrowly for DXRL-involved antennas reveals the lack of previous efforts. The literature review on DXRL-based antennas was presented in Chap. 2 where the history of HAR antennas was presented. Following such efforts, this work presented some HAR antennas which were new from two distinct aspects. Firstly, it was the first time that HAR EBG cells and whole radiating structures based on them were proposed. Secondly, it was the first attempt to prototype such HAR antennas using DXRL fabrication. The latter is described in this section.

## C.2 DXRL Prototyping Efforts

A sample SE-EBG-RA is designed in HFSS for application to DXRL. As seen in Fig. C.2, the antenna is finalized in HFSS and a layout with GDSII format is created by the software. The file is then exported to ADS<sup>51</sup> software for some specialized post-processing.

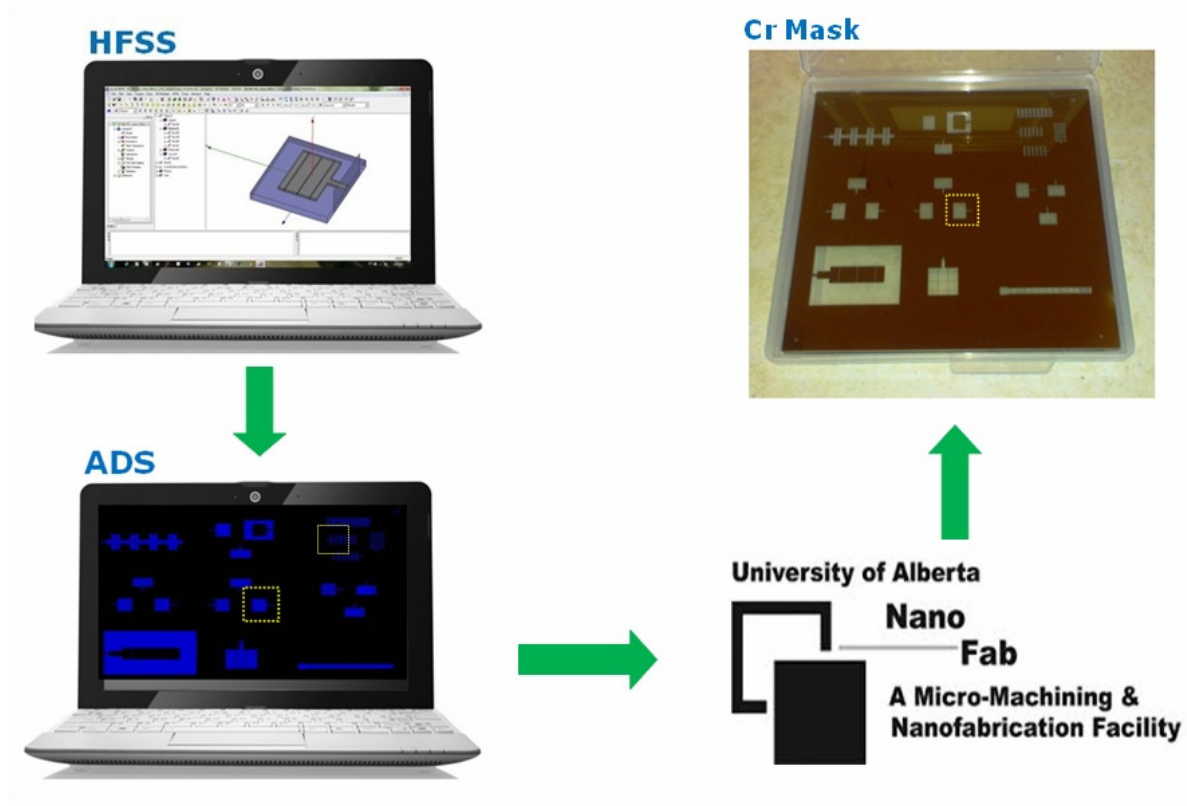


Fig. C.2. The progression from antenna simulation and design to Cr mask.

The first processing is to round any sharp corner by a radius of  $3\mu\text{m}$  to avoid cracks in the thick resist layer during exposure and development processes. The second is to fracture any of the polygons of the layout that have more vertices than 199 (this part has been performed in Layout Editor software). This is a limit set by the laser writer, which is later used for making a Cr mask, which will be the basis for fabricating an X-ray mask. When the layout is ready, it is sent to the NanoFab microfabrication facility at the University of Alberta (or any similar vendor) to make a Cr mask. This mask is composed of a glass sheet as the substrate and a thin layer of patterned Cr. The Cr mask is only usable along with UV light. Thus, the next step is to make a

<sup>51</sup> Advanced Design Systems

copy of this mask, which is compatible with X-rays. To do this, the Cr mask is used in a UV lithography process to fabricate an Au on graphite-wafer based mask with the same layout.

Graphite is an inexpensive rigid substrate material with off-the-shelf availability of different grades and different thickness, and safe handling [20], which was first introduced as an X-ray mask membrane in [21]. Rigid graphite offers some desirable properties, such as moderate X-ray absorption, relatively low cost, and electrical conductivity [21]. Its high thermal conductivity also helps with dissipating the X-ray energy absorbed in the Au layout patterns [22], thereby protecting the fine feature sizes. It is also generally robust for handling and easy to process, compared to other fragile thin-membrane materials such as titanium, and associated fabrication processes. However, there are also downsides such as being a dirt-spreading material in a clean room environment, and limited obtainable smoothness on sidewalls of the HAR gaps, fundamentally due to the grain size limit of wafers (grains are  $1\mu\text{m}$  or larger). The large grains may cause some unfavorable striations on the sidewalls. Therefore, it is important to understand that this roughness (up to  $1\mu\text{m}$ ) could set a limit on the maximum frequency of RF components fabricated by such masks, while also noting that this limit is still high enough for many of the RF applications. When it comes to naturally high efficiency antennas of the present work, this roughness is somewhat less problematic as the efficiency is not directly affected by loss, but indirectly through the aforementioned equation,  $\eta = R_r / (R_r + R_L)$ . Accordingly, for the proposed high-performance HAR antennas for which  $R_r \gg R_L$  (radiation dominating loss), graphite could be a reasonable candidate, even at very high frequencies. To quantitatively show the effect of loss, a typical matched SE-EBG-RA has  $R_r \sim 50\Omega$ , and  $R_L \sim 4\Omega$ , which gives  $\eta = 92\%$ . According to (2.10), roughness could multiply  $R_s$  by 2, which means loss and the  $R_L$  will double. In that case,  $R_L \sim 8\Omega$  and the new efficiency will be 87%, which is still very high. Fig. C.3 describes some details of the process of X-ray mask fabrication based on UV-lithography.

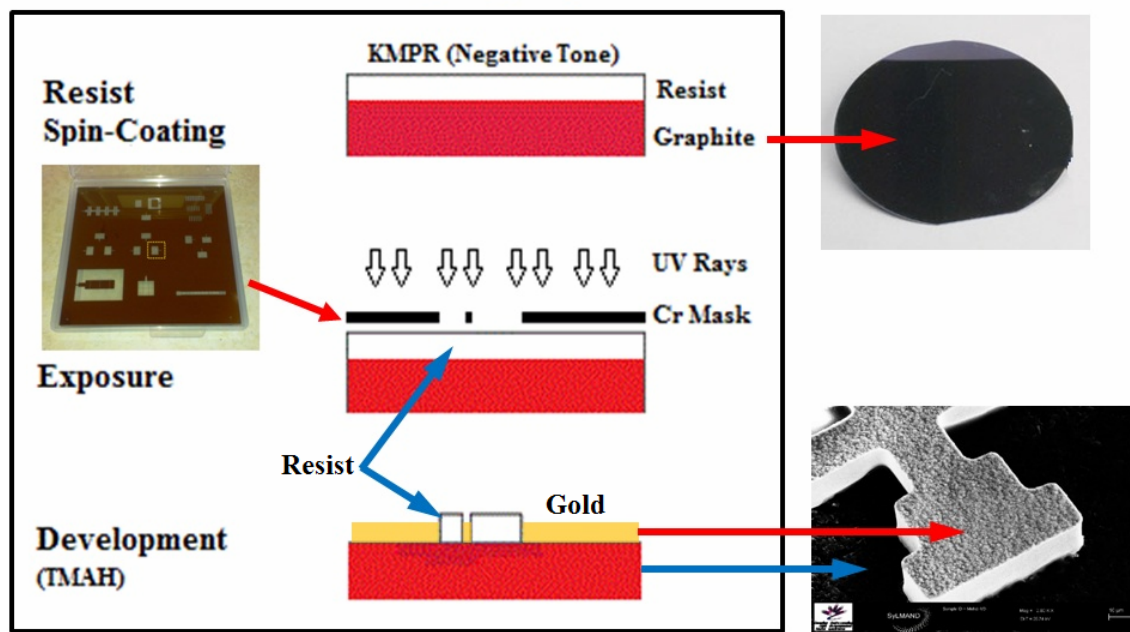


Fig. C.3 Different steps of the UV lithography process using the Cr mask towards fabrication of a graphite X-ray mask.

As seen, a round graphite mask of 250 $\mu$ m thickness is used as the substrate for the X-ray mask. A 27 $\mu$ m layer of KMPR<sup>52</sup> is then spin-coated on the graphite wafer. The next step is to place the patterned Cr mask in proximity to the prepared wafer, with a 10 $\mu$ m shim to protect the surface of the resist from rubbing against the mask surface. Next, using the UV source (500Watt Oriel Light), the KMPR is exposed to the UV light. The exposure time is adjusted based on the wattage set on the source, the recommended dose in the KMPR data sheet, and some extra experiments performed to fine-tune the dose. As recommended by the resist datasheet, a glass filter (PL-360-LP from Omega Optical) is used between the source and the sample to purify the spectrum; specifically, to cut wavelengths shorter than 365nm (i-line UV). This enhances the quality of patterning and provides vertical sidewalls, archived in Fig. C.5 (c).

After exposure, the sample is submerged in a substance called developer. In case of the KMPR resist, as recommended by the datasheet, TMAH (a well-known developer) is used for a deliberately set time. This time is recommended in the datasheet but could be different and has to be adjusted based on several experiments for the best feature quality. The next step is to electroplate the absorber on the graphite. The most important factor defining quality in this case

<sup>52</sup> Commercial name of a well-known photo-resist

is the verticality of the plated sidewalls observed under the microscope. After successful pattern transfer (exposure followed by development), the conductive nature of graphite assists as a seed layer to be utilized for electroplating of the wafer in the voids. A few test samples were prepared using Ni plating, to assess the feasibility before the final gold plating, as shown in Fig. C.4. For the best sample, the KMPR was removed and the Ni sidewalls were inspected. The result of the best obtained Ni-plated mask features in this study is shown in Fig. C.5 (c). As seen from the SEM micrograph, the sidewalls are quite vertical for a deep UV exposure (verticality achieved is  $\sim 87$  degrees). After making sure that verticality of the sidewalls is satisfactory, similar process steps were repeated to make another sample, this time plated with Au. The electroplating was performed at CAMD<sup>53</sup> in the Louisiana State University and our inspection shows a thickness of 22 to 24 $\mu\text{m}$ .

Fig. C.4 shows the result of the complete lithography process, which are five printed antennas on the Au-on-graphite mask wafer. The antennas are repeated multiple times for redundancy. As seen, fine features are realized, with practical minimum gap size measured to be 18.8 $\mu\text{m}$ , likely accurate enough for the current EBG antenna application.

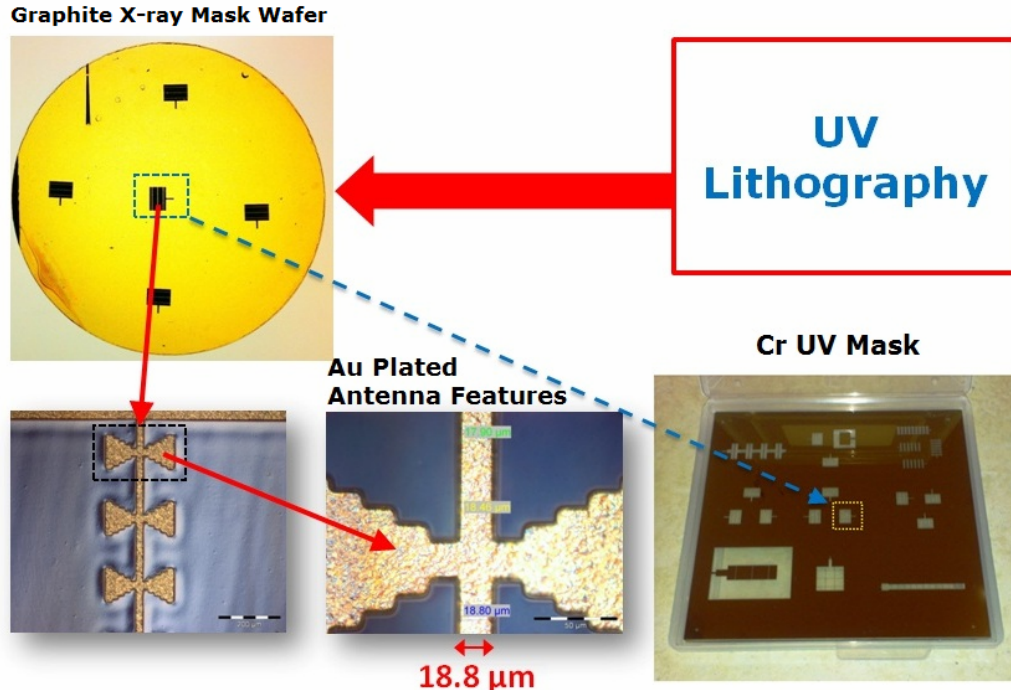


Fig. C.4 Different views of the fabricated graphite mask, with one of the antennas on the mask highlighted; SEM micrographs of one representative gap and the associated pillars are included.

<sup>53</sup> Center for Advanced Microstructures & Devices



By comparison, the same gap size on the layout is  $18\mu\text{m}$ . This is quite respectable, given the relatively crude UV-lithography process applied, and the direct pattern transfer to thick UV resist in a single exposure step. If required, more accurate features could be expected, for instance with E-beam lithography or other high resolution primary patterning, and possibly an intermediate transfer step into thinner resist with soft X-ray lithography. In developing this graphite mask, some of the efforts have been unsuccessful, due to incorrect dose (yielding sloped sidewalls), over electroplating, or electroplating underneath the resist. Some of these conditions are shown in Fig. C.5.

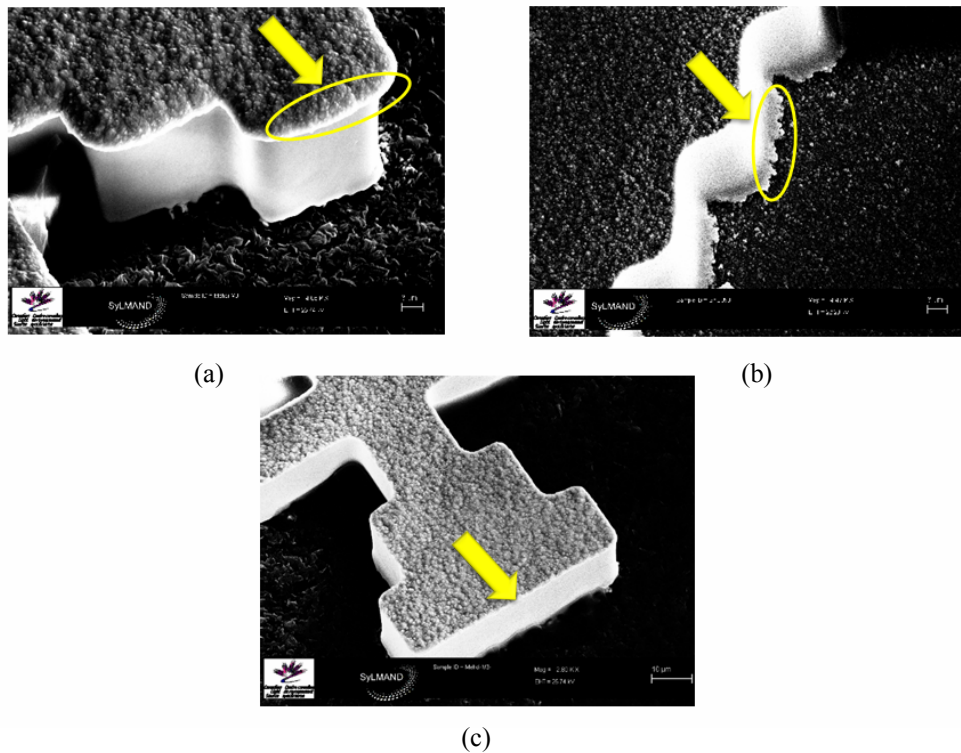


Fig. C.5. Unsuccessful attempts due to over plating (a), plating underneath the resist (b), and incorrect dose resulting in sloped sidewalls (b); the best wafer obtained with vertical sidewalls is also shown (c).

To prepare the mask for X-ray lithography exposures, a support ring was glued to the wafer as in Fig. C.6.

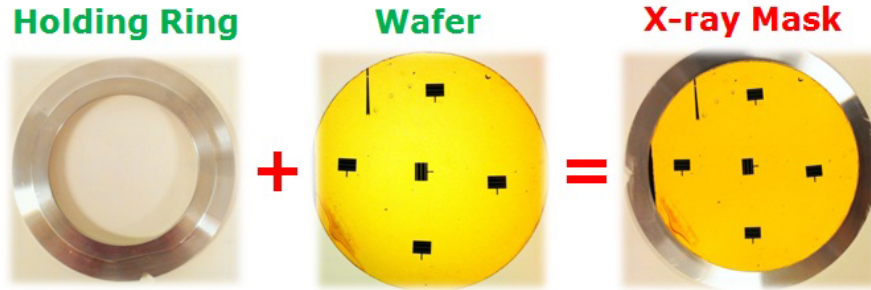


Fig. C.6. Attaching a support ring to the wafer to achieve the graphite X-ray mask processed at SyLMAND.

The next step after obtaining the X-ray mask is to expose sample HAR antenna patterns using the mask. The X-ray lithography is carried out at SyLMAND, a laboratory located at the end of one of the CLS beamlines. As depicted in Fig. C.7, the sample and the mask are mounted at the scanner where users gain access to the X-ray beam for X-ray lithography. Fig. C.7 shows the sample and mask in place. After placement, the scanner door will close and exposure will take place.

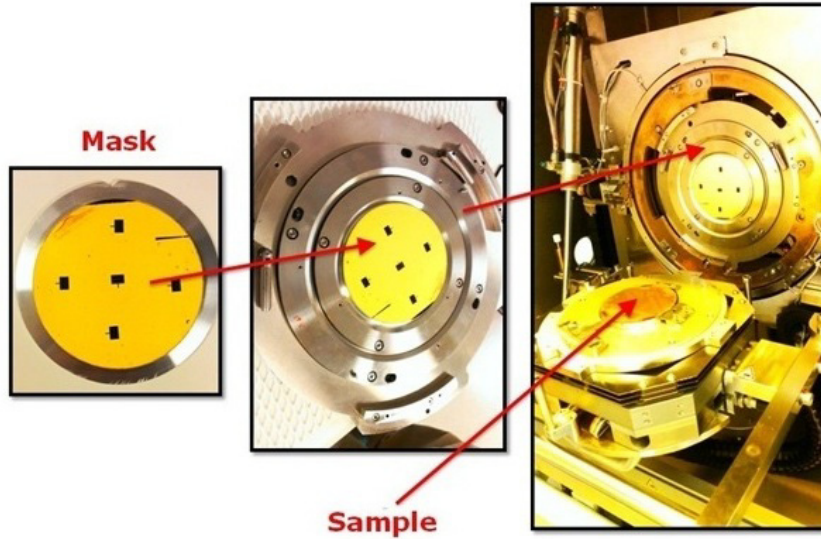


Fig. C.7. Description of how the X-ray mask and the sample are mounted onto the scanner; photos are created by the author and show the fabricated X-ray mask and the sample.

The first sample shown in Fig. C.8 is a test sample composed of a Si wafer (the second sample is fabricated on an alumina substrate with  $\epsilon_r=9.9$ ) with a Ti/TiOxide seed layer sputtered on the surface, and a 150 $\mu$ m thick PMMA resist glued on the top. PMMA is a well-known positive-tone resist which is non-sensitive to natural light, but is sensitive to X-rays.



This sample has undergone the exposure with calculated dose using the graphite mask in Fig. C.6. The dose depends on the graphite and KMPR resist thicknesses (KMPR is  $27\mu\text{m}$  and is left on the mask). It also depends on the thickness of PMMA on the sample. A software called DoseSim takes every parameter into account and calculates the required exposure dose for a specific condition. The goal is to reach a different but appropriate dose simultaneously at the bottom and top of the PMMA resist resulting in vertical features at the end of the process. The spectrum of the beamline is adjusted using the available mirrors and filters to provide the dose recommended by the DoseSim. Fig. C.8 shows this sample after both the exposure and development.

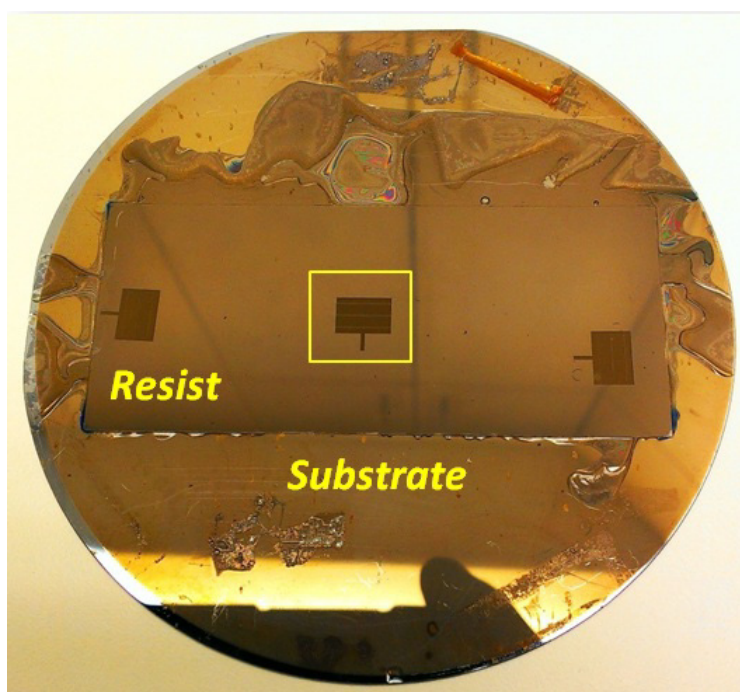


Fig. C.8. The first sample wafer undergoing an X-ray lithography experiment. The same designs shown on the Cr mask (Fig. C.4), and then translated to the X-ray mask, are transferred into a  $150\mu\text{m}$  thick PMMA resist on a Si substrate.

Inspection shows that in some locations, development has sufficiently removed the PMMA and the seed layer is accessible for plating. However, it is necessary to try to have every location well-exposed and sufficiently developed. Most likely, the calculated and delivered dose is not yet appropriate for this particular mask/substrate material sandwich, and requires further optimization, both in the calculated parameters, and also adjusting the beamline and scanner

parameters to achieve these. It should be emphasized that application-specific sample preparation, exposure, and development required for X-ray lithography, are typically very time-consuming, especially, at the research stage, as SyLMAND processes and equipment are still under development. Therefore, optimization of the exposure and other parameters required for fabrication is recommended as a future work. Fig. C.9 (a) shows what the structure should ideally resemble after successful development. Because the gaps are very narrow, yet tall, during the exposure, secondary radiations from the substrate caused by X-rays could undesirably illuminate the interface between PMMA structures and the substrate. This causes the developer to get underneath and delaminate the resist from substrate. Pillars shown in Fig. C.9 are added [23] to the layout to improve the adhesion.

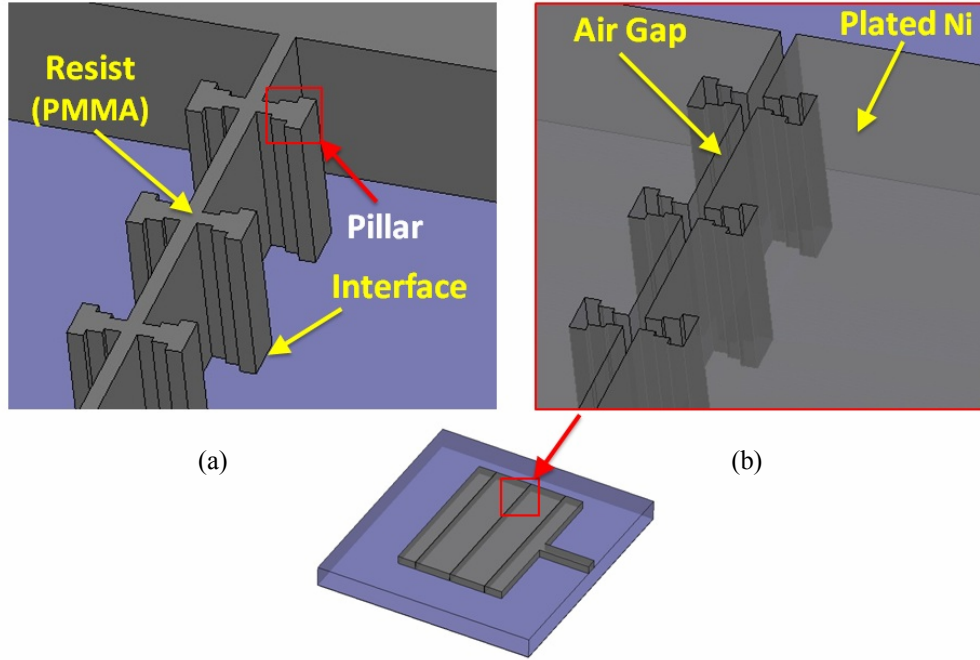


Fig. C.9. 3D view of how the antenna shown in Fig. C.8 should look after development (a); 3D view of the antenna when the voids in Fig. C.9 (a) are filled with electroplating.

These pillars tend to decrease the overall parallel plate capacitance of gaps. However, HFSS simulation shows that the reduction is small ( $< 2\%$ ) and could be taken into account.

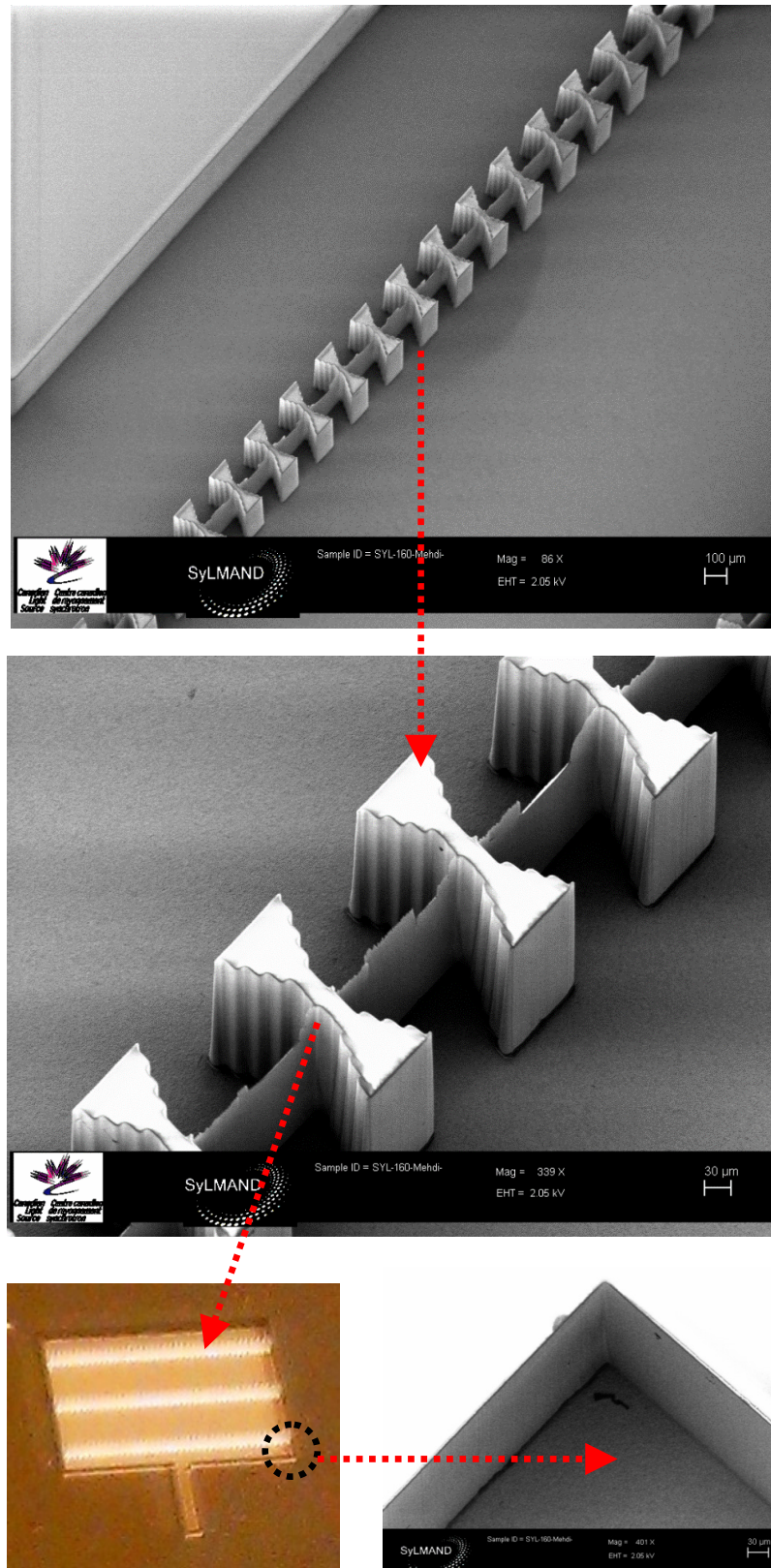


Fig. C.10. SEM micrographs of the second antenna sample after the development step.

A second sample, which is similar to Fig. C.9, was also fabricated which shows the results that are more promising. For this sample, shown in Fig. C.10, the PMMA is thicker at 500 $\mu$ m, which is thick enough to plate 400 $\mu$ m of Ni, required for the actual antenna design (400  $\mu$ m thick Ni with 18 $\mu$ m gaps: AR  $\sim$  22). The substrate is 1mm alumina in this case.

As seen, the sidewalls have generally good verticality, but the features have shrunk in one lateral dimension more than the other dimension. Adhesion of the resist to the substrate is also very good and the Ti/Ti Oxide seed layer is fully accessed for electroplating Ni. Therefore, it could be the matter of readjusting the exposure parameters and making more trial samples before the plating could occur and the antenna could be finalized.

If the structure is developed perfectly as depicted in Fig. C.9 (a), the gaps could be plated using the seed layer, and the result would resemble Fig. C.9 (b). As seen, the remaining PMMA in the gaps would be stripped away after plating, using X-ray flood exposure and development. In addition, the Ti seed layer must be etched using Hydrofluoric acid, to isolate the metal structures.

From this point on, the last step of the microfabrication is to dice the antenna off the wafer. Fig. C.11 shows a thin antenna fabricated by UV lithography (rather than X-ray lithography) and the Cr mask pattern transferred to an alumina wafer.

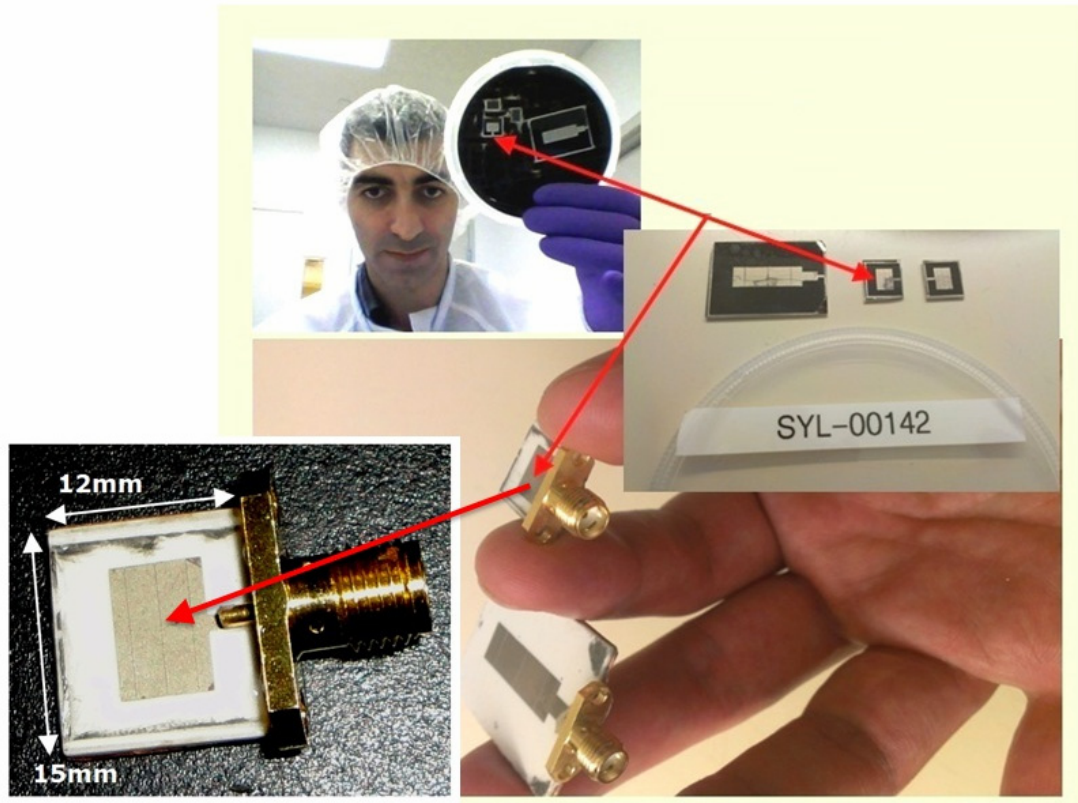


Fig. C.11 An example of dicing and attaching the microwave connector to antennas; the prototype shown is made by UV lithography and Ni plating on Alumina, and is successfully used to verify the circuit model in Sec. 4.4.

The metal is  $4\mu\text{m}$  electroplated Ni and the gaps are  $27\mu\text{m}$ . The performance of this antenna was presented in Sec. 4.4. It is important to note that in terms of Ni electroplating (although thinner), dicing, and connector mounting, the process for this thin prototype will be very similar to what the HAR antenna in Fig. C.8 or C.10 would undergo. The antenna in Fig. C.11 is diced using a diamond-tip dicer. Then the SMA connector is attached using Silver Epoxy conductive glue.



### C.3 Conclusion

This section presented efforts to date on microfabrication of an HAR SE-EBG-RA prototype using both UV lithography and X-ray lithography, which also included developing processing steps for a graphite X-ray mask. The mask was employed in an X-ray lithography exposure, to demonstrate the feasibility of fabricating HAR SE-EBG-RA antenna devices. The DXRL process was carried out up to the electroplating step for two samples and the challenges were described. Overall, a clear view of the whole DXRL microfabrication process, starting from the concept (antenna simulation), and ending with the prototype (antenna sample) was rendered. Using similar microfabrication steps, various thin-metal prototypes were fabricated using UV lithography, and tested as presented in the earlier Chapters.

### References

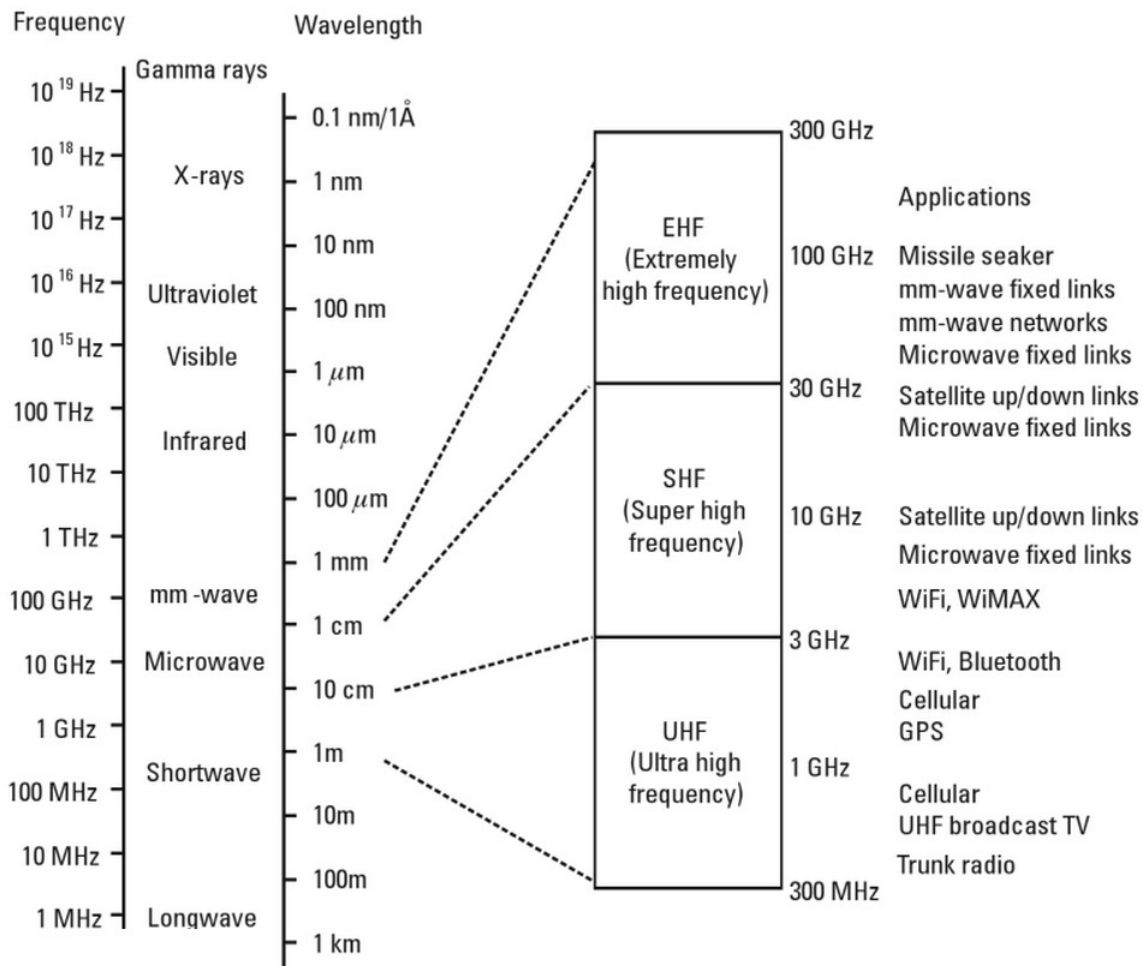
- [1] E.W. Becker, W. Ehrfeld, P. Hagmann, A. Maner, and D. Münchmeyer, "Fabrication of Microstructures with High Aspect Ratios and Great Structural Heights by Synchrotron Radiation Lithography, Galvanoforming, and Plastic Moulding (LIGA process)," *Microelectronic Engineering*, vol. 4, pp. 35-56, 1986.
- [2] E. W. Becker, W. Ehrfeld, D. Munchmeyer, H. Betz, A. Heuberger, S. Pongratz, W. Glashauser, H. J. Michel, and V. R. Siemens, "Production of separation nozzle systems for uranium enrichment by a combination of X-ray lithography and galvanoplastics," *Naturwissenschaften*, vol. 69, pp. 520-523, 1982.
- [3] E. Spiller, "Early history of X-ray lithography at IBM," *IBM J. RES. DEVELOP.*, vol. 37, no. 3, pp. 291-297, May 1993.
- [4] W. Menz, J. Mohr, and O. Paul, *Microsystem Technology*. Weinheim: Wiley-VCH, 2001.
- [5] M. J. Madou, *Fundamentals of Microfabrication: The Science of Miniaturization*, CRC Press, 2002.
- [6] M. J. Jackson, *Microfabrication and nanomanufacturing*. Boca Raton, FL: CRC/Taylor & Francis, 2006.
- [7] Willke, T.L.; Gearhart, S.S., "LIGA micromachined planar transmission lines and filters," *IEEE Trans. Microwave Theory Tech.*, vol. 45, no. 10, pp. 1681-1688, 1997.
- [8] D. Munchmeyer and J. Langen, "Manufacture of three-dimensional microdevices using synchrotron radiation," *Rev Sci Instrum*, vol. 63, no. 1, pp. 713-721, Jan. 1992.
- [9] Willke, T.L.; Gearhart, S.S., "Novel micromachined LIGA microstrip transmission lines and filters," *IEEE International Microwave Symposium Digest (MTT-S)*, 1996.
- [10] McCormick, M.; Chowanietz, E.; Lees, A., "Microengineering design and manufacture using the LIGA process," *Engineering Science and Education Journal*, vol. 3, no. 6, pp. 255-262, 1994.
- [11] Ma, Z., Klymyshyn, D. M., Achenbach, S., Börner, M., Dambrowsky, N., Mohr, J., "An Ultra-Deep High-Q Microwave Cavity Resonator Fabricated using Deep X-Ray Lithography," *IEICE Transactions on Electronics*, E90-C, pp. 2192-2197, 2007.

- [12] H. C. Jayatilaka, D. M. Klymyshyn, M. Börner, and J. Mohr, "Compact thick metal diplexer with multi-coupled folded half wavelength resonators," *Progress In Electromag. Research C*, vol. 18, pp. 1-8, 2011.
- [13] D.M. Klymyshyn, M. Boerner, D. Haluzan, E. Gono Santosa, M. Schaffer, S. Achenbach, J. Mohr, "Vertical High-Q RF-MEMS Devices for Reactive Lumped Element Circuits," *IEEE Trans. Microwave Theory Tech.*, vol. 58, no.11, pp. 2976-2986, Nov. 2010.
- [14] Y.M. Shin, J. K. So, K. H. Jang, J. H. Won, A. Srivastava, S.T. Han, J. H. Kim, S. S. Chang, R. K. Sharma and S. N. Joshi, G. S. Park, "Experimental Investigation of 95GHz Folded Waveguide Backward Wave Oscillator Fabricated by Two-Step LIGA," 7<sup>th</sup> *IEEE Inter. Conf. Vacuum Electronics*, USA, April 2006.
- [15] J. C. Tucek, D. R. Whaley, D. A. Gallagher, V. O. Heinen, K. E. Kreischer, D. C. Mancini, R. Divan, J. Yaeger, D. Ryding, "LIGA Fabrication of Folded Waveguide Circuits," 4<sup>th</sup> *IEEE Inter. Conf. Vacuum Electronics*, 2003.
- [16] Park, K.Y.; Park, J.Y.; Choi, H.K.; Lee, J.C.; Lee, B.; Kim, J.H.; Kim, N.Y.; Kim, G.H.; Kim, D.W.; Bu, J.U.; Chung, K.W., "A novel Ka-band bandpass filter using LIGA micromachined process," *Asia Pacific Microwave Conference*, 2000.
- [17] Y. M. Shin, G.S. Park, S.T. Han, J.I. Kim, "Design of W-band coupled-cavity TWT by LIGA fabrication," 3<sup>rd</sup> *IEEE International Vacuum Electronics Conf. (IVEC)*, 2002.
- [18] Jill Hruby, "Overview of LIGA Microfabrication," *Proc. of American Institute of physics conf.*, 2002.
- [19] Steven S. Gearhart and Theodore Willke, "Integrated Antennas and Filters Fabricated Using Micromachining Techniques," *IEEE Aerospace Conference*, CO, USA, March 1998.
- [20] Yohannes M. Destaa, Georg Aigeltinger', Kevin J. Zancaa, Phil Coanec, Jost Göttert, Michael C. Murphya, "Fabrication of Graphite Masks for Deep and Ultra-deep X-ray Lithography," *Proceedings of SPIE*, vol. 4175 (2000), 122-130.
- [21] Philip Coane, Robert Giasolli, Francesco De Carlo, Derrick C. Mancini, Yohannes Desta, and Jost Göttert, "Graphite-based x-ray masks for deep and ultradeep x-ray lithography," *Journal of Vacuum Science & Technology B* 16, 3618 (1998).
- [22] Sven Achenbach, Martin Boerner, Seichin Kinuta, Walter Bacher, Juergen Mohr, Volker Saile, Yasunori Saotome, "Structure quality in deep X-ray lithography applying commercial polyimide-based masks," *Microsyst Technol* 13:349–353.
- [23] S. Achenbach, D. Klymyshyn, D. Haluzan, T. Mappes, G. Wells, J. Mohr, "Fabrication of RF MEMS Variable Capacitors by Deep X-Ray Lithography and Electroplating," *Proc. High Aspect Ratio Micro-Structure Technology* (HARMST 2005), Gyeongju, Korea, June 2005.

# Appendix D

## The Electromagnetic Spectrum and Wireless Applications

The electromagnetic spectrum (left), the radio spectrum applicable to medium and high data rate communications (middle), and typical wireless applications at these frequencies (right) [1] © Artech House 2010<sup>54</sup>.



### Reference

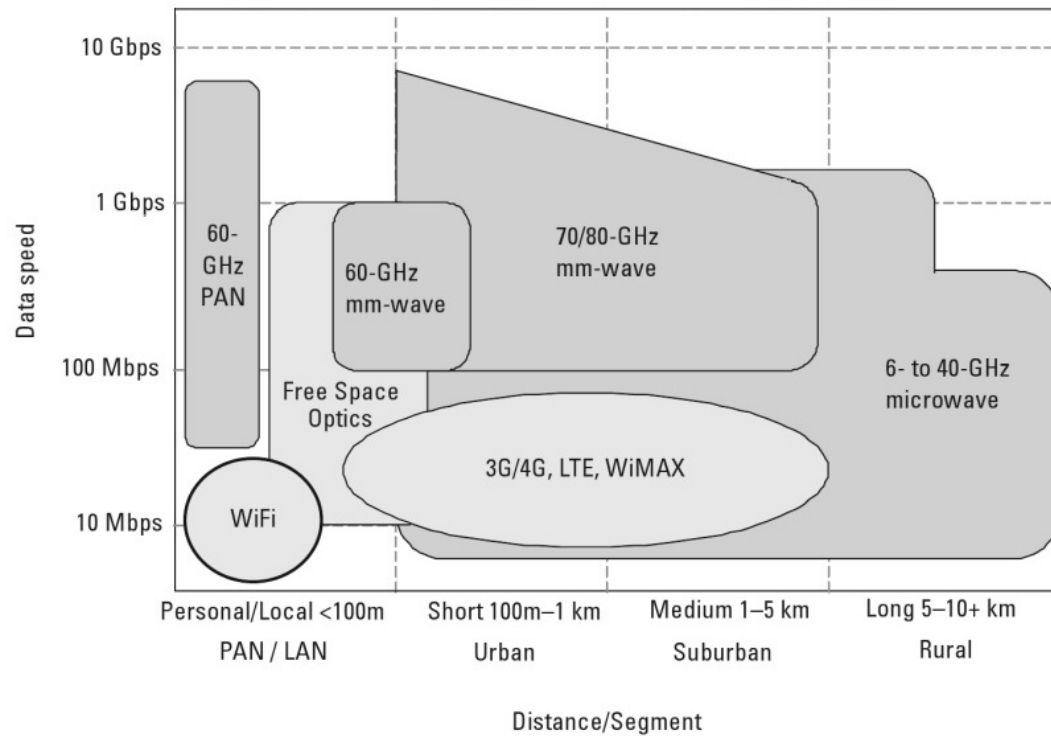
[1] Jonathan Wells, *Multigigabit Microwave and Millimeter-Wave Wireless Communications*, Artech House, 2010.

<sup>54</sup> Permission to use is acquired from Artech House Inc.



# Appendix E

The high data rate wireless landscape [1]<sup>55</sup>.



## Reference

- [1] J. Wells, "Faster than fiber: The future of multi-G/s wireless," *IEEE Microwave Magazine*, vol. 10, no. 3, pp. 104-112, May 2009.
- [2] R. Fisher, "60 GHz WPAN Standardization within IEEE 802.15.3c," *International Symposium on Signals, Systems and Electronics*, Montreal, Que.2007.

<sup>55</sup> © IEEE 2009; In this figure, personal area network (PAN), mostly wireless (WPAN [2]) is a wireless network used for fast data transmission among devices like laptops, cell phones, and personal digital assistants like cameras. It can be expanded not only to locally connect such devices, but also to connect them to the internet. A simple example of WPAN is the connectivity that the Bluetooth provides.